

Joint final report/gemeinsamer Schlussbericht

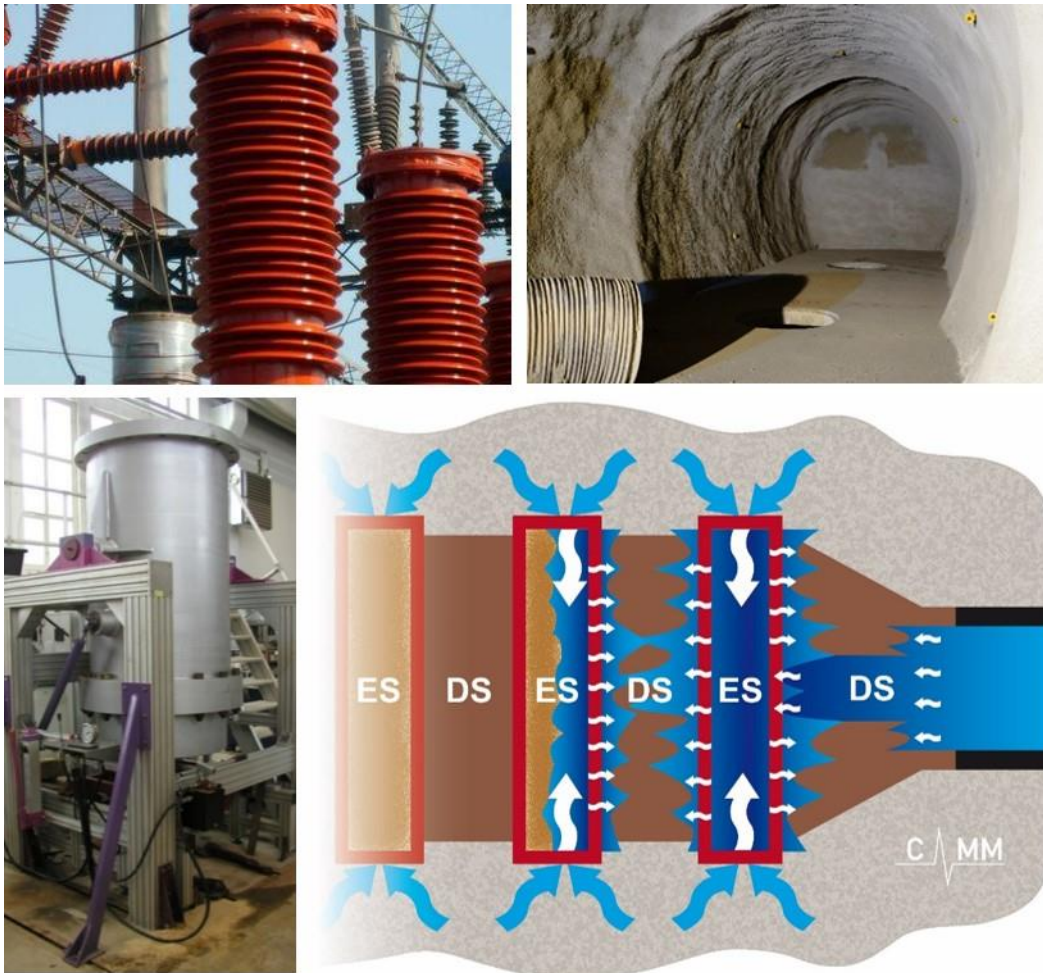
Joint project: Vertical hydraulic sealing system based on the sandwich principle - preproject (Sandwich-VP)

Verbundprojekt: Vertikales hydraulisches Dichtsystem nach dem Sandwich-Prinzip – Vorprojekt (Sandwich-VP)

Funding agency/Zuwendungsgeber: German Federal Ministry for Economic Affairs and Energy/Bundesministerium für Wirtschaft und Energie

Funding reference/Förderkennzeichen: 02E11587A / 02E11587B

01.07.2017 – 30.06.2019 (24 months)



Karlsruher Institut für Technologie

Gesellschaft für Anlagen- und Reaktorsicherheit (GRS)
gGmbH



Supported by:



Federal Ministry
for Economic Affairs
and Energy

on the basis of a decision
by the German Bundestag

MANAGED BY



PTKA

Project Management Agency Karlsruhe

Karlsruhe Institute of Technology

The Sandwich-VP was part of SW-A and SW-B experiments at Mont Terri rock laboratory.

BGR, Swisstopo, Enresa, NWMO, RWM and ENSI contributed to SW-A and SW-B with own resources.

Responsibility for the content of this publication lies with the authors.

Authors

Katja Emmerich, Rainer Schuhmann, Franz Königer, Peter Bohac, Laure Delavernhe
Competence Center for Material Moisture CMM, Karlsruhe Institute of Technology (KIT-CMM), Karlsruhe

Klaus Wieczorek, Oliver Czaikowski
Gesellschaft für Anlagen- und Reaktorsicherheit (GRS) gGmbH, Braunschweig

Jürgen Hesser, Hua Shao
Federal Institute for Geosciences and Natural Resources (BGR), Hannover

David Jaeggi, Paul Bossart
Swisstopo, Bern, Switzerland

Jürgen Hansmann
Eidgenössisches Nuklearsicherheitsinspektorat (ENSI), Brugg, Switzerland

Matthias Gruner, Martin Hofmann, Jan Aurich
TU Bergakademie Freiberg (TUBAF)

Christopher Rölke, Till Popp
Institute of Geomechanics GmbH Leipzig (IfG)

Ralf Diedel, Matthias Schellhorn, Sarah Häußler
Stephan Schmidt Group (SSG), Langendernbach

Uwe Glaubach, Thomas Wilsnack
IBeWa Engineering partnership for mining, water and landfill technology, Wilsnack and Partners, Freiberg

Gerhard Kemper
GGG GmbH – Geotechnology, Geoinformatics and Services, Speyer

José Luis García-Siñeriz
Amberg, Alcobendas, Spain

Maria Villar, Carlos Gutiérrez-Álvarez, Rubén J. Iglesias
CIEMAT, Madrid, Spain

Content

Summary (German/English)	5
Introduction	9
1 State of the art – Shaft seals (WP1)	13
1.1 Shaft sealing Whiteshell URL (Canada)	13
1.2 Experimental shaft sealing HADES URL (Belgium)	18
1.3 Experimental borehole sealing Mont Terri URL (Switzerland)	23
1.4 Experimental shaft sealing in Salzdettfurth mine (Germany)	27
1.5 Experimental drift sealing in Sondershausen (Germany)	32
1.6 Input from the Beacon project	40
2 Definition of objectives of the large-scale experiment (WP2)	43
3 Test site (WP3)	45
3.1 Construction	45
3.2 Geology of Niche 7	48
4 Materials for sealing and equipotential layers (WP4)	51
4.1 Methods	51
4.1.1 Sample preparation	51
4.1.2 X-ray diffraction analysis (XRD)	51
4.1.3 X-ray fluorescence analysis (XRF)	51
4.1.4 Simultaneous thermal analysis (STA)	51
4.1.5 Cation exchange capacity (CEC) measurement and analysis of exchangeable cations	52
4.1.6 Conductivity measurement and analysis of dissolved ions	52
4.1.7 pH and fluid density	53
4.1.8 Water content (w) and moisture (w_m)	53
4.1.9 Bulk, dry, specific density (ρ_b , ρ_d , ρ_s), effective montmorillonite dry density (EMDD)	53
4.1.10 Water adsorption isotherms	54
4.1.11 Particle size distribution (PSD)	54
4.1.12 Water adsorption according to Enslin-Neff	55
4.1.13 Swelling pressure (p_s), gas permeability and liquid permeability	56
4.1.14 Suction pressure measurement and water retention curves (WRC)	62
4.1.15 Rising height	65
4.1.16 Time-domain reflectometry (TDR)	66
4.2 Fluids	71
4.2.1 Pearson water	71
4.2.2 Tap water and deionized water	72
4.2.3 NaCl brine	72
4.3 Materials for sealing layers	73
4.3.1 Material selection, processing and compaction	73
4.3.2 Water adsorption isotherms and storage	76
4.3.3 Calcigel	78
4.3.3.1 Phase content	78
4.3.3.2 CEC, exchangeable cations and soluble ions	78
4.3.3.3 Water retention curve	79
4.3.4 Secursol UHP	80
4.3.4.1 Phase content	80
4.3.4.2 CEC, exchangeable cations and soluble ions	81
4.4 Materials for equipotential layers	82
4.4.1 Water retention curves	82
4.4.2 Rising height	86
4.4.3 RRSB net	88
4.4.4 Saturated hydraulic conductivity	91

4.5 Gravel	92
4.6 Swelling pressure test	93
4.6.1 Calcigel	93
4.6.2 Secursol UHP	94
4.6.2.1 Porosity, initial saturation and gas permeability	94
4.6.2.2 Swelling pressure and liquid permeability	96
4.6.3 Summary	99
4.7 MiniSandwich experiments	100
4.7.1 Experimental procedure	100
4.7.2 Results (HM)	103
4.7.3 Results (C)	106
4.8 Semi-technical scale experiments (HTV)	108
4.8.1 Experimental design	108
4.8.2 HTV-5	110
4.8.2.1 Experimental process	110
4.8.2.2 Pressure	111
4.8.2.3 Fluid propagation	113
4.8.2.4 Dismantling	119
4.8.2.5 Water content and density	119
4.8.2.6 Ion transport and cation exchange	122
4.8.3 HTV-6	128
4.8.3.1 Experimental process	128
4.8.3.2 Pressure	128
4.8.3.3 Fluid propagation	132
4.8.3.4 Dismantling	132
4.8.3.5 Water content and density	133
5 Experiment design (WP5)	137
5.1 Dimension	137
5.2 Hydration system	138
6 Scoping calculations (WP6)	139
6.1 Simulations using Code_Bright (GRS)	139
6.1.1 Geometrical model	139
6.1.2 Physical model	140
6.1.3 Material data	141
6.1.4 Simulation variants, schedule, and boundary conditions	142
6.1.5 Results	144
6.1.5.1 Pore pressure before excavation of Gallery 18 West	144
6.1.5.2 Situation before Sandwich seal emplacement in shaft 1	144
6.1.5.3 Situation after pressurizing the injection chamber	146
6.1.5.4 Further evolution (hydraulic simulation)	147
6.1.6 Perspective	149
6.2 OGS simulations (BGR)	149
6.2.1 Scoping calculations for in-situ experimental design	149
6.2.2 Determination of Sandwich parameters using data from MiniSandwich test	150
6.2.3 Estimation of in-situ test duration under different test conditions	153
6.3 COMSOL simulation (ENSI)	154
6.4 Conclusions	155
7 Construction techniques and installation (WP7)	157

8 Instrumentation (WP8)	161
8.1 Rock instrumentation	162
8.2 EDZ characterization	166
8.3 Shaft 1 instrumentation	166
8.3.1 Water content measurement	168
8.3.2 Pore pressure and total pressure measurements	170
8.3.3 Relative humidity and temperature	171
8.3.4 Temperature	171
8.3.5 Displacements	171
8.4 Wireless data transmission	172
8.4.1 Introduction	172
8.4.2 Adapting the existing concepts	173
8.4.3 In-situ feasibility test	173
8.5 Data acquisition and storage	176
9 The large-scale experiment (WP9)	177
Abbreviations	179
Acknowledgements	181
References (incl. publications of the project)	183
Appendix	

Summary (German)

Die sichere Einlagerung radioaktiver Abfälle soll durch diversitäre und redundante Barriersysteme in einem Endlager gewährleistet werden. Neben dem Wirtsgestein sind geotechnische Barrieren wie Schachtverschlüsse von besonderer Bedeutung. Bentonite gelten in verschiedenen internationalen Konzepten für Endlager für radioaktive Abfälle in allen Arten von Wirtsgesteinen als das bevorzugte Dichtungsmaterial für geotechnische Barrieren. Dennoch sind Fragen der Planung, Konstruktion und Prüfung von langzeitsicheren Barrieren und deren Komponenten nach wie vor von großer Bedeutung.

Ein vielversprechendes Konzept für Dichtungselemente, insbesondere in Tongestein, ist das vom KIT entwickelte Sandwich-System. Dieses besteht aus abwechselnden Schichten aus Bentonit (den Dichtsegmenten, DS) und Equipotentialsegmenten (ES) mit höherer hydraulischer Leitfähigkeit. Fingering innerhalb der Dichtung sowie der Bypass entlang der Kontaktzone zum Wirtsgestein und der Auflockerungszone (ALZ) können reduziert werden, wodurch eine homogene Hydratation und Quellung die Wirksamkeit des Dichtsystems deutlich verbessert.

Laborexperimente in verschiedenen Maßstäben, die die Funktionalität des Sandwich-Systems belegen, wurden erfolgreich abgeschlossen. Der nächste Schritt ist ein in situ Experiment, bei dem die Wechselwirkung mit dem Wirtsgestein berücksichtigt wird. Für die Durchführung eines solchen Experiments eignet sich besonders das internationale Felslabor Mont Terri (CH) im Opalinuston, um die vertikale Installation des Sandwich-Dichtungssystems zu demonstrieren und seine Interaktion mit Opalinuston zu untersuchen. Da der geplante Großversuch eine umfassende Planung erfordert, wurde das Sandwich-Vorprojekt (VP) im Rahmen des Förderkonzeptes des Bundesministeriums für Wirtschaft und Energie - "Forschung zur Entsorgung radioaktiver Abfälle" (2015-2018) in Zusammenarbeit mit internationalen Partnern durchgeführt.

Das Arbeitsprogramm wurde in neun Arbeitspakete (AP) unterteilt. Die Auswertung bestehender Versuche an Verschlussystemen lieferte notwendige Informationen zur Implementierung eines Schachtverschlusses (AP1). Fünf Hauptziele des Großversuchs (Machbarkeit der Installation; Untersuchung des Sättigungsprozesses; Qualifizierung von Mess- und Überwachungstechniken; Bewertung der Dichtwirkung und Auswertung/Validierung sowie Risikomanagement) wurden im AP2 definiert. Im Felslabor Mont Terri (MTRL) wurde eine Nische in der unteren sandigen Fazies des Opalinustons als Versuchsort für den Großversuch erstellt (AP3). Materialparameter für verschiedene in Deutschland geförderte Rohstoffe für DS und ES in Wechselwirkung mit Pearson Wasser, der Porenflüssigkeit von Opalinuston im Felslabor Mont Terri, wurden in Einzelmaterialtests sowie in MiniSandwich und in halbtechnischen Experimenten (AP4) untersucht. Auf der Basis einer Dimensionsanalyse werden 4 (3) DS einer selbstverdichtenden binären Bentonitmischung, die mit 5 (4) ES sandwichartig angeordnet sind, in die zwei Versuchsschächte eingebaut. Eine Druckkammer am Boden jedes Schachtes zusammen mit einem doppelten Back-up Hydratisierungssystem ermöglicht die Aufsättigung des Dichtungssystems (AP5). Modellrechnungen (AP6) zeigten, dass das Experiment ohne eine unzulässige gegenseitige Wechselwirkung zwischen den beiden Schächten oder den Dichtungssystemen in den Schächten und dem Tunnel durchgeführt werden können. Darüber hinaus bestimmt die Saugspannung des Bentonits und nicht der Injektionsdruck die Aufsättigung. Beide Schächte mit einem Durchmesser von 1,2 m werden mit einem einzigen Kernrohr (AP7) gebohrt. Insgesamt werden etwa 75 Sensoren pro Schacht zur Überwachung des Experiments installiert. Die Instrumentierung des Opalinustons liefert den Ausgangszustand des Gesteins vor der Abtäufung der Schächte. Änderungen der Gesteinseigenschaften werden während des

Experiments umfassend überwacht. Weitere Sensoren werden an der Grenzfläche Schachtwand/Dichtungssystem sowie im Dichtungssystem selbst (AP8) installiert. Die Dauer des Großversuchs ist derzeit auf vier Jahre ausgelegt. Abtäufung, Probenahme, Instrumentierung, Installation und Durchführung des Experiments sind im Entwurf des Testplans (AP9) detailliert beschrieben, der als separates Dokument verfügbar ist.

Summary (English)

The safe containment of radioactive waste should be provided by a diverse and redundant barrier system in underground repositories. In addition to the host rock, geotechnical barriers such as shaft seals are of particular importance. Bentonites are considered as the favored sealing material for geotechnical barriers in various international concepts for radioactive waste repositories in all types of host rocks. Nevertheless, questions regarding the design, construction and testing of structures and their components which are reliably functioning in the long-term are still of considerable importance.

A promising concept for seal elements, especially in clay rock, is the Sandwich system developed by KIT. The respective seal consists of alternating layers of bentonite (the sealing layers, DS) and equipotential layers (ES) with higher hydraulic conductivity. Fingering inside the seal as well as bypass along the contact zone to the host rock and the excavation damaged zone (EDZ) can be reduced. A homogeneous hydration and swelling promotes high performance.

Mock-up experiments showing the functionality of the sandwich system have been successfully completed. The next step is a large-scale experiment taking into account the interaction with the host rock. For performing such an experiment, the international Mont Terri rock laboratory (CH) situated in Opalinus clay offers an excellent site for demonstration of the vertical installation of the Sandwich sealing system and to study its interaction with Opalinus clay. Since the envisaged large-scale experiment requires comprehensive planning, the Sandwich pre-project (VP) in the frame of funding concept of the Federal Ministry of Economics and Energy - "Research on Radioactive Waste Disposal" (2015-2018) was carried out in cooperation with international partners.

The work program was divided in nine work packages (WP). The evaluation of existing experiments on seals provided necessary information on the implementation of a shaft seal (WP1). Five main objectives of the large-scale experiment (Feasibility of installation; investigation of the saturation process; qualification of measurement and monitoring techniques; assessment of sealing effectiveness and evaluation/validation as well as risk management) were defined in WP2. A niche was excavated at Mont Terri rock laboratory (MTRL) in the lower sandy facies of the Opalinus clay to provide the test site for the large-scale experiment (WP3). Material parameters for different raw materials mined in Germany for DS and ES in interaction with Pearson water, which is the pore fluid of Opalinus clay at Mont Terri rock laboratory, were studied in single material tests as well as in MiniSandwich and in semi-technical scale experiments (WP4). The two experimental shafts feature 4 (3) DS of a self-compacting binary bentonite mixture sandwiched with 5 (4) ES based on dimension analysis. A pressure chamber at the bottom of each shaft together with a double back-up hydration system will enable the saturation process of the sealing system (WP5). Scoping calculations (WP6) showed that the experiment could be performed without an inadmissible mutual interaction between the two shafts or the seal systems in the shafts and the gallery. Furthermore, the bentonite suction pressure and not the injection pressure will govern the resaturation. Both shafts of a diameter of 1.2 m will be drilled with a single core barrel (WP7). In total about 75 sensors per shaft will be installed for monitoring of the experiment. Instrumentation of the Opalinus clay rock will provide the initial state of the rock prior to excavation and changes of rock properties will be extensively monitored during the experiment. Further sensors will be installed at the interface of the shaft and the sealing system as well as in the sealing system itself (WP8). The duration of the large-scale experiment is currently scheduled for four years. Excavation, sampling, instrumentation, installation and the conduct

of the experiment are detailed in the draft test plan (WP9), which is available as separate document.

Introduction

Hazardous and radioactive wastes that cannot be utilized any further require careful management and disposal. In 2016, the total waste generated in the EU-28 by all economic activities and households amounted to 2,533,000,000 t. Thereof 100,000,000 t were classified as hazardous waste (Eurostat 2018). These waste volumes are increasing and have decoupled from economic growth. The amount of hazardous waste is now dependent on its legal definition (EUA, 2003). The total solid nuclear waste inventory generated until 2018 was estimated to be 6,317,000 m³ by the International Atomic Energy Agency (IAEA, 2018). Of this amount 22,000 m³ are high-level wastes (HLW).

Both hazardous and radioactive wastes have to be disposed of in underground disposal facilities defined as class 5 (IV of a scale from 0 to IV) landfills for hazardous waste in the "Integrated Landfill Ordinance". The legal regulations (in Germany: KrW-/AbfG, AtomG), together with the implementing and administrative regulations and the site-specific safety regulations, must be observed. For the permanent storage of hazardous waste, still operating or decommissioned mines (preferably in salt formations) can serve as suitable repositories. For radioactive waste, an agreement exists according to which newly built underground repositories are recommended. Salt, clay, and crystalline rocks are suitable as host rocks for underground storage. Nevertheless, host rock-specific safety and repository concepts still remain to be developed.

The safe containment of radioactive waste should be provided by a diverse and redundant barrier system (BMU 2010; StandAG, 2017). For isolating the final waste package and to avoid potential failures in deep geological disposal systems, the Geological or Natural Barrier (GB) and the Engineered Barrier System (EBS) have to be considered. These two barriers form the so-called multi-barrier system.

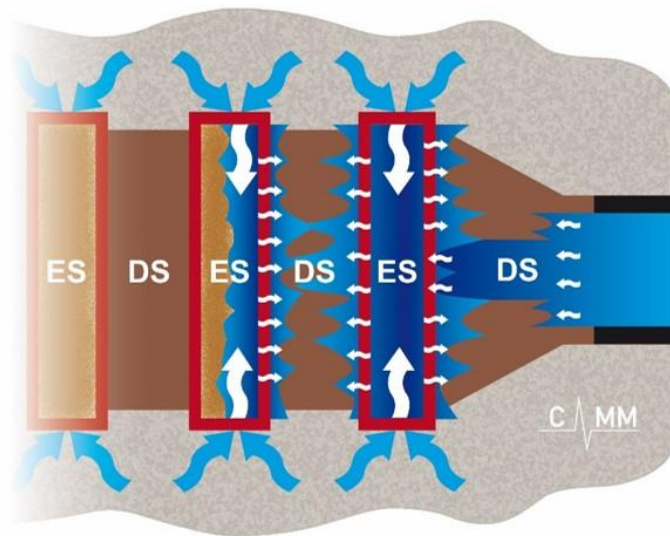
In claystone repository concepts the safe long-term containment of nuclear waste is mainly based on the barrier function of the host rock. Geotechnical barriers (EBS) possess a major sealing function by closing potential pathways along the technically created openings until remaining voids of the repository are fully closed by rock convergence and swelling of the backfill (Jobmann et al., 2016).

Bentonites are considered a favorable sealing material for geotechnical barriers in various international concepts for radioactive waste repositories, i.e. in claystone formations (Switzerland, France, ...) (ENSI, 2012) and in crystalline rock formations (Sweden, Finland, ...) (Gruner, 2010). Furthermore, bentonites are envisaged for shaft seals of repositories in salt formations (Müller-Hoeppe *et al.*, 2012a; Müller-Hoeppe *et al.*, 2012b; Kudla, 2013).

Bentonite based seal concepts commonly consist of a static abutment and a sealing core. The bentonites are installed as dry as possible (granules, pellets or bricks), since they expand in contact with water and generate a swelling pressure. On the other hand, the bentonites should be plastic enough so that a cross section filling seal can be built and a potential rock deformation does not lead to failure. The saturation behavior of bentonites and bentonite mixtures and the resulting swelling pressure together with fluid and gas permeability were studied in laboratory experiments. Installation and monitoring of backfill were tested in semi-technical scale and small-scale in-situ experiments (Breidung, 2002; Mayor *et al.*, 2005; Kupfer and Brandelik, 2004; Schuhmann *et al.*, 2009; Rothfuchs *et al.*, 2012; Svemar *et al.*, 2016). Sand/bentonite mixtures developed by GRS were studied with respect to potentially gas releasing wastes. These mixtures develop a lower swelling pressure and thus a lower gas entry pressure. Consequently, high gas pressures from gas releasing waste within the repository can be avoided (Rothfuchs *et al.*, 2012).

Uniform wetting of the bentonite is the prerequisite for a high functionality and performance. Still, fingering is a known phenomenon in soil physics that leads to an accelerated water flow

along preferential pathways later followed by a water break through and inhomogeneous swelling of the bentonite. The Sandwich sealing system was developed by KIT-CMM (Nüesch *et al.*, 2002). In contrast to conventional monolithic constructions of the sealing element, consisting of one material only, the new system combines layers of different hydraulic properties. The Sandwich sealing system consists of sealing layers (DS) of bentonite and equipotential layers (ES) that are characterized by a higher hydraulic conductivity. Within the ES fluid is evenly distributed over the cross section of the seal. Water bypassing the seal via the EDZ or penetrating the seal inhomogeneously along sensors or by fingering is contained (Schuhmann *et al.*, 2009) and homogeneous hydration and swelling of the DS result. Monitoring by sensors installed in the Sandwich sealing system during operation is possible (e.g. wireless signal transmission) without moisture propagating along sensor cables. Full saturation is obtained faster and the Sandwich sealing system can act as a gas valve.



Sandwich sealing system

The DS ensure the required sealing properties. The ES equalize the wetting of the DS. It can assimilate bypassing water. Due to its capillary properties, a two-dimensional planar wetting of the bentonite interfaces is guaranteed. The ES contributes significantly to the stability of the seal. Due to the smaller dimensions of the individual components, prefabrication is also conceivable, while the ES also contributes to construction and safety engineering. The following aspects of ES must be investigated in particular: the interface to bentonite (DS) (drying out, cracks, temperature, water transport) and the potential ratios (capillary matrix potential). The critical points requiring further investigation (DS-ES interface, installation condition, etc.) could be identified using construction and safety engineering. The bentonite in DS is installed in the air dry state in the form of shaped bricks, pellets, briquettes, granules or mixtures. Relevant and extensive experience exists in this field.

The DS will be constructed much smaller than the previously known monoliths. This will ensure higher quality with regard to homogeneity, density and interface contact to the rock (edges, especially ridges). For the ES, use of dusty, gassing, biologically non-inert and corrosive materials (according to mining law) is excluded. During construction, the positions of fissures, cracks and distortions in the rock must be taken into account. The hydraulic performance of the ES must be dimensioned accordingly. The stability of the ES, which are made of unstable material as a rule, must be ensured by suitable structural measures. The grain structure must also be sufficiently stiff, e.g. to absorb pressure from the rock. No matter how small the volume

reduction in the ES is, the desired positive effect of the swelling pressure of the DS can be diminished. On the other hand, the swelling pressure could be controlled in this way. The material of the ES must be installed in such a way that the suction pressure difference in the ES does not cause any drying in the DS, even during the construction phase. Stability against temperature gradients must be ensured (thermally induced water transport). The possibility of pre-assembly must also be taken into account, under consideration of the permissible dimensions and weights. Special attention must be paid to the transition from DS to ES. At this interface, the following aspects shall be investigated in particular:

- Drying of the sealing segment (during construction)
- Crack formation in the sealing segment
- Moisture loss of the sealing segment
- Effect of a temperature gradient

The seal system will be validated for different host rocks, taking particularities of each host rock into account. In principle, the seal system can be used for all host rocks (salt, crystalline, clay) if it is dimensioned appropriately. For clay or claystone, two specific boundary conditions have to be taken into account:

- In the rock contour surrounding the seal limited water pathways exist, i.e. depending on sufficient potential difference water transport from the host rock into the seal or vice versa is possible.
- Clay based host rocks exhibit a geotechnical behavior similar to that of the DS material, i.e. special considerations have to be made regarding the choice of material. The DS/host rock transition must be designed in such a way that any distortions that may occur in the host rock do not propagate unhindered through the seal. Sufficient stability of structural conditions must also be ensured.

Based on material properties and corresponding to the specific needs of the repository the seal has to be dimensioned as a function of the estimated fluid mechanics and thermodynamics variables (Truckbrodt, 1996). Every physical quantity can be represented as a power product of the basic dimensions [l, t, m, T], where l represents the length, t the time, m the mass and T the temperature. For n dimensionless quantities and m dimensions, n - m dimensionless arguments arise (Buckingham Pi theorem).

The moisture penetration in the seal can be represented as a function of flow:

$$Q = f(k_u, \rho_l, \nu_l, g, B, y, v) \quad (T = \text{konst.})$$

with k_u denoting unsaturated hydraulic conductivity, ρ_l density of the liquid, ν_l viscosity of the liquid, g gravitational acceleration, B and y being the geometric lengths (width and height or depth) and v velocity. At the time of observation, the seal is intact, i.e. $Q = 0$. The energy loss in the seal corresponds to the hydrostatic pressure. The reference values are y, ρ_l, ν_l . All other values can be displayed in a dimensionless manner, e.g. the unsaturated hydraulic conductivity.

$$[k_u] = [y]^{a_1} [\rho_l]^{b_1} [\nu_l]^{c_1} \quad \text{with } a_1 = 1, b_1 = -1 \text{ and } c_1 = 2$$

This procedure is implemented for all measures. When resolving according to the exponents, four key numbers are obtained:

$$(k_u/v), (v/\nu_l * y), (g * y / \nu_l^2), (B/y)$$

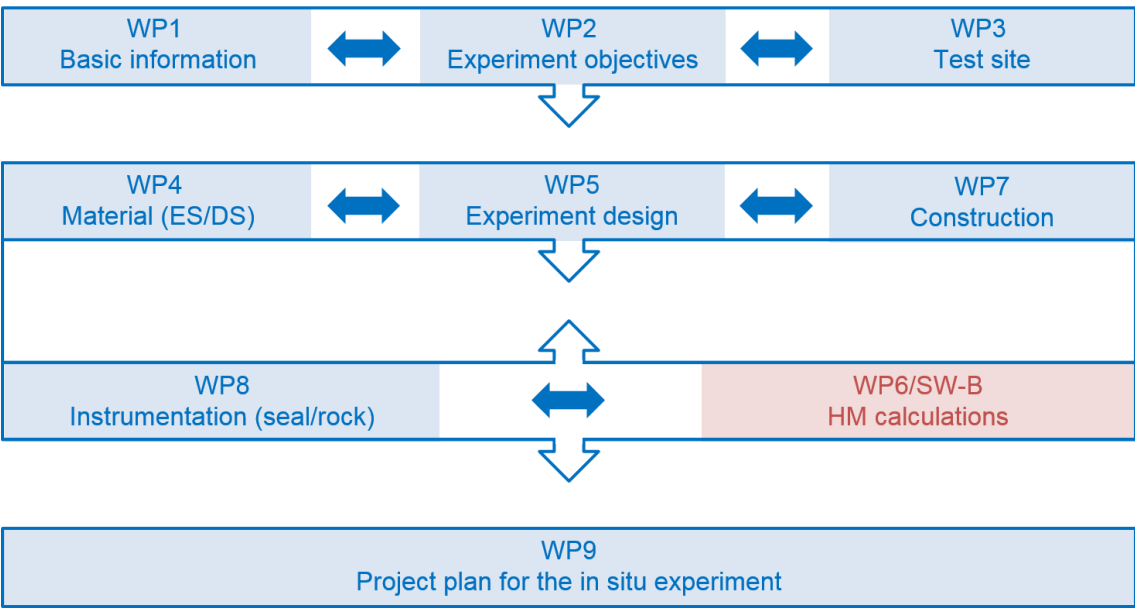
As a result, the fluid properties and geometry are retained. The test scale can be defined with the aid of dimension analysis.

Shaft sealing systems play a major role in safety concepts, because access to the deep storage area requires piercing at certain points through the geological barrier. This represents the most likely pathway of radionuclides between the repository and the biosphere. Shaft seals will limit fluid inflow from adjoining rock in the early stage after closing the repository and delay the release of possibly contaminated fluids from the repository at a later stage. The duration of proper functioning of the shaft seals results from the site-specific safety concept, e.g. the German concept covers 50,000 years (Jobmann et al., 2016). Design of shaft seals depends on site-specific conditions in the host rock and adjoining rock formations (Jobmann et al., 2015).

The modular concept for static and hydraulic elements of shaft seals was refined in ELSA I (02 E 10921) and II (02 E 11193) (Kudla et al., 2013; Kudla et al., 2016) based on the repository models NORTH and SOUTH for claystone formations in Germany, which were defined in the AnSichT project (02E11061). Both concepts differ considerably due to the different intersected rock formations (Jobmann et al., 2016), but use the hydraulic Sandwich sealing system (Nüesch et al., 2002) as a component of the lower seal in the host rock (Herold et al., 2018). Opalinus clay of the Middle Jurassic is considered the host rock formation in the repository model SOUTH.

Functionality of the Sandwich sealing system under the inflow of Pearson water (pore fluid of Opalinus clay (Pearson et al., 2003) was proven on the semi-technical scale in ELSA II and Sandwich-VP (02 E 1158) for a defined fluid injection pressure. Furthermore, material parameters for different national raw materials for DS and ES in interaction with Pearson water were studied. Determination of material parameters on the laboratory scale and proof of functionality on the semi-technical scale are necessary but not sufficient to validate the long-term performance of the Sandwich sealing system. A large-scale in-situ experiment is mandatory to study the processes in and performance of any sealing system under real conditions in interaction with a potential host rock (Van Geet et al., 2009).

The international Mont Terri rock laboratory (CH) situated in Opalinus clay offers an excellent site for demonstration of the vertical installation of the Sandwich sealing system and to study its interaction with Opalinus clay. The sandy facies of the Opalinus clay at the Mont Terri rock laboratory is similar to the Opalinus clay formation considered in the repository model SOUTH. Comprehensive planning of the in-situ experiment has been performed in the Sandwich-VP (SW-A/SW-B) project. Work was divided into nine work packages.



1 State of the art – shaft seals (WP1)

While material parameters of sealing materials were studied in detail on the laboratory scale (chapter 1.6) and the functionality of the Sandwich sealing system was proved on the semi-technical scale, only few large-scale experiments of bentonite seals were performed. The Whiteshell URL (Canada) in crystalline rock was sealed after completion of the research activities (Enhanced Sealing Project (ESP) (chapter 1.1). In clay formations, only one experimental shaft seal mock-up test was performed at the HADES URL, in plastic clay rock (chapter 1.2). In Germany two large-scale experiments with bentonite seals were performed, in rock salt formations only: (1) as part of a shaft seal system in the Salzdettfurth salt mine and (2) as sealing system in a drift in the salt mine Sondershausen (chapter 1.4 and 1.5). In the Sondershausen test, fingering and large axial displacements of the seal were observed, which caused the dry density and swelling pressure to decrease. In addition, borehole sealing tests were performed at the Mont Terri rock laboratory (chapter 1.3).

1.1 Shaft sealing Whiteshell URL (Canada)

Project name/Acronym Enhanced Sealing Project (ESP)	Location Whiteshell Laboratory, Manitoba, Winnipeg, Canada	Type /Scale Two full-scale shaft sealings
Lead organizer/Main partners ANDRA, NMMO, CNL, Posiva, SKB	Start date/End date 2008-2019 3 phases	Reference concept if pertinent
Installation material parameters Main shaft: bentonite/sand (40/60) Ventilation shaft: bentonite/sand (70/30) $\rho_d = 1800 \text{ kg/m}^3$, $w = 12\%$	Fluid saturation natural	Interfaces/Host rock Granitic (Canadian Shield) Main shaft: drill and blast Vent shaft: raise-bored
Instrumentation Seal main shaft: 100 sensors	Modeling COMSOL Multiphysics	Main processes studied <input checked="" type="checkbox"/> T <input checked="" type="checkbox"/> H <input checked="" type="checkbox"/> M <input type="checkbox"/> C
Main objectives of the experiment or modeling study Closure of the URL and limiting of mixing of saline rock pore fluid below fracture zone 2 and fresh near-surface groundwater Demonstration of ability to construct shaft seals Optional: THM monitoring and data collection for future numerical modeling		
Main learning points and relevance to the project Feasibility of installation Natural saturation from water inflow through granitic host rock within about eight years 300 m vertical data transfer for long term monitoring sensor Fiber-optic sensors failed within six years		
Remaining open questions Transfer to clay host rock		
References Martino <i>et al.</i> , 2011; Priyanto <i>et al.</i> , 2011 and 2013; Dixon <i>et al.</i> , 2017		

Setup

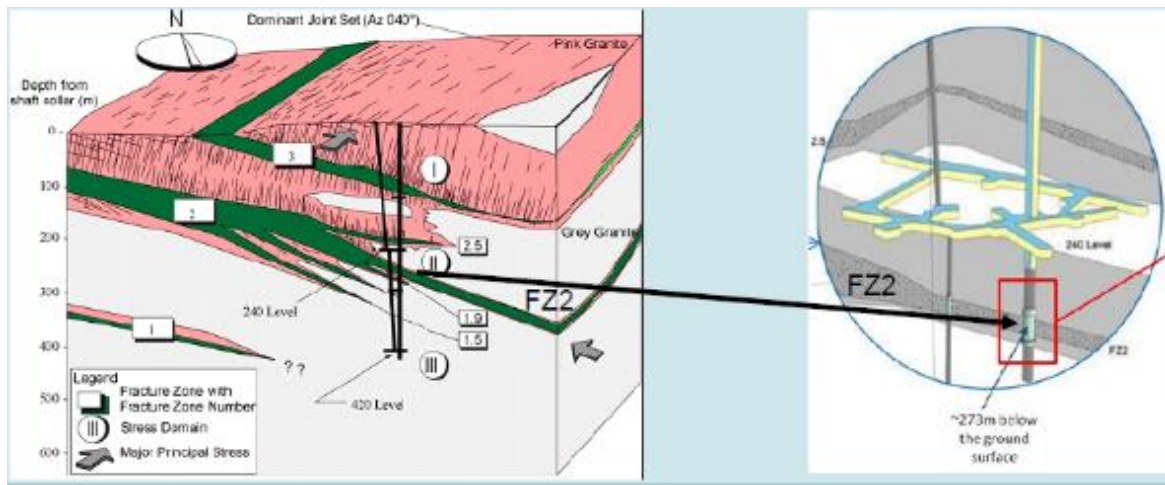


Figure 1.1 Underground layout, fracture zones and sealings (left vent shaft, right main shaft) Dixon *et al.*, 2017

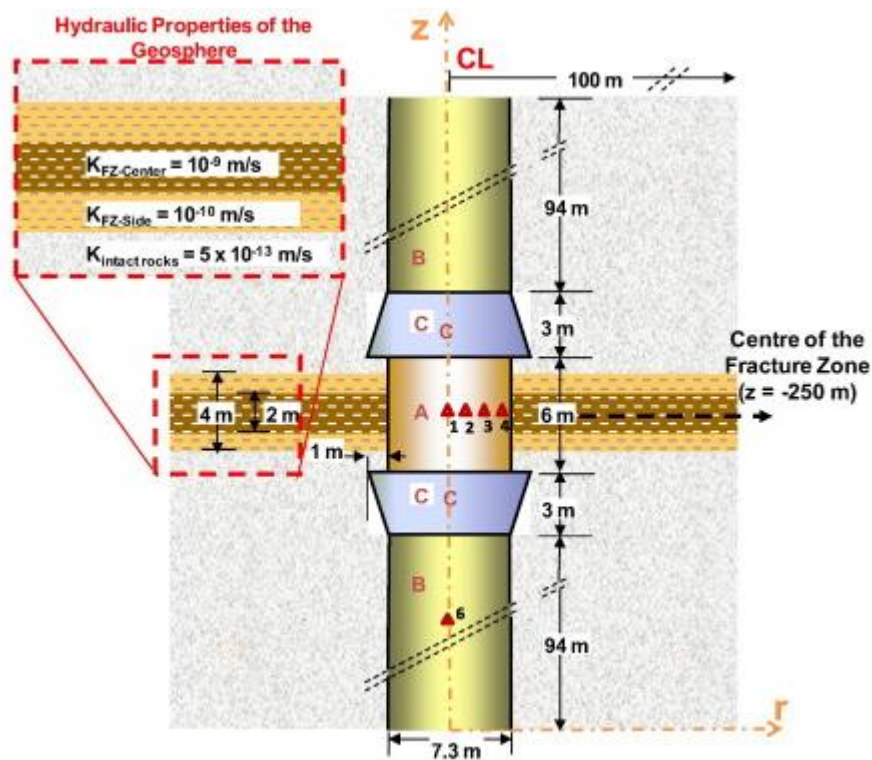


Figure 1.2 Configuration of main shaft seal (Priyanto *et al.*, 2011)

Host rock properties

Granitic (Canadian shield)

Operation of the URL since 1980's, decommissioning and demolition between 2008 and 2014

$10^{-12} - 10^{-13}$ m/s and 10^{-9} m/s in EDZ and $10^{-9} - 10^{-10}$ m/s in fracture zone 2

Porosity 0.003

Dimension and material

	Main Shaft	Ventilation shaft
Depth (below ground surface)	273 m	similar
Plug height	6 m	4.5 m
Plug diameter	4.8 m	1.8 m
Volume	109 m ³	12 m ³
Material	40% Wyoming Bentonite* 60% Qz sand, (<u>dry mass portion</u>) *80% Smectite	70% Kunigel VI Bentonite+30% Qz sand blocks (dry density 2000 kg/m ³) from TSX project Crushed blocks to fill perimeter gaps and level surface
CEC (bentonite)	80-100 cmol(+)/kg	
Initial water content	12%	
Specific density	2.7 t/m ³	
Dry density	1.8 t/m ³	1.8 t/m ³ (average)
Porosity	0.33	
Initial saturation	65%	
Initial swelling pressure	0.92 MPa	
EMDD	1.05 t/m ³	
Hydraulic conductivity	10^{-12} m/s	

Concrete plug - abutment

Low-heat high-performance concrete (LHHPC) (modified according to Gray and Shenton, 1998), wedge-shaped, 3 m high, keyed 0.5 m into shaft wall (Fig. 1.2, upper plug smaller than lower plug due to shaft diameter)

Porosity 0.009 (!), hydraulic conductivity 10^{-12} m/s (Priyanto *et al.*, 2011)

Standard Design Mix for LHHPC (kg/1 m³)

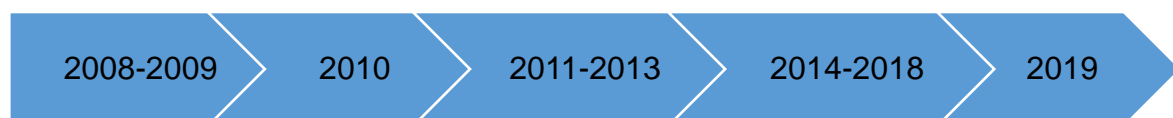
Cement (Type 50) 96.31, Silica fume 96.31, Silica flour 192.42, Sand 888.14, Coarse aggregate 1031.92, Superplasticizer (sodium naphthalene sulfonate based) (dry mass) 10.00, (superplasticizer content was modified by adding 5% more), Water 109.30

Instrumentation

- Only main shaft, shafts are connected below and above seals, equal hydraulic pressure
- Redundancy and overlap of sensor types
- 100 sensors (64 short term up to 3 a, 36 long term)
- 2014: 30/36 sensors working
- 2017: 22/36 sensors working
 - All fiber-optic sensors failed within 6 a
 - Most vibrating wire sensors were operational
 - TDR were operational

Bentonite/sand	Moisture/Water content	TDR Thermocouple psychrometer
	Total pressure	Fiber-optic total pressure cell Vibrating wire total pressure cell
	Pore-water pressure	Vibrating wire piezometer Fiber-optic piezometer
Rock	Hydraulic pressure	Packer with vibrating wire piezometer
Concrete	Hydraulic pressure	Vibrating wire piezometer
	Total pressure	Vibrating wire total pressure cell
	Temperature	Thermocouple
	Strain	Fiber-optic deformation sensor
	Vertical displacement	Fiber-optic displacement transducer

Operation/Hydration



Installation Intentional flooding below sealings (from 420 m level ?)	Post- construction monitoring	Natural water inflow Flooding level 240 (above sealing) completed	Water inflow ≈ 2.6 m ³ /d (0.15 m/d) since end of 2014 Flooding completed by early 2019 (1600 d) Saturation of bentonite 100% predicted for early 2019	Brief period of monitoring in hydraulic steady state
--	-------------------------------------	--	---	---

2017: ≈ 173 m water column (100 m below ground surface)

Liquid

Above fracture zone 2: Fresh water

Below fracture zone 2: Saline fluid (up to 90 g/l total dissolved solids)

Modeling

HM modeling, e.g. prediction of pore water pressure difference across the shaft seal and pore water pressure at the seal position was performed using COMSOL.

Monitoring data will be used for performance modeling, which is expected to be difficult in part due to the difficulty in establishing all the features, events, and processes (FEPs) affecting the installation.

Results

2011 nearly complete saturation of outer 0.5 m perimeter ($\approx 41 \text{ m}^3$)

Early 2015 little water uptake in inner core

Late 2016 well advanced saturation in clay fill (predicted saturation in 2016 later corrected to early 2019)

Considerable stress equilibration still remains to occur

Poor hydraulic connection between upper and lower shaft section and fault zone 2, i.e. good sealing has been achieved and maintained

1.2 Experimental shaft sealing HADES URL (Belgium)

Project name/Acronym A large-scale in situ demonstration test for repository sealing in an argillaceous host rock (RESEAL)	Location HADES URL, Mol, Belgium	Type /Scale Shaft seal and borehole seal
Lead organizer/Main partners SCK·CEN, CEA, ONDRAF/NIRAS, ANDRA, ENRESA, CIEMAT, UPC	Start date/ End date 1996-2007 2 phases	Reference concept if pertinent FoCa clay, French and Belgian concept
Installation material parameters FoCa clay (Paris Basin) pellets/powder (50/50) w = 6%	Fluid Saturation Artificial Synthetic clay water (SCW)	Interfaces/Host rock Plastic Boom Clay Experimental shaft from experimental work 1982-1983
Instrumentation Seal: 146 sensors Rock: 66 sensors	Modeling CODE-BRIGHT CAST3M	Main processes studied <input type="checkbox"/> T <input checked="" type="checkbox"/> H <input checked="" type="checkbox"/> M <input type="checkbox"/> C
Main objectives of the experiment or modeling study Feasibility (design, safe installation) Confidence building / HM process understanding Performance assessment (diffusive transport in near field)		
Main learning points and relevance to the project Feasibility of installation Clay host rock (but plastic) Hydration system design too complex		
Remaining open questions Upscaling to 1:1 and long-term processes Transfer to indurated clay host rocks Covering of phenomenological repository conditions (natural hydration, gas migration...)		
References Villar, 2004; Van Geet <i>et al.</i> , 2009		

Setup

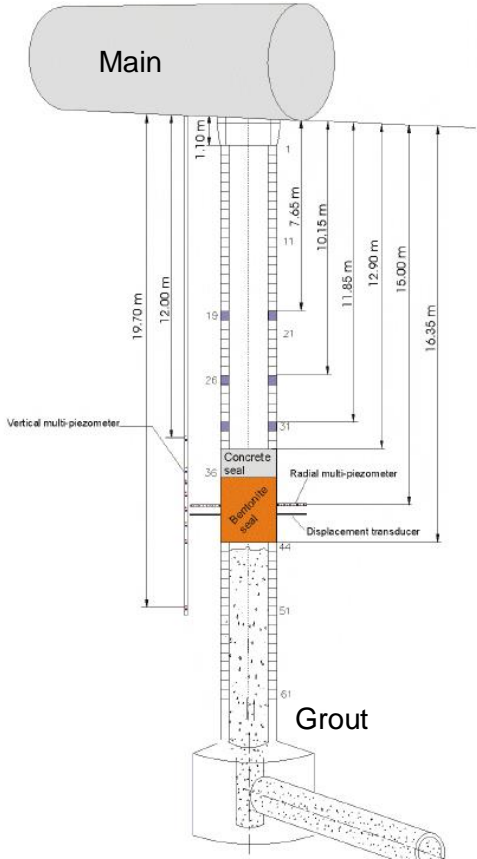


Figure 1.3 Sealing layout (Van Geet *et al.*, 2009)

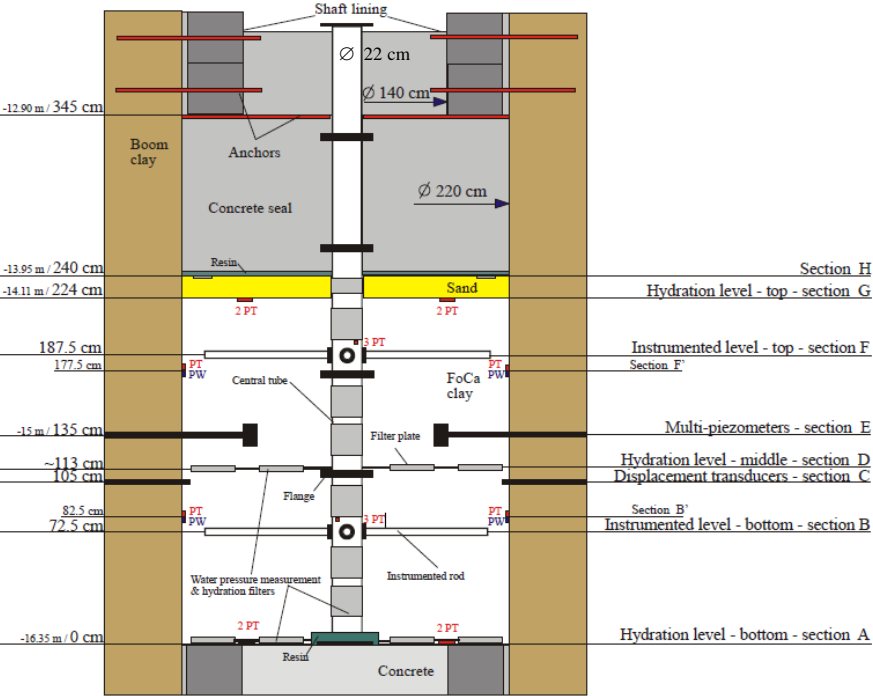


Figure 1.4 Instrumentation of sealing (Van Geet *et al.*, 2009)

Host rock properties

Plastic Boom clay, experimental shaft from experimental work 1982-1983, was brick-lined until start of installation (about 15 a)

Hydraulic conductivity: $k_H \approx 5 \cdot 10^{-12}$ m/s; $k_V \approx 2.5..3.5 \cdot 10^{-12}$ m/s ($k_H \approx 2k_V$)

Dimension and material of of the seal

Depth (under main gallery)	13.95 m – 16.35 m
Concrete plug	h = 1.05 m
Height	2.24 m
Diameter	2.1 – 2.2 m
Volume	≈ 8.4 m ³ (no information on total sensor volume)
Material	FoCa clay (Fourges-Cahaignes clay, Paris Basin) 85-90% Ca-sat. Kao/Bei (0.5) (Villar 2004)
CEC	71 cmol(+)/kg, Ca ²⁺ (73.1), Mg ²⁺ (6.5), Na ⁺ (3.6), K ⁺ (0.8)
Water content (105 °C) (storage 60%rH 20 °C)	10-12%
Water content installation	W _{GT} = 6% (7-8% for production of pellets)
Specific density	2.675 t/m ³
Dry density	1.45 t/m ³ (lower 0.6 m); 1.3 t/m ³ (upper 1.64 m) Resulting overall: 1.33 t/m ³ Increased to 1.41 t/m ³ due to volume decrease by displacement
Bulk density	1.54 t/m ³ (bottom)/ 1.36 t/m ³ (top)
Initial saturation	19% / 15%
Initial hydration state (est.)	6 H ₂ O/Ca ²⁺ ; 2W
Expected swelling pressure	(0.85/0.2 MPa) 0.27 MPa (0.58 MPa) ($p_s = 0.0061\rho_d^{13.272}$)
EMDD	0.82 t/m ³ (because of interstratification)

Instrumentation

Seal	117 sensors
Temperature	Thermocouples
Total stress	Effective stress, swelling pressure
rH	2 different types of rH sensors
Saturation/water content	Thermal pulse
Displacement	Potentiometer and wire-extensometer
Water pressure	Piezometers

Seal/Rock interface	29 sensors , partially inside the seal
Water pressure	
Total stress	
rH	
Temperature	
Rock	66 sensors
Total stress	
Displacement	
Water pressure	

Liquid

Synthetic Clay Water (SCW) 2.28 g/l

MgCl₂*6H₂O (22 mg), KCl (25 mg), Na₂SO₄ (0.3 mg), NaCl (10 mg), NaHCO₃ (1170 mg), H₃BO₃ (43 mg), NaF (11 mg), CaCO₃ (1000 mg, calcium saturated by an excess of solid)

Operation/Hydration



Planning and host rock monitoring	Installation	Artificial hydration 56% of total saturation of seal 2006 Gas break-through test Hydraulic shock test RN migration test in EDZ	Data analysis RN migration test in seal planned	?
-----------------------------------	--------------	--	--	---

Installation: pellets (25x25x15 mm)/powder (50/50)

Lower 0.6 m vibro-compactor; upper 1.64 m manual filling

Central tube with sand layer at top of seal and 2 levels (mid and bottom of seal) of horizontal filters for vertical saturation

Hydration through sand layer at the top of the seal did not work due to a leak

Atmospheric pressure to 0.3 MPa (pump) plus water column at the 3 different depths (0.14, 0.155, 0.17 MPa)

Complex hydration scheme with gas break-through and hydraulic shock test (1.25 MPa) in 2006

After removal of shaft lining, inward convergence of host rock for 0.5 a. Afterwards, seal pushes outward 0.5-1 a. Thereafter, four years inward convergence of host rock and afterwards again swelling of the seal.

Modeling

CODE_BRIGHT: coupled THM problems in double porosity media extended for geotechnical problems in which two overlapping porous media play an important role (as is the case of the highly expansive clays considered in RESEAL) (Sanchez, 2004)

CAST3M software program (Verpeaux et al., 1988). Elementary validations have been realized for the two H, M models:

- Experimental and analytical validation for H model (Bernard-Michel and Genty, 2006);
- Code comparison for the BBM constitutive law in M model (Filippi, 2007).

Results

Seal	
Saturation of seal	56% (1950 L out of 3477 L)
rH	100%
k	$\approx 10^{-12}$ m/s
Gas break-through at 56% saturation	1.3 MPa
Total stress	0.8-1.05 MPa
Pore pressure	0.1-0.5 MPa
Effective stress (swelling pressure?)	0.46-0.71 MPa (4.6-7.1 bar)
Displacement	Volume decrease of 5%
Seal/Rock interface	
rH	100%
Rock	
k	$\approx 10^{-12}$ m/s
Displacement	See operation/hydration

1.3 Experimental borehole sealing in Mont Terri URL (Switzerland)

Project name/Acronym Self-sealing Barriers of sand/bentonite mixtures in a clay repository (SB)	Location Mont Terri Rock Laboratory, St-Ursanne, Switzerland	Type /Scale Borehole seal (four boreholes in-situ and mock-up tests)
Lead organizer/Main partners GRS, NAGRA	Start date/ End date 2003 – 2012 (2 Phases)	Reference concept if pertinent
Installation material parameters Sand/bentonite mixtures (65/35 and 50/50) (Calcigel) w = 6% (bentonite), 1% (sand) One borehole with granular MX-80 for comparison	Fluid saturation Artificial saturation with synthetic clay water (Pearson Water A1)	Interfaces/Host rock Steel/Opalinus clay
Instrumentation Seal: swelling pressure sensors (2 per borehole) Seal and rock: pore pressure sensors	Modeling Code_Bright	Main processes studied <input type="checkbox"/> T <input checked="" type="checkbox"/> H <input checked="" type="checkbox"/> M <input type="checkbox"/> C
Main objectives of the experiment or modeling study Qualify sand/bentonite mixtures as material for engineered barriers with reduced cohesion and gas entry pressure to allow for discharge of corrosion gases while maintaining sufficiently low permeability to water and sufficiently high swelling pressure		
Main learning points and relevance to the project The focus of the experiment was on sand-bentonite mixtures. The data from the borehole with pure bentonite are few. More sensors in the rock would have been needed to better understand the system.		
Suggestions for the Sandwich project / Remaining open questions Interaction with the rock needs to be better understood.		
References Rothfuchs <i>et al.</i> , 2012; Wieczorek <i>et al.</i> , 2017		

Setup

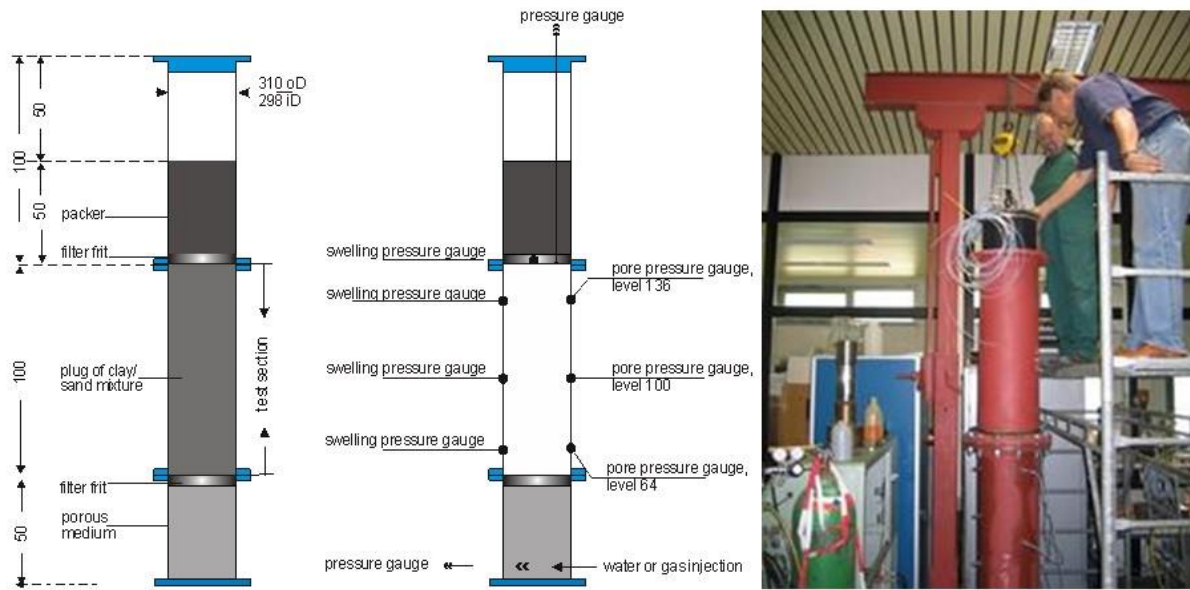


Figure 1.5 Overview of SB mock-up design and instrumentation (Rothfuchs *et al.*, 2012)

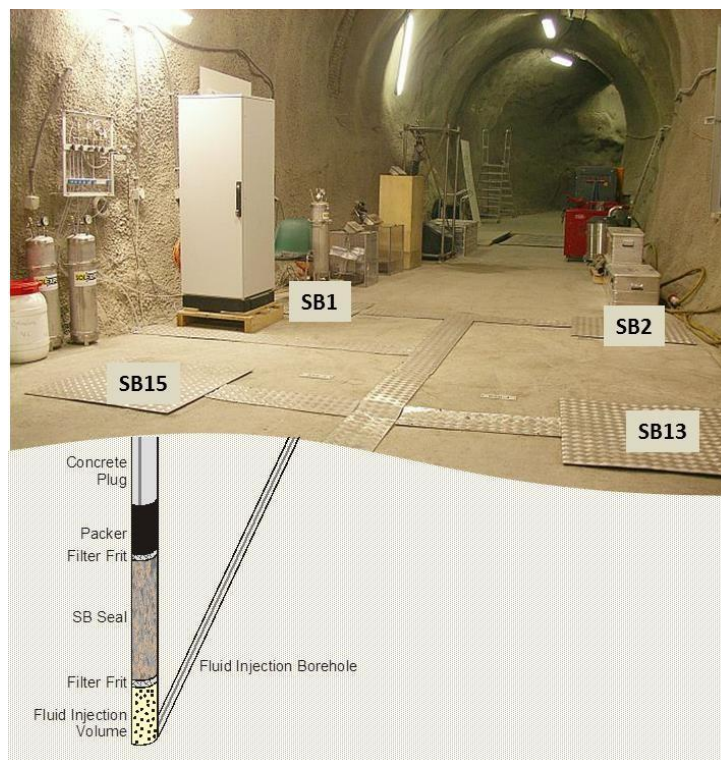


Figure 1.6 Overview of SB in-situ configuration. SB1 and SB2: boreholes with 65/35 sand/bentonite seal, SB15: borehole with 50/50 sand/bentonite seal, SB13: borehole with pure bentonite seal

Host rock properties

Opalinus clay, shaly facies.

Permeability: $k \approx 2 \cdot 10^{-20} \text{ m}^2$; porosity 0.16

Dimension and material of the seal

Depth (under gallery)	1.9 m – 2.9 m (SB1/SB2), 2.4 m – 2.9 m (SB13/SB15)
Concrete plug	$h = 0.5 \text{ m}$
Height	1.0 m (SB1/SB2), 0.5 m (SB13/SB15)
Diameter	0.31 m
Volume	$\approx 0.075 \text{ m}^3$ (SB1/SB2), 0.038 m^3 (SB13/SB15)
Material	65/35 sand/Calcigel (SB1/SB2), 50/50 sand/Calcigel (SB15), MX-80 (SB13)
Initial water content	2.9 – 3.7%
Specific density	$\approx 2.675 \text{ t/m}^3$
Dry density	1.62 t/m^3 (SB1), 1.77 t/m^3 (SB2)
Bulk density	1.72 t/m^3 (SB1), 1.91 t/m^3 (SB2), 1.64 (SB13), 1.69 (SB15)
Expected swelling pressure	0.2 – 0.4 MPa (for the sand/bentonite mixtures)

Instrumentation

Seal	4 sensors per borehole	
Total stress		
Water pressure		
Seal/Rock interface	none	
Rock	5 sensors	
Water pressure	piezometers	

Liquid

Synthetic Clay Water (Pearson Water A1)

Na ⁺ [mmol/l]	K ⁺ [mmol/l]	Ca ²⁺ [mmol/l]	Mg ²⁺ [mmol/l]	Cl ⁻ [mmol/l]	SO ₄ ²⁻ [mmol/l]
235	1.7	25	16	287	14

Operation/Hydration



Laboratory investigations Scoping calculations	Mock-up tests Installation of in-situ tests	Artificial hydration	Gas break-through tests Post-mortem sampling and investigation
---	--	----------------------	---

Test procedure:

- Borehole instrumentation
- Determination of installation density of the granular sand/bentonite mixture
- Determination of initial gas permeability
- Water injection from the bottom to re-saturate the seal
- Determination of seal permeability to water at full saturation
- Gas injection and determination of gas entry pressure and permeability after break-through
- Determination of the final water content in the seal by post-mortem sampling and analysis

Water bypass in SB1 and SB15, successful test only in SB2

Longer time to full saturation than expected

Modeling

Hydro-mechanic simulation with Code_Bright

Results

Seal	
Saturation of seal	about fully saturated (SB2)
k	$\approx 4 \cdot 10^{-18} \text{ m}^2$ (SB2)
Gas break-through at 56% saturation	0.45 MPa (SB2)
Total stress	0.15 – 0.19 MPa (SB2)

1.4 Reference shaft sealing in Salzdetfurth mine (Germany)

Project name/Acronym SA II (BMBF 02C0516)	Location Salzdetfurth Mine K+S, DE	Type /Scale In situ (1 : 2 ... 3) test in a drilled shaft (D = 2.5 m)
Lead organizer/Main partners K+S / TU BAF / IfG / DBE / GRS	Start date/ End date August 1996 / September 2002	Reference concept if pertinent Shaft sealing concept "Salzdetfurth" (reference concept)
Installation material parameters Bentonite (Calcigel), briquettes/granulate (70/30) w = 10% (air dry) ρ_d 1.70..1.75 t/m ³	Fluid saturation Saturated NaCl solution Max. fluid pressure 7 MPa	Interfaces/Hostrock Natural rock salt Stasfurt (Na2)
Instrumentation 109 sensors in 19 layers in the sealing system	Modeling Yes Groups/Codes: IfG: FLAC DBE: TOUGH2 GRS: EMOS	Main processes studied <input type="checkbox"/> T <input checked="" type="checkbox"/> H <input checked="" type="checkbox"/> M <input type="checkbox"/> C Input flow rate Swelling pressure Bentonite density change Moisture distribution
Main objectives of the experiment or modeling study Qualify bentonite mixtures (briquettes and granulate) for hydraulic element of shaft sealing systems for salt mines (static element: column of crushed basalt or diabase, tested separately); Verification of the technical feasibility and reliability		
Main learning points and relevance to the project A hydraulic conductivity of $< 5 \cdot 10^{-10}$ m/s and a swelling pressure of 1 MPa are necessary for the sealing performance of bentonite shaft sealing elements in salt mines. This parameters can be reached, if the bentonite is installed with a minimum water content (equilibration water content to the air) and a dry density of > 1.6 t/m ³ , i.e. by using a binary mixture of 70% Calcigel briquettes (volume 10 cm ³) and 30% Calcigel granulate 0-3 mm (obtained by soft crushing and classification of dry bentonite compacts). At a fluid pressure of 4 MPa the input hydraulic conductivity of the whole system (sealing element with surrounding rock salt) was $5.8 \cdot 10^{-11}$ m/s and $4.4 \cdot 10^{-11}$ m/s at 7 MPa. A swelling pressure of about 1 MPa was reached and the sealing behavior of the bentonite sealing system was improved with time and with increasing load. The dismantling of the sealing system provided the moisture distribution in the sealing system and the condition of the surrounding rock salt in the final step of the experiment.		
Suggestions for the Sandwich project / Remaining open questions The main topics of the experiment are recommended to be repeated, but the following topics could be solved differently: Integration of ES for a more homogenous fluid spreading in the sealing elements. Improvement of the instrumentation for the monitoring of the fluid spreading in the sealing system, especially in the contact zone to the surrounding rock.		
References Bredung, 2002 ; Sitz <i>et al.</i> , 2003 ; Gruner <i>et al.</i> , 2008 ; Wilsnack <i>et al.</i> , 2008		

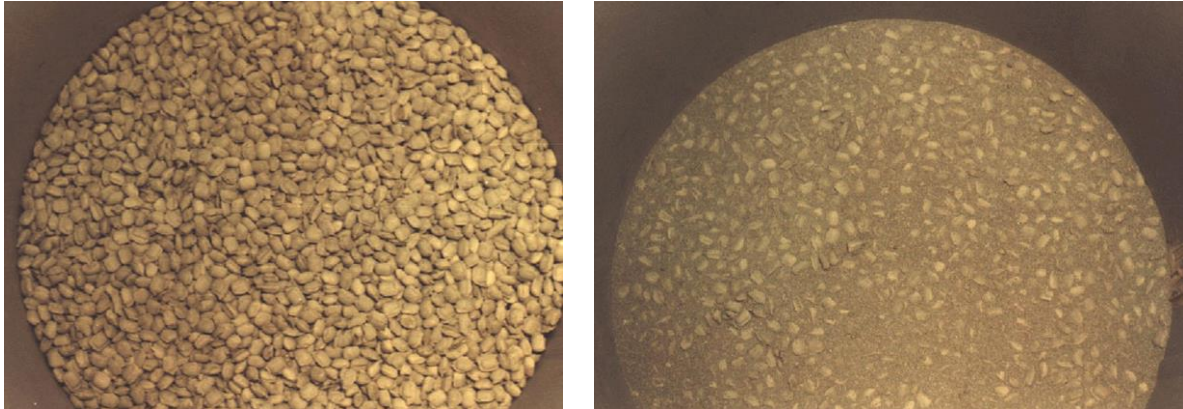


Figure 1.8 First step: emplacement of briquettes (left), second step: adding of granulate during compaction (right)

In a pilot test under lab conditions for measuring the DS properties, the used binary bentonite mixture was tested in a special device of 800 mm in diameter (Fig. 1.9). The maximum fluid pressure was 10 MPa. The test fluid – a NaCl solution with a concentration of 250 g/l NaCl - was loaded from below.



Figure 1.9 Pilot test of sealing elements (actually set up)

Instrumentation

The instrumentation of the sealing system was done by DBE.

109 Sensores in 19 layers in the sealing system (Fig. 1.10):

- Fluid pressure
- Water content/Moisture
- Total pressure
- Pore pressure
- Displacement
- Temperature

The applied fluid volume was measured separately.

Six additional geoelectric measurement chains for the determination of moisture spreading were operated by GRS.

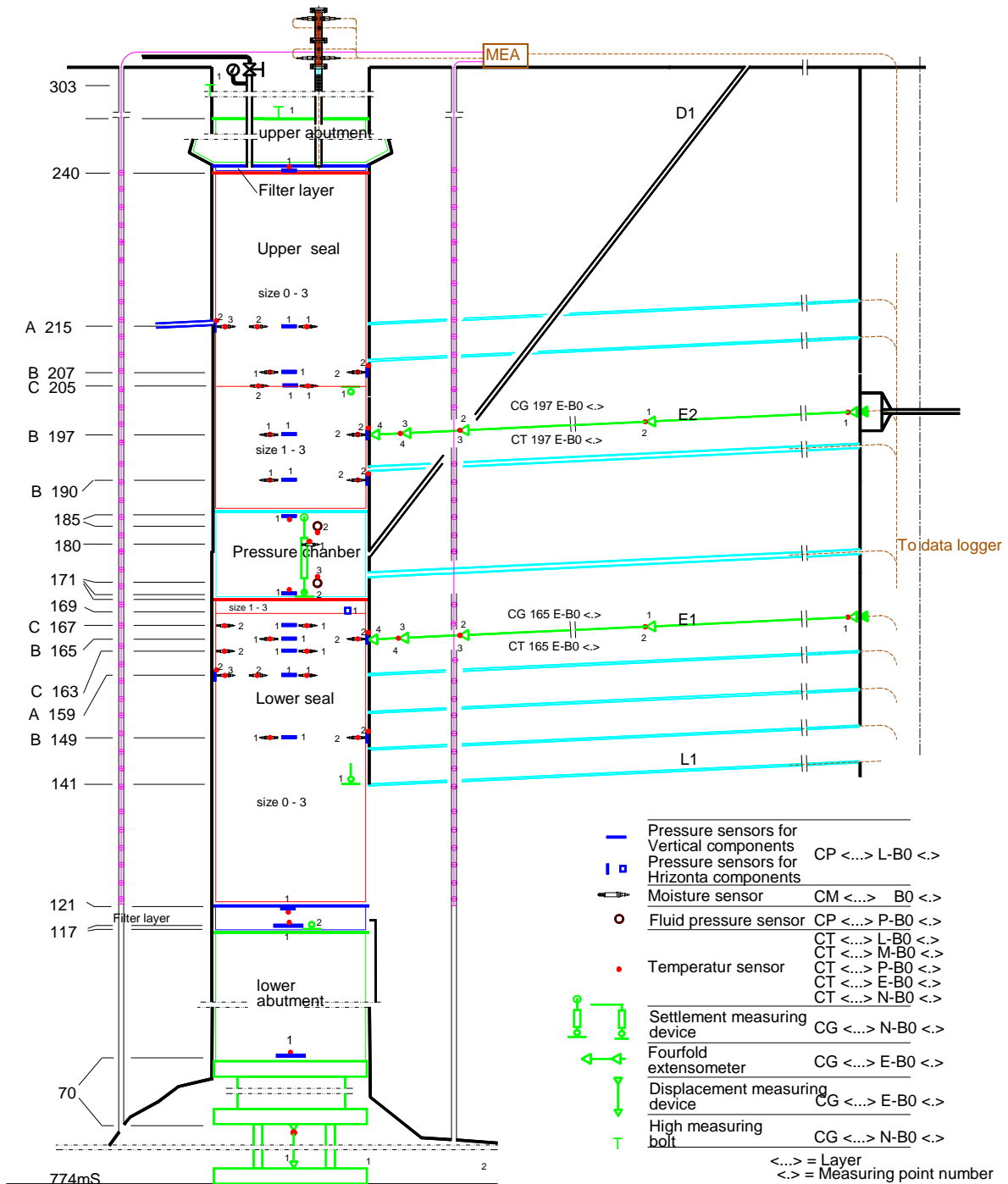


Figure 1.10 Instrumentation of the bentonite sealing setup

Operation/Hydration

22.8.2000: start – filling of the pressure chamber

5.9.2000: fluid pressure 0.05 MPa (0.5 bar)

30.10.2000 – 19.3.2001: constant pressure phase at 4 MPa (40 bar)

18.5.2001 – 29.8.2001: constant pressure phase at 7 MPa (70 bar)

5.11.2001 – 23.12.2001: dismantling of the sealing elements

Modeling

Geomechanical modeling of the bentonite sealing element: FLAC (IfG)

Hydraulic modeling (TOUGH2 – DBE) shows, that the full saturation of the lower sealing element at fluid pressure 4 MPa could be reached after 400 a. Fluid output at the downstream cross section area will be about 6.3 l/a.

Modeling of the long-term behavior of a shaft sealing system in four scenarios with EMOS (by GRS).

Results

At a fluid pressure of 4 MPa, the effective input hydraulic conductivity of the whole system (sealing element with surrounding rock salt) was $5.8 \cdot 10^{-11}$ m/s and $4.4 \cdot 10^{-11}$ m/s at 7 MPa. The results of stress distribution in the bentonite sealing element revealed a swelling pressure of 1 MPa. The sealing behavior of the bentonite sealing system was improved with time and increasing load. The dismantling of the sealing system provided the moisture distribution in the sealing system and the condition of the surrounding rock salt at the final step of the experiment.

The saturated zone in the bentonite reached up to 0.7 m in the upper sealing element and up to 0.4 m in the lower sealing element. In the bentonite mixture of the lower sealing element granulate of 0-3 mm was used typically. In the bentonite mixture of the upper sealing element a granulate 1-3 mm was used. In this case, fluid input was deeper. The higher moisture content of the bentonite in contact with the surrounding rock salt showed that fluid flow in the contact zone of the rock salt surface was approximately 1 m ahead (Fig. 1.11).

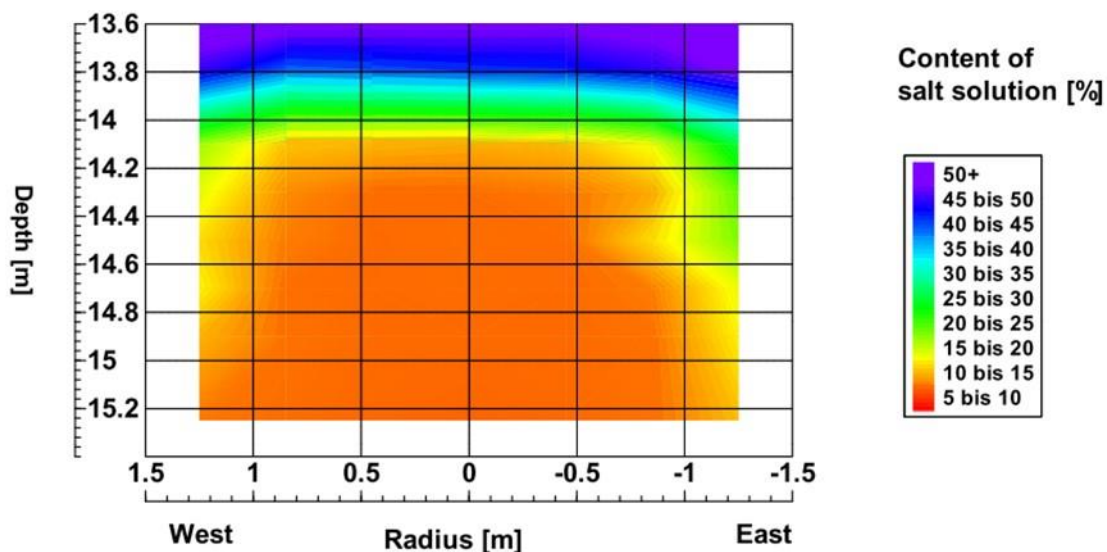


Figure 1.11 Salt brine distribution [wt.-%] in the lower sealing element after the test (West – East section)

1.5 Experimental drift sealing in Sondershausen (Germany)

Project name/Acronym SDH	Location Sondershausen Salt Mine, GSES Company, DE	Type /Scale In situ (1 : 2) test in a drift (A = 11.2 m ²)
Lead organizer/Main partners TU BAF / IfG / IBeWa / ERCOSPLAN / GSES / TS-BAU	Start date/ End date October 1997 / March 2003	Reference concept, if pertinent Drift sealing concept with bentonite blocks
Installation material parameters Blocks of bentonite (Calcigel)/sand (60/40) w = 7 ... 10% (air dry) $\rho_b = 2.25\text{-}2.30 \text{ g/cm}^3$ 250 x 125 x 62.5 mm	Fluid saturation Saturated NaCl-solution Max. fluid pressure 8 MPa	Interfaces/Host rock Natural rock salt Stassfurt (Na ₂)
Instrumentation 80 sensors in three layers	Modeling IfG: FLAC IBeWa: TWO PHASE	Main processes studied <input type="checkbox"/> T <input checked="" type="checkbox"/> H <input checked="" type="checkbox"/> M <input type="checkbox"/> C Input flow rate Swelling pressure Bentonite density change Moisture distribution
Main objectives of the experiment Qualify bentonite blocks for sealing elements in drift sealing systems for salt mines Verification of the technical feasibility and reliability of these bentonite sealing elements		
Main learning points and relevance to the project Production of blocks with $\rho_d > 1.6 \text{ g/cm}^3$ of pure air dry bentonite is difficult Bentonite blocks with 50% or 40% quartz sand can be produced in an industrial plant Unusual high axial displacements of the static abutment ¹ occurred with increasing fluid pressure up to 8 MPa. As a consequence, the total length of the sealing element increased from 5.00 m to 5.17 m. Density reduction in the first meter of the fluid side by 20% - 25% decreased swelling pressure from 0.9-1.1 MPa to 0.3 MPa and permeability of the sealing element increased from $< 10^{-17} \text{ m}^2$ to $10^{-16} - 3 \cdot 10^{-17} \text{ m}^2$.		
Suggestions for the Sandwich project / Remaining open questions Upgrade of the design of the sealing element; avoid a rectangular cross section with sharp corners; Integration of ES for a more homogeneous fluid spreading in the sealing elements Improvement of the instrumentation for the monitoring of fluid spreading in the sealing system, especially in the contact zone to the surrounding rock; More detailed investigation of the mineral composition and the anisotropy of the surrounding rock Direct permeability measurements on the contour zone with surface packer Construction of a sufficiently stiff abutment with selection of appropriate building materials and execution of numerical stability calculations No cable packs in cemented grooves and no technical installations piercing through the sealing element		
References Sitz <i>et al.</i> , 2001; Sitz <i>et al.</i> , 2002; Gruner <i>et al.</i> , 2008		

¹The building materials were selected with respect to the general requirement of long-term stability in the salt environment. First, it was planned to construct a basalt masonry as abutment. As precisely dimensioned basalt blocks were not available, however, highly compressed crushed salt blocks were used, which showed a sufficiently high strength in the dry state, as proven by lab tests and parallel geomechanical modeling. Due to un-estimated preferential fluid flow through the excavated damage / contact zone and through the brine canal (Fig. 1.12) during pressurization, the salt blocks were wetted, which resulted in a drastic loss of strength. Thus, the abutment was not able to withstand the loadings, leading to a significant displacement of the DS element.

Setup

The drift sealing system was constructed in a tunnel-shaped drift driven into a rock salt layer with a TBM 35 years ago. Permeability measurements showed unfavorable high values directly at the rock contour that decreased with increasing depth. This demonstrated the impact of the excavation-affected area and was the reason why the circular cross section (re-cutting of the EDZ) of 3 m in diameter was replaced by a rectangular cross section of 3.50 m x 3.20 m, the length of the sealing element was determined, and additional sealing slots were installed.

The dam sealing system (Fig. 1.12) consists of the following elements (from the pressure side to the air side):

- Pressure chamber I, filled with sand for the establishment of the pressure with saturated NaCl brine.
- A layer of filter stones for the moistening of the bentonite and to prevent a transport of saturated bentonite into pressure chamber I.
- Main sealing element with highly compacted bentonite blocks, including sealing slots.
- Pressure chamber II for the determination of the tightness of the surrounding rock and of the sealing element I as well as for the direct pressure built-up on the static abutment in the final testing stage.
- Sealing element II (a special mastic asphalt in combination with bitumen and covered by bentonite blocks).
- A prismatoid static abutment (angle of the planes to the axis approx. 14°), tacking up the fluid pressure and rock pressure (constructed of highly compressed rock salt blocks)¹.
- A groove in the center of the bottom underneath the construction with a cross section of 0.3 m x 0.3 m (brine-canal) with four tubes for pressurization, de-aeration and control as well as cables to the sensors. The groove was sealed by filling all openings with highly compressed bentonite meal.

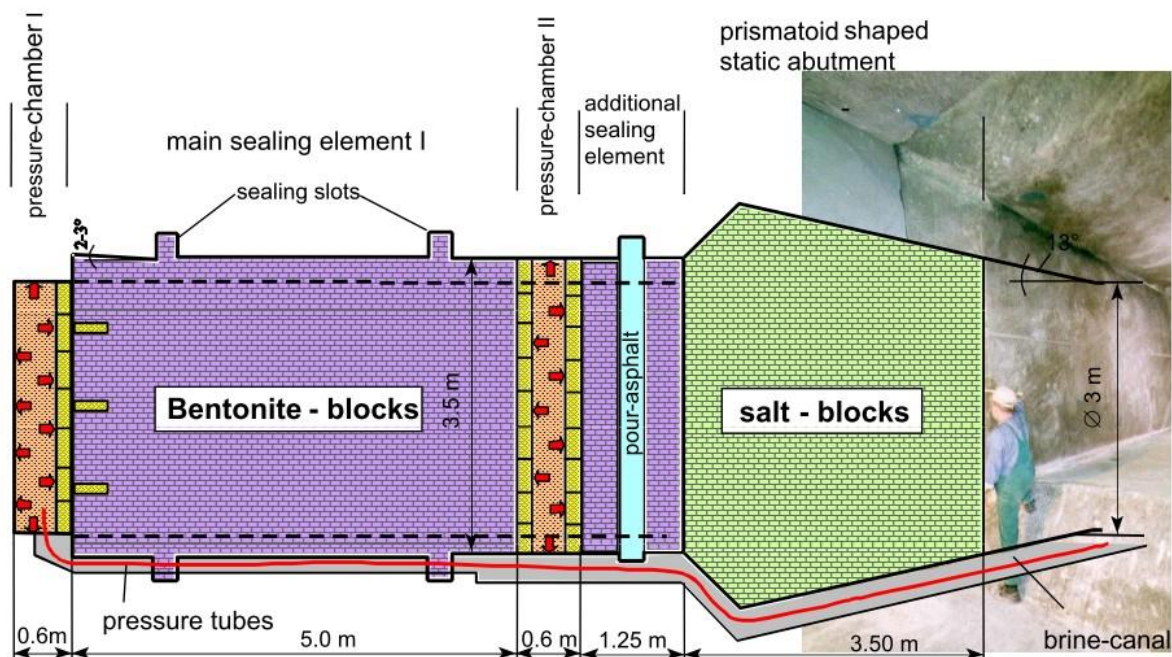


Figure 1.12 Set up of the Sondershausen – drift seal project

Material

Natural Ca-bentonite was preferred as sealing material under rock salt conditions. For the project, Calcigel bentonite was selected as the reference material having the following properties to ensure the performance of the bentonite sealing element: (1) a hydraulic conductivity of $< 5 \cdot 10^{-10}$ m/s and (2) a swelling pressure of ≥ 1 MPa. These parameters can be reached when the Calcigel is emplaced with a minimum water content (air-dry) and a dry density of > 1.6 t/m³.

Bentonite brickwork proved to be a suitable sealing element in horizontal openings (Fig.1.13). The blocks had a bentonite content from 30% up to 70%. The standard size was (250 x 125 x 62.5) mm and they could be cut easily with a saw.

The hydraulic conductivity of single blocks was $< 2 \cdot 10^{-11}$ m/s and the swelling pressure of single blocks reached > 2 MPa.

The rock salt gas permeability (as measured immediately after re-cutting the rock contour and directly before emplacement of the plug) at the roof (10^{-15} m²) was two orders of magnitude higher than permeability at the walls and at the bottom ($10^{-17} - 10^{-18}$ m²). This was attributed partly to the salt bedding and the flat roof.



Figure 1.13 Single bentonite block, emplacement of blocks (both left) and sealing element before dismantling (right)

Instrumentation

80 sensors (Fig. 1.14) in three measuring layers for the measuring of

- Fluid pressure,
- Contact pressure,
- Moisture content,
- Swelling pressure
- Extensions.

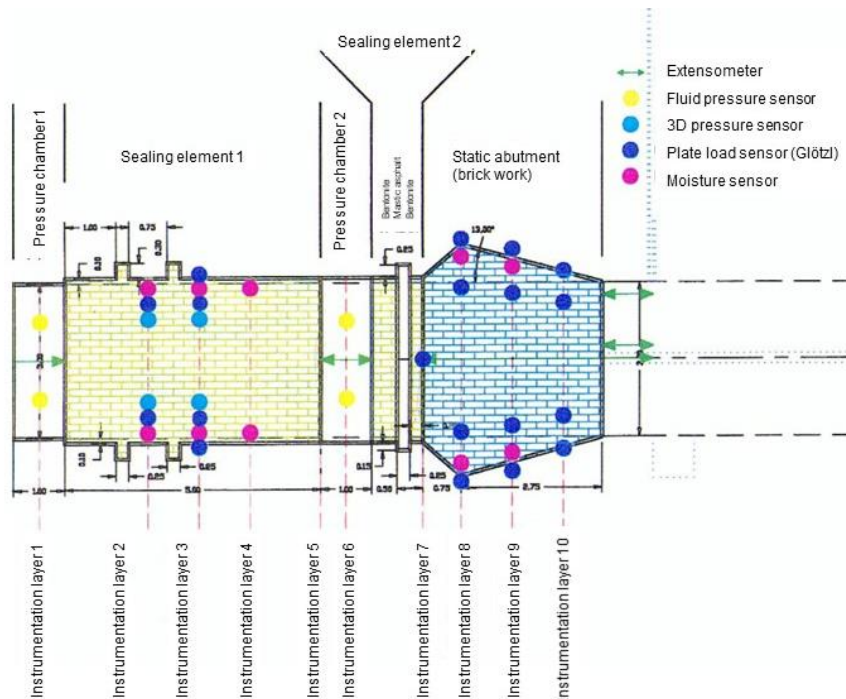


Figure 1.14 Instrumentation of the Sondershausen project

Operation/Hydration

13.09.2000	start: filling of the pressure chamber with saturated NaCl solution
17.10.2000	start of fluid pressurization
09.05.2001	end of the constant pressure phase 3.35 MPa (33.5 bar)
16.05. – 30.08.2001	injection of bentonite suspension and technical service work
15.09.2001	fluid pressure 4 MPa (40 bar) reached
17.11.2001	fluid pressure 8 MPa (80 bar) reached
29.22.2001	end of fluid pressurization
06.01.2002	start of dismantling

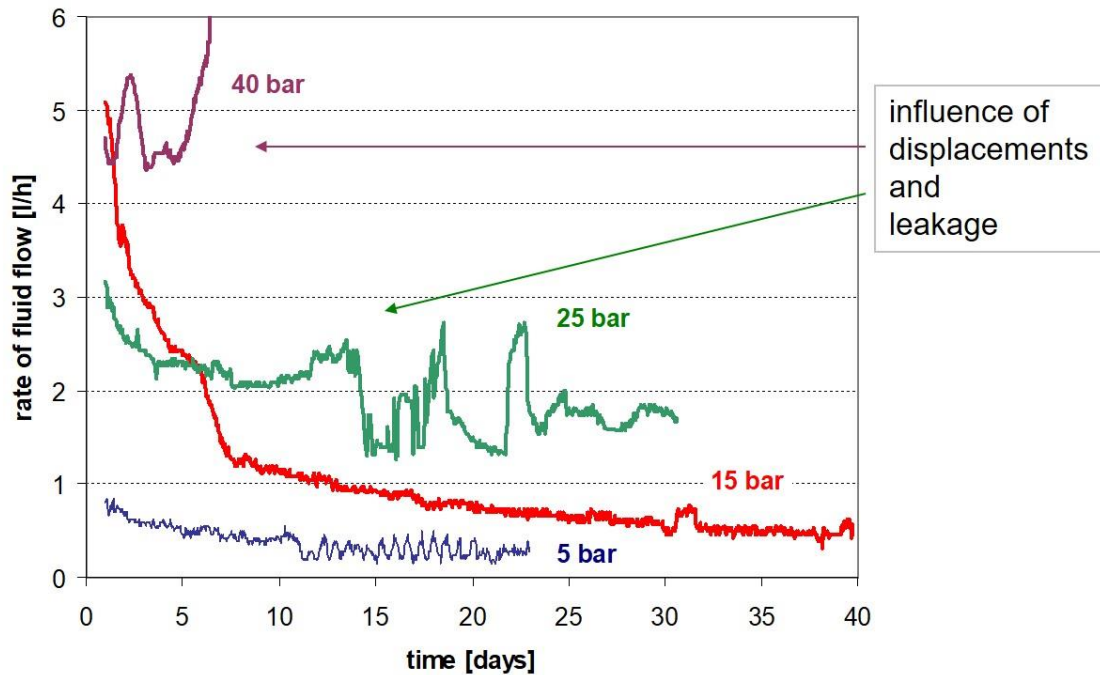


Figure 1.15 Input fluid flow by constant fluid pressure

Modeling

Geomechanical modeling for proof of stability of the static abutment in interaction with the developing swelling of the bentonite sealing element and fluid pressurization: FLAC (IfG)

Hydraulic modeling (TWO PHASE (Nekrassov, A., 2002) – IBeWa): two-phase flow in bentonite blocks, empirical evaluation of capillary pressure – saturation relationship (BROOKS & COREY).

Results

Axial displacements of the various dam elements are related to the strength loss of the static abutment because of unfavorable selection of the brickwork material¹. Due to progressive wetting of the salt bricks, axial displacements rapidly increased with increasing fluid pressure up to 8 MPa (80 bar) and reached a time-dependeent rate of 20 mm/d. With a constant fluid pressure of 8 MPa, this displacement rate first decreased to 5 mm/d and then still increased due to the instability of the static abutment.

The axial displacement of the static abutment also resulted in an axial displacement of the air side of the sealing element. The fluid side of the sealing element expanded back by the swelling pressure of the bentonite. The total length of the sealing element increased from 5.00 m to 5.17 m. The increased length resulted in a density reduction in the sealing element. This density reduction focused on the first meter of the fluid side of the sealing element. In this area the density reduction was 20% - 25% and resulted in a higher hydraulic conductivity and a lower swelling pressure. The permeability of the sealing element was $< 10^{-17} \text{ m}^2$. In the areas with reduced density (bottom, front of pressure side) the permeability of the sealing material was measured to be in the range of $10^{-16} - 3 \cdot 10^{-17} \text{ m}^2$.

The swelling pressure of the sealing element could be determined from the contact pressure measured between the sealing element and the salt contour at various fluid pressures. The swelling pressure is the residual contact pressure without fluid pressure. At the beginning of

the test, the swelling pressure was in the range between 0.9 and 1.1 MPa (9 – 11 bars). At the test end, the swelling pressure in the layer 1.35 m from the pressure side decreased to 0.3 MPa (3 bar), because the bentonite density was reduced by expansion (Fig. 1.16).

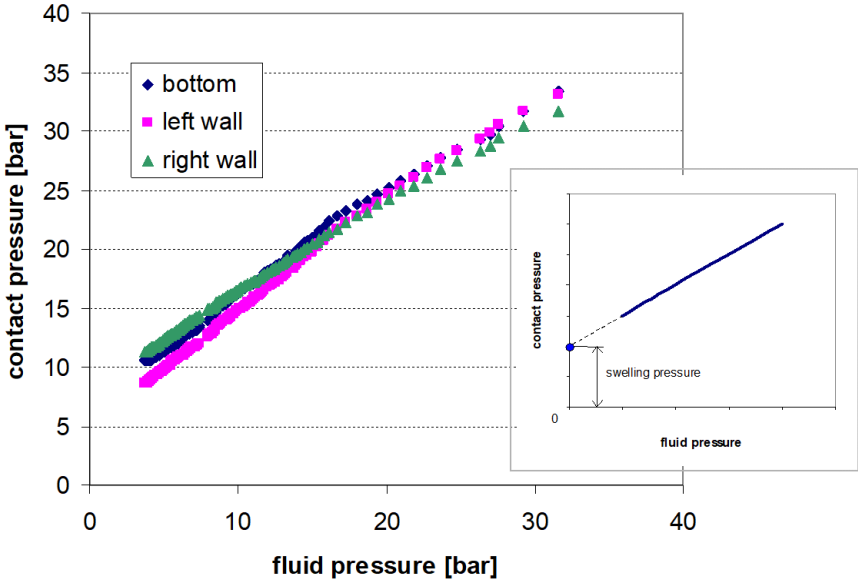


Figure 1.16 Contact pressure between sealing element and salt contour (1.35 m from pressure side)

Moisture content distribution of the sealing element was determined after the dismantling of the sealing element (Fig. 1.17). Moistening of the sealing element was irregular, it was found mainly in the contact zone to the rock and especially at the bottom of the sealing element. At the bottom, on the right wall and in the corners, salt brine flowed along the whole length of the sealing element. The moistening front arrived from the pressure side in the cross section after 1.5 – 1.6 m (Fig. 1.17).

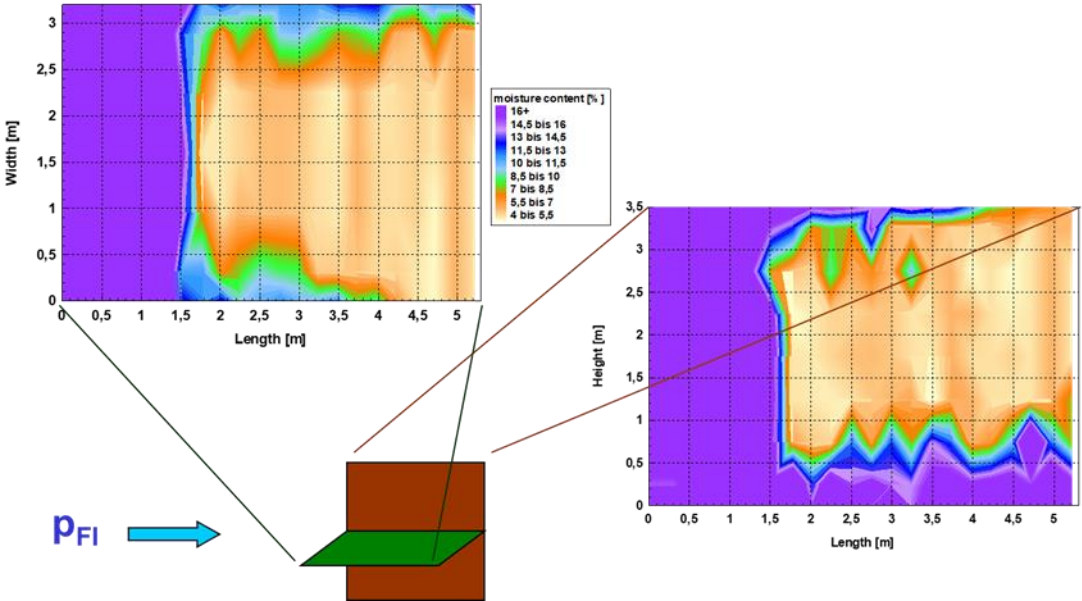


Figure 1.17 Moisture content distribution in the bentonite sealing element – results of dismantling

This results is in agreement with the permeability measurements in the disturbed zone in rock salt and with the results of the inspection of the cemented groove with the tubes and cables. After dismantling of the sealing element the permeabilities measured at the roof (10^{-15} m^2) were higher by two orders of magnitude than permeabilities at the walls and at the bottom ($10^{-17} - 10^{-18} \text{ m}^2$). The permeability of the sealing element was $< 10^{-17} \text{ m}^2$. In the areas of reduced density (bottom, front of pressure side) the permeability of the sealing material was measured to be in the range of $10^{-16} - 3 \cdot 10^{-17} \text{ m}^2$. The permeability of the salt cement mortar was $2 \cdot 10^{-18} - 9 \cdot 10^{-18} \text{ m}^2$. Using tracer tracks, however, found, that salt brine flowed in the cement material along cracks and cables. Another problem was that salt brine also flowed inside some cables between the wire covers (Fig. 1.18).

Finally, it has to be stated that with the Sondershausen drift seal test the general suitability of bentonite sealing systems in rock salt formations has been proven. However, unfortunate design and material selection influenced the overall rating of the test outcome.

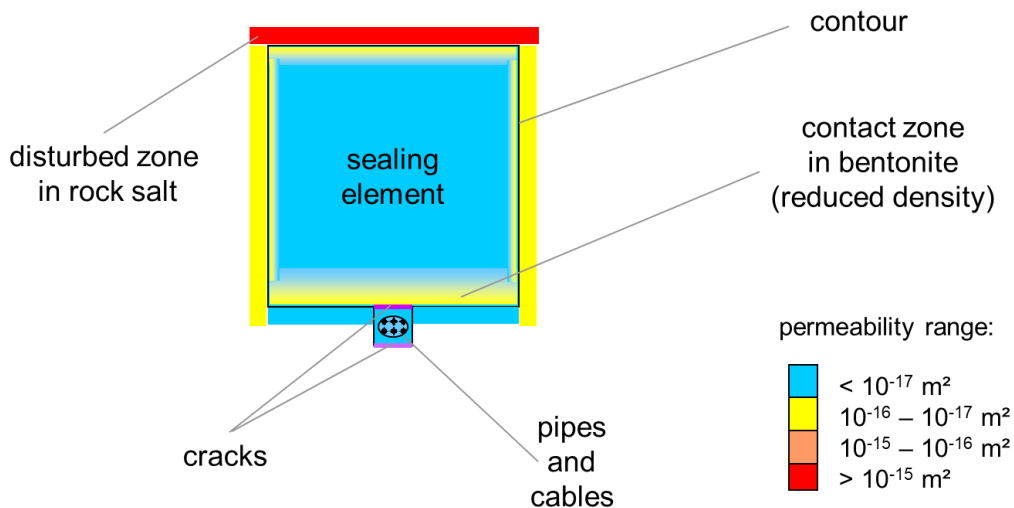


Figure 1.18 Permeability values around the sealing element area

1.6 Input from the Beacon project

The main objective of the EC-funded international project Beacon (Bentonite Mechanical Evolution, June 2017 – May 2021) is to enhance understanding of the mechanical evolution of a bentonite barrier in a nuclear waste repository, with the focus lying on bentonite homogenization and persistence or development of inhomogeneities. The work is organized in the following work packages:

WP1 - Definition of assessment case/application to the assessment case

WP2 - Collection and compilation of existing data and available models

WP3 - Model development

WP4 - Laboratory testing

WP5 - Testing, verification and validation of the models

WP6 - Civil Society interaction

WP7 - Training and dissemination

WP8 - Management and coordination

WP9 - Ethics requirements

For the Sandwich project, the work packages 2, 3, and 4 are of special interest, since they provide valuable data and model approaches relating to bentonite behavior. This is especially useful for the interpretative modeling of the Sandwich experiment.

In the WP2 deliverable D2.2 “Review of data and models on the mechanical properties of bentonite available at the start of Beacon” (Thatcher *et al.*, 2017), the data of more than 60 experiments addressing more than 10 types of bentonite were compiled and evaluated by around 30 organizations. Short descriptions were provided for each experiment, and an evaluation table was created. These results are available to the Sandwich project.

WP3, model development, has already provided a deliverable (Gens, 2018) on the constitutive models available at the start of Beacon. Models are currently checked and calibrated. A deliverable on model improvements is scheduled for August 2019.

New laboratory experiments are performed in WP4 of the Beacon project. A total of 21 experiments are currently running. Table 1.1 gives an overview of the experiments' characteristics. The current state will be documented in a deliverable that is planned for August 2019. This deliverable will be also available to the Sandwich project.

Table 1.1 Experiments performed in Beacon WP4

Identification			Setup		Material		Experiment conditions					Outcome			
Partner in charge	Experiment name	Main objective	Type of experiment	Sample size	Bentonite	Block/granular	Dry density	Initial degree of saturation / water content	Solution	Mechanical boundary conditions	Hydraulic boundary conditions	Temperature	Measurements	Data resolution	Remarks
KIT	SPIN (Single Pellet Investigations - preliminary title)	Density / porosity distribution evolution on pellet-scale and influence on overall buffer permeability	Swelling test, limited volume increase	= 10 mm	MX-80	Single pellet	Will be determined	Will be determined	Pearson water	Constant volume cell, limited volume increase of pellet	One-sided re-saturation	Ambient	Spatially resolved - swelling pressure - water content - porosity distribution overall permeability	mm	
BGS	SITS (Swelling in to voids - very preliminary title)	Evolution in swelling pressure, porosity and density as different height blocks of bentonite swell into a fixed volume. Tests repeated with ambient and elevated temperatures at with two different salinities	Swelling test into fixed volume	Diameter 60mm, vessel length 120 mm. Sample length variable.	MX-80	Blocks	Will be determined axially and radially to determine variations after swelling	Will be measured but blocks will start at = 100% to reduce test times	Distilled and NaCl balance to Swedish groundwater	Constant volume with multiple stress measurements	Resaturation from both ends of the vessel	Ambient and 90° C	Spatially resolved: swelling pressure; porosity, water content, density, etc, plus potentially bulk permeability	Around 10 mm for post-mortem sub sampling	
CIEMAT	MGR	Check density homogenisation upon saturation of two materials initially different (pellets/block)	Hydration at constant volume in an oedometer	Cylinder, 100x100 mm	FEDEX (MX-80?)	Combination of block/granular	1.6 g/cm ³ (block), 1.3 g/cm ³ (pellets)	13.5% (block), 10.1% (pellets)	Deionised water	Constant volume	Saturation through the pellets surface under controlled low flow	Ambient	Water intake, swelling pressure, postmortem (density, water content, MIP, XRD)		
CIEMAT	Window	Check density homogenisation upon saturation of two materials initially different (pellets/block)	Hydration at constant volume in a transparent cell	121x121x20 mm	FEDEX (MX-80?)	Combination of block/granular	1.6 g/cm ³ (block), 1.3 g/cm ³ (pellets)	13.5% (block), 10.1% (pellets)	Deionised water	Constant volume	Saturation through the pellets surface under low pressure	Ambient	Water intake, images, postmortem (density, water content, MIP, XRD)	mm	Complementary to MGR, qualitative
CIEMAT	GAP liquid	Follow density changes in a block sample saturated under limited axial swelling conditions	Hydration of a block sample with liquid water allowing limited axial swelling (initial gap)	Cylinder, 50x25 mm	FEDEX (MX-80?)	Block	1.65 g/cm ³	13,5%	Deionised water	Limited axial swelling (depending on the size of the gap)	Saturation from the surface opposite to the gap	Ambient	Water intake, postmortem (density, water content, MIP)	mm	
CIEMAT	GAP vapour	Follow density changes in a block sample saturated under limited axial swelling conditions	Hydration of a block sample with vapour water allowing limited axial swelling (initial gap). Perforated cell	Cylinder, 38x28 mm	FEDEX	Block	1.7-1.5 g/cm ³	14%	Water vapour	Limited axial swelling (depending on the size of the gap)	Saturation from the gap surface	20° C	Water intake, postmortem (density, water content, MIP)	mm	
JYU	Partly constricted swelling experiment - preliminary title	Dry density and water content profiles and axial swelling pressures from both ends of the chamber as a function of time during wetting.	Swelling test, limited volume increase (initial sample 10 mm high with 4 mm gap)	20 mm	Bara Kade	Block	Initially 1.5-1.7 g/cm ³	= 17% water content	Will be determined	Constant volume cell, limited volume increase of block	One-sided re-saturation	Ambient	1D water content and dry density distributions and axial swelling pressure from both ends of the chamber	Sub mm	Full measurement series to be started soon
JYU	Small scale homogenization experiment - preliminary title	Wetting of block-air-block-air... kind of sample and the state of its homogenization as a function of time	Swelling test, limited volume increase	10-20 mm, to be determined	Bara Kade	Block	Will be determined	Will be determined	Will be determined	Constant volume cell, limited volume increase of block	Will be determined	Ambient	1D water content and dry density distributions and axial swelling pressure from both ends of the chamber	Sub mm	In planning
CU	Investigation of microstructure, hydraulic and mechanical properties of the Czech bentonite	Description of microstructural changes under different hydraulic paths and mechanical response on the saturation of compacted samples	WRC, MIP, ESEM, swelling experiments in oedometer	5 cm diameter, 1 cm height (oedometer tests)	BCV	Block (oedometer tests)	1,27; 1,6 and 1,9 g/cm ³ for WRC, MIP and ESEM. Dry densities for oedometer tests will be determined	Corresponding to initial water content of bentonite powder (= 10%)	Distilled water	Constant load swelling + compression (oedometer tests)	One-side saturation (oedometer tests)	Ambient	Swelling under constant load, swelling pressure after re-compression		

Table 1.1 (continued)

CTU	Hydraulic and mechanical properties of the Czech bentonite	Hydraulic properties, density distribution, total pressure	Swelling tests - constant volume and constant load	Constant volume - 3 cm diameter, 2 cm height; constant load - 5 cm diameter, 1 cm initial height	BCV, B75	Block	Dual density - 1.3 & 1.7 for constant volume; 1.3 - 1.8 for constant volume; initial 1,27; 1,6 and 1,9 g/cm ³ for constant load	10%	Water	Constant volume cell (attached to permeameter); constant load swelling + compression (oedometer tests)	One side saturation	Ambient and 60°C	Constant volume cells - water intake, total pressure at one end, density distribution at the end; swelling under constant load ("deformation" on each load step)		
CEA	Stress Field evolution during Bentonite Homogenization (preliminary title)	Density evolution and pressure field on simplified heterogeneities	Isochoric swelling test	Diameter 57 mm	MX-80	Several (>=4) configurations	Will be determined (average = 1.5 g/cm ³)	Will be determined	LSMHM synthetic site water	Constant volume cell	One-sided / two-sided re-saturation	Ambient	Axial stress, 9 local pressure sensors (3 heights, 3 radial positions), 3 RH sensors (3 heights)		Post-mortem density and water content local measurements, some MIP
CEA	Tomobento	Qualitative evaluation of the homogenization of a pellet/powder mix using in situ X-ray tomography	Swelling test, limited volume increase	Diameter 57 mm	MX-80	Single pellet + powder	Will be determined	Will be determined	LSMHM synthetic site water	Quasi-constant volume cell	One-sided re-saturation	Ambient	3D X-ray absorption coefficient field	30 µm	
EPFL		The influence of initial granulometry on final as-hydrated state	Isochoric saturation followed by compaction	Height 12.5 mm, diameter 35 mm	MX-80	Granular	Various	Hygroscopic water content	Distilled water	Oedometric cell, radial displacement prevented	Two-sided saturation	Ambient	Swelling pressure, final granulation	Displacement: micron; swelling pressure: 0.6 MPa, saturation pressure: 1 kPa	
EPFL		The influence of initial granulometry on final as-compacted state	Compaction	Height 12.5 mm, diameter 35 mm	MX-80	Granular	Various	Hygroscopic water content and $w_{nit} \approx 20\%$	Distilled water	Oedometric cell, radial displacement prevented	For samples of $w_{nit} \approx 20\%$ - saturation by vapour equilibrium technique	Ambient	Final void ratio, final granulation	Displacement: micron; swelling pressure: 0.6 MPa, saturation pressure: 1 kPa	
EPFL		The influence of the different hydro-mechanical paths on final macroscopic properties and local homogeneity of compacted samples	Free swelling; free swelling followed by compaction: isochoric saturation followed by compaction	Height 12.5 mm, diameter 35 mm	MX-80	Granular	1.4 kg/cm ³	Hygroscopic water content	Distilled water	Oedometric cell, radial displacement prevented	Two-sided saturation	Ambient	Final void ratio after each type of experiment, final pore size distribution, swelling pressure in case of isochoric saturation test	Displacement: micron; swelling pressure: 0.6 MPa, saturation pressure: 1 kPa	
EPFL		Volumetric response of bentonite sample during air injection phase	Isochoric saturation followed by the measurement of water permeability and gas injection	Height 20 mm, diameter 40 mm	MX-80	Granular	1.4 kg/cm ³	Hygroscopic water content	Distilled water	Triaxial cell	Two-sided saturation	Ambient	Radial and axial swelling pressure, coefficient of permeability, volumetric response on air injection	Displacement: micron; swelling pressure: 0.8 MPa, saturation pressure: 1 kPa	
EPFL		Influence of the degree of saturation on the shearing behaviour at the bentonite-steel interface	Isochoric saturation using vapour equilibrium technique followed by shearing test	Height 15 mm, base 30x30 mm	MX-80; FEBEX	MX-80: granular; FEBEX: blocks	To be determined	To be determined	Various	Direct shear apparatus	Two sided saturation with vapour equilibrium technique	Ambient; (60° C)	Swelling pressure; interface friction angle; interface adhesion	Displacement: micron; swelling pressure: to be determined, saturation pressure: to be determined	

2 Definition of objectives of the large-scale experiment (WP2)

The aim of the main project is to perform a large-scale in-situ experiment using a Sandwich sealing system. The following objectives were defined:

1. Feasibility of installation
 - a) Scale transition (semi-technical scale to large scale, but not full scale)
 - b) Meeting requirements of real scale (e.g., workplace safety)
 - c) Hydration system
 - d) Compaction of DS und ES around the sensors
2. Investigation of the saturation process
 - a) Hydration of the seal by injection
 - b) Resaturation of the host rock
 - c) Interaction of the EDZ with the equipotential and sealing layers
3. Qualification of measurement and monitoring techniques (instrumentation)
 - a) Durability of instrumentation
 - b) Multi-parameter monitoring (fiber-optics)
 - c) Optional: wireless data transmission
4. Assessment of sealing effectiveness
5. Evaluation and validation, risk management - second experimental shaft
 - a) Back-up for failures due to experiment design and execution
 - b) Allowing for the evolution of a pronounced EDZ before seal emplacement
 - c) Variation of emplacement technology – partly saturated ES

3 Test site (WP3)

3.1 Construction

Niche 7 was excavated from April 5 - 20, 2018 with a daily advance rate varying between 1.5 to 3.0 m. Niche 7 is located entirely in the lower sandy facies of the Opalinus clay, in the southern part of the existing rock laboratory (Fig. 3.1). The niche was excavated by the contractor Rothpletz and Lienhard Cie with a road header ET120 exhibiting an operating weight of 35 t. Niche 7 has a total length of 17.5 m from the southern side wall of the future Gallery 18 (Fig. 3.2). As Gallery 08, Niche 7 was excavated in a horseshoe shape of 5.4 m in diameter. Two layers of sprayed shotcrete of 8 cm with synthetic fibers and 12 cm thickness without fibers, respectively, lead to a diameter of 5.0 m after construction (Fig. 3.3). Between the two shotcrete layers a steel net K196 is arranged. No anchors were drilled in this niche. In order to survey the convergences of the niche, two INVAR convergence sections were installed at NM5 and NM12 respectively. At the beginning and at the end of the niche two pairs of HEB160 steel arches were installed in order to enhance the stability of the niche. The invert of the niche was concreted on May 24, 2018. The thickness of the concrete is in the order of 60 cm. Two reservations of 1.2 m in diameter were built for future shafts (Fig. 3.4 and 3.5). Along the axes of each future shaft another HEB 160 steel arch was placed for later installation of a massive hook (possibility to attach heavy equipment during shaft sinking and backfilling). The reservations are covered with sturdy steel lids.

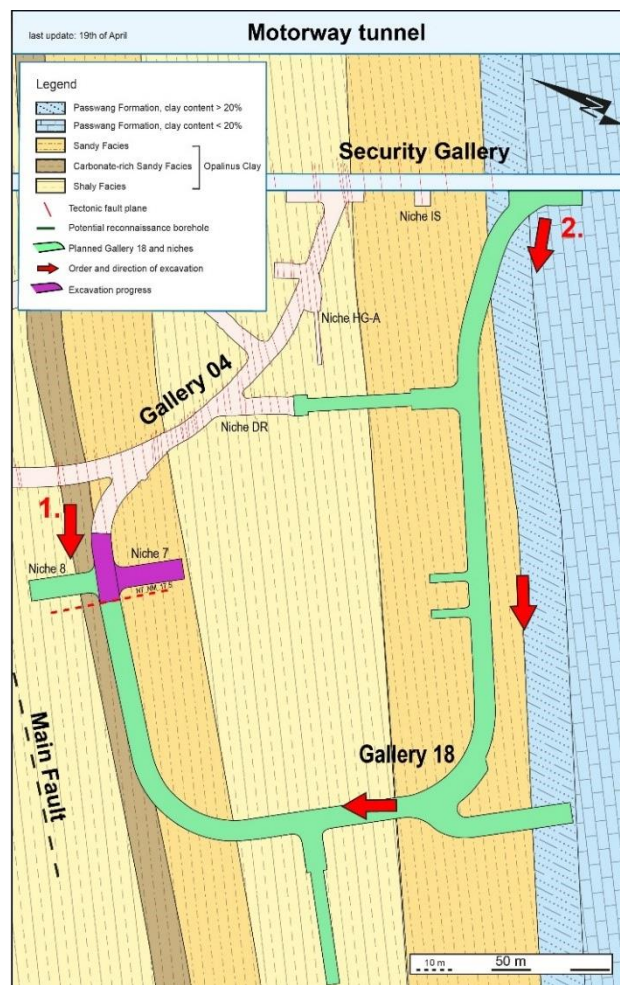


Figure 3.1 Location of Niche 7 in the new part (green) of the Mont Terri rock laboratory

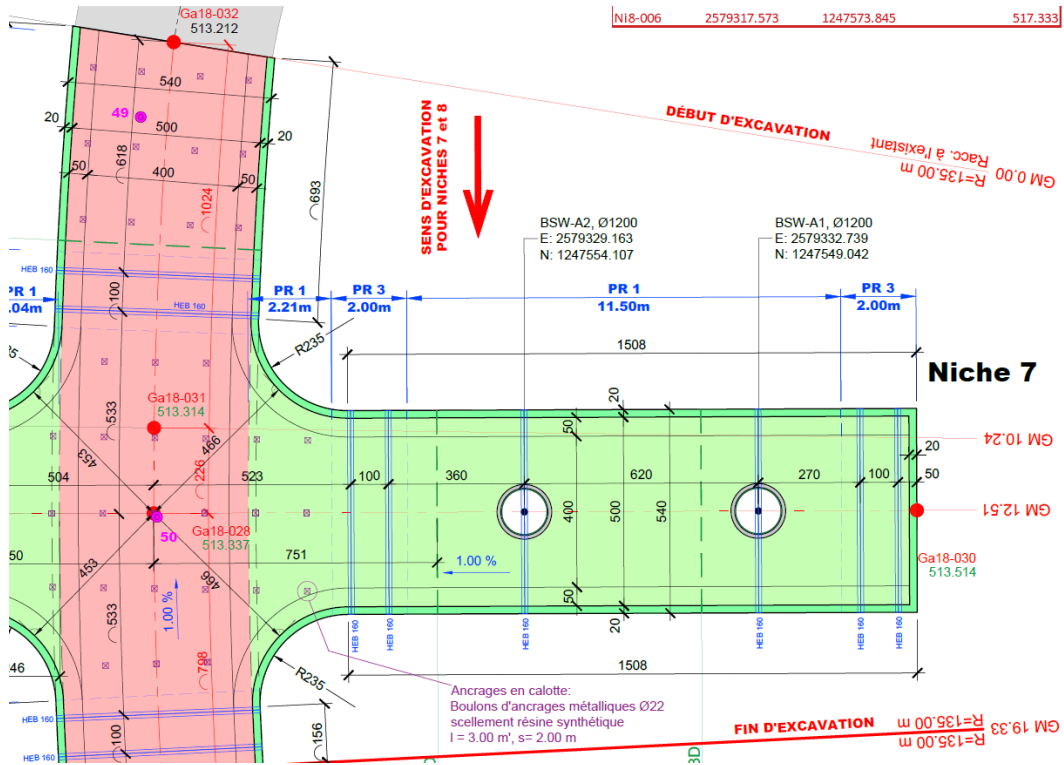


Figure 3.2 Niche 7 with the localization of the HEB 160 steel arches and the two reservations of 1200 mm diameter for the future sandwich shafts BSW-A1 and BSW-A2

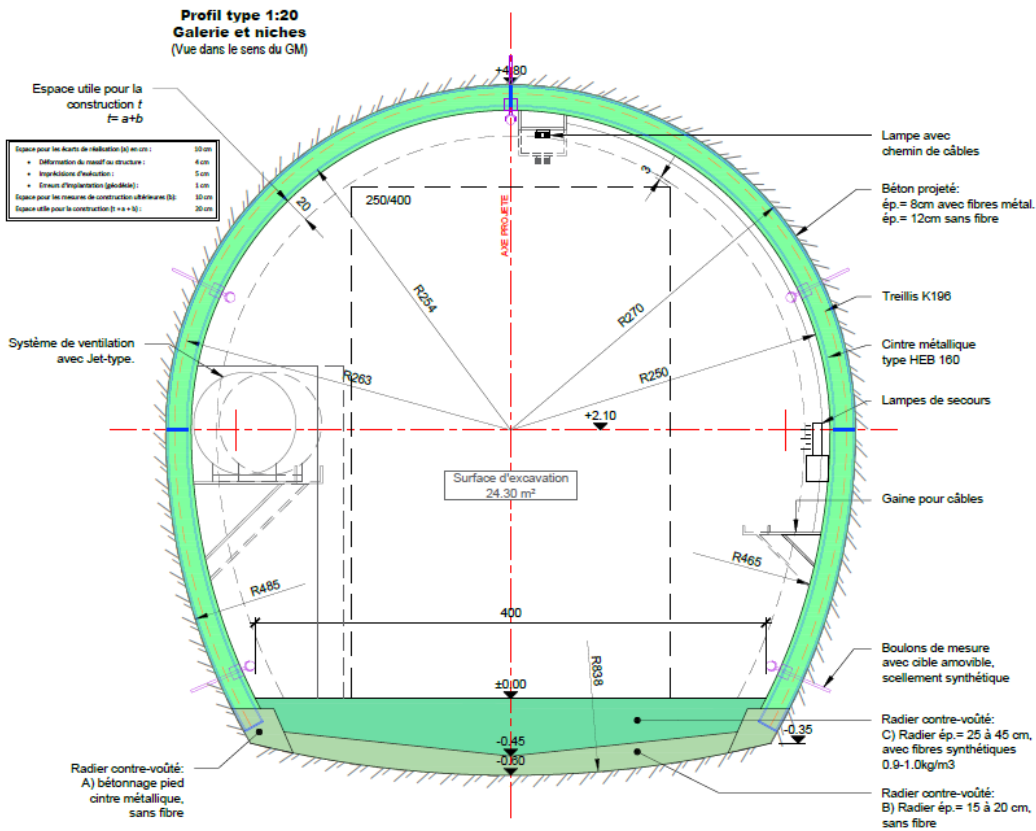


Figure 3.3 Section of Niche 7 with basic elements

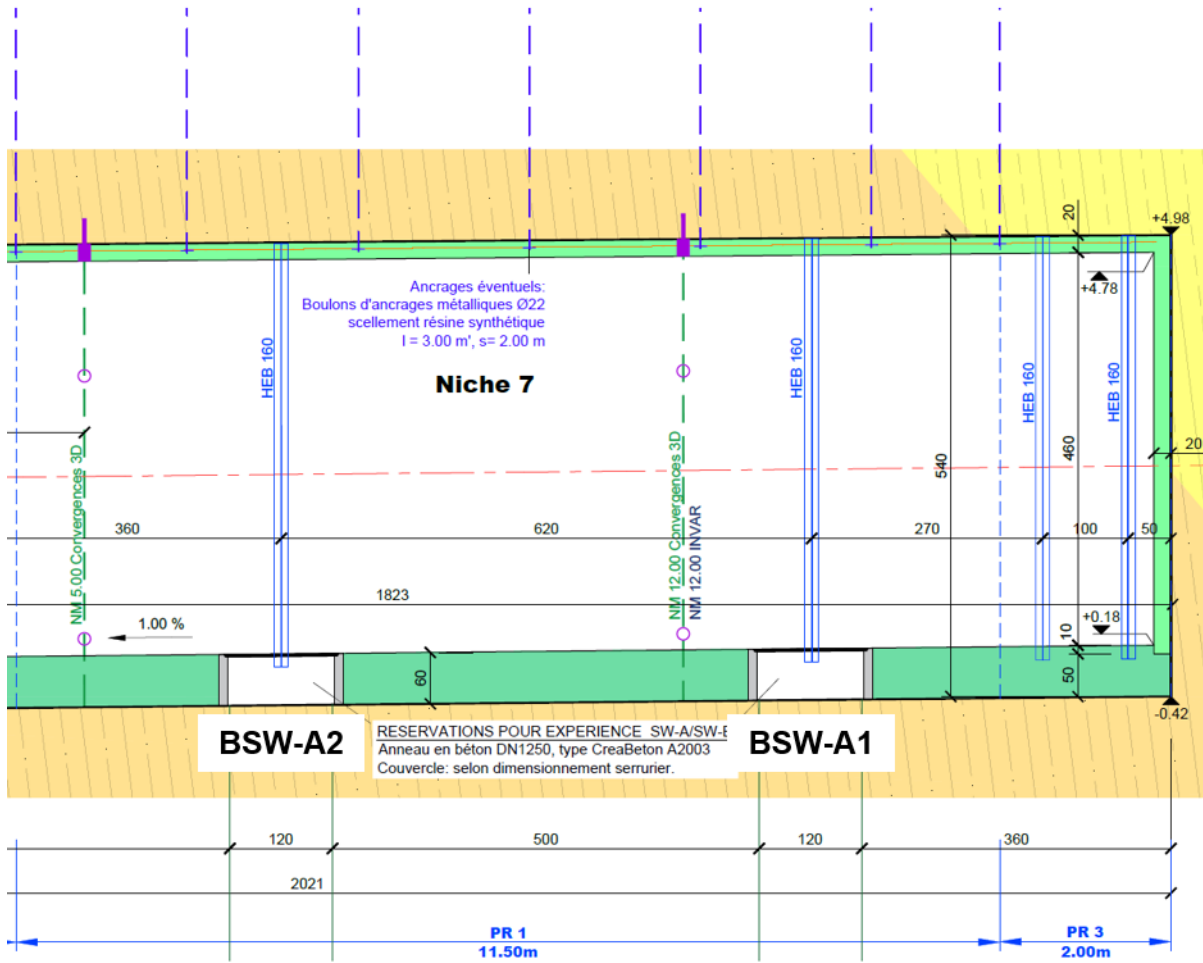


Figure 3.4 Vertical section of Niche 7, showing the two reservations and the positions of the steel arches

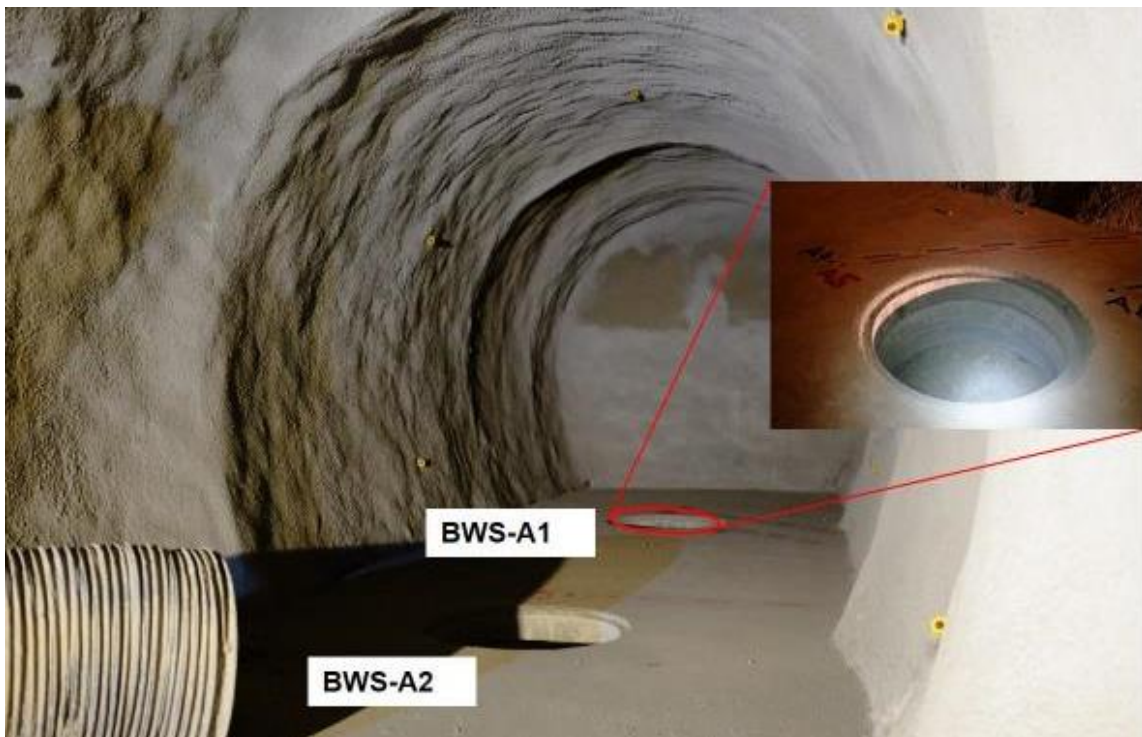


Figure 3.5 View of Niche 7 right after construction and view of reservation for future shaft BSW-A1

3.2 Geology of Niche 7

Niche 7 is entirely located in the lower sandy facies of the Opalinus clay (Fig. 3.6). The crosscutting Ga18 goes along the transition from carbonate-rich sandy facies below to sandy facies above. This boundary is rather transitional and difficult to detect on the outcrop. The carbonate-rich sandy facies is characterized by silty clay with numerous up to 20 cm thick accumulations of carbonate biodetritus. As regards the overall content of quartz and calcite the carbonate-rich sandy facies is very comparable to the sandy facies above with quartz contents of 20-50% and calcite contents of 10-60%. Clay mineral phases are illite, I/S interstratifications, chlorite and kaolinite (Bossart and Thury, 2008). The excavation of Niche 7 was parallel to dip direction or perpendicular to the strike of bedding. Thus from a rock mechanical point of view the excavation took place in a favorable direction. At the very end of the niche, in the ceiling part the transition to the upper shaly facies was encountered, which is a transitional boundary on the outcrop as well. The niche was excavated within 8 working days (Tab. 3.1) with variable excavation progress and duration.

Bedding in Niche 7 is dipping with 45° towards 146° (SSE). At the entrance of the niche, structurally controlled breakouts were observed at locations, where bedding is oriented tangentially to the gallery. At the two pillars on both sides of the entrance, stress induced breakouts with some reactivation of bedding planes were observed. Bedding parallel faults were observed at NM5.5. Although some striations were observed movement of those rare bedding parallel faults most probably was small. At NM13.5, some structurally controlled breakouts were observed at the tunnel ceiling, which continued until NM17.5, which marks the end of the niche. At NM16, a last distinct bioclastic layer was observed, which marks the upper boundary of the sandy facies (Fig. 3.7).

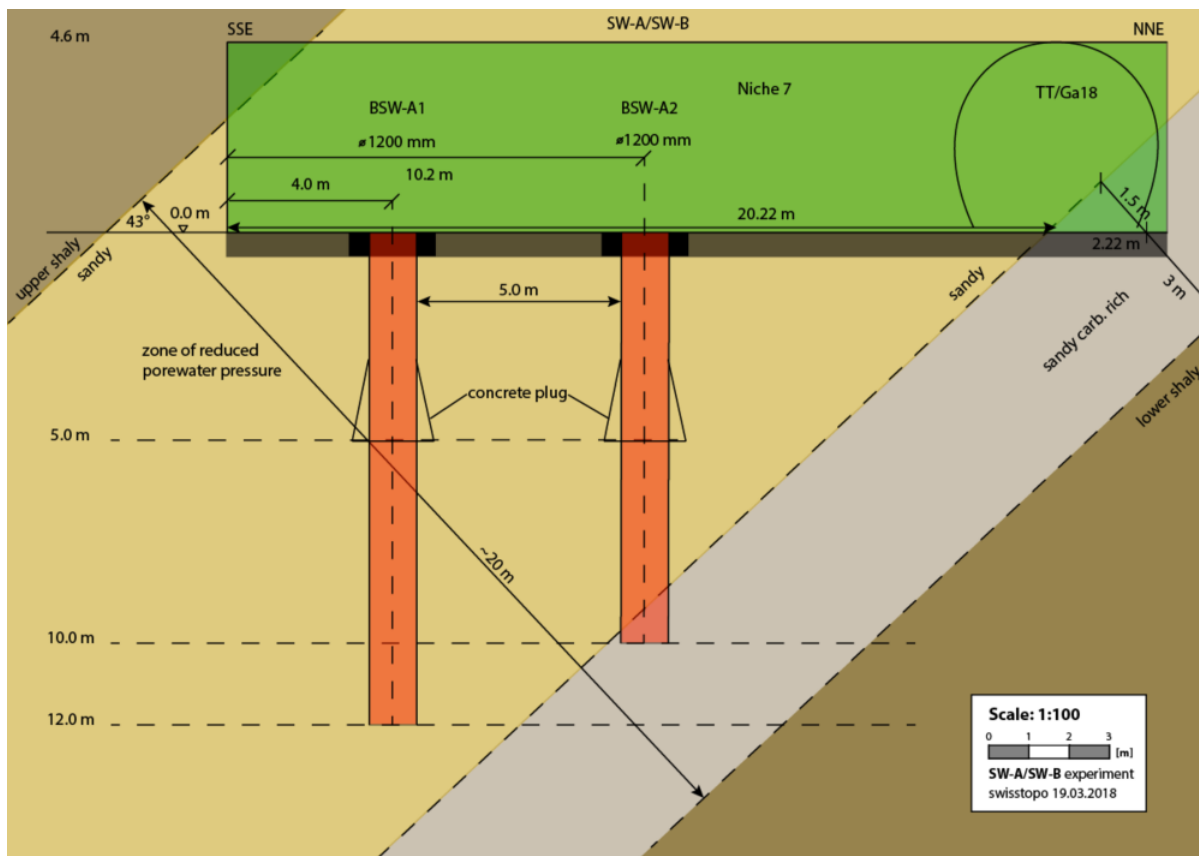


Figure 3.6 Vertical section of Niche 7 with most important geological boundaries (prediction)

Table 3.1 Data of Niche 7 excavation

Niche 7 NM [m]	Date [dd/mm/yy]	Progress [m]	Excavation time [h]	Lithology
1.5	05.04.2018	1.5	13.5	lower sandy facies
3.5	11.04.2018	2.0	8	lower sandy facies
5.5	13.04.2018	2.0	8	lower sandy facies
8.0	16.04.2018	2.5	15.5	lower sandy facies
10.5	17.04.2018	2.5	6	lower sandy facies
13.5	18.04.2018	3.0	6	lower sandy facies
16.0	19.04.2018	2.5	7.5	lower sandy facies / transition to upper shaly facies
17.5	20.04.2018	1.5	6	upper shaly facies
invert	24.05.2018	-	-	lower sandy facies / upper shaly facies

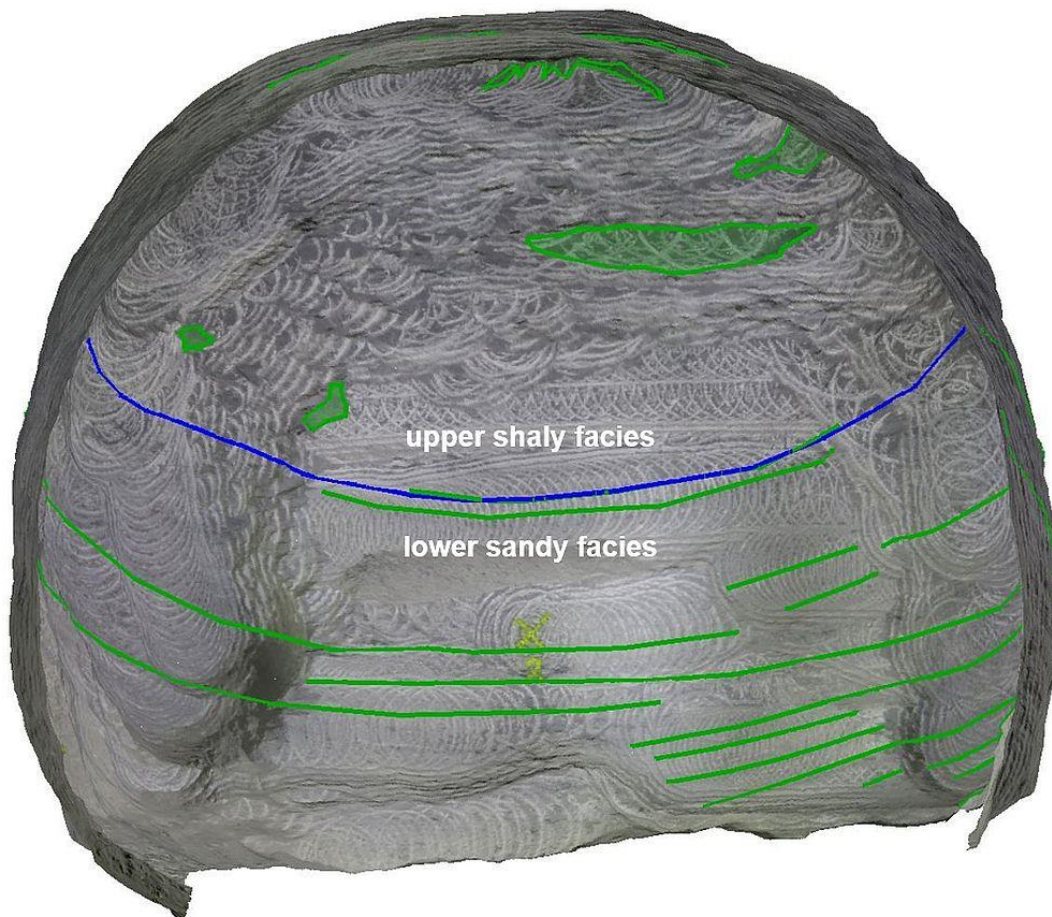


Figure 3.7 Niche diameter = 5.4 m (view from Ga18 towards Niche 7); mapping of tunnel front at NM16, showing the transition from lower sandy facies to upper shaly facies; lithology: green lines...bedding trace

4 Materials for sealing and equipotential layers (WP4)

4.1 Methods

4.1.1 Sample preparation

Size reduction

Pieces of basalt gravel were crushed using a jaw crusher (AEG). Rock fragments were homogenized and crushed by an agate vibrating-disc mill TS (SIEBTECHNIK GmbH, Mülheim an der Ruhr, Germany).

The powder was divided by quartation until aliquots of about 10 g were obtained.

Bentonite pillows and compacted bentonite (e.g. from HTV-5 or HTV-6) were manually crushed using a hammer. The samples were protected in a polyethylene bag to avoid contamination. Afterwards, the crushed material was ground using an agate mortar and pestle (Pulverisette, FRITSCH GmbH, Idar-Oberstein, Germany) and sieved at 500 μm .

Powder samples < 500 μm were further milled using the McCrone Micronizing mill with zirconium oxide cylindrical grinding elements (McCrone Microscopes and Accessories, Westmont, IL, USA) for quantitative XRD analysis.

Aliquotation

Rock fragments and powders were divided by either quartation or a rotary sample divider (Laborette 27) (FRITSCH GmbH, Idar-Oberstein, Germany) with V-shaped channel vibratory feeder (Laborette 24) until representative aliquots were obtained.

4.1.2 X-ray diffraction analysis (XRD)

Mineralogical quantification of Calcigel was performed by X-ray diffraction (XRD) measurements on powder samples < 500 μm . Samples were milled using the McCrone Micronizing mill with zirconium oxide cylindrical grinding elements (McCrone Microscopes and Accessories, Westmont, IL, USA). A second pattern was measured after addition of about 10% of internal standard ZnO (purity > 99%, Merck KGaA, Darmstadt, Germany) manually homogenized using an agate mortar. A Bruker D8 Advance A25 diffractometer (Bruker AXS GmbH, Karlsruhe, Germany) equipped with a LYNXEYE XE Detector (opening degree 2.94° and 192 channels) was used. Patterns were recorded between 2 and 80° 2 θ with CuK α radiation, a counting time of 2 s and a step size of 0.02° 2 θ , a fixed slit of 0.18°, Soller collimator of 2.5° (primary and secondary side) and an automatic knife edge for powder samples. Rietveld software "AUTOQUAN" (Version 2.8.0; GE Inspection Technologies GmbH, Ahrensburg, Germany) was utilized for quantitative analysis (Kleeberg and Bergmann, 2002).

4.1.3 X-ray fluorescence analysis (XRF)

The major elements were quantified in duplicate from the materials < 500 μm by X-ray fluorescence analysis (XRF) (Philips MagiX PRO spectrometer, PANalytical B.V. Almedo, Netherlands) equipped with a rhodium X-ray tube (3.2 kW) using air-dry powder samples fused with Li₂B₄O₇ (mixing ratio 1:7). The loss on ignition was determined separately at 1000 °C.

4.1.4 Simultaneous thermal analysis (STA)

The thermal behavior was studied by simultaneous thermal analysis (STA). The measurements were performed on a STA 449 C Jupiter (NETZSCH-Gerätebau GmbH, Selb, Germany) equipped with a thermogravimetry/differential scanning calorimetry (TG/DSC) sample holder. The STA is connected to a quadrupole mass spectrometer (MS) 403 C Aëolos (InProcess Instruments (IPI)/NETZSCH-Gerätebau GmbH, Selb, Germany) by a heated quartz glass capillary (T = 230 °C). The evolved gases with m/z = 18 (for H₂O), 44 (for CO₂) and 64

(for SO_4^{2-}) were followed. Measurements were done under synthetic dry air (SynA; 79 wt.% N_2 / 21 wt.% O_2 ; 50 mL/min) combined with N_2 (20 mL/min) (protective gas).

4.1.5 Cation exchange capacity (CEC) measurement and analysis of exchangeable cations

CEC was measured by the Cu-trien method according to Meier and Kahr (1999) with changes according to Steudel *et al.*, (2009). Approximately 50 mg of sample were weighed into a 50 ml centrifugation tube. Then, 10 mL of Millipore water and 5 mL of a copper-triethylenetetramine (Cu-trien) solution of 0.01 mol/L were added. The dispersions were shaken for 3 h and then centrifuged at 4500 rpm for 10 min (Multifuge 3S-R, Heraeus Holding GmbH, Hanau, Germany). Subsequently, the absorbance of the supernatants at a wavelength (λ) of 580 nm was determined by a UV-Vis spectrophotometer (Genesys 10 UV, Thermo Electron Corporation, Waltham, MA, USA) using polystyrene microcuvettes (Lab logistics Groups GmbH, Meckenheim, Germany) with a path length of 1 cm. The concentrations of Cu-trien in the supernatants were determined from a calibration curve and CEC was calculated (eq. 4.1).

$$CEC = \frac{v_{Cu-trien} * [c_{Cu-trien} * V_{Cu-trien} - c_{Cu-trien,s} * (V_{Cu-trien} + V_{H_2O})]}{m_d} * 10^5 \quad (4.1)$$

CEC	cmol(+)/kg	cation exchange capacity
$v_{Cu-trien}$	-	valence of the Cu-trien complex (equal to 2 at a pH between 5.2 and 10.7) (Delavernhe <i>et al.</i> , 2015)
$c_{Cu-trien}$	mol/L	concentration of initial Cu-trien solution
$V_{Cu-trien}$	mL	volume of the initial Cu-trien solution
$c_{Cu-trien,s}$	mol/L	concentration of the Cu-trien in the supernatant
V_{H_2O}	mL	volume of deionized water
m_d	mg	mass of the anhydrous sample calculated from moisture after drying at 200 °C

The concentrations of exchangeable cations were analyzed from supernatant by inductively coupled plasma - optical emission spectrometry (ICP-OES) (Optima 8300 DV, Perkin Elmer Inc., Waltham, MA, USA).

4.1.6 Conductivity measurement and analysis of dissolved ions

Conductivity was determined using conductometer WTW LF 318 (Xylem Analytics Germany Sales GmbH and Co. KG, Weilheim in Oberbayern, Germany). Approximately 2 g of the sample were weighed into 50 mL centrifuge tube and 40 mL of Millipore water were added. The admixture was shaken for 24 h. Thereafter, the samples were centrifuged at 4500 rpm for 10 min. The conductivity and the temperature were measured directly in the supernatant. The concentrations of the cations Na^+ , Ca^{2+} , Mg^{2+} , and K^+ , and anions Cl^- and SO_4^{2-} were analyzed from filtered supernatant (filtered through a 0.45 μm filter, syringe filter, cellulose acetate, $d = 25$ mm, LLG-Labware GmbH, Meckenheim, Germany). Cations were analyzed by ICP-OES method and anions by ionic chromatography (Dionex LC 20 with conductivity detector CD 20, Dionex GmbH, Sunnyvale, California, USA).

Salt content was calculated as a sum of cations and anions (in wt.-%) determined by conductivity measurement of supernatant.

4.1.7 pH and fluid density

The pH of fluids was measured with FiveEasy FE20 pH meter equipped with Inlab Expert Pt1000 electrode (Mettler Toledo) at room temperature in open containers (flasks, bottles, etc.). Stirring with a teflon stirrer was applied in large fluid volumes.

Fluid density was measured with a hydrometer at room temperature. Room temperature was recorded.

4.1.8 Water content (w) and moisture (w_m)

The water content and moisture of the materials were determined mostly in duplicate after heating at 105 (110) °C, 200 (240) °C or 240 °C for 24 h or until constant weight ($\Delta m < 0.1\%$) was obtained (DIN 52102). Heating to 200 °C (or 240 °C) is necessary to dehydrate swellable clay minerals (Emmerich *et al.*, 2018) in bentonites. For heating, various furnaces were used (e.g. furnace B180 Nabertherm GmbH, Lilienthal, Germany).

The mass of the subsamples used for water content measurement (100 mg - 200 g) was chosen according to the particle/aggregate size of the sample and available balance.

The water content was calculated with respect to dry mass of the sample after heating (eq. 4.2), while moisture was calculated in relation to the initial mass of the sample (eq. 4.3).

$$w = \frac{m_{H_2O}}{m_d} \quad \text{and} \quad w [\%] = w * 100 \quad (4.2)$$

$$w_m = \frac{m_{H_2O}}{m_w} \quad \text{and} \quad w_m [\%] = w_m * 100 \quad (4.3)$$

w	[-] or %	water content
w _m	[-] or %	moisture
m _{H₂O}	g	released water during heating at 105 or 200 °C
m _d	g	sample mass after heating
m _w	g	initial sample mass prior to heating

4.1.9 Bulk, dry, specific density (ρ_b, ρ_d, ρ_s), effective montmorillonite dry density (EMDD)

Bulk density (4.4)

$$\rho_b = \frac{m_w}{V_t}$$

Dry density (4.5a; 4.5b)

$$\rho_d = \frac{m_s}{V_t}$$

Specific density (4.6)

$$\rho_s = \frac{m_s}{V_s}$$

$$\rho_d = \frac{\rho_b}{1 + w}$$

m _w	g	initial sample mass
m _s	g	solid mass (sample mass after drying at 105 or 200 °C)
V _t	cm ³	total volume
V _s	cm ³	volume of the solid

Specific (or grain) density can also be measured with a gas pycnometer (e.g. Pycnomatic ATC Porotec) according to DIN 66137-2, or a water (deionized and deaired) pycnometer in case of

non-swelling materials (UNE 103-302-94) or calculated from the crystal structure of minerals (eq. 4.7). For both measurements, dehydration of samples by oven heating is required.

$$\rho_s = \frac{m_{UC}}{V_{UC}} \quad (4.7)$$

m_{UC}	g	mass of unit cell
V_{UC}	cm ³	volume of unit cell

The EMDD (ρ_{EMD}) is calculated (Dixon *et al.*, 1985) based on the smectite content of a bentonite (eq. 4.8).

$$\rho_{EMD} = (1 - f) * \left(\frac{\rho_d}{1 - \frac{f * \rho_d}{\rho_s}} \right) \quad (4.8)$$

f	[-]	mass fraction of non-smectitic material in the sample from quantitative phase analysis by XRD
---	-----	---

Porosity (4.9a; 4.9b)

$$n = \frac{V_p}{V_t}$$

$$n = 1 - \frac{\rho_d}{\rho_s}$$

Saturation (4.10a; 4.10b)

$$S = \frac{V_w}{V_p}$$

$$S = \frac{w}{\frac{\rho_w}{\rho_d} - \frac{\rho_w}{\rho_s}}$$

V_p	cm ³	pore volume
V_w	cm ³	volume of pore fluid
ρ_w	g/cm ³	density of pore fluid

4.1.10 Water vapor sorption isotherms

Samples are dried at 95 °C in vacuum ($p \approx 1\text{mTorr}$ or $0.133 \cdot 10^{-3}$ Pa) for 24 h. Measurements are performed with Hydrosorb 1000 (Quantachrom).

4.1.11 Particle size distribution (PSD)

Particle size measurements can be performed in different ways. The calculation theory used as a basis is decisive for the evaluation. The particle size distributions (PSD) shown are evaluations according to Fraunhofer theory, which is based on spherical shapes.

Sedimentation

Determination of PSD by sedimentation in Sedigraph Typ III of the micromeritics company can be performed only in liquid dispersion and is restricted to particle sizes of $d < 63 \mu\text{m}$. PSD is determined as weight% (wt.-%).

Laser granulometry

PSD can be measured for samples dispersed either in air or in a liquid. Volume% values are determined on the basis of the diffraction angle that is produced when the light waves of a laser beam hit a particle.

For the wet application, a dispersing solution was prepared (1,600 g deionized water with 5 g of dispersing additive BASF Dispex AA4040). 0.2 g of raw material mixed with 10 mL of the dispersing solution were measured with a Malvern Mastersizer 2000.

4.1.12 Water adsorption according to Enslin-Neff

The water adsorption test according to the German standard DIN 18132 was carried out in the Enslin-Neff device (Fig. 4.1) after a maximum of 24 h.

The water adsorption capacity (w_a) is the ratio of the amount of water (m_w) adsorbed by the dried sample to the dry mass (m_d) of the sample (eq. 4.11). The mass of the adsorbed water is calculated according to eq. 4.12. 1 g of air dry material was used and the initial water content was added to the additionally adsorbed water.

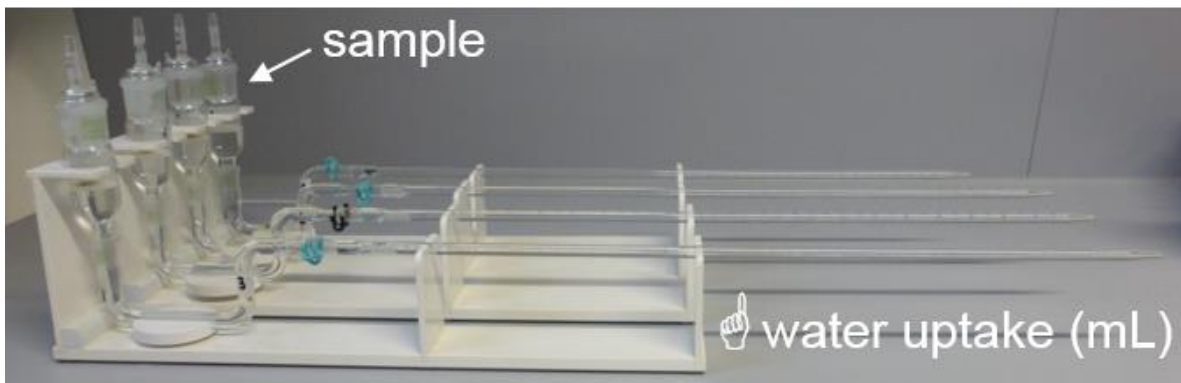


Figure 4.1: Enslin-Neff device

$$w_a[\%] = \frac{m_{H_2O}}{m_d} * 100 \quad (4.11) \quad \text{with} \quad m_w = (V_w - V_k) * \rho_w \quad (4.12)$$

V_w	cm^3	volume of adsorbed water at time t
V_k	cm^3	volume of evaporated water at time t
ρ_w	g/cm^3	density of the water for temperature during the measurement

4.1.13 Swelling pressure (p_s), gas permeability and liquid permeability

Swelling pressure (1)

The swelling pressure tests were carried out in pressure cells (Fig. 4.2) adopted from IfG Leipzig (Freyer *et al.*, 2015). The cells allow swelling pressure tests on 50 mm diameter samples with a length ≤ 50 mm. Apart from the simple structure and operation, these cells were used for the following reasons:

- possibility of monitoring the mass of the swelling pressure cells in order to determine the mass increase of the bentonite samples as a result of the ongoing saturation process,
- installation of volume-stable confined samples for the determination of swelling pressure and liquid permeability,
- representative but limited sample volume to limit the time required to saturate the samples.

Bentonite pillows were crushed to 0-10 mm prior to installation into the cells. The crushed material was compacted in the cell to the target bulk density for a defined water content.

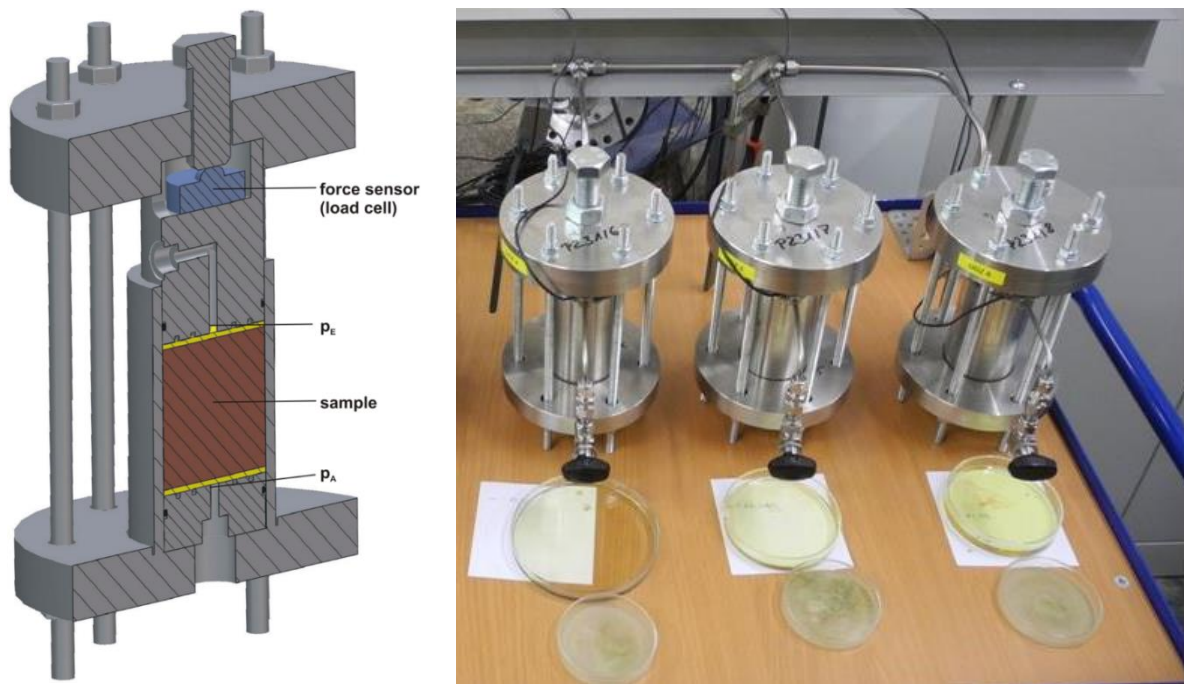


Figure 4.2 Swelling pressure cells (IBeWa)

Prior to the installation of the swelling pressure cells, a sandstone or bronze frit was placed at both ends of the compacted bentonite to prevent solid transport. Swelling pressure measurements were performed with tap water (Freiberg/Saxony) and Pearson water (chapter 4.4) at 23 ± 3 °C.

The saturation with a liquid was carried out with hardly any pressure from below acting on the downstream open cell. It is known from the experience of flow tests or saturation experiments that the ongoing swelling process and the associated reduction in permeability on the upstream side lead to the development of a low-permeability, saturated sample section. The permeability and length of this section determines the progression of the saturation front in the sample. Depending on the fluid pressure applied, this sample section can simultaneously act as a "mechanical cylinder" and effect subsequent densification of the unsaturated sample material

(compressibility increases with increasing water content). In a working hypothesis it is assumed that, as a consequence, the sample section has a low permeability, less than the final permeability in the completely saturated state. It is assumed that over a longer period, after complete saturation of the bentonite sample, redistribution and equalization of the density in the sample leads to a homogeneous permeability distribution. Corresponding processes were observed in various semi-technical experiments. Depending on the initial permeability, the swelling pressure behavior, the permeability of the saturated bentonite sample as well as on the geometry of the sealing system, this effect has to be taken into consideration for the processes on a large scale.

In order to prevent an influence of the described effect, the hydration of bentonite samples was carried out with a very small pressure difference across the sample in the order of 20 kPa. This difference was largely kept constant over the entire period of saturation. For the ongoing saturation process of a sample, a superposition of the liquid flow in the pore space due to the capillary pressure conditions in the sample and the hydrostatic pressure of the inflowing liquid have to be considered.

The saturation process was continued until no increase of swelling pressure and saturation was detectable. After reaching this sample state, the samples in the cells were relieved by separating from water supply.

Over the duration of a test, the following measurement data were recorded:

- Hydrograph of upstream fluid pressure,
- Hydrograph of load cells,
- Cumulative mass of water,
- Hydrographs of mass of the swelling pressure cell,
- Temperature and air pressure.

Swelling pressure (2)

For another set of samples standard oedometers and high-pressure oedometers were used. The procedure for sample preparation and mounting in the oedometer cell was the same. The clay was uniaxially compacted with its air-dry water content at dry densities between 1.3 and 1.6 g/cm³ in stainless steel rings. The inner diameter of the rings was between 36 and 50 mm and the initial height of the clay specimen was 12 mm. Filter paper (Whatman 54) and porous filters were placed on the top and bottom of the samples.

In the standard oedometers (Fig. 4.3), the oedometer cell was filled with Pearson water (chapter 4.2.1) and the deformation was monitored continuously. To maintain a constant specimen volume during saturation, lead weights were added manually to the oedometer frame lever arm. Ideally the vertical strain shall not drift excessively from ± 0.005 mm, thus preventing both the swelling and the consolidation of the sample. The test was considered to be completed when, under a constant vertical load, no strain was observed for at least 24 h. With this system the swelling pressure exercised by the sample is determined from the load that has to be applied for the volume of the sample to be kept constant during saturation, taking into account the sample surface area and the value of the lever arm. The deformation experienced by the equipment upon loading was previously calibrated and taken into account when the loads were added and for computation of the final strain of the specimens.

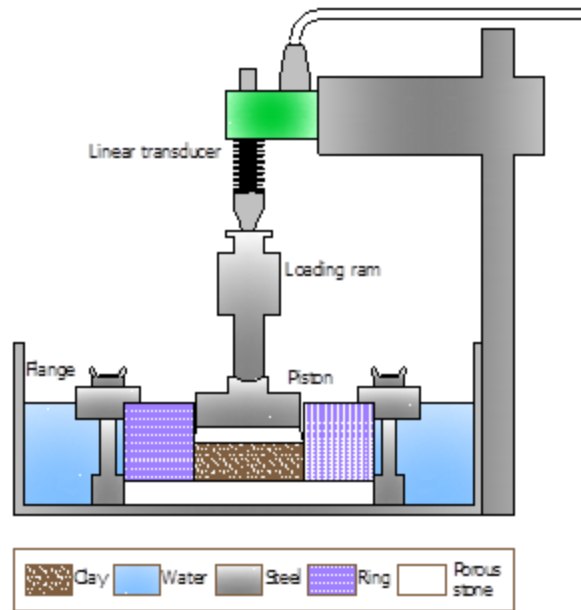


Figure 4.3 Schematic cross section of a standard oedometer cell

A custom-built high-pressure oedometer (Fig. 4.4) was also used to measure swelling pressure. It allows to keep the sample volume constant, while the water intake and the axial pressure developed on saturation are measured. The sample, compacted in a ring and confined between porous stainless steel sinters, was hydrated at constant volume through the bottom surface with Pearson water from a water column (pressure of 15 kPa), while the upper outlet remained open to atmosphere. At the same time, a load cell installed in the loading frame measured the swelling pressure exerted by the clay. Two linear strain transducers measured the small vertical deformation of the specimen, which was mainly due to load cell and frame deformability. An automatic volume change apparatus measured the water intake of the specimen. The values of load, strain and water intake were recorded automatically. After complete saturation (assumed when swelling pressure stabilized), the pressure registered was considered the swelling pressure value for the dry density attained. The actual density may differ slightly from the former due to the small displacement allowed by the equipment (about 10 μm when a vertical stress of 2.2 MPa is applied), and this was taken into account.

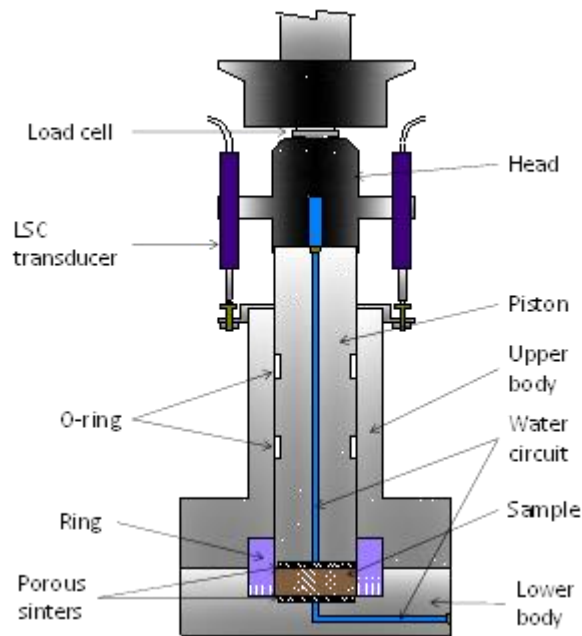


Figure 4.4 Schematic layout and photograph of the high-pressure oedometer equipment

The tests were performed at laboratory temperature. On completion of the tests, the height of the sample was checked and the water content of the specimen was determined by oven drying at 200 °C for 24 hours.

Gas permeability

The gas permeability tests were carried out on the initial compacted specimens in oedometer cells described under swelling pressure (1). Due to the initial moisture content of the compacted material, it can be assumed that the determined permeabilities are effective gas permeabilities for the saturation state in the pore space. Despite potential influence of the two-phase flow in the compacted specimens, the determined effective gas permeability is considered as a descriptive parameter for the initial permeability of the compacted material.

Gas permeability was determined in a steady state flow test with technical nitrogen. In the experiment, the sample was tested at several constant gas pressure differences. The gas flow rate for steady flow conditions was measured. When evaluating the results for the different pressure levels, the influence of the Klinkenberg effect and/or turbulence effect on the measured flow process was assessed.

Liquid permeability

Liquid permeability was determined using the saturated samples of the swelling pressure tests described under swelling pressure (1). As fluid, the liquids used for the saturation were applied. For the determination of permeability, the transient two-chamber experiment method was used (Fig. 4.5). Permeability determination is based on the model-based evaluation of the time-dependent flow process simulated in the experiment and measured. A pressure pulse in the input chamber triggers the flow process. The pressures measured over the experimental period in the input and output chambers describe the flow process and form the essential basis for model-supported determination of the permeability from the experimental data.

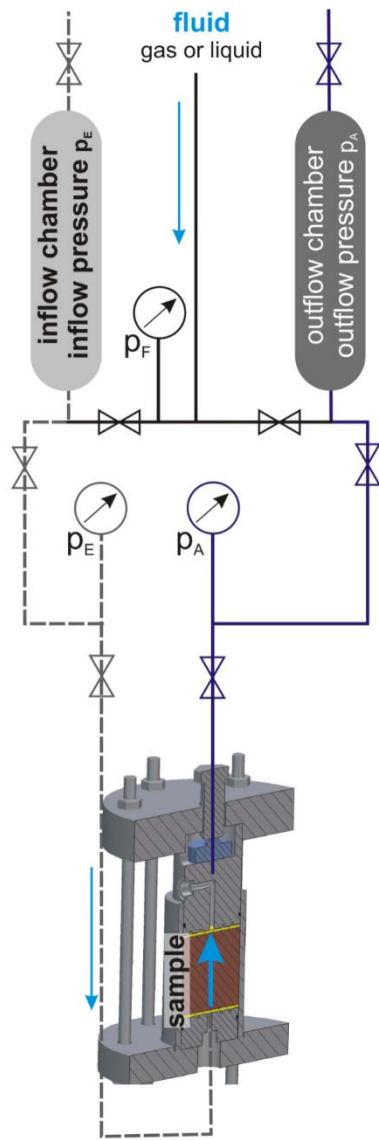
The determination of permeability is based on an evaluation of the temperature-controlled flow tests using the following information and data:

- Sample structure and geometry
- Experiment configuration - volumes of inlet and outlet chamber, piping system, test specimens,
- Thermodynamic properties of the flowing fluid - dynamic viscosity, density, compressibility for the thermodynamic conditions of the experiment,
- Pressure curves for the inlet and outlet chamber.

Each test is evaluated by combining the experimental knowledge in a numerical model. Depending on the structure of the test specimen, the evaluation of permeability is possible using a two- or three-dimensional model for a flow space with cylinder geometry (Fig. 4.6). Spatial discretization of the model can be adjusted depending on the sample geometry and the detailed knowledge on the sample. For the numerical model (Fig. 4.6), the location- and time-dependent solution of the partial differential equation for the isothermal, single-phase flow of gas or liquid (finite-difference method) is calculated. Determination of the permeability takes place by adapting the pressure profiles calculated for the input and output chambers to the measured pressure profiles. The adaptation takes place by a variation of the parameters of permeability and porosity.

If the porosity of the material was determined in accompanying investigations, this can be used as the starting value of the model-based parameter identification. If there are no results for the porosity, empirical values for the investigated materials are used as starting values. The objective function of the parameter identification is the minimization of the least square error for the measured and calculated pressure profiles (Fig. 4.6). For the flow of liquid in an initially non-saturated pore space, an influence of the two-phase flow and the interactions between liquid and rock cannot be excluded. A differentiation of the processes often is not possible without detailed investigations. In this situation, the pulse tests are repeated for liquid permeability tests until a reproducible pressure profile is detected in subsequent tests. For these conditions, it is assumed that the pressure pulse or the resulting pressure responses have spread in a saturated, "fully reacted" flow space.

The permeability is evaluated on the basis of the pulse test, finally assessed to be representative. By varying the experimental configuration, the testing method allows to determine the permeability for gases and liquids in the range $10^{-14} > k > 10^{-22} \text{ m}^2$ and the effective porosity. The porosity is identified on the basis of the mass balance modeled for the gas flow process. This porosity is effectively involved in the flow process. For this reason, it may be smaller than the predetermined initial value of the total porosity.



p_M – confining pressure
 p_E – inflow pressure
 p_A – outflow pressure
 p_F – fluid pressure

Figure 4.5 Schematic sketch of liquid permeability measurement

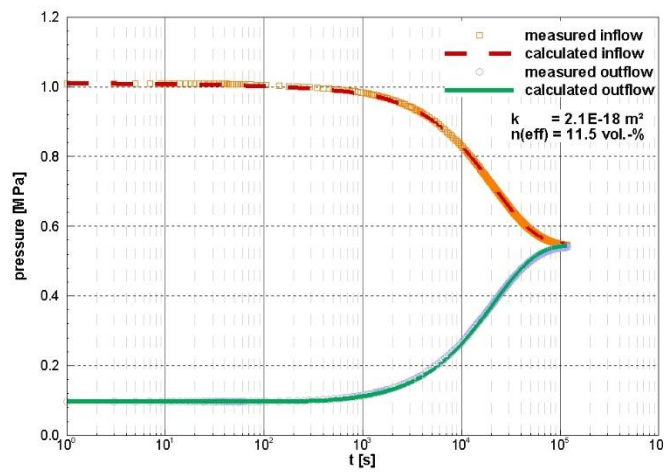
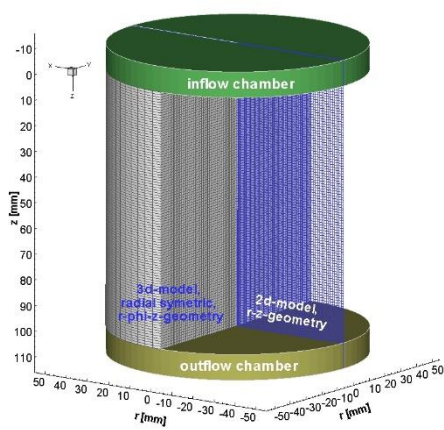


Figure 4.6 Scheme of numerical model and example of model-based fitting

4.1.14 Suction pressure measurement and water retention curves (WRC)

The relative humidity and temperature of the compacted samples were measured with psychrometers or capacitive sensors depending on their water content. The relative humidity of samples with a higher water content was measured with psychrometers Wescor Elitech PST-55-30-SF with stainless steel filters (Fig. 4.7) connected to a Wescor Elitech PSYPRO data logger. These sensors of 6 mm in diameter and 30 mm in length operate in a suction pressure range from 50 to 6200 kPa with a precision of $\pm 1\%$ FS. The capacitive transmitters used for samples with a lower water content were Sensirion SHT75 which have a precision of 2% rH in the range from 20 to 80%.

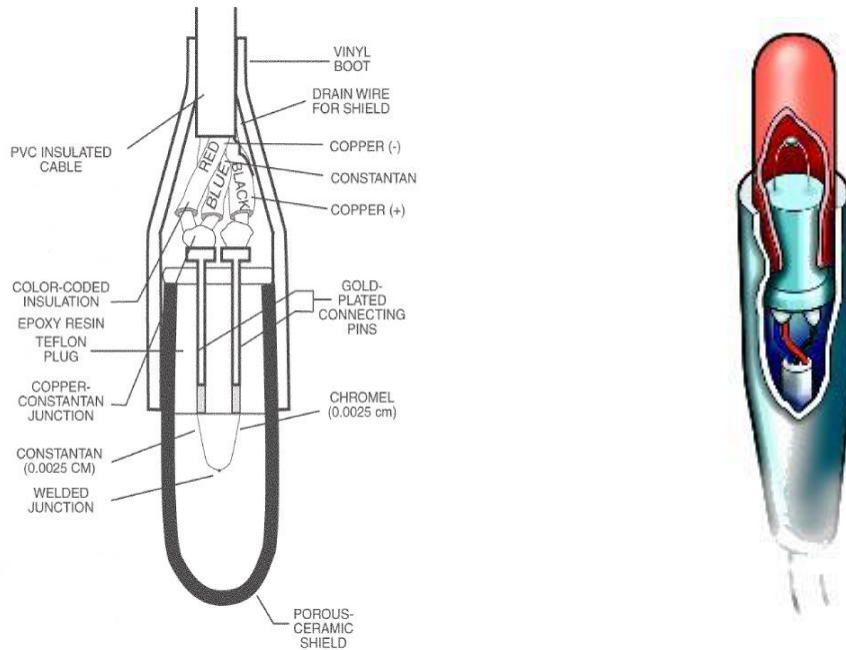


Figure 4.7 Schematic representation of a psychrometer

To convert the values of relative humidity to suction pressure values the Kelvin's law (eq. 4.13) was used.

$$s = -10^6 * \frac{R * T}{V_m} * \ln\left(\frac{RH}{100}\right) \quad (4.13)$$

rH	%	relative humidity
s	MPa	suction pressure
R	8.3145 J/mol·K	universal constant of gases
T	K	absolute temperature
V_m	$1.80 \cdot 10^{-5} \text{ m}^3/\text{mol}$	molar volume of water

The samples were prepared with different water contents to determine suction pressure in relation to the water content and define the water retention curves. To this end, each material was mixed with the quantity of Pearson water necessary to obtain the final water content desired taking into account the initial water content of the materials. These mixtures were preserved in hermetic plastic bags for several days to ensure good homogenization. In those

cases in which the water content required was lower than the initial water content of the materials, the samples were dried by subjecting them to a low relative humidity inside a desiccator with sulphuric acid solutions or by placing them in the oven at 110 °C for short, controlled periods of time. The rH of the samples compacted with their as-received water contents was also measured.

The samples thus prepared were compacted in stainless steel cells at a dry density of 1.5 g/cm³ for Calcigel and 1.55 g/cm³ for the rest of materials by applying uniaxial pressures of between 0.1 and 60 MPa. The samples had diameters of 70 mm and heights of 50 or 70 mm, depending on the sensor used for the measurement, psychrometers or capacitive sensors for suction pressures below or above 6 MPa, respectively (Fig. 4.8). A hole was drilled in the center of the upper part of the cylinders to insert the sensors. For the capacitive sensors, the hole had a diameter of 11 mm and a depth of 35 mm. For the psychrometers, a double hole was drilled to fit the shape of the sensor head, with a diameter of 6 mm at the bottom and 8 mm close to the block surface, and a total depth of 25 mm. A disc of PVC was placed on top of the block and the cell was sealed with plastic film to prevent moisture loss during the measuring process (Fig. 4.9). The time necessary for stabilization of the measurement was between 2 and 6 h depending on the material and its water content. The tests were performed at laboratory temperature.



Figure 4.8 Psychrometers (left) and capacitive sensor (right) inserted into the compacted samples

Upon completion of the tests, the sample was dismantled and the water content of the material was determined in two fragments by oven drying. Samples were dried at 110 °C for 48 h and weighed (which allowed to determine the water content under standard conditions in the laboratory) and then put in the oven at 200 °C for 24 h or directly dried at 200 °C for 24 h, which yielded the water content used in this report.



Figure 4.9 Measurement of suction pressure in compacted samples

The water retention curves in terms of degree of saturation were fitted to the van Genuchten expression (1980) (eq. 4.14; see also eq. 6.3) or Fredlund and Xing (1994) expression (eq. 4.15)

$$S_r = S_{lr} + (S_{ls} - S_{lr}) \left[\frac{1}{1 + \left(\frac{S}{P}\right)^{\frac{1}{1-\lambda}}} \right]^\lambda \quad (4.14)$$

S_r		degree of saturation
S_{lr}		residual degree of saturation
S_{ls}		maximum degree of saturation
P	MPa	parameter linked to the air entry value
λ	$0 < \lambda < 1$	parameter that controls the shape of the retention curve

Suction pressure in this equation is $P_g - P_l$ (P_g is the gas pressure in the pores and P_l is the liquid –water- pressure in the pores). Hence, it is matric suction pressure, although total suction pressures were measured in this work.

$$S_r = S_{lr} + (S_{ls} - S_{lr}) \left[\frac{1}{\ln \left[e + \left(\frac{S}{a}\right)^n \right]} \right]^m \quad (4.15)$$

a	MPa	inflection point of the curve, closely related to the air-entry value
m and n		parameters that control the slope of the curve

In both equations the residual degree of saturation, S_{lr} , was set to 0% and the maximum degree of saturation, S_{ls} , to 100%. For fitting, the software SWRC FIT version 3 was used (Seki, 2007).

4.1.15 Rising height

The rising height of ES materials is tested in a harp of Plexiglas columns with a length of up to 300 cm and with 46 mm inner diameter and 50 mm outer diameter (Fig. 4.10). The resulting material volume is about 5000 cm³. The columns are vertical during the test, but can be tilted during filling to avoid air pillows that will cause disruption of hydration or settlings during hydration. Rising height was tested with tap water (Speyer), Pearson water and 4 M NaCl solution (chapter 4.2). A height of 300 cm corresponds to a pF value of 2.5. Materials had to be found that fulfilled this requirement. Thereby, the type of liquid plays an important role. The finer the material, the higher the rising height. However, the tested materials were rather slow, but it was assumed that the slowest materials were most likely to reach the required rising height.

The material was poured into each column from above in portions of about 1 kg each. Short, powerful taps on the outer column wall were applied until no settlement of the material could be detected to prevent change in volume of the material during hydration. The bottom of the column was closed with a filter paper through which the water could enter. About 5 mm of coarse sand were filled into an 800 mL beaker and the column with the sample was placed on it. The 200 mL mark was selected as the fluid level. The fluid level was about 3 cm above the column bottom. At the beginning of the experiment 100 mL of fluid were added, which then corresponded to about this 200 mL mark. The start time was recorded. Test fluid was filled up to a certain level in the beakers and the fluid uptake was determined volumetrically. The rising fluid front was visually detected by the discoloration of the solid material.



Figure 4.10 Harp of plexiglas columns

The fluid level in the beaker was then kept as constant as possible. Each refill was recorded in terms of time and quantity, typically together with the rising heights.

The fluid movement was very fast at the beginning of the experiment and became slower with the duration of the experiment. In the beginning, it had to be read hourly, towards the end only weekly. After the gradient of the fluid front has remained constant, the experiment was kept for some time to observe the additional fluid absorption.

4.1.16 Time domain reflectometry (TDR)

In time domain reflectometry (TDR), a short high-frequency pulse (approx. 1 MHz to 3 GHz) is applied via a coaxial connecting cable to a sensor embedded in the material to be measured (Fig. 4.11). The pulse runs to the end of the sensor, is reflected there and returns to the TDR system. The time the pulse takes to reach the end of the sensor and back is determined and converted into a volumetric water content via a material-dependent transfer function or into a gravimetric moisture/water content (w_m/w), if the installation density is known.

In this case, the sensors are TAUPE cable sensors, consisting of a flat ribbon cable with three copper conductors connected to the coaxial cable on one side and open on the other side. The transitions are sheathed with a two-component resin for protection against penetrating fluid. The pulse produces an electromagnetic field between the conductors, which detects a volume of the surrounding material, the radius of which corresponds approximately to the distance between the conductors. With the TAUPE cable sensor, this is 25 mm, i.e. the TDR signal detects moisture from a volume of up to 25 mm around the middle conductor.

The resulting signal is the reflection factor R ; it describes the portion of the signal reflected for each variation in impedance along the path between the TDR system and the sensor end. The rest of the signal moves on, with the signal intensity being slightly attenuated by each further reflection. Impedance changes are: The transition between the coaxial cable ($R = 0$) and the sensor start ($R > 0$), all differences in ϵ'_b (= moisture, salinity, density changes, different materials) ($-1 < R < +1$) as well as the sensor end ($R = 1$; reflection at the open end).

In order to increase the sensitivity of the TDR system, a fixed window with a selectable number of equidistant points along the sensor part from shortly before the start to about 4 times the sensor length (adjustable in the measuring software) is selected instead of the entire distance between coaxial cable and sensor. The windows length is proportional to the square root of ϵ'_b . This means if $\epsilon'_b = 16$, the windows length should be 4.

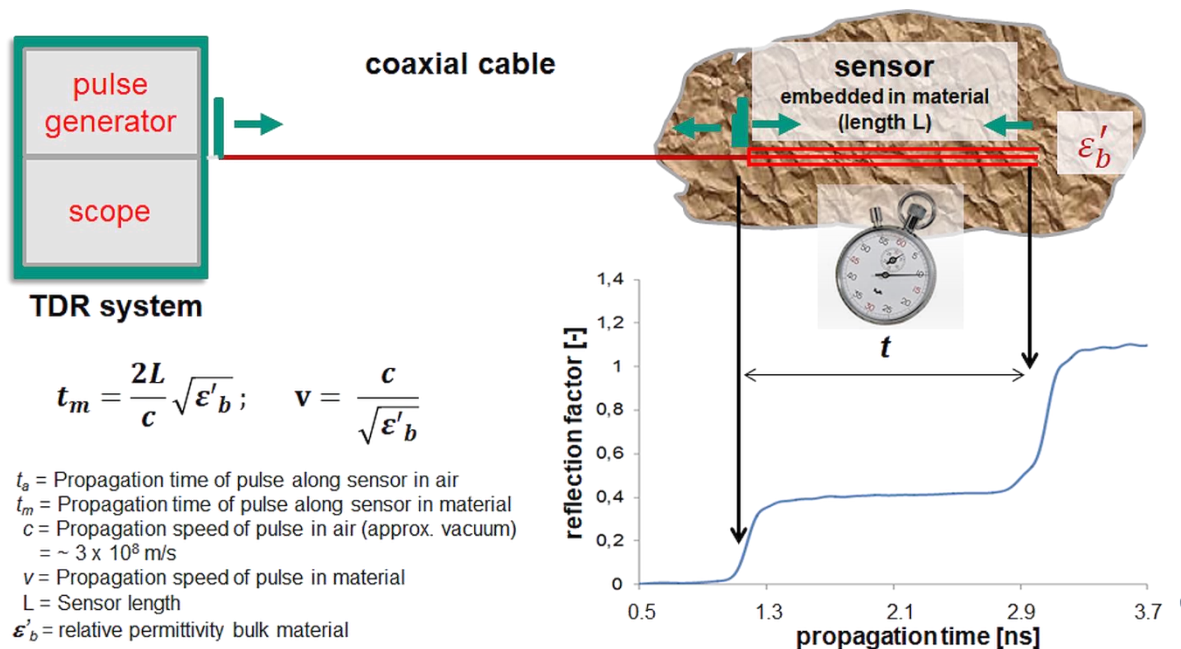


Figure 4.11 TDR method and determination of the propagation time

The propagation time t of the pulse results from the material-dependent propagation velocity v along the sensor of length L and back ($2L$). The dielectric properties of a porous material are

greatly altered by the addition of fluid. The relative dielectric permittivity (related to vacuum) ϵ' of air is 1, of dry soil material between about 2 and 7, and of water at room temperature about 80. Depending on the pore volume and its loading with fluid, ϵ'_b of the material mixture of porous material, pore air and fluid can reach values of up to about 20.

Evaluation of TDR measurements

Usually, the integral moisture/water content is determined by evaluating the moisture-dependent transit time of a pulse along the sensor embedded in the material. However, a position-dependent description of moisture changes at the sensor would be desirable. There are different approaches available. One of them derives the electrical properties of the sensor (capacitance, inductance, resistance) and from them the local moisture in a homogeneous material by means of a mathematical inverse reconstruction procedure. Such methods, however, are computationally complex and limited in their accuracy. For this reason, a method is used which draws conclusions with respect to the spatially distributed dielectric permittivity simply from the amplitude of the reflected TDR signal and relates it to a reference state, e.g. the dry state.

Determination of the integral moisture/water content

The TDR signal measured on a longer sensor, such as the TAUPE cable sensor, usually has the shape shown in Fig. 4.12. On the far left the curve starts with a part of the coaxial cable having a reflection factor of about "0". The transition between this part and the sensor start is steep and has a positive reflection factor, because the geometry of the ribbon cable has a higher characteristic impedance than the coaxial cable. Depending on the electrical conductivity of the surrounding material, the attenuation of the pulse changes along the sensor and, thus, the amplitude decreases towards the end. This limits the possible sensor length in practice.

The influence of moisture is particularly evident in the length of the sensor component in the TDR signal: with increasing moisture, the propagation speed of the pulse decreases due to the increasing effective dielectric permittivity of the material mixture. The signal needs more time to move forward on the sensor and backward after reflection at the sensor end; the signal end shifts to the right.

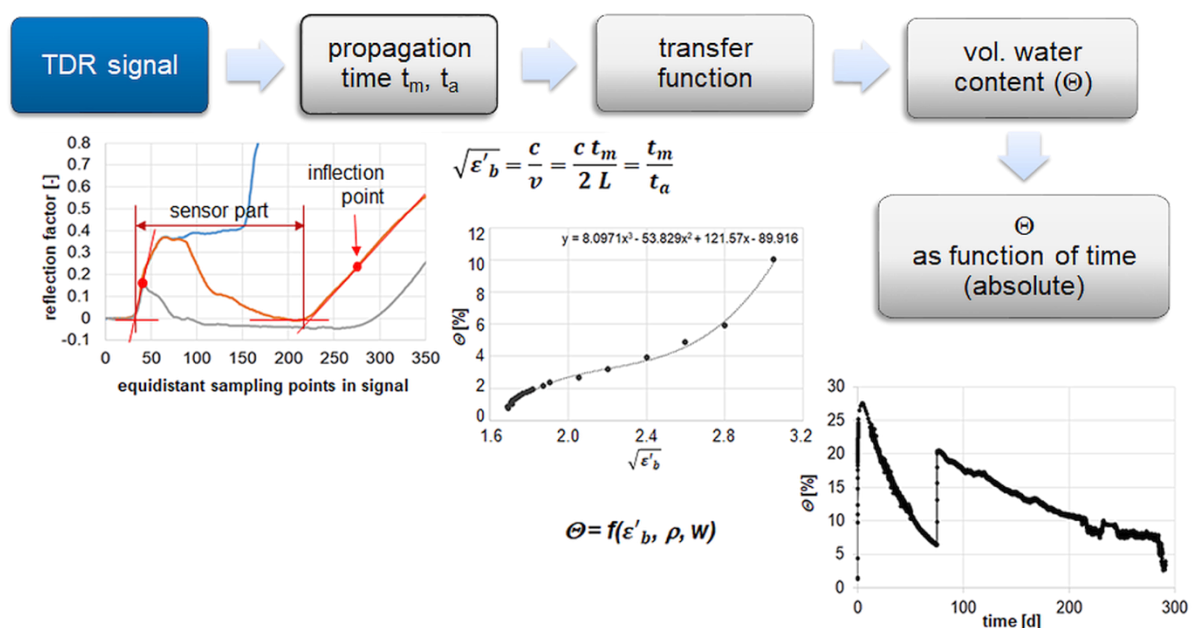


Figure 4.12 Method for determining the integral volumetric water content from the propagation time of TDR signals (m: material; a: air)

The integral volumetric water content is determined in several steps from the TDR signal along a sensor. (1) The first step is the determination of the beginning and end of the sensor from the signal according to the tangent method. The maxima of the first derivative of the signal show the inflection points of the ascents at the beginning and end of the sensor. The points of intersection with the horizontal by the minimum to the left determine the beginning and end of the sensor component in the TDR signal. (2) For the calculation of the relative (compared to vacuum, here approximated in air) effective dielectric permittivity ε'_b , the ratio of the measured propagation time in the material t_m to that in air t_a is needed. (3) Since there is no direct physical relationship between ε'_b and the volumetric water content, a calibration with the material used under identical installation conditions must be carried out in the laboratory for an exact determination of the water content. The gravimetric moisture/water content of these samples is determined by drying. If the bulk/dry density (eq. 4.2-4.6) is known, the result is converted to the volumetric water content θ (eq. 4.16). (4) The data of the TDR measurements are related to the moisture series and the density and lead to a transfer function (calibration) from the measured relative dielectric permittivity to the volumetric water content. (5) The TDR signals recorded over the duration of the experiment provide an image of the moisture changes over time.

$$\theta = \frac{V_w}{V_t} = w_m * \frac{\rho_b}{\rho_{H_2O}} = w * \frac{\rho_d}{\rho_{H_2O}} \quad (4.16)$$

Determination of the spatial distribution of moisture along the sensor (dTDR)

For the spatial representation of moisture distribution along a longer sensor, the change in the signal propagation time is irrelevant. Only the amplitude distribution of the reflection factor is of importance here. In the case of conventional, quasi-point sensors, this is of no interest, since the possibility of a local reconstruction along the sensor does not make sense, as the respective rise times of the signal at the beginning and end of the sensor are in the order of magnitude of the propagation time to be measured. The necessary local resolution then is not given. Long sensors, where the rise times of the pulse are small compared to the total propagation time, show variations of the amplitude in the signal course due to moisture and, thus, allow to obtain locally resolved moisture.

The methods described for amplitude evaluation are approximately equivalent in terms of resolution; in the case of semi-technical tests, the homogeneity of the material is not given and a reliable assignment of the moisture distribution is not possible. For this reason, the reflection factor from the TDR raw signal is used directly to describe the moisture change compared to a known reference condition. The method is called differential time-domain reflectometry dTDR. Compared to mathematical reconstruction methods, the dTDR method is simpler to apply, requires less computing capacity, and provides a sufficiently accurate spatial resolution for most applications.

The available data must also be prepared in several steps (Fig. 4.13). In the first step, the measured TDR data must be normalized in length, thus eliminating the influence of material moisture on the signal length. Along the length of the sensor, moisture can vary significantly and cause corresponding amplitude differences in the reflection factor. The normalization assigns the moisture distribution to its almost correct position along the sensor. An exact mapping would require more precise consideration of the influence of moisture on the local amplitude, which is not necessary in practice.

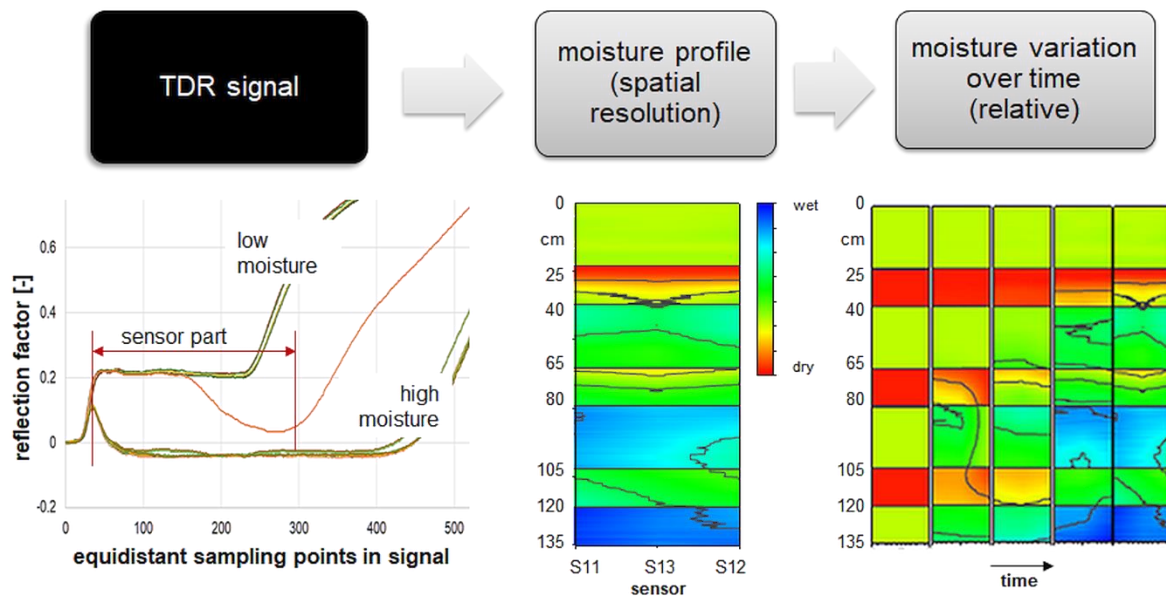


Figure 4.13 Method for determining the spatial distribution of moisture from TDR signals

Start and end points are easy to modify compared to integral moisture detection. The start point is near the maximum of the first rise and the end point is slightly after the start of the rise at the end. The normalized length can be assigned directly to the physical length of a sensor. The resulting image still contains electrical properties of the sensor, such as characteristic impedance and signal loss along the sensor. In combination with a higher electrical conductivity of the surrounding material, the signal along the sensor may become smaller and smaller. With longer sensors (> 3 m) the reflections at local moisture changes in the signal become increasingly smeared and thus less visible in the amplitude. This can be remedied largely by subtracting the signal of a known condition, e.g. the installation condition, from each current measurement signal as a reference point by point. As a result, the electrical properties of the sensor as well as the disturbing material properties are greatly reduced. For large moisture variations, it may be necessary to take into account the attenuation of the electromagnetic signal along the sensor, which is dependent on moisture and material. A linear dependence is sufficient as a first approximation. The resulting signal is the differential TDR (dTDR) signal, which now contains the moisture information along the sensor. If the initial distribution of moisture in the system is known, it can be superimposed on the dTDR signal and thus represents further moisture development (e.g. ES $< 1\%$ water content, DS approx. 11% water content).

Otherwise, any condition can be defined as reference. Then the result is not an absolute moisture but the relative change of moisture compared to the reference. It can be calibrated by the moisture of dismantled samples. The data obtained in this way can be displayed as a three-dimensional time series with the sensor length and the time as abscissa. The moisture can be displayed as color graphics, for example. Several similar sensors installed in parallel in one plane in the experiment are evaluated individually and the results between the sensors are interpolated linearly point by point. This makes it possible to determine the local distribution of moisture in the plane spanned by the sensors and to display it as a color graphic. Here, reddish colors correspond to a drier state than the reference state and bluish colors indicate areas of higher moisture (Fig. 4.14).

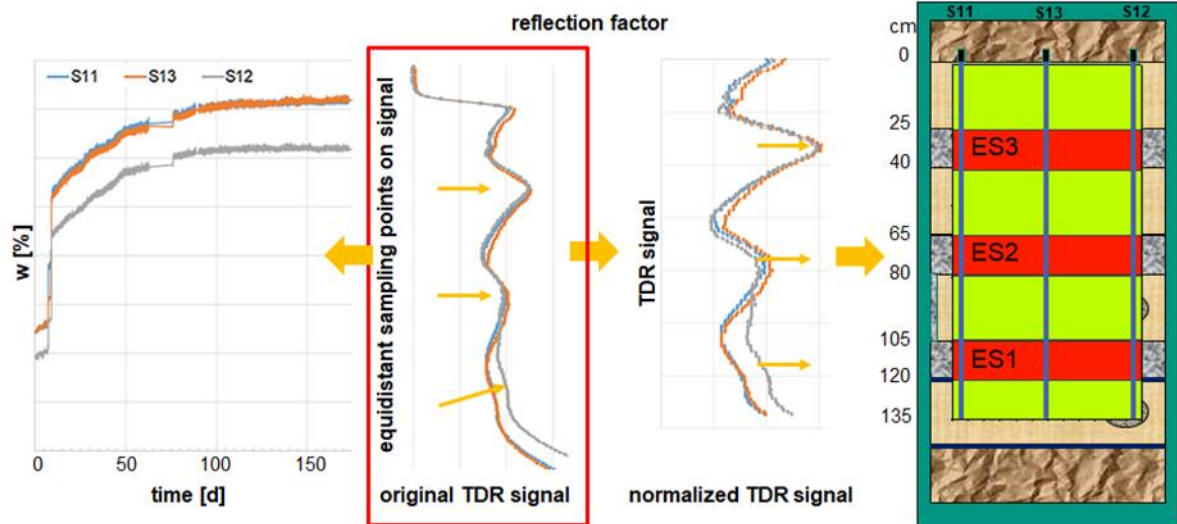


Figure 4.14 Comparative representation of both evaluation methods

4.2 Fluids

4.2.1 Pearson water

Pearson water (Wersin *et al.*, 2013) close to A3 composition (Pearson, 1998) that resamples the pore fluid of the sandy facies of Opalinus clay at Mont Terri URL (Pearson, 2003) was used (Tab. 4.1) for swelling pressure and permeability measurements, MiniSandwich experiments, HTV-5 and HTV-6 and rising height tests with ES materials.

Table 4.1 Pearson water

	Wersin <i>et al.</i> , 2013 NAGRA NAB 12-54			Pearson, 1998 A1 A3 Van Loon <i>et al.</i> , 2003			
	[g/mol]	[mmol/L]	[mg/L]	[mmol/L]	[mg/L]	[mmol/L]	[mg/L]
Na ⁺	23	164	3772	240	5526	128	2951
K ⁺	39.1	2.55	100	1.61	63	0.81	31
Mg ²⁺	24.3	9.17	223	16.91	411	4.94	120
Ca ²⁺	40.1	11.9	477	25.77	1033	6.94	278
Sr ²⁺	87.6	-	-	0.50	44	0.32	28
Cl ⁻	35.45	160	5672	300	10621	130	4607
SO ₄ ²⁻	96.1	24	2306	14.07	1353	11.47	1102
HCO ₃ ⁻	61	0.54	33	0.48	29	0.60	36
pH	[-]	7.6		7.6		7.9	
Dynamic viscosity (25 °C)	[mPa*s]	0.98					

Solutions of sodium and potassium salts, CaCl₂ and MgCl₂ (Tab. 4.2) were prepared separately in suitable volumes of deionized water to prevent precipitation. Afterwards the three solutions were combined and deionized water was added to obtain the final volume.

Table 4.2 Salts for Pearson water preparation

Salt	M	γ	c
	[g/mol]	[g/L]	[mol/L]
NaCl	58.5	12.38	0.21
Na ₂ SO ₄	142	2.00	0.014
NaHCO ₃	84	0.04	0.5*10 ⁻³
KCl	74.6	0.12	0.002
CaCl ₂ * 2 H ₂ O	147 (111+36)	3.793	0.026
MgCl ₂ * 6 H ₂ O	203.3 (95.3+108)	3.457	0.017

4.2.2 Tap water and deionized water

Table 4.3 Parameter of deionized water and tap water (* from literature)

	Deionized water	Tap water	
		Freiberg (Saxony) (03/2017)	Speyer (05/2017)
κ [$\mu\text{S}/\text{cm}$]	0.3	196	563
pH	5.5	8.3	7.4
ρ [g/mL] 20 °C	0.998*	n.d.	n.d.
η [$\text{mPa}\cdot\text{s}$] 15 °C	1.14*		
η [$\text{mPa}\cdot\text{s}$] 20 °C	1.00*		
η [$\text{mPa}\cdot\text{s}$] 25 °C	0.89*	0.98	n.d.
[mmol/L]			
Na^+	n.d.	0.4	0.57
K^+	n.d.	0.04	0.06
Mg^{2+}	n.d.	0.14	0.43
Ca^{2+}	n.d.	0.54	2
Sr^{2+}	n.d.	n.d.	n.d.
Cl^-	n.d.	0.43	0.23
SO_4^{2-}	n.d.	0.26	< 0.05
HCO_3^-	n.d.	n.d.	5.44

4.2.3 NaCl brine

Few experiments were performed with a 4M NaCl (density 1.15 g/cm³) simulating pore fluid of rock salt.

4.3 Materials for sealing layers

4.3.1 Material selection, processing and compaction

Few bentonites from all over the world (MX-80, FEBEX, Kunigel..) were studied for application in geotechnical barriers at different scale. Results show, that HMC properties of bentonites differ strongly. The aim of the current project was to test German Ca-bentonites for application in the DS of Sandwich sealing systems in interaction with artificial pore water of Opalinus clay (chapter 4.2.1). Ca-bentonite from Bavaria (Calcigel by Clariant) and from the Westerwald region (Secursol UHP by SSG) were characterized and compacted for use in MiniSandwich and semi-technical scale experiments.

Results from studying different national raw materials provide a tool kit for DS construction and strongly reduce dependence on business decisions by different suppliers and international trade policy.

For the HTV-5 (chapter 4.8.2), raw Calcigel was dried to a moisture of about 10% and ground by a hammer mill to a grain size $< 500 \mu\text{m}$ (100%; 93% $< 125 \mu\text{m}$). The ground Calcigel was compacted on a gutter press. The pillows with a square base area (Tab. 4.4) had a volume of about 10 cm^3 . 500 kg of the pillows were crashed to a particle size smaller than 3 mm (Fuller distribution).

To reach a high dry density during installation and low hydraulic conductivity in the DS, an enhanced concept of a binary mixture was developed. One component of such a binary mixture is a bentonite pellet of 15-20 mm length and 10 mm in diameter ($V \approx 1.5 \text{ cm}^3$). The second component that will perfectly fill the pores (Fig. 4.15) between the pellets is either a bentonite or a mineral material, if EMDD and swelling pressure have to be adjusted. Pore filling materials must have a shape of small flakes or granules. Ideally, the dimension of such flakes is less than one tenth of the diameter of the pellets.



Figure 4.15 Pouring density test; briquette filling (left) and filling with briquettes and granulate (right)

For producing pellets extrusion is an established process technology for tests on the pilot and production scales. Feasibility of pellet production for both bentonites was tested on the pilot scale with moisture between 23 and 27%. Afterwards, pellets were dried under ambient laboratory conditions to a moisture between 12 and 20%. These dried pellets were used for the swelling expansion tests as well as for the determination of the mechanical strength.

With the currently available extrusion technology, it is only possible to produce stable pellets with a bulk density of about 1.7 g/cm³. To reach higher densities, briquetting should be used. From a stock pile of Secursol UHP a 50 t batch with a moisture of ≈ 32% was extracted. After representative sampling and characterization the material was approved for further processing (ratio MgO/K₂O > 4, CEC > 80 cmol(+)/kg). In the next step, about 30 t of the bentonite were dried under production conditions at 105 °C with a drum dryer of type TT 190/5TGBAG by Allgaier. At the end, about 15 t of bentonite with a moisture of 10.7% were available for briquetting.

The dried bentonite was milled by a roll crusher (type WMZ 30a by Händle) to a grain size lower than 5.6 mm and was sieved with a screening plant of type S1564 (Mogensen) to obtain a target fraction of 0-3.15 mm for briquetting. First, the fraction > 8 mm consisting of quartz, basaltic relicts and other particles was rejected. Second, the fraction < 8 mm was split into the target fraction < 3.15 mm and the fraction 3.15 – 8 mm was crushed on a rolling mill until the targeted fraction < 3.15 mm was reached.

Pilot test were carried out at an external production site for briquetting, with particular attention being paid to the following aspects:

- dimension of pockets (3 cm³, 10 cm³)
- roller speed, corresponding to pressure time
- pressure
- density of briquettes

With the large pockets no stable briquettes could be formed under the given conditions of particle size distribution and moisture. In contrast, the smaller pockets worked well and were chosen for the production (Fig. 4.16). Finally, ≈ 12 t of briquettes were available for further processing.



Figure 4.16 Left: feeding material Secursol UHP (G1580) < 3.15 mm; middle: briquetting roller, pocket dimension 3 cm³; right: briquettes ready for shipping in big bags for HTV-6

With the briquetting process, bulk densities between 2.12 and 2.15 g/cm³ (dry densities between 1.89 and 1.92 g/cm³, respectively) were achieved and the bulk densities of the extrusion process of ≈ 1.7 g/cm³ were exceeded significantly. Further increase of the densities will probably be reached with a slightly reduced moisture of the feeding material (9.5 - 10%) and a finer particle size distribution.

After the briquetting process, ≈ 1 t of the briquettes were ground again to get pre-compacted pore fillers of the same bentonite as the briquettes. The briquettes with a rectangular base size of 3 x 1 cm and a height of 1 cm (Fig. 4.16 right) were crushed by a rolling mill of type 865

(Händle) to < 2 mm to test the pourability. To ensure a high packing density of briquettes with pore fillers, different sub-fractions of the fraction < 2 mm were tested on a laboratory scale. The best result was achieved with the fraction of 0.25 – 1.4 mm. Finally, the pre-crushed fraction of 0-2 mm was sieved to this target fraction with a production-scale Mogensensizer.

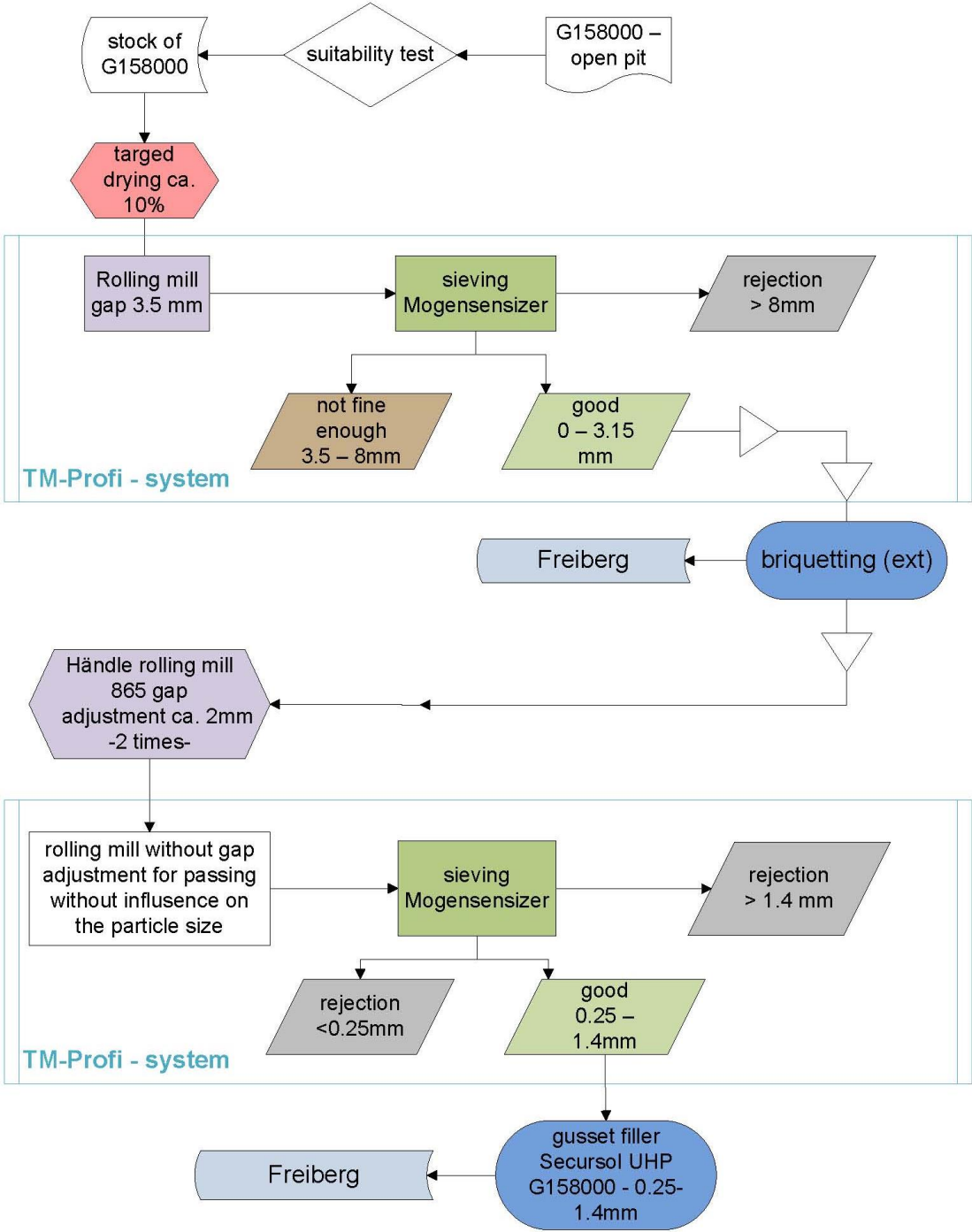




Figure 4.17 Flow chart for raw material treatment and briquetting of Secursol UHP (G1580)

Table 4.4 Calcigel pillows and pore filling material after production

	Moisture (200 °C)	[%]	10
	Water content	[%]	11.1
	Bulk density	[g/cm ³]	2.2
	Dry density	[g/cm ³]	1.98
	Pore filling material Fuller distribution	[mm]	0-3
	Bulk pouring density pillows	[g/cm ³]	1.123
Length 3.5 cm	Dry pouring density pillows		1.01
Width 3.5 cm	Bulk pouring density binary mixture (60:40)	[g/cm ³]	1.64
Height 1 cm	Dry pouring density binary mixture	[g/cm ³]	1.48

The specific density of Calcigel measured after drying at 200 °C was 2.74 g/cm³, while the calculated specific density from phase content (Tab. 4.6) was 2.76 g/cm³.

Table 4.5 Secursol UHP pillows and pore filling material after production

	Moisture (200 °C)	[%]	10.7
	Water content	[%]	12.0
	Bulk density	[g/cm ³]	2.14
	Dry density	[g/cm ³]	1.91
	Pore filling material	[mm]	0.25-1.4
	Bulk pouring density pillows	[g/cm ³]	1.156
Length 3 cm	Dry pouring density pillows		1.04
Width 1 cm	Bulk pouring density binary mixture (70:30)	[g/cm ³]	1.59
Height 1 cm	Dry pouring density binary mixture	[g/cm ³]	1.42

The specific density of Secursol UHP calculated from the phase content was 2.77 g/cm³ (Tab. 4.10), whereas the specific density measured after drying at 200 °C was 2.77 g/cm³ (Tab. 4.11).

4.3.2 Water adsorption isotherms and storage

After the briquetting process, it was noted that the briquettes rehydrated under ambient conditions (rH 45-55%). Thereby, the moisture of Secursol UHP ($\approx 13.8\%$) increased more strongly than the moisture of Calcigel ($\approx 11.7\%$). This could be explained by the dependence of the equilibrium water content (Fig. 4.18 and 4.19) on the smectite content and structure of the smectite.

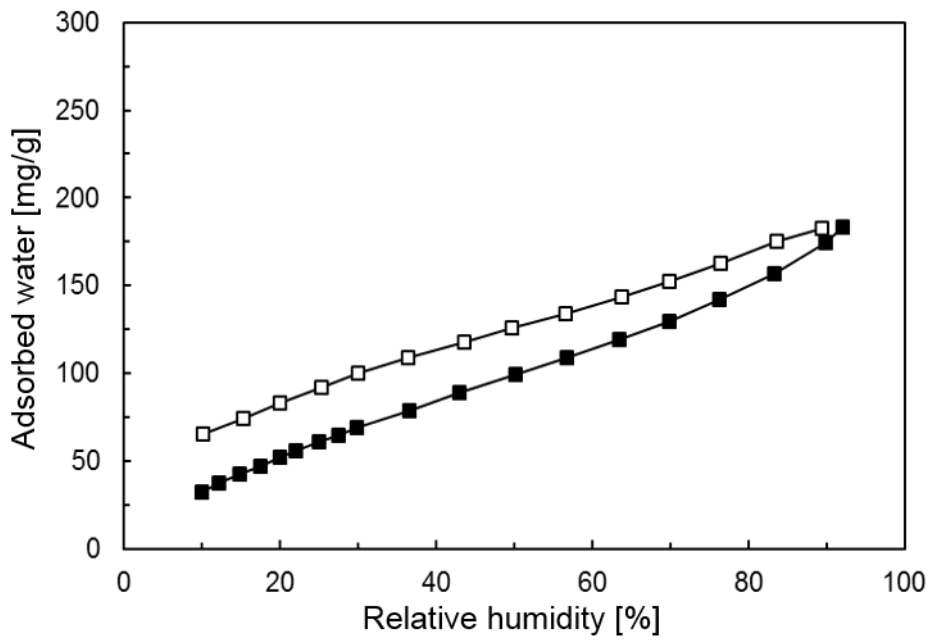


Figure 4.18 Water adsorption isotherm (20 °C) for Calcigel

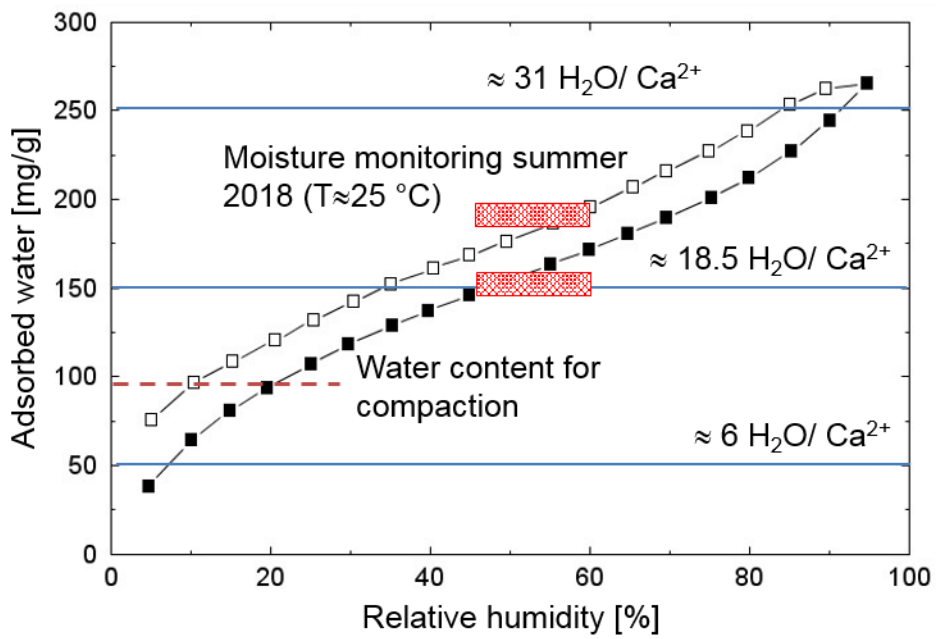


Figure 4.19 Water adsorption isotherm (20 °C) for Secursol UHP

4.3.3 Calcigel

4.3.3.1 Phase content

Table 4.6 Phase content and specific density

	[wt.%] 2W	[wt.%] anhydrous	ρ_s [g/cm ³]
Smectite (montmorillonite)	64	61	2.75
Muscovite	17	19	2.81
Quartz	10	11	2.66
Chlorite	2	2	3.0*
Kaolinite	2	2	2.6
Plagioclase	1	1	2.67 [#]
Calcite	1	1	2.71
Dolomite	2	2	2.84
Rutile	1	1	4.23
Total	100	100	2.76

*) average, depending on iron content, #) average for solid solution series albite-anorthite

4.3.3.2 Cation exchange capacity, exchangeable cations and soluble ions

Table 4.7 CEC and exchangeable cations

	CEC	Na ⁺	Ca ²⁺	Mg ²⁺	K ⁺	sum
			[cmol(+)/ kg]			
Calcigel pillow	68 ± 1	5.5 ± 0.1	43.8 ± 0.1	21.4 ± 0.4	1.4 ± 0.1	72.1 ± 0.5
Calcigel granulate	68 ± 1	5.5 ± 0.1	45.7 ± 0.7	22.0 ± 0.2	1.4 ± 0.1	74.6 ± 1.0
			[%]			
Calcigel pillow		7.6 ± 0.1	60.7 ± 0.4	29.7 ± 0.4	2.0 ± 0.1	
Calcigel granulate		7.3 ± 0.1	61.3 ± 0.1	29.5 ± 0.1	1.9 ± 0.1	
			[mg/g]			
Calcigel pillow		5.49 ± 0.01	8.77 ± 0.01	2.60 ± 0.05	0.56 ± 0.01	
Calcigel granulate		5.47 ± 0.11	9.17 ± 0.13	2.67 ± 0.03	0.56 ± 0.01	

Table 4.8 Conductivity and soluble anions and cations

Materials	Conductivity [mS/cm]	Anions		Cations			
		Cl ⁻	SO ₄ ²⁻	Na ⁺	Ca ²⁺	Mg ²⁺	K ⁺
				[mg/g]			
Calcigel pillow	0.15	0.86 ± 0.01	1.5 ± 0.2	0.63 ± 0.01	0.25 ± 0.05	0.14 ± 0.01	0.06 ± 0.01
Calcigel granulate	0.15	0.76 ± 0.08	1.5 ± 0.1	0.63 ± 0.01	0.20 ± 0.10	0.12 ± 0.06	0.06 ± 0.01

4.3.3.3 Water retention curve

Calcigel bentonite had a high water retention capacity due to its smectite content. The shape of the WRC reflected the existence of adsorption processes typical of clays, with water contents being relatively high even for high suction pressures. Saturation > 100% can be explained by the fact that these degrees of saturation were computed with a water density value of 1 g/cm³, which is not accurate for smectites, since the density of adsorbed water can be higher than this value (Villar, 2002; Marcial, 2003; Lloret and Villar, 2007). The WRCs in terms of degree of saturation were fitted to the van Genuchten expression (1980) (eq. 4.12, Fig. 4.20) with parameters given in Tab. 4.9.

Table 4.9 Suction pressure measurements in compacted Calcigel and fitting parameters

Compaction pressure [MPa]	ρ_d [g/cm ³]	w [%]	S _r [%]	s [MPa]	Parameter determined prior to installation	
22	1.50	5.4	18	435	w (110 °C) [%]	11.4
20	1.51	7.2	25	277	w (200 °C) [%]	12.5
18	1.52	12.6	44	111	ρ_s [g/cm ³]	2.70
14	1.53	16.4	57	49		
7	1.50	20.8	70	23	Fitting parameters	
7	1.51	23.7	81	15	P [MPa]	22.4
7	1.52	25.8	90	13	λ	0.359
6	1.51	27.9	95	11		
6	1.49	30.0	100	10		
28	1.44 ^a	35.0	107	2.20		

^a this value was not used to compute the average dry density

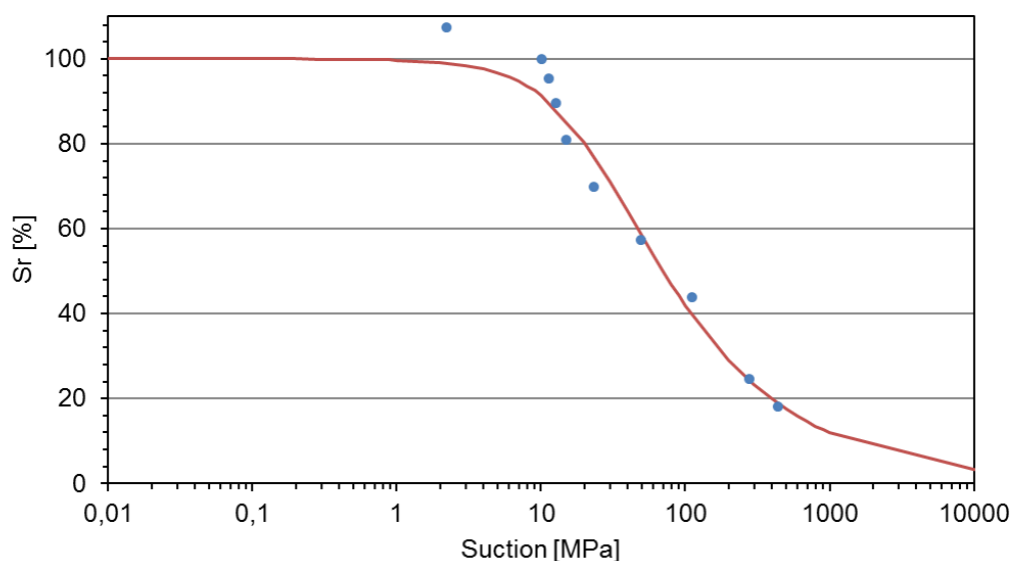


Figure 4.20 Fitting of the water retention curve of Calcigel to the van Genuchten (solid lines)

4.3.4 Secursol UHP

The Westerwald bentonites are of Miocene age and consist of highly altered tuffs of late Oligocene age. These altered tuffs overlie kaolinitic-illitic clays for ceramic application (Fig. 4.21). The smectite content of the altered tuffs exhibits grades of up to 90%. The altered tuffs are mined at three open pits of the SSG (Arborn, Ruppach, Salz). Secursol UHP (former G1580) is mined in Ruppach-Goldhausen (Fig 4.22).



Figure 4.21 Open pit Ruppach-Goldhausen, North Lower Saxony, from top to bottom: basalts (gray); altered tuffs (brown, Secursol UHP); illitic-kaolinitic clays



Figure 4.22 30.000 t of mined Secursol UHP, stored in the North of Lower Saxony pit

4.3.4.1 Phase content

Table 4.10 Phase content and specific density* of Secursol UHP

	[wt.%] 2W	[wt.%] anhydrous	ρ_s [g/cm ³]
Smectite (di-/trioctahedral)	83	80	2.75
Quartz	7	8	2.66
Kaolinite	4	5	2.6
Plagioclase	2	2	2.61
Anatase	3	4	3.78
Apatite	1	1	3.16
Total	100	100	2.77

*) ρ_s calculated based on crystal structure

Table 4.11 Specific density (measured) and water content after storage under ambient laboratory conditions

Drying temperature	Number of measurements	w	w_m	ρ_s
[°C]		[%]	[%]	[g/cm ³]
60	5	7.9 ± 0.2	7.3	2.56 ± 0.01
105	6	12.0 ± 0.2	10.7	2.66 ± 0.01
200	3	15.1 ± 0.1	13.1	2.77 ± 0.01

4.3.4.2 CEC, exchangeable cations and soluble ions

Table 4.12 CEC and exchangeable cations

	CEC	Na ⁺	Ca ²⁺	Mg ²⁺	K ⁺	Sum
	[cmol(+)/ kg]					
Secursol UHP pillow	90 ± 1.3	1.45 ± 0.12	100.28 ± 2.60	31.99 ± 0.99	2.91 ± 0.11	136.64 ± 3.81
Secursol UHP granulate	88 ± 1.6	1.74 ± 0.08	95.14 ± 2.66	30.71 ± 0.74	2.93 ± 0.06	130.52 ± 3.54
	[%]					
Secursol UHP pillow		1.06 ± 0.08	73.39 ± 1.90	23.41 ± 0.72	2.13 ± 0.08	
Secursol UHP granulate		1.34 ± 0.06	72.89 ± 2.04	23.53 ± 0.57	2.24 ± 0.05	
	[mg/g]					
Secursol UHP pillow		0.28 ± 0.02	17.00 ± 0.45	3.29 ± 0.10	0.96 ± 0.03	
Secursol UHP granulate		0.34 ± 0.01	16.01 ± 0.45	3.13 ± 0.08	0.96 ± 0.02	

Table 4.13 Conductivity and soluble cations

Materials	Conductivity	Cations			
		Na ⁺	Ca ²⁺	Mg ²⁺	K ⁺
	[mS/cm]	[cmol(+)/kg]			
Secursol UHP pillow	18.2	0.4 ± 0.0	1.6 ± 0.1	1.5 ± 0.0	0.1 ± 0.0
Secursol UHP granulate	19.9	0.5 ± 0.0	1.3 ± 0.0	1.2 ± 0.1	0.1 ± 0.0
		[mg/g]			
Secursol UHP pillow		0.07	0.28	0.15	0.04
Secursol UHP granulate		0.09	0.21	0.13	0.04

4.4 Materials for equipotential layers

ES materials are characterized by a hydraulic conductivity that exceeds that of DS materials by several orders of magnitude. Either silty loams or mixtures of mineral materials (Schuhmann *et al.*, 2009) can reach such a high hydraulic conductivity. While data from benchmark experiments for ES materials with a rising height of > 300 cm exist (Schuhmann *et al.*, 2009), optimization is needed for construction practice. It was attempted to reduce the number of components of mineral mixtures for ES and to identify new raw materials for ES.

Particle size distribution and mineralogy determine the hydraulic properties of ES materials. Finely grained non-swelling rocks, ground carbonates, and fillers from rock processing (like basalts, gabbros, granite and others) were studied (Tab. 4.14) and assessed in comparison to benchmark material M1000 and its components. Fillers from rock processing were rejected after preliminary tests.

Table 4.14 Materials for potential use in ES

Material	Provider	Description	CEC [cmol(+)/kg]	ρ_s [g/cm ³]*
N45	Nivelsteiner Sandwerke	Fine sand; quartz (99%), traces of muscovite, kaolinite, orthoclase, rutil ¹		2.65
FS700	Amberger Kaolinwerke Eduard Kick GmbH & Co. KG	Silt; quartz (14%), feldspar (55%), kaolinite (28%), dioct. illite/mica (3%) [#]		
Arginotec GI	Arginotec GmbH & Co. KG	Clay; dioct. illite/mica (78%), kaolinite (10%), calcite (12%) [#]		
BMK	<i>bmk</i> Steinbruchbetriebe GmbH & Co. KG	Shell limestone, filter residue; calcite (50%), dolomite (29%), dioct. illite/mica (10%), Chlorite (6%)		
M1000	-	N45 (33%), BMK (17%), FS700 (42%), Arginotec (8%)		
Dolomite	SSG	dolomite (99%)		
Saprolite coarse	SSG	Quartz, dioct. illite/mica, chlorite, kaolinite,	4	
Saprolite fine	SSG	Quartz, dioct. illite/mica, kaolinite	1	
Loam	SSG	Quartz (60 %), smectite (13 %), dioct. illite/mica (13 %), kaolinite (10 %), other (< 4 %)		
E501	-	N45 (33.3%), saprolite coarse (25%), dolomite (41.7%)		
E502	-	N45 (55%), FS700 (30%), saprolite fine (15%)		
E503	-	N45 (55%), FS700 (15%), saprolite fine (30%)		

*) from data sheet or measured #) Schuhmann *et al.*, 2009

4.4.1 Water retention curves

The water content obtained for the two heating temperatures was very low and nearly the same (Tab. 4.15) for all equipotential materials. Only Arginotec GI had a much higher equilibrium water content under ambient conditions than the other materials. Specific density (Tab. 4.15) was measured with a pycnometer (chapter 4.1.9).

Table 4.15 Water content and specific density

	BMK	M1000	FS700	N45	AGT
Water content 110 °C / 48 h [%]	0.4	1.1	0.1	0.1	13.4
Water content 200 °C / 24 h [%]	0.4	1.1	0.1	0.1	13.8
Specific density [g/cm ³]	2.76	2.65	2.58	2.66	2.74

Samples were installed with a dry density of 1.54-1.58 g/cm³ (Tab. 4.16 to 4.17). Compaction pressure to obtain the target dry density at lowest water content varied between 3 and 61 MPa (Tab. 4.16 to 4.17). The different water contents were obtained by adding Pearson water to the materials received or by slightly drying them (chapter 4.1.14). Two different compaction systems were used, resulting in the different precision of the compaction pressure value. Accuracy of the measurement also varied depending on the sensor used to measure suction pressure, a psychrometer or capacitive sensor. The degree of saturation was computed from the actual water content, dry density and the specific density of the solids (Tab. 4.15). The highest water content of Arginotec GI was obtained for a dry density considerably lower than the nominal value (Tab. 4.17), because it was very close to full saturation and some material was lost during compaction.

Table 4.16 Suction pressure measurements in compacted N45 and BMK

Compaction pressure [MPa]	N45				BMK				
	ρ_d	w	S _r	s	Compaction pressure	ρ_d	w	S _r	s
	[g/cm ³]	[%]	[%]	[MPa]	[MPa]	[g/cm ³]	[%]	[%]	[MPa]
7	1.54	0.1	0	122	3.3	1.55	0.4	1	118
39	1.56	1.6	6	7	3.3	1.56	2.2	8	7
34	1.56	2.7	10	0.42	2.2	1.55	4.2	15	1.55
33	1.57	4.2	16	0.38	2.2	1.56	7.2	26	1.19
34	1.58	6.7	26	0.36	2.2	1.58	9.0	33	0.97
31	1.58	8.0	31	0.35	1.5	1.56	11.0	40	0.90
23	1.57	10.4	40	0.32	1.4	1.57	13.0	48	0.86
29	1.56	14.6	55	0.28	0.7	1.55	16.0	57	0.77
28	1.56	20.5	78	0.27	0.1	1.64	21.6	88	0.76

Table 4.17 Suction pressure measurements in compacted FS700 and Arginotec GI

Compaction pressure	FS700				Compaction pressure	Arginotec GI			
	ρ_d	w	S_r	s		ρ_d	w	S_r	s
	[MPa]	[g/cm ³]	[%]	[MPa]		[MPa]	[g/cm ³]	[%]	[MPa]
61	1.56	0.1	1	171	27	1.55	3.3	12	210
61	1.57	1.8	7	6	20	1.51	6.8	24	68
56	1.59	4.1	17	1.18	20	1.56	13.7	50	31
48	1.59	6.7	28	0.95	20	1.57	17.9	66	19
48	1.58	8.6	35	0.94	15	1.50	20.6	74	14
52	1.59	10.4	43	0.82	11	1.51	24.1	89	7
50	1.59	11.4	48	0.77	7	1.52	26.3	98	2.37
50	1.57	13.4	54	0.74	7	1.56	27.9	101	1.13
38	1.57	20.1	80	0.47	4	1.55	28.8	103	0.78
					10	1.50	31.8	106	0.62

Table 4.18 Suction pressure measurements in compacted sample M1000

Compaction pressure	ρ_d	w	S_r	s
[MPa]	[g/cm ³]	[%]	[%]	[MPa]
5.5	1.54	1.1	4	38
6.3	1.56	2.7	10	8
5.1	1.56	4.0	15	0.80
5.1	1.55	7.3	28	0.44
5.5	1.56	9.9	38	0.33
5.1	1.57	10.7	41	0.27
4.8	1.57	11.8	46	0.27
3.5	1.56	20.7	78	0.28

Arginotec GI had a water retention capacity significantly higher than the remaining materials, because of its finely grained clay minerals content (Tab. 4.14). The shape of the WRC for Arginotec also differed from those of the other ES materials (Fig. 4.23) and reflected the existence of adsorption processes typical of clays, with water contents being relatively high even for high suction pressures, whereas the others corresponded to materials retaining water by capillarity and having larger pore sizes. The curves for all the ES materials were similar for suction pressures above 5 MPa, with very low water contents that reached 0% for suction pressures between 100 and 200 MPa. Below a certain suction pressure (between 1.5 and 0.4 MPa, depending on the material), the changes in suction pressure with water content were very small, particularly for the fine sand N45, which displayed the typical water retention curve

of a material with a uniform grain size in the fine sand range (0.2-0.6 mm). Most of the ES materials reached degrees of saturation higher than 90%. A saturation > 100% was observed for Arginotec GI. This can be explained by the fact that these degrees of saturation were computed using a water density value of 1 g/cm³, which is not accurate for some clays, since the density of adsorbed water can be higher than this value (Villar, 2002; Marcial, 2003; Lloret and Villar, 2007).

The water retention curves in terms of degree of saturation were fitted to the van Genuchten expression (1980) (eq. 4.12). For materials BMK and FS700 the experimental data fitted slightly better to the Fredlund and Xing (1994) expression (eq. 4.13) resulting in fitting parameters (Fig. 4.24, Tab. 4.19).

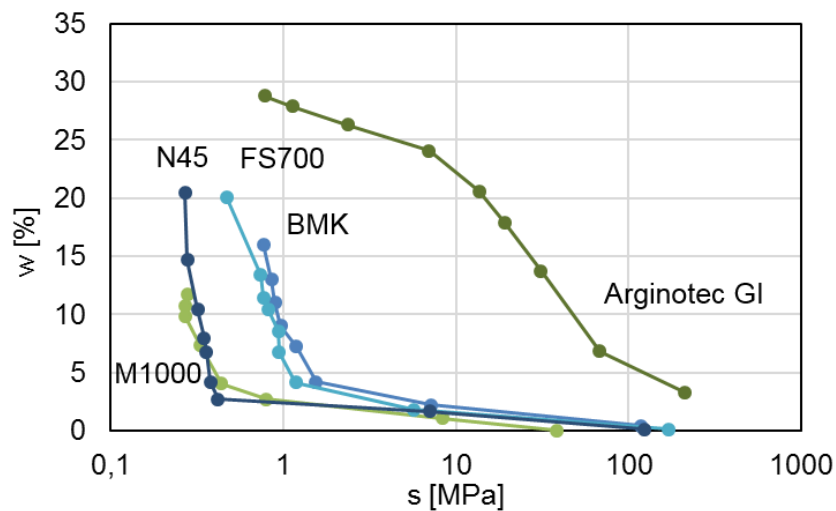


Figure 4.23 Water retention curves as function of suction pressure

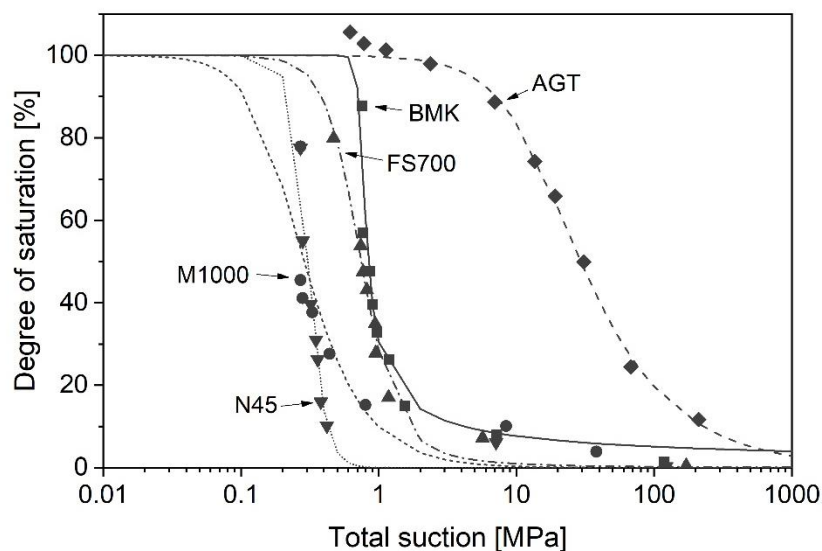


Figure 4.24 Water retention curves relating to the degree of saturation, fitting to the van Genuchten (solid lines) and the Fredlund and Xing (dotted lines) expressions

Table 4.19 Fitting parameters of the water retention curves

Reference	N45	BMK	FS700	Arginotec GI	M1000
P [MPa]	0.3	0.8	0.7	14.8	0.2
λ	0.861	0.805	0.725	0.457	0.594
a [MPa]		0.73	0.69		
n		20.28	3.35		
m		0.65	2.10		

4.4.2 Rising height

Samples were installed in the air dry state with a water content (105 °C) < 1% except for Arginotec GI with 6.6%. Fine sand N45 reached a characteristic height of about 60 to 70 cm within 5 d increasing only slightly afterwards (Fig. 4.25). Both BMK and FS700 show good rising properties and reached 200 cm within 60 and 30 d, respectively, (Fig. 4.25) and fluids are still rising in the columns.

Mixtures E501 to E503 (Tab. 4.14) showed horizontal cracks (Fig. 4.26) due to settlings during hydration which resulted in a capillary barrier. Cracks had to be closed by recompaction to sustain capillary rising of the water to the final height. Both E501 and E502 reached 150 cm within 100 d (Fig. 4.26) but were much slower than the benchmark of M1000. Test of E503 was terminated because of even slower rising.

Table 4.20 Installation parameters

Material	E501	E502	E503	FS700	BMK	N45	Arginotec GI
Bulk density [g/cm ³]	1.742 ± 0.039	1.823 ± 0.022	1.656 ± 0.005	1.340 ± 0.004	1.593 ± 0.021	1.555 ± 0.007	1.324 ± 0.017

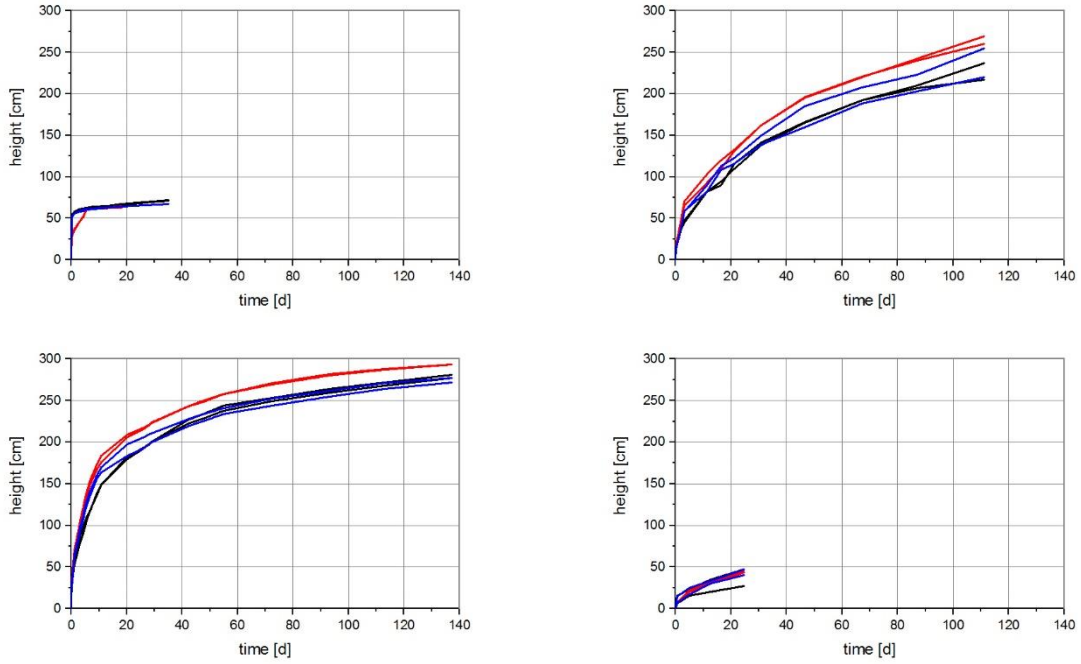


Figure 4.25 Variogram of rising heights upper left N45, upper right BMK, lower left FS700, lower right Arginotec GI (red: Pearson water, blue: 4 M NaCl brine, black: deionized water)

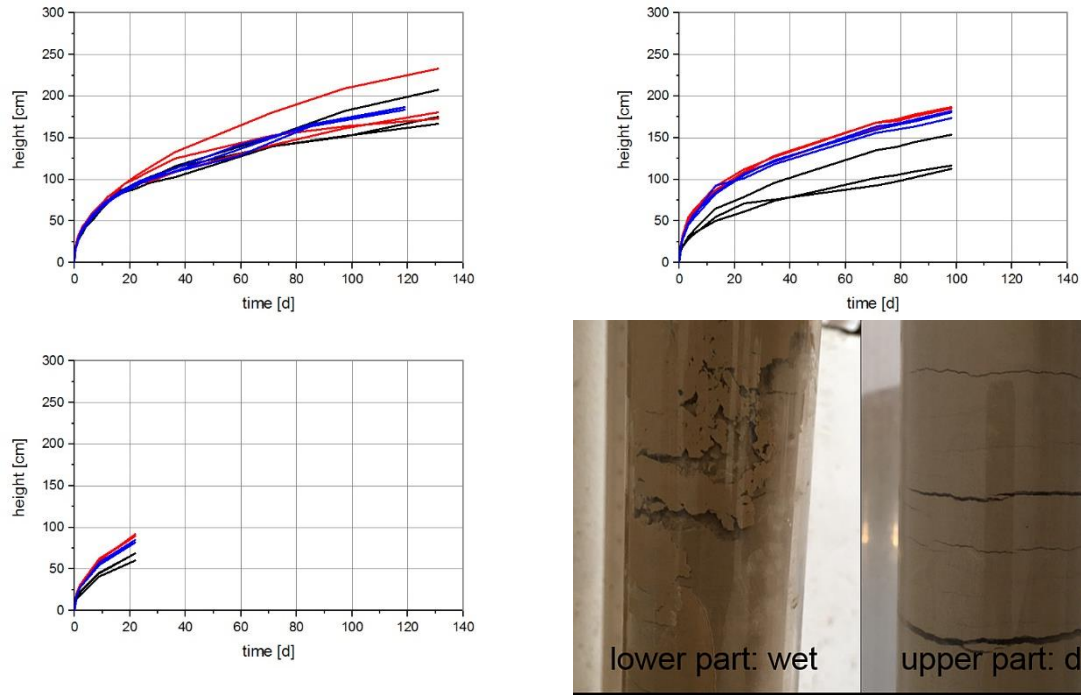


Figure 4.26 Variogram of rising heights upper left E501, upper right E502, lower left E503, lower right settling E501 (red: Pearson water, blue: 4 M NaCl brine, black: deionised water)

4.4.3 RRSB net

The first application of the RRSB net was to characterize the particle size distribution of processed coal. Later it was transferred to general raw material processing steps like grinding and sieving. The general advantage is the possibility to compare different particle size distributions by a single number, the $\tan \alpha$. In the ceramic industry, the RRSB net is used to determine the filtration behavior of liquefied ceramic masses for the pressure casting system. The gradient of the entire particle spectrum was equated with the corresponding possible packing density, where $n = 0$ describes the densest and $n = \infty$ the loosest structure. A dependence of the uniformity parameter n ($\tan \alpha$) on the filtration behavior was established. This resulted in good filtration behavior for loose particle structures (high $\tan \alpha$) and poor filtration behavior for dense particle structures (low $\tan \alpha$). It may be expected that the above mentioned filtration behavior may be transferred to the capillarity for the ES materials. In particular, the $\tan \alpha$ of certain materials required for the project was evaluated.

Column tests (chapter 4.4.2) to determine the rising height in ES materials are very time consuming. Duration is up to several months. For this reason, a theoretical approach was to be developed for a faster and sound assessment of new raw materials or mineral mixtures for ES. The corresponding tool was to describe the packaging and capillarity of ES materials before starting the long lasting column test. One candidate was the so-called "RRSB net" (named after Rosin, Remmler, Sperling, Bennett) that is also described in DIN EN 66145 (Representation of particle size distribution). To use this tool, granulometric measurements have to be carried out. In the RRSB net the PSD (volume distribution) is plotted in a network with double logarithmically divided ordinates and a single logarithmically divided abscissa (Fig. 4.27). When the PSD follows the RRSB function (eq. 4.17 and 4.18), a straight line results.

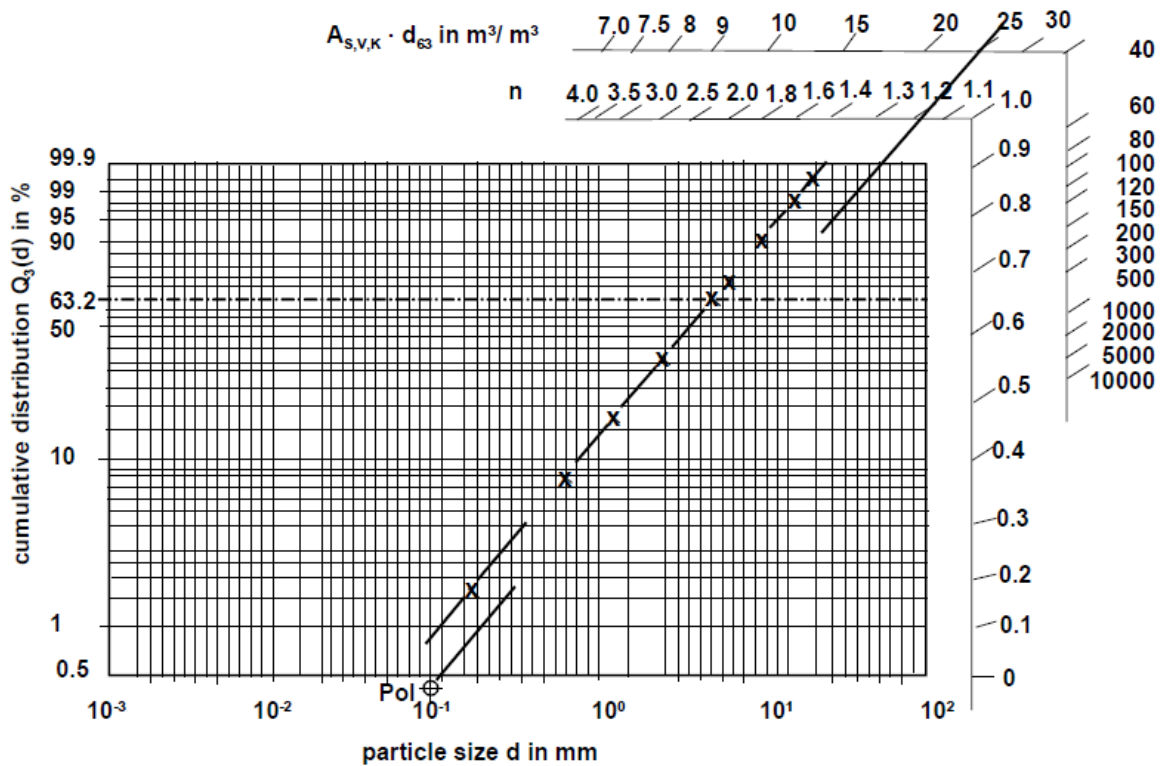


Figure 4.27 RRSB net (Tomas, 2014)

$$D(d) = 1 - R(d) = 1 - \exp\left[-\left(\frac{d}{d'}\right)^n\right] \quad (4.17)$$

D	mm	passage
d	mm	particle equivalent diameter
R	mm	residue
d'	mm	fineness parameter 1
d	mm	assigned equivalent diameter
n		slope of the line (fineness parameter 2)

Converting and logarithmizing eq. 4.17 twice results in

$$\begin{aligned} \lg \lg \frac{1}{1 - D(d)} &= n * \lg d - n * \lg d' + \lg \lg e \\ &= n * \lg d + c \end{aligned} \quad (4.18)$$

The function can then be described alone by the fineness parameters, so by the slope n and the abscissa d' of a selected point (eq. 4.18). If the line can be moved parallel to itself in the pole, the gradient can be read on the inner scale of the mesh.

To determine the relevant PSD wet and dry dispersion (chapter 4.1.11) of ES materials were tested. Whereas the PSDs of fine sand (N45) after wet and dry dispersion are quite similar, the results for clay (Fig. 4.28) differ strongly. ES materials also interact with fluids during application. For this reason, the wet dispersion method was finally selected for subsequent measurements.

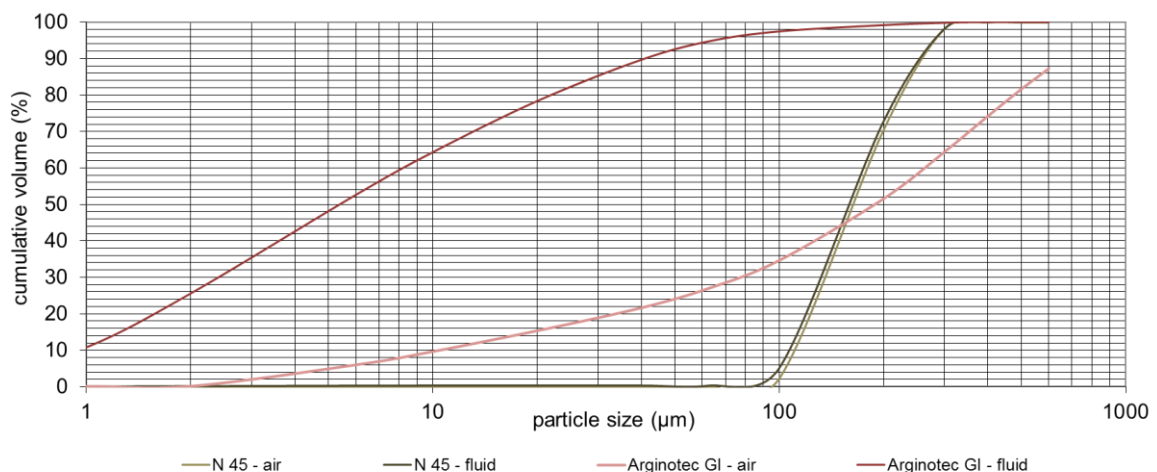


Figure 4.28 Particle size distribution of clay (Arginotec GI) and fine sand (N45) after dispersion in air and dispersion liquid

PSD of the clays are similar (Fig. 4.29). However, the coarse saprolite showed an unexpected effect. During dispersion in water the coarse aggregates dispersed to the primary PSD. This result corresponds to the post-compaction observed during the column test, when the “coarse

clay” disintegrated under the influence of water with the consequence of dense packaging and settling in the column that led to an interruption of capillarity.

The PSD of dolomite differed from the PSD of BMK and was closer to the PSD of FS700 (Fig. 4.29). The PSD of FS700 was characterized by a certain lack of finely grained particles.

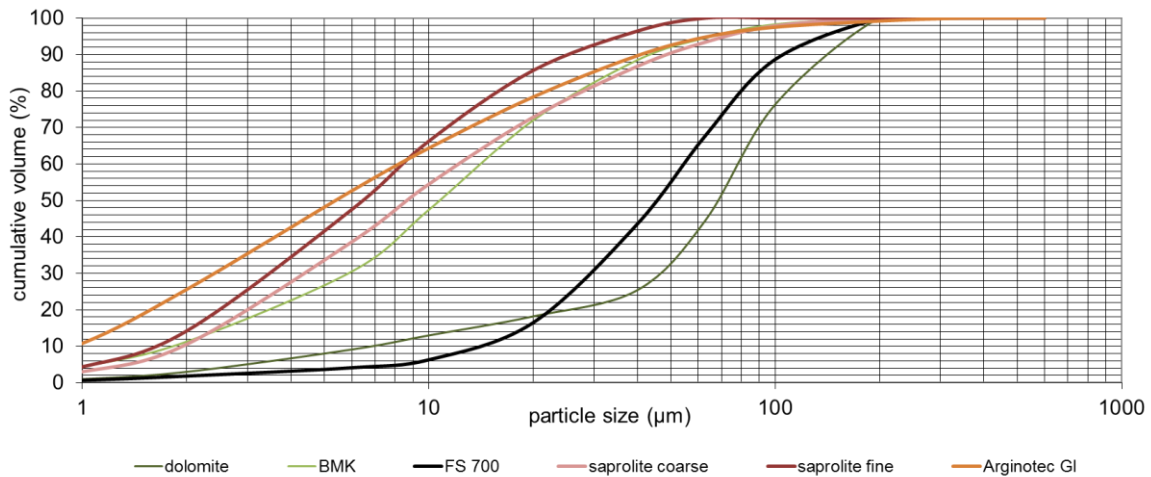


Figure 4.29 Particle size distribution after dispersion in dispersion liquid

Analogous to the comparable particle size distribution (PSD) the fine clays (with exception of the saprolite fine) show a low $\tan \alpha$ (Tab. 4.21). Feldspar FS 700 and dolomite, significantly coarser than the clays and comparable in their PSD, show comparable $\tan \alpha$ as well. For the coarsest material, fine sand N45, the highest $\tan \alpha$ of 4.0 was calculated.

These results, that are in accordance with the description of the filtration behavior of ceramic masses in the ceramic industry, could be a future tool for the pre-calculation of an ideal composition of a raw material mixture for the ES. In a first step, the M1000 mixture (Schuhmann *et al.*, 2009) and the corresponding $\tan \alpha$ will be chosen as benchmark for further investigations. Subsequent calculations of different mixing ratios of different raw materials will be carried out with the aim to identify mixtures with a $\tan \alpha$, that is comparable with the M 1000 benchmark mixture. This approach has then still to be verified by real column tests.

In addition, the water adsorption of raw materials, measured by the Enslin-Neff method (chapter 4.1.12), is also seen as an approach for predicting the rising height. It is well known, that smectites with their swelling capacity exhibit a very high water adsorption of more than 100%. In this case, the mineralogy dominates over the influence of grain size distribution. However, only non-swellable raw materials were used for the column tests. Therefore, the influence of the water adsorption should be limited exclusively to the grain size distribution and only influenced weakly by mineralogy. The Enslin-Neff values for dolomite and limestone MBK are the same (41 and 40 %), whereas the grain size distribution is significantly different (Fig. 4.29). Therefore, a mineralogical influence or a micro porosity is also assumed here, which is not yet known in detail.

Because of the protracted experiments for the rising height (Fig. 4.25 and 4.26), too few data are available so far to identify a significant correlation between $\tan \alpha$ and/or water adsorption after Enslin-Neff. Additionally, the compaction of the raw material during filling of the columns must be taken into account because of its influence on the final capillarity of the mixture. These data must be collected for more different raw materials during the next steps of investigations.

Table 4.21: Tan α of different ES materials from PSD determined by laser granulometry of suspensions and water uptake (Enslin-Neff)

Material	tan α	Water uptake [%]
dolomite	1.404	40.7
saprolite coarse	1.009	61.8
saprolite fine	1.232	56.5
FS 700	1.568	n.d.
BMK	1.013	40.1
N 45	4.000	n.d.
Arginotec GI	1.042	87.8

4.4.4 Saturated hydraulic conductivity

Based on the particle size distribution (Fig. 4.28) a saturated hydraulic conductivity was calculated for fine sand N45 according to Beyer (1964) as implemented in HydrogeoSieveXL v2.3 UK (Devlin, 2015) as a function of temperature (Tab. 4.22).



Table 4.22 Hydraulic conductivity of fine sand (N45)

Temperature [°C]	Saturated hydraulic conductivity [m/s]
10	$1 \cdot 10^{-4}$
20	$1.32 \cdot 10^{-4}$
25	$1.49 \cdot 10^{-4}$

4.5 Gravel

Basalt gravel 22/32 mm and 32/63 mm (Tab. 4.23) was used in HTV-5 and HTV-6 in the bottom pressure chamber.

Table 4.23 Chemical composition from XRF (normalized to 100%) of basalt gravel

Basalt gravel	SiO ₂	Al ₂ O ₃	Fe ₂ O ₃	MgO	CaO	K ₂ O	Na ₂ O	TiO ₂	P ₂ O ₅
22/32 mm									
	42.71	11.19	13.16	14.36	11.01	3.10	3.10	2.35	0.81
32/63 mm									
	49.71	13.76	11.30	8.06	8.53	1.81	3.61	1.81	2.41

The main phases of pyroxene, plagioclase, olivine and feldspathoid groups of both particle sizes are characteristic of basalt. The coarser basalt contained an amorphous phase. Small amounts of zeolites and other minerals were identified (Tab. 4.24).

Table 4.24 Phase content of basalt gravel

Phases	22/32 mm	32/63 mm
	[wt.%]	
Amorphous	-	15.6 ± 4.2
Pyroxene	43.1 ± 1.2	21.9 ± 1.3
Olivine	19.6 ± 0.8	9.5 ± 0.9
K-feldspar	1.7 ± 0.6	5.7 ± 1.2
Plagioclase	7.7 ± 0.9	27.8 ± 2.3
Feldspathoid	13.7 ± 0.8	3.1 ± 1.0
Zeolite	2.6 ± 0.6	5.1 ± 1.2
Apatite	0.6 ± 0.5	1.3 ± 0.5
Anatase	2.2 ± 0.5	-
Magnetite	-	3.9 ± 0.5
Mica	3.9 ± 0.9	1.7 ± 0.9
Smectite (Mg-rich)	4.3 ± 1.2	0.2 ± 0.1
Talc	-	2.8 ± 1.1
Tridymite	0.5 ± 0.2	1.4 ± 0.3

4.6 Swelling pressure test

4.6.1 Calcigel

Five swelling pressure tests were carried out with Calcigel SW-A samples and Pearson water as hydration fluid. Three swelling pressure tests with Calcigel and Pearson water were carried out in standard oedometers (STD, Fig. 4.3), in which saturation takes place by flooding at atmospheric pressure. The two others tests were performed in high-pressure oedometers in which saturation takes place by injecting water at a low pressure (EAP, Fig. 4.4). In the case of the standard oedometers, the differences between the initial and final dry densities of the samples (Tab. 4.25) were caused by the difficulty of keeping the volume of the samples constant while taking into account the equipment deformation on loading. In the case of the EAP oedometers, these differences were caused by the slight deformation allowed by the equipment. The final degree of saturation > 100% can be explained by the fact that calculations were made using a water density value of 1 g/cm³, which is not accurate for some clays (particularly smectites), since the density of adsorbed water can be higher than this value (Villar, 2002; Marcial, 2003; Lloret and Villar, 2007).

Table 4.25 Results of the swelling pressure tests of Calcigel with Pearson water

device	Installation			Final			t (days)	T	P _s
	ρ _d [g/cm ³]	w (200 °C) [%]	S _r [%]	ρ _d [g/cm ³]	w (200 °C) [%]	S _r [%]			
STD	1.28	10.1	25	1.31	45.1	115	26	23.1	0.5
STD	1.37	11.6	32	1.38	39.9	113	43	23.1	1.0
STD	1.57	13.4	50	1.56	31.8	117	55	22.7	4.8
EAP	1.32	12.0 [#]	31	1.32	44.9 [#]	115	98	22.6	0.3
EAP	1.51	13.3	46	1.50	34.8	117	88	22.6	1.9

[#]) 110 °C

The relation between swelling pressure and final dry density (Fig. 4.37, chapter 4.6.3) is exponential and although few data are available, the following tentative correlation between swelling pressure (P_s, in MPa) and dry density (ρ_d, in g/cm³) is proposed:

$$\ln P_s = 10.10 \rho_d - 14.23 \quad (4.19)$$

In the tests performed in the high-pressure oedometer, it was possible to record the vertical pressure evolution with increasing saturation of the samples (Fig. 4.31). The two curves display the characteristic pattern of expansive materials, whose axial pressure develops non-monotonically: they show an initial quick increase, followed by a decrease, and finally reaching of the equilibrium pressure (Imbert and Villar 2006). The magnitude of the intermediate decrease depends, among other factors, on the dry density. The decrease is gaining importance for higher dry densities. The equilibrium swelling pressure can be below or above the initial pressure peak, which also depends on the dry density.

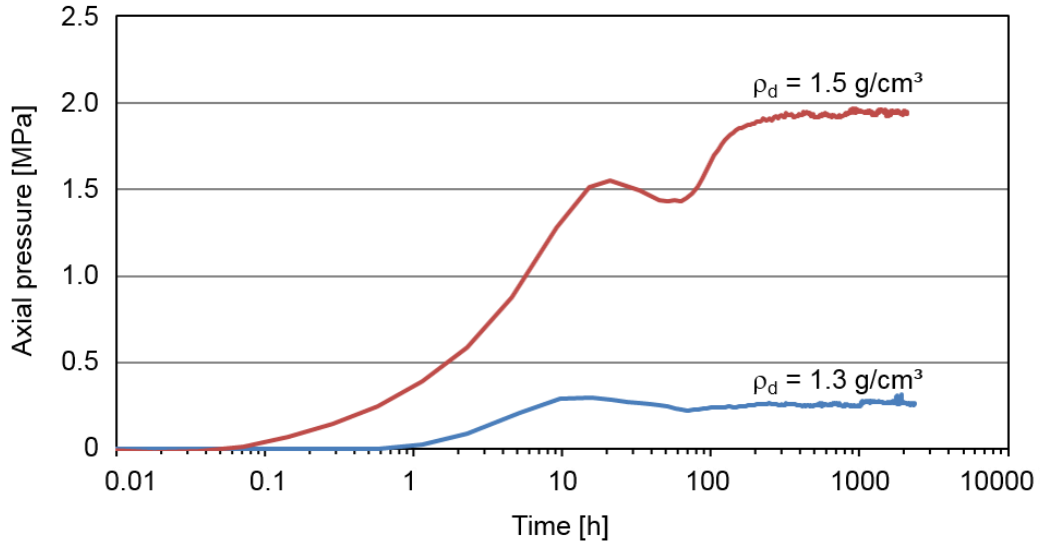


Figure 4.31 Evolution over time of axial pressure developed by Calcigel samples saturated with Pearson water in EAP oedometers

4.6.2 Secursol UHP

4.6.2.1 Porosity, initial saturation and gas permeability

The water content was determined at 60, 105 and 200 °C (Tab. 4.24) prior to installation of the swelling pressure tests. Drying at 105 (110) °C is common practice according to DIN EN 12880. For this reason, this water content and related material parameters were taken as reference values. Dry density, porosity and saturation (Fig. 4.32, Tab. 4.24) were calculated according to eq. 4.5, 4.9 and 4.10 and the specific density was measured (Tab. 4.11).

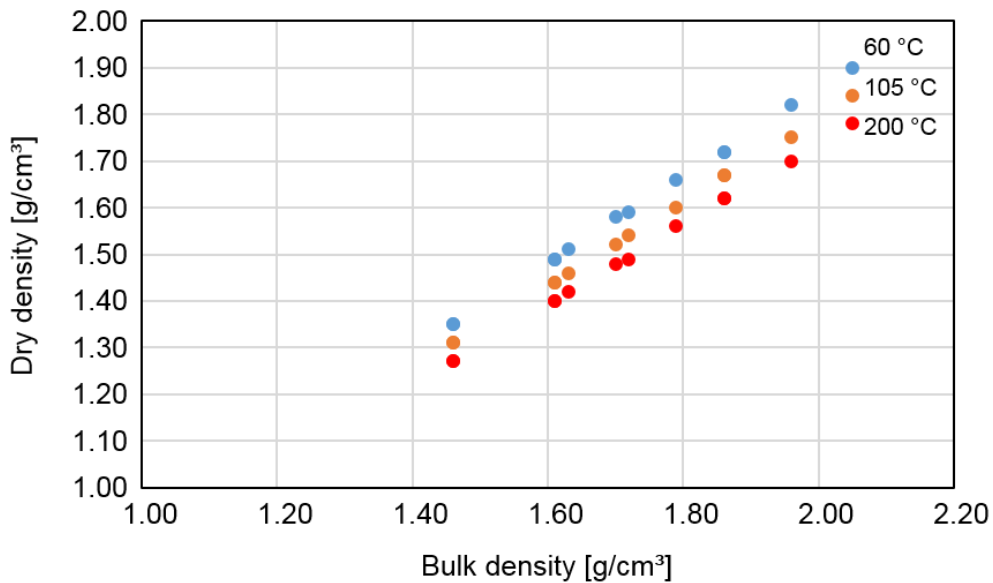


Figure 4.32 Installation dry density as function of bulk density during installation and water content determined at different temperatures (chapter 4.2.4) for Secursol UHP (HTV-6 gap filling material)

The pore space saturation with liquid allows for an assessment of the gas flow conditions in the initial state of the installed samples and an estimation of the fluid volume needed for saturation.

It is assumed, that by drying at 60 °C, only the water in the pore space will be removed. This is considered to be representative of the gas flow processes and two-phase flow processes in the samples (Herold *et al.*, 2016; Wilsnack, 2017). The pore space saturation with liquid significantly determines the capillary pressure and the effective permeability (eq. 6.2 and 6.3 in section 6.1.2). It has a decisive influence on the duration of the assessed and/or predicted flow processes in the unsaturated system.

Secursol UHP as installed with a water content (105 °C) of 11.7% has an effective gas permeability (Fig. 4.33) of $1.4 \cdot 10^{-15} \text{ m}^2$ to $3.7 \cdot 10^{-12} \text{ m}^2$ for the different installation densities.

At the relatively low liquid pore space saturation (60 °C) of 0.20 to 0.29 (Tab. 4.26) the effective gas permeability determined for the initial state of the samples is considered to be the absolute permeability. According to the impact of the capillary pressure depending on the pore size distribution, it can be assumed that the flow determining macropores are largely unaffected by the liquid saturation.

Table 4.26 Porosity and saturation as a function of bulk density during installation and water content determined at different temperatures for Secursol UHP (HTV-6 gap filling material)

Bulk density [g/cm ³]	Water content			Porosity			Saturation		
	60 °C	105 °C	200 °C	60 °C	105 °C	200 °C	60 °C	105 °C	200 °C
1.46		0.117		0.47	0.51	0.54	0.22	0.31	0.35
1.46		0.117		0.47	0.51	0.54	0.22	0.31	0.35
1.61		0.117		0.41	0.46	0.50	0.28	0.38	0.43
1.61		0.117		0.41	0.46	0.50	0.28	0.38	0.43
1.63		0.120		0.40	0.45	0.49	0.29	0.39	0.44
1.70	0.079	0.117	0.151	0.38	0.43	0.47	0.32	0.43	0.48
1.72		0.120		0.37	0.42	0.46	0.33	0.44	0.49
1.79		0.119		0.35	0.40	0.44	0.37	0.48	0.54
1.86		0.117		0.32	0.37	0.42	0.41	0.53	0.59
1.86		0.114		0.32	0.37	0.42	0.41	0.53	0.59
1.96		0.117		0.28	0.34	0.39	0.51	0.63	0.67
2.05		0.117		0.25	0.31	0.36	0.58	0.71	0.75

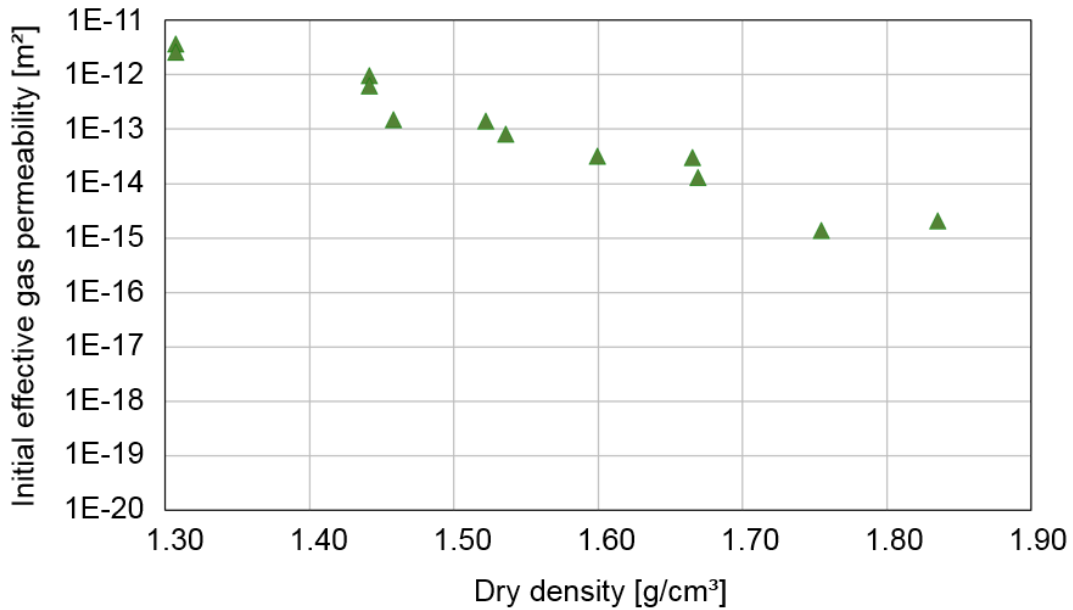


Figure 4.33: Initial gas permeability in function of dry density during installation and water content determined at 105 °C for Secursol UHP (HTV-6 gap filling material)

4.6.2.2 Swelling pressure and liquid permeability

Depending on the water content (105 °C) of 11.7% and dry density during installation, a swelling pressure of 1.47-17.52 MPa for tap water (Freiberg/Saxony, Tab. 4.3) and 1.92-11.02 MPa for Pearson water was determined (Fig. 4.34 and 4.35). The highest swelling pressures of 11.45 MPa and 17.52 MPa were determined for the samples with dry densities of 1.75 g/cm³ and 1.84 g/cm³ in contact with tap water. The swelling pressure curves (Fig. 4.34 and 4.35) show that the maximum pressure was not reached. To prevent damages on the pressure cells the experiments were terminated.

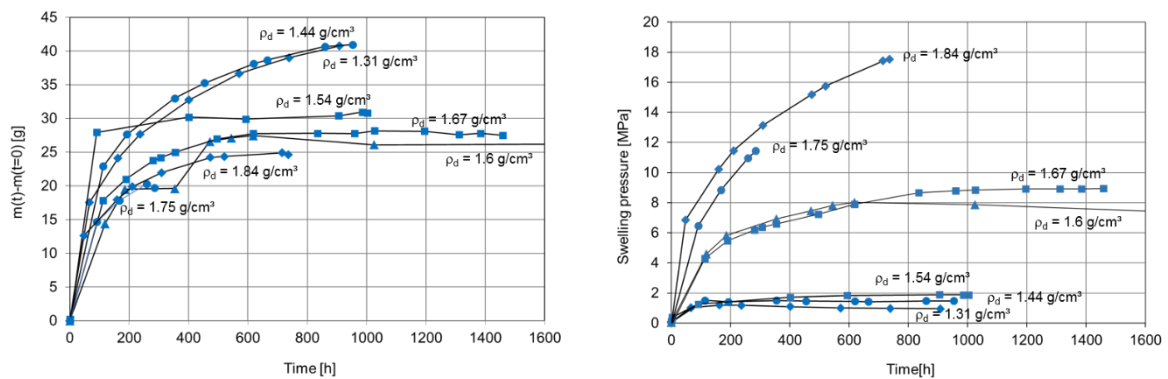


Figure 4.34 Mass change and swelling pressure development of Secursol UHP installed with a water content (105 °C) of 11.7% and saturated with tap water (Freiberg/Saxony, Tab. 4.3)

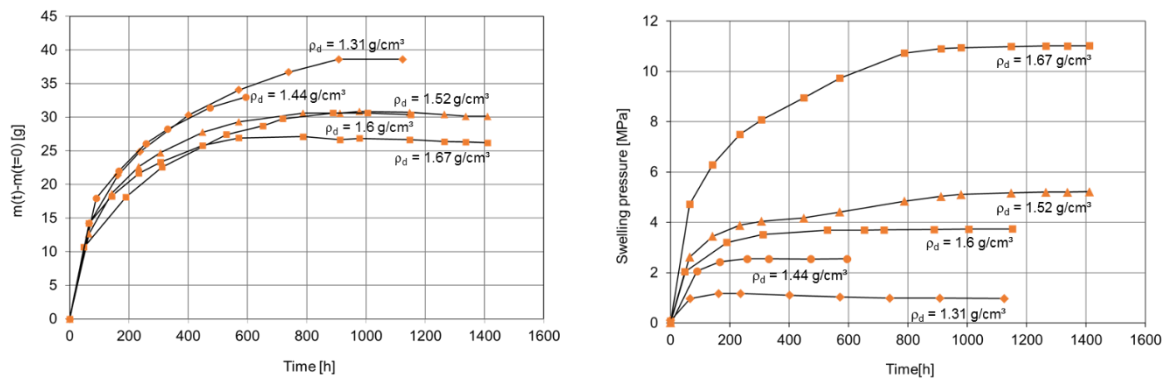


Figure 4.35 Mass change and swelling pressure development of Secursol UHP installed with a water content (105 °C) of 11.7% and saturated with Pearson water (Tab. 4.3)

The swelling pressures for samples with dry densities of 1.46 g/cm³ and 1.54 g/cm³ in contact with tap water (Freiberg/Saxony) are too low when compared to the obvious trend of swelling pressure depending on the installation dry density (Fig. 4.34 and 4.35). This behavior cannot be explained by the experimental data and the course of the experiment. It is assumed that the volume determination during sample installation is subject to an uncertainty. In addition, it cannot be ruled out that installation of the bentonite bodies (installation in 3-4 layers using a hydraulic pressing device) influences the swelling behavior.

For all samples almost a mass constancy was reached at the end of the experiment (Fig. 4.34 and 4.35). This indicates maximum liquid saturation in the pore space and the highest the swelling pressure is assumed. For the lower installation densities, a longer period of time seems to be required until mass constancy is achieved. This result is somewhat unexpected due to the higher initial permeability of the samples at lower installation dry density. It is assumed that this effect is due to lower capillary pressures, higher residual gas saturation and reduced effective liquid permeability in the initial phase. At the same time, the samples with the lower installation densities show the largest increase in mass. This is due to the high porosities and also has an influence on the time required to reach the maximum acceptable liquid mass. The sometimes unsteady curves of mass-uptake for individual samples are due to experimental boundary conditions. The experience gained from weighing the samples in the test procedure has shown that they are susceptible to errors and require highly precise weighing conditions. This is largely due to the fact that the swelling pressure cells have to be removed completely from the measurement setup for weighing. With the small changes in mass over the duration of the experiment, even small differences in the weighted test components (for example, by changing pipe connections and/or fittings) can lead to considerable difficulties in interpreting the mass change. In addition, it cannot be prevented that the liquid contained in connected pipe ends causes uncertainties of weighing and mass differences. These pipe ends cannot be assessed reliably with respect to their filled volume or mass. The mass increase until the end of the swelling pressure test characterizes the maximum liquid uptake of the sample over the duration of the test. The estimated saturation > 0.9 shows a high degree of saturation of the pore space for all samples. For the experiments in contact with Pearson water, there is a slight increase in maximum saturation with increasing installation dry density. This result is in good correlation with the experience of swelling pressure studies in Herold *et al.*, 2016. Observed differences in maximum saturations are very small and the maximum saturations in contact with tap water (Freiberg/Saxony) showed no trend. For some samples, a maximum saturation > 1 was determined. Possible reasons are the above mentioned uncertainties, resulting from the weighing of the pressure cells and the small mass differences due to the mass uptake. In addition, even small deviations in the

installation volumes of the sample body and in the bulk density can lead to the determination of too high saturations.

The liquid used for the swelling pressure tests was also used for permeability testing. For samples with installation bulk densities of $> 1.46 \text{ g/cm}^3$, a pressure difference of about 1500 kPa was applied for the permeability tests with liquid. For the two samples with an installation bulk density of 1.46 g/cm^3 , a liquid pressure of about 620 kPa was applied. As expected, permeability decreased with increasing installation dry density of the material (Fig 4.36). To illustrate the decrease in permeability of the material as a consequence of swelling induced redistribution of the pore size distribution in bentonite, the liquid permeability was normalized by dividing by the initial gas permeability. Normalization yielded a decrease in liquid permeability by a factor of $6.8 \cdot 10^{-6}$ to $3.3 \cdot 10^{-4}$ referred to the initial gas permeability but no trend depending on the installation dry density could be derived from this normalization.

The permeability of Secursol UHP for tap water varied between $3.3 \cdot 10^{-19}$ and $2.5 \cdot 10^{-17} \text{ m}^2$ ($N = 3$) and the permeability for Pearson water varied between $1.9 \cdot 10^{-19}$ and $2.5 \cdot 10^{-16} \text{ m}^2$ ($N = 5$) as a function of dry density at the installation water content ($105 \text{ }^\circ\text{C}$) of about 11.7%.

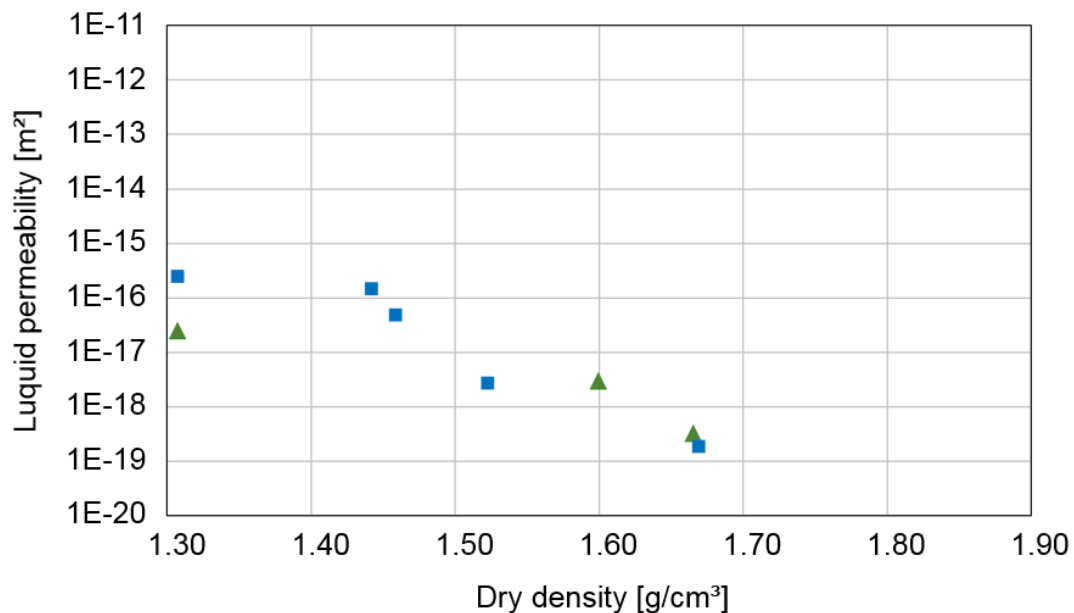


Figure 4.36 Liquid permeability depending on the installation dry density ($105 \text{ }^\circ\text{C}$) (green triangle: tap water (Freiberg/Saxony), blue squares: Pearson water)

4.6.3 Summary

For both bentonites a higher swelling pressure was observed under saturation with Pearson water (Fig. 4.37) and the steady increase of the swelling pressure with increasing dry density.

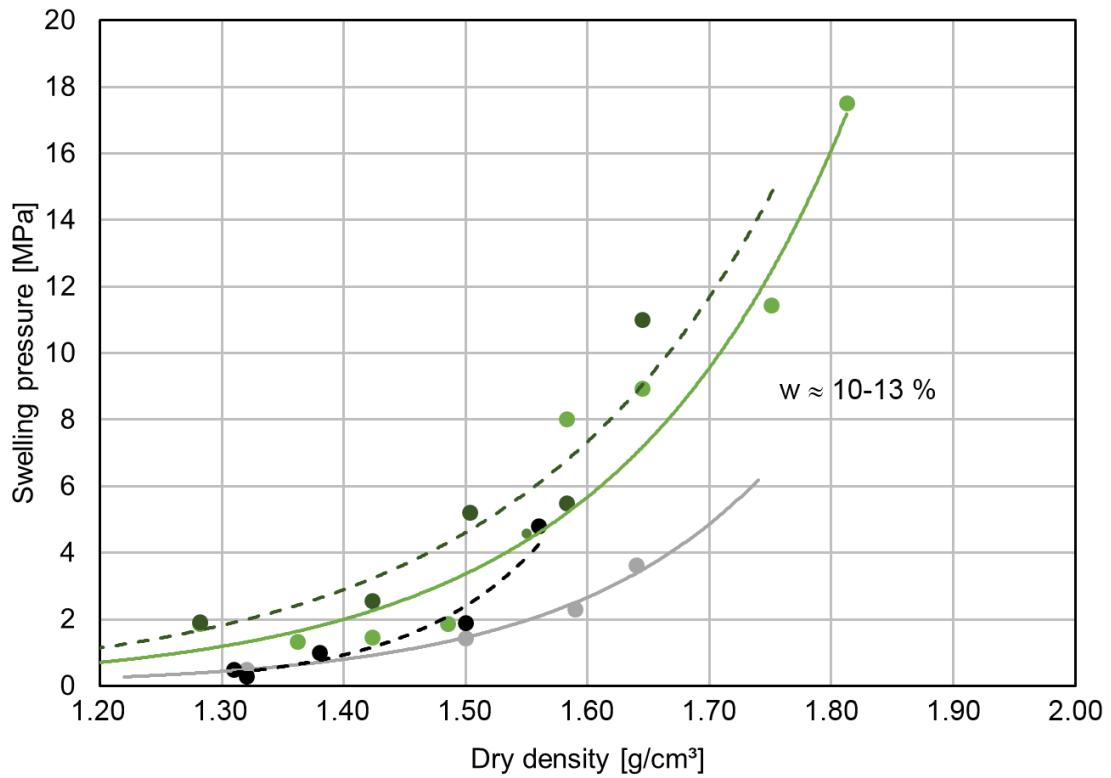


Figure 4.37 Swelling pressure of Calcigel (grey) (Kudla et al., 2020) and Secursol UHP (green); solid lines tap water, dashed line Pearson water

4.7 MiniSandwich experiments

Numerical evaluation of the HTV experiments (and of the currently planned large-scale in-situ tests) requires a sufficient understanding of the underlying material processes, e.g. swelling and the corresponding permeability decrease associated with geochemical changes, as well as a validated material parameter base. For this purpose, the MiniSandwich experiments were realized. They are small-scale tests (90 mm in diameter, about 800 cm³ in volume) measuring the swelling and fluid flow parameters on well-prepared sample assemblies. These lab experiments pursue two specific goals: (1) material selection and (2) quantitative investigation of coupled HMC processes of various bentonites under defined conditions for a vertical sequence of sealing (DS) and equipotential layers (ES).

4.7.1 Experimental procedure

Four modified oedometer cells were constructed as steel tubes with two movable pistons and filter plates for adjusting well-defined saturation conditions (Popp *et al.*, 2015). The cells were located in hydraulic load frames (Fig. 4.38 left). The axial strain during swelling of the specific bentonite material was measured by three gauges (displaced by 120°). During the test, the axial strain was regularly reset to zero by increasing the axial load measured by a load cell under quasi-constant volume conditions. During saturation, the fluid volume balance (in- and outflow ⇒ fluid storage capacity) was monitored and the stationary fluid permeability was calculated. The fluid was collected at the outflow and was analyzed to study ion transport and cation exchange processes.

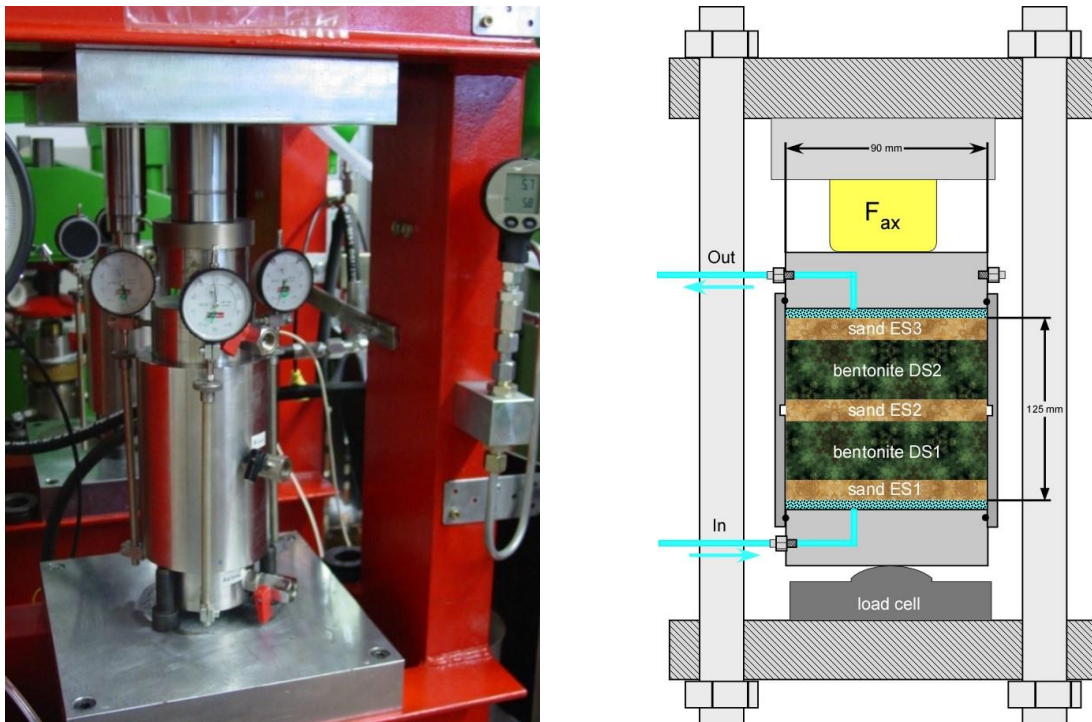


Figure 4.38 Experimental setup. Left: Hydraulic testing rig with oedometer cell; right: Schematic sketch of the oedometer cell

The MiniSandwich specimens consisted of three ES sandwiched by two DS of bentonite (Fig. 4.38). ES were made of fine sand. The bentonite in DS was either Calcigel or Secursol UHP. The total sample height varied between 125 and 131 mm (Tab. 4.26). Secursol UHP was tempered with N45 in two tests to modify EMDD.

MiniSandwich experiments were performed in series (3 to 5) of two experiments that were run in parallel. The bentonite was installed either in air-dry state or after conditioning by drying over concentrated H_2SO_4 for several months to study different initial hydration states of the smectite (1W/2W) (Tab. 4.26). After installation of the MiniSandwich (Fig. 4.39), the gas accessible porosity and the initial gas permeability were determined as starting conditions.

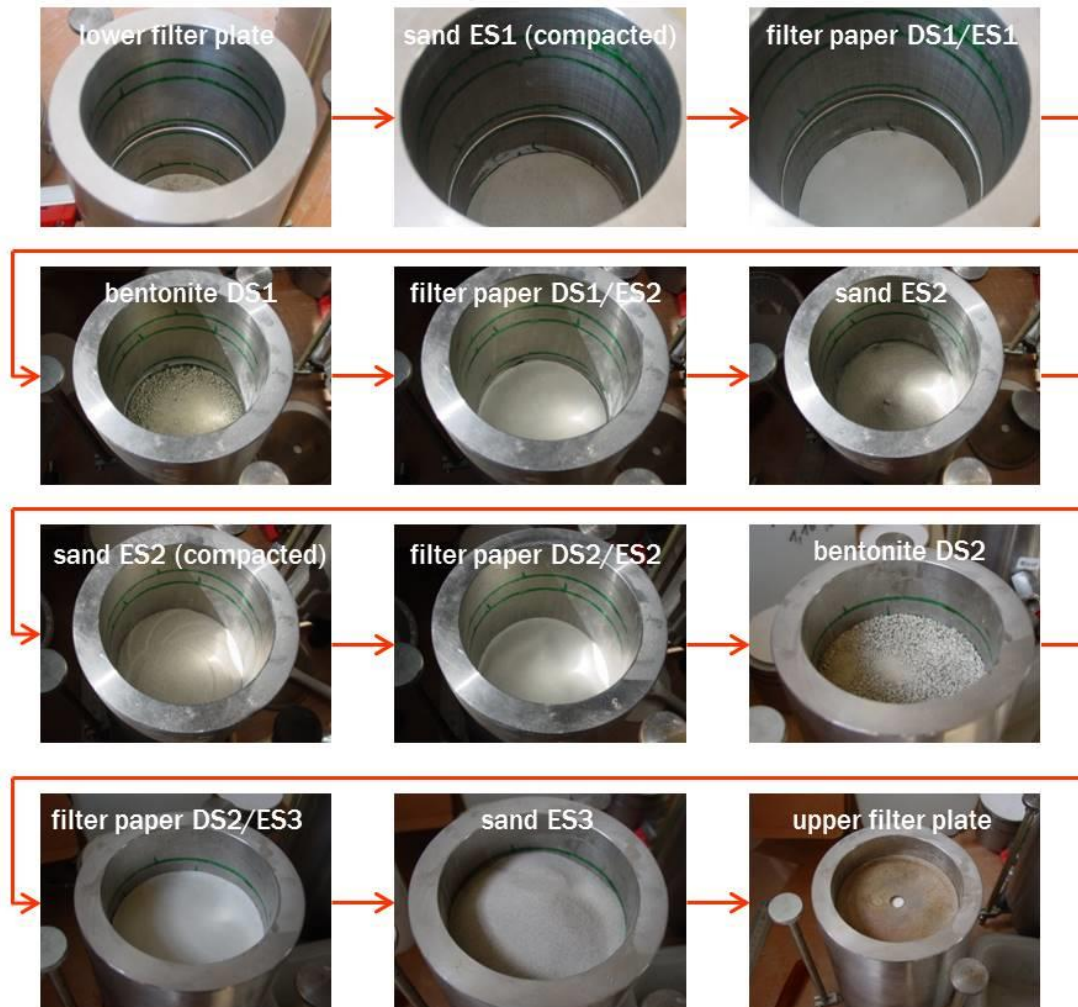


Figure 4.39 Installation of MiniSandwich

Saturation of the MiniSandwich was achieved using either NaCl brine (Oe5-Oe6) or Pearson water (Oe7-Oe10) (chapter 4.2) at an injection pressure of 0.1 to 0.3 MPa (Tab. 4.26). The development of the swelling pressure and the hydraulic permeability were measured. After saturation and development of steady state flow conditions, the outflow fluid was monitored for its ion content over a feasible period. Afterwards, each MiniSandwich was dismantled (Fig. 4.40) and analyzed for its water content and chemical/mineralogical changes.



Figure 4.40 Stepwise dismantling of the saturated MiniSandwich specimens: left: wet sand (ES1 Oe7); right: compact bentonite (DS2 Oe8)

Table 4.26 Setup of MiniSandwich Oe5 to Oe10

		Series 3		Series 4		Series 5	
		Oe5	Oe6	Oe7	Oe8	Oe9	Oe10
Fluid		NaCl-brine		Pearson water		Pearson water	
Injection pressure	[MPa]	0.1 for 607 d/ 0.3 afterwards		0.1		0.3	
DS							
Material		Calcigel		Calcigel		Tempered Secursol UHP	
w (200 °C)	[%]	3.7	10.2	3.7	10.2	3.1	12.9
Hydration state		1W	2W	1W	2W	1W	2W
ρ_b	[g/cm ³]	1.61	1.69/1.73	1.61/1.59	1.71/1.69	1.37/1.34	1.50/1.42
ρ_d	[g/cm ³]	1.55	1.53/1.57	1.55/1.53	1.55/1.53	1.33/1.30	1.33/1.26
ρ_{EMD}	[g/cm ³]	1.25	1.23/1.27	1.25/1.23	1.25/1.23	1.04/1.01	1.04/0.97
ES							
Material		N45		N45		N45	
w	[%]	< 0.1	< 0.1	< 0.1	< 0.1	< 0.1	< 0.1
Total length	[mm]	125	126	125.5	125	131	130
Calculated fluid uptake	[mL]	311	262	313	261	380	315

4.7.2 Results (HM)

Series 3 (Oe5 and Oe6, Calcigel, NaCl brine)

During hydration, a nearly constant swelling pressure was reached within a short time of less than 100 d, but at material specific pressure levels (Fig. 4.41, Tab. 4.27). Swelling pressure of the dried Calcigel was about 1.4 MPa and swelling pressure of the air-dry Calcigel was in the order of 0.7 MPa.

In the case of the air-dry Calcigel the breakthrough of the brine happened on day 180, with in- and outflow becoming nearly constant at a resulting permeability of $9 \cdot 10^{-18} \text{ m}^2$ (Fig. 4.41, Tab. 4.27). Note that a short phase of brine inflow stagnation occurred before the breakthrough, until a coeval fluid and gas outflow happened more or less simultaneously. This may indicate air buffer effects inside the partly saturated Calcigel matrix.

For the bentonite in 1W state the breakthrough was significantly delayed in earlier MiniSandwich experiments (Emmerich *et al.*, 2017), but stagnation of fluid inflow was observed, too.

On day 607, the injection fluid pressure was increased to 0.3 MPa to receive more fluid for analysis and to faster reach a (quasi) steady state of ions in the outflow fluid. The increased injection pressure resulted in a significant flow rate increase. Both tests are still running and will be continued.

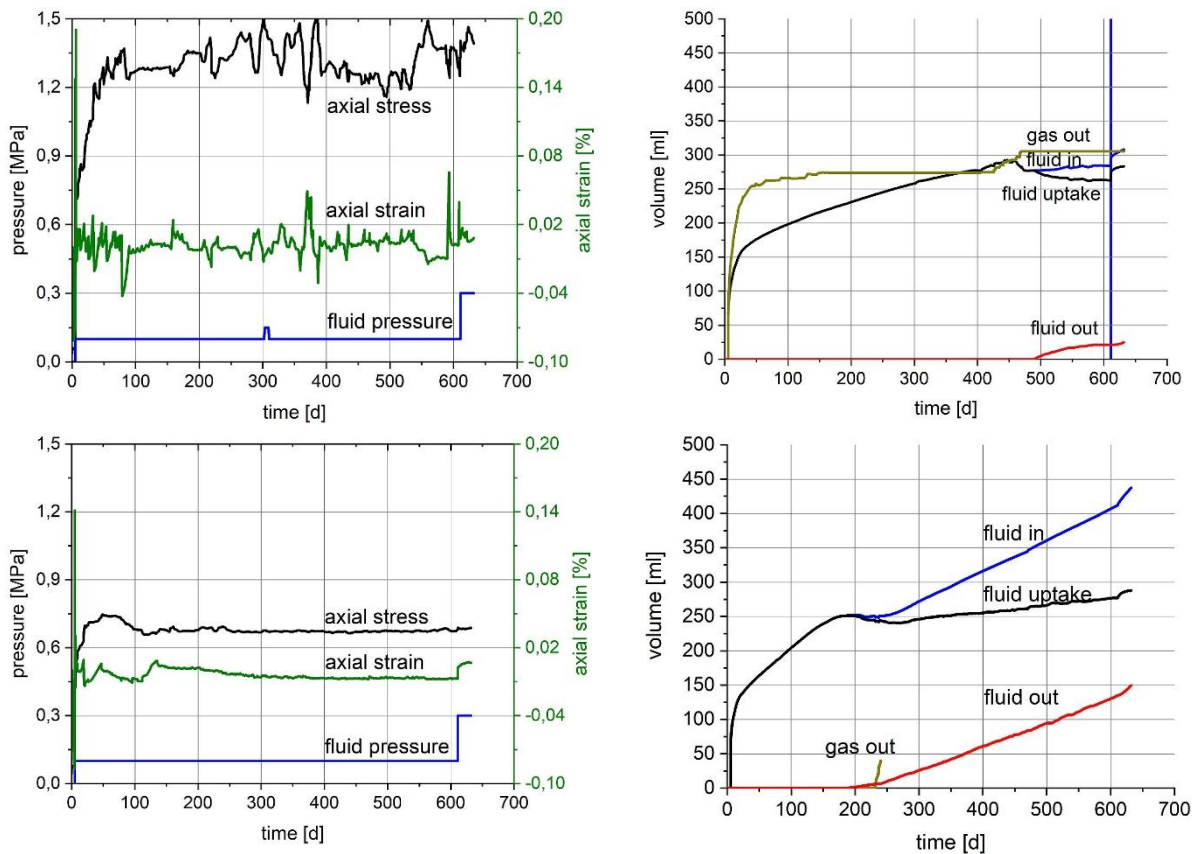


Figure 4.41 MiniSandwich MH behavior (top: Oe5; bottom: Oe6)

Series 4 (Oe7 and Oe8, Calcigel, Pearson water)

In series 4 Calcigel was again used as DS material, but Pearson water was applied as the hydration fluid with an injection pressure of 0.1 MPa. At the beginning of the experiment, the evaluation of the fluid inflow rates resulted in a fluid permeability in the order of 10^{-14} m² for both MiniSandwich (Fig. 4.42, Tab. 4.27). Parallel to fluid inflow, swelling started. The swelling pressure for the air-dry Calcigel (Oe8) was measured to be 0.6 MPa in the beginning (first 20 d) and reached a maximum of 1.2 MPa at the end. The dried Calcigel started with a swelling pressure in the order of 1.0 MPa (after 20 d) that increased to 2.2 MPa (after 420 d) (Tab. 4.27, Fig. 4.42).

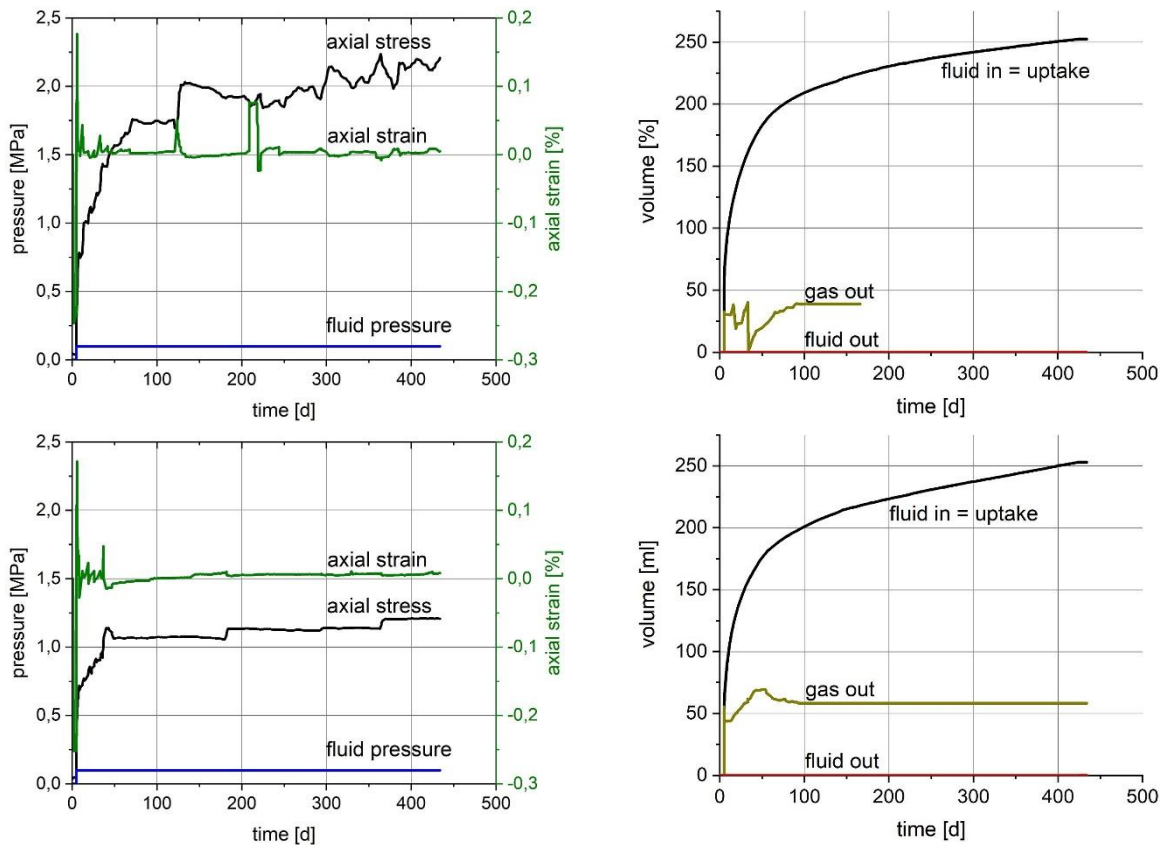


Figure 4.42 MiniSandwich MH behavior (top: Oe7; bottom: Oe8)

Both MiniSandwich tests were terminated after about 430 d as still no fluid outflow was observed. The inflow permeability for both experiments at this point was in the order of $2 \cdot 10^{-18}$ m² (Tab. 4.27). After dismantling all layers were sampled and analyzed. In both tests, the ES1 became nearly fully saturated ($w = 24.9$ and 26.2% , respectively) and the DS1 and DS2 layers had a water content in the range of 27-33%. The ES2 and ES3 layer were nearly dry ($w = 0.08$ - 0.73%).

Series 5 (Oe9 and Oe10, tempered Secursol UHP, Pearson water)

The test conditions of series 5 were qualitatively equal to series 4 but Secursol UHP (chapter 4.3.4) was used in the DS. To achieve an EMDD similar to the Calcigel mixtures of Secursol UHP with fine sand (1:0.28) which is 78.125% Secursol UHP were prepared for the DS (Tab. 4.26). The target dry density of the tempered Secursol UHP of 1.40 g/cm³ (corresponding to an EMDD of 1.10 g/cm³) could not be reached during installation in Oe9. Therefore, the target dry density of DS in Oe10 was adjusted (Tab. 4.26).

Pearson water in both tests was injected at 0.3 MPa and fluid breakthrough occurred after less than 20 days resulting in nearly steady state flow conditions (Fig. 4.43). The average flow rate was about 50 mL per week. The swelling pressure of Secursol UHP with Pearson water was in the order of 0.5 MPa for the dried bentonite and 0.7 MPa for the air-dry material. Both injection pressure and fine sand admixture accelerated liquid breakthrough but again an influence of the bentonite hydration state during installation could be observed. For both tests, the (steady state) fluid permeability after 150 d was in the order of $5 \cdot 10^{-17} \text{ m}^2$ (Tab. 4.27). The tests are still ongoing until constant ion concentrations will be observed in the outflow fluid.

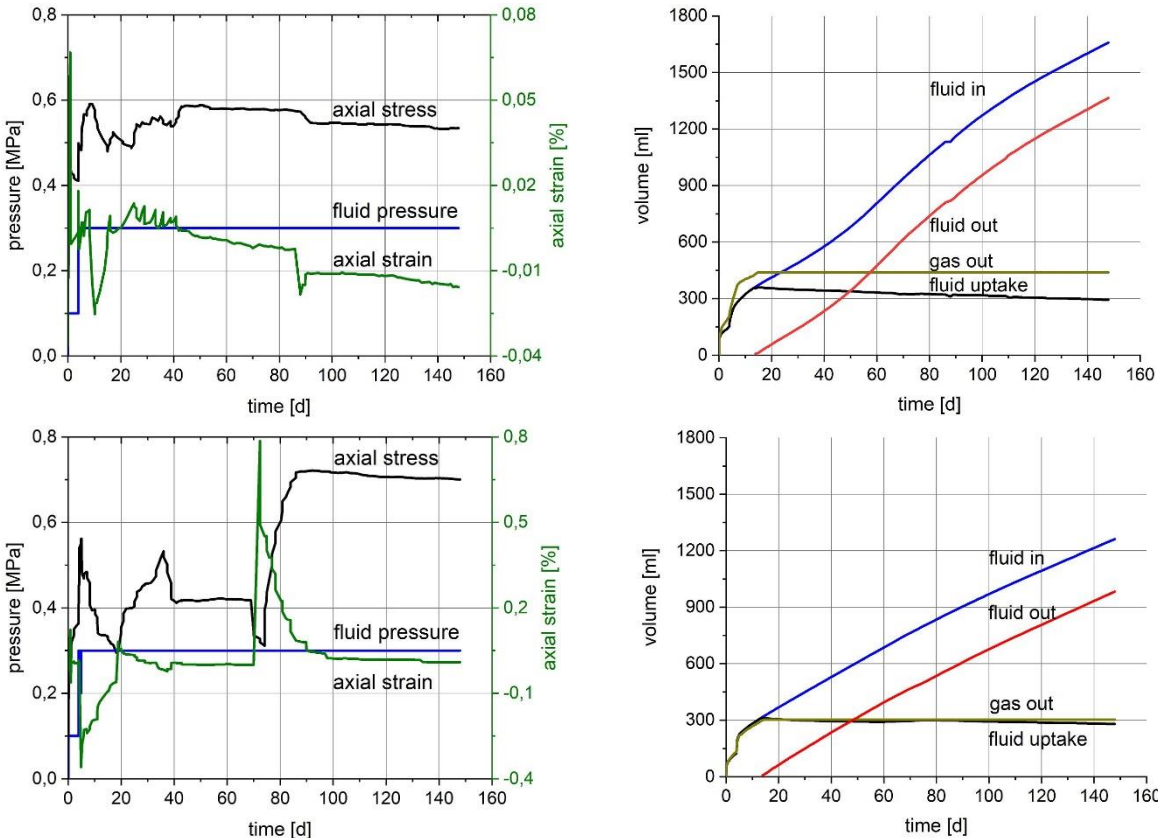


Figure 4.43 MiniSandwich MH behavior (top: Oe9; bottom: Oe10)

In all tests the fluid permeability decreased over time from 10^{-14} m^2 (initial state) to the order of 10^{-17} to 10^{-18} m^2 . The final swelling pressures varied depending on the bentonite (Calcigel or Secursol UHP), its EMDD and fabric, the used fluid type (NaCl brine or Pearson water) and the initial hydration state of the DS material.

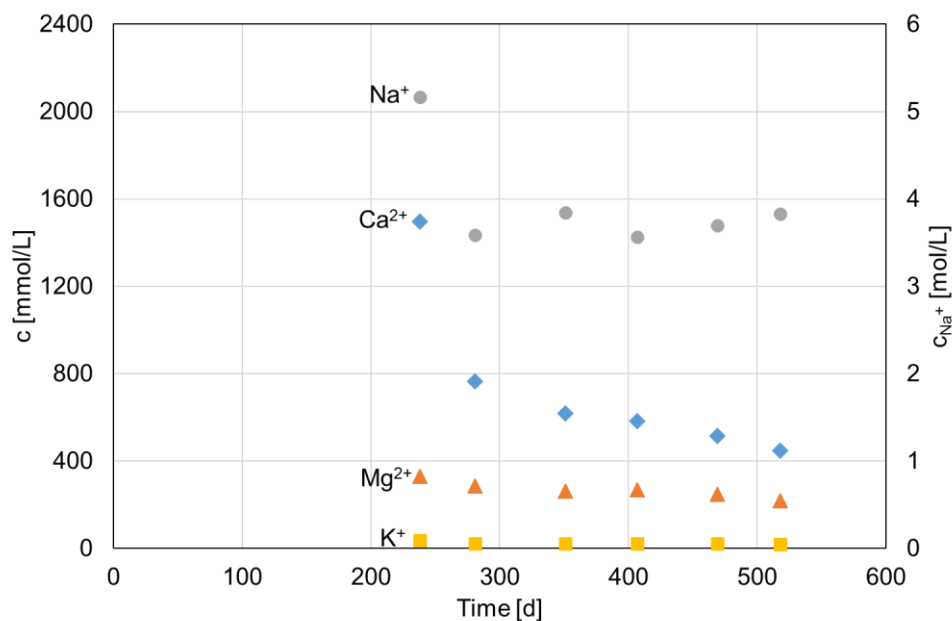
The continuously measured HM parameters, changed with time according to the saturation process. They represented a high quality database for numerical back analysis of the tests (chapter 6.2.2).

Table 4.27 Experimental outcomes of MiniSandwich experiments

		Series 3		Series 4		Series 5	
		Oe5	Oe6	Oe7	Oe8	Oe9	Oe10
Gas accessible porosity	[%]	60.5	39.4	54.1	37.7	66.8	46.5
Gas permeability	[m ²]	6.7*10 ⁻¹⁴	4.7*10 ⁻¹⁴	6.2*10 ⁻¹⁴	4.5*10 ⁻¹⁴	8.7*10 ⁻¹²	5.6*10 ⁻¹²
Break through	[d]	490	180	-	-	20	20
Fluid uptake	[mL]	283	288	252	253	293	279
Swelling pressure	[MPa]	1.5	0.7	2.2	1.2	0.5	0.7
Quasi steady state fluid permeability	[m ²]	4.2*10 ⁻¹⁸	1.2*10 ⁻¹⁷	1.8*10 ⁻¹⁸	2.6*10 ⁻¹⁸	5.4*10 ⁻¹⁷	4.2*10 ⁻¹⁷
Duration *) ongoing	[d]	> 630*	> 630*	430	430	> 150*	> 150*
Fluid volume through the sample	[mL]	25	150	0	0	1364	983

4.7.3 Results (C)

Both percolation with 4 M NaCl brine and Pearson water resulted in the dissolution of carbonates in Calcigel and Secursol UHP and cation exchange of natural Ca²⁺/Mg²⁺ in the interlayer of smectite by Na⁺. The dissolution of carbonates was enhanced in 4 M NaCl (Fig. 4.44) which was in agreement with earlier MiniSandwich experiments (Emmerich *et al.*, 2017) and studied in detail in Bohac *et al.*, (2019). So far, not enough outflow fluid from Oe5 could be collected for analysis.

**Figure 4.44** Cations in fluid out flow Oe6 (Calcigel (2W) in DS with 4 NaCl)

Bentonite installed in 1W state resulted in higher dissolution of carbonates and faster increase of Na^+ in the outflow of Oe9 (Fig. 4.45) compared to Oe10 (Fig. 4.46), although break through occurred at the same time for both MiniSandwich.

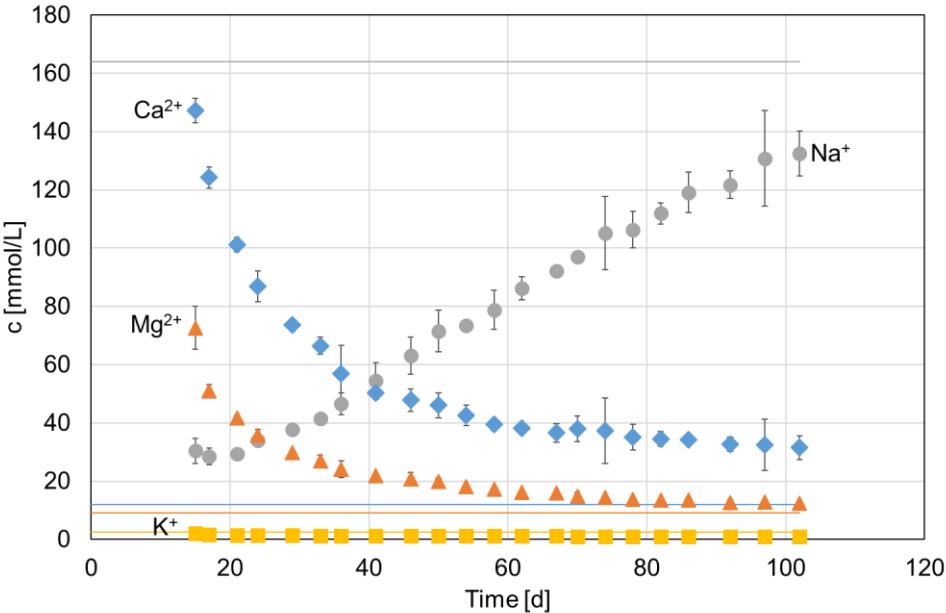


Figure 4.45 Cations in the fluid out flow of Oe9 (tempered Secursol UHD (1W)/N45 in DS with Pearson water); horizontal lines: composition of Pearson water (Tab. 4.1)

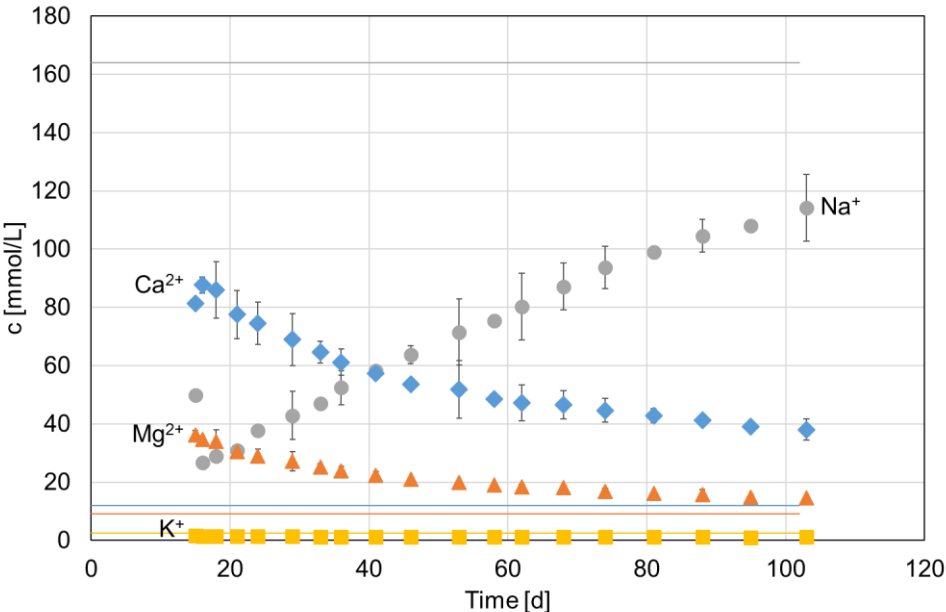


Figure 4.46 Cations in the fluid out flow of Oe10 (tempered Secursol UHD (2W)/N45 in DS with Pearson water); horizontal lines: composition of Pearson water (Tab. 4.1)

4.8 Semi-technical scale experiments (HTV)

HTV-5 was performed within the ELSA project. Mineralogical and chemical analyses of HTV-5 and realization of HTV-6 were part of the current project. Mineralogical and chemical analyses of HTV-6 will be conducted later. Pearson water was used in both HTV-5 and HTV-6. Calcigel was installed in the DS of HTV-5, Secursol UHP was used in the DS of HTV-6.

For comparison, the experimental setups and procedures of both HTV will be described here, while details of HTV-5 can also be found in (Kudla *et al.*, 2020).

The objective of both experiments was to simulate vertical sealing under the inflow of pore water characteristic of clay host rocks and to test different German bentonites for the DS (chapter 4.2 and 4.3).

4.8.1 Experimental design and installation

Experimental designs and material parameters during installation were comparable for both HTV-5 and HTV-6 (Tab. 4.28). The height of the steel column was 180 cm and the diameter was 80 cm. Four DS with a height of 25 cm each and three ES with a height of 15 cm each were installed on top of a gravel layer of 20 cm at the bottom of the column, acting as a pressure chamber. A gravel layer of 15 cm was installed on top of the Sandwich sealing system as abutment (Fig 4.47). The DS consisted of bentonite, while the ES, the sand lenses to simulate inhomogeneities in DS1 and DS2 (Fig. 4.47 and 4.48 left) as well as the hydraulic short circuit via DS2 (Fig. 4.47 and 4.48 right) to simulate an excavation disturbed zone (EDZ) between ES2 and ES3 were made of fine sand N45.

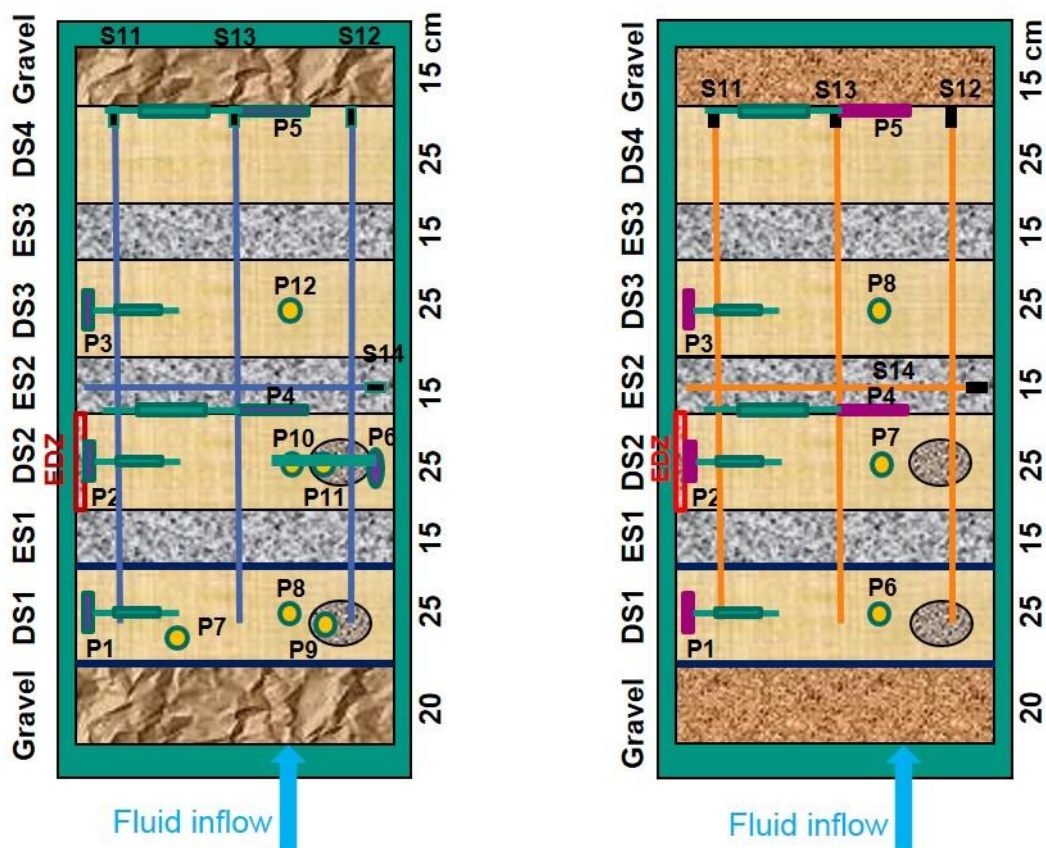


Figure 4.47 Experimental setups with sensors of HTV-5 (left) and HTV-6 (right)



Figure 4.48 HTV-6 – sand lenses for the simulation of local fault zone in bentonite (left) and artificial EDZ with sand (right)

Table 4.28 Installation parameters of the DS and ES in HTV-5 and HTV-6

Layer	HTV-5				HTV-6			
	W _{110 °C} [%]	ρ _d [g/cm ³]	W _{240 °C} [%]	ρ _d [g/cm ³]	W _{105 °C} [%]	ρ _d [g/cm ³]	W _{200 °C} [%]	ρ _d [g/cm ³]
DS4	11.1	1.64	12.7	1.62	11.1	1.55	14.1	1.51
ES3	0.1	1.55			0.0	1.59		
DS3	11.1	1.65	12.7	1.63	11.8	1.53	14.8	1.49
ES2	0.1	1.56			0.0	1.57		
DS2	11.1	1.69	12.7	1.66	11.5	1.52	14.5	1.48
ES1	0.1	1.57			0.0	1.58		
DS1	11.1	1.69	12.7	1.66	11.6	1.54	14.6	1.50

The resulting EMDD (200 °C) (eq. 4.8) was 1.28-1.32 g/cm³ for Calcigel in HTV-5 and 1.33-1.36 g/cm³ for Secursol UHP in HTV-6.

The pore volume in the lower gravel layer was 41.25 dm³ for HTV-5 and 33.7 dm³ for HTV-6. Moisture sensors (TAUPE-TDR cable sensors) were installed vertically (S11 to S13) and horizontally in the middle of ES2 (S14). S11 to S13 started at a height of 13 cm in DS1.

Pressure development was monitored with flat pressure cell (types EEKE 10/20 K200 Z4 and EEKE 10/20 KM200 Z4 VA2, company Glötzl, measuring range 0 ... 200 bar) in the DS towards the wall (P1-P3, P6) (Fig. 4.49) and at the DS2/ES2 interface (P4, HTV-5 only) as well as with spherical total pressure sensors (type PA-7LC, encapsulated in silicone, company Keller, measuring range 0 ... 150 bar) in the DS1-DS3 (P7-P12). On top of DS4 a flat pressure cell (Glötzl, type EEKE 10/20 KM200 Z4 VA2) was installed (Fig. 4.49)

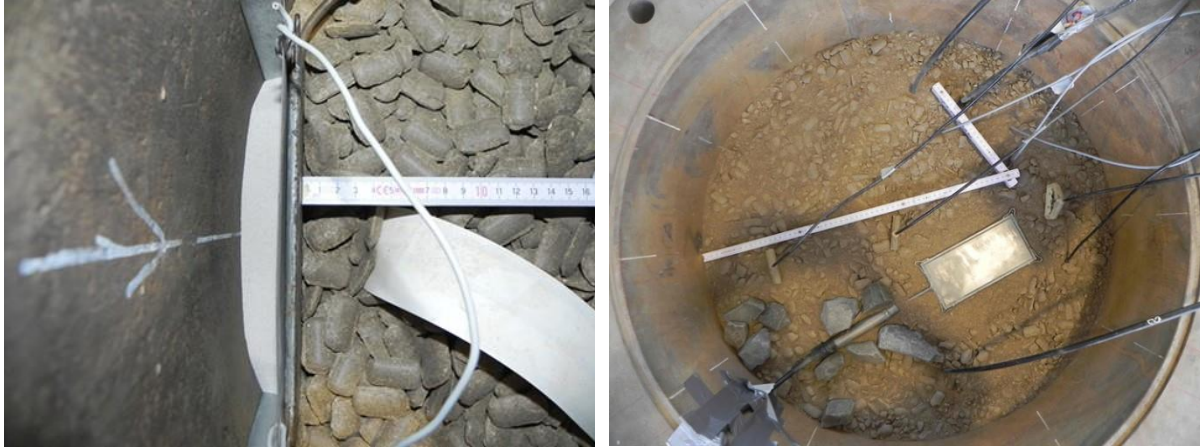


Figure 4.49 Flat pressure cell (Glötzl) near the column wall with adjacent TDR TAUPE sensor in DS2 HTV-6 (left); flat pressure cell (Glötzl) at the top of DS4 (HTV-6) (right)

The position of each layer (segment) was determined by laser distance measurements at 7 points (Fig. 4.50).



Figure 4.50 HTV-6, ES3 – laser distance measurement

4.8.2 HTV-5

4.8.2.1 Experimental process

The experiment started on May 04, 2017 with the dry measurements. Afterwards, hydration started with 0.5 MPa (5 bar) fluid pressure. Pressure increased up to 10 MPa (100 bar), when the entering fluid quantity did not increase any further (Fig. 4.51). After 276 days (February 04, 2018), the inlet valve was closed and the pump switched off in order to observe possible settling during the unpressurized phase. Dismantling began on the 285th day (February 12, 2018). A large number of samples (chapter 4.8.2.4 ff) were taken from all layers to determine the gravimetric water content for comparison of TDR measurements and for mineralogical and chemical analysis.

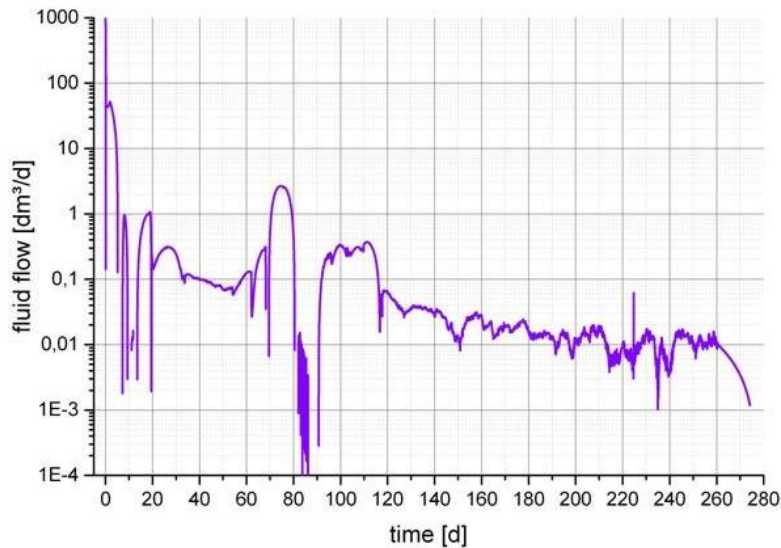


Figure 4.51 Fluid flow in HTV-5

4.8.2.2 Pressure

Fluid pressure and temperature

Temperature varied between 17 °C at the beginning from 28 °C to 13 °C at the end of HTV-5 (Fig. 4.52). This obviously influenced the pressure curve of the spherical pressure transducers (Fig. 4.52). It was unclear whether the pressure transducers or the signal path were effected directly. At the low initial pressure of approx. 0.5 MPa (5 bar), no significant effect on the pressure sensors was observed (Fig. 4.52).

On the second day, a fluid leak was detected at sensor S14. It was presumably caused by a fluid breakthrough along S12 due to pressure surges resulting from switching the pump on and off to fill the fluid reservoir. Hence, S14 was found to be insufficiently protected against fluid entry. For this reason, S14 was temporarily disconnected from the electronics to prevent damage. Shortly after increasing the pressure to about 1 MPa, fluid consumption increased for a short time, but the pressure dropped to 0.2 MPa (2 bar) and then slowly increased to about 0.7 MPa (7 bar).

On the 5th day, further pressure increase to 1.5 MPa (effective 1.2 MPa) took place. Towards the evening, a leak was detected in the pressure sensor P8 in DS1, which led to the complete failure of the electrical system. The pump was switched off and all measurements except for the non-directional pressure sensors were restarted. Since the system was not supplied with new fluid, the change in the pressure readings was due to the increase in swelling pressure.

On the 9th day, S14 was reconnected after no further fluid leak had been detected. On the 10th day, the spherical pressure sensors were restarted and on the 15th day the pump was restarted at 10 bar. Further pressure increases followed on day 21 (1.5, 1.75 MPa), day 22 (2.25, 2.5 MPa), day 23 (2.75, 3.0 MPa), day 57 (4.0 MPa) and day 65 (6.0 MPa). On the 71st day, 8.0 MPa was set and the pressure dropped sharply. After reducing the pressure to 6.0 MPa, the effective pressure was 3.1 MPa. Consequently, fluid injection pressure was further reduced to 3.0 MPa. The increase on the 72nd day (4.0 MPa), 92nd day (5.0 MPa), 93rd day (6.0 MPa), 98th day (7.0 MPa), 99th day (8.0 MPa), 106th day (9.0 MPa) and on the 107th day to 10.0 MPa set pressure proceeded without problems. The measured fluid pressure leveled off to values between 9.0 and 9.2 MPa by the end of the test (day 286). Fluid consumption rose from 171 to 174.5 kg after the last pressure increase.

Pressure development in DS1

Due to the close proximity to fluid injection, the pressure sensors in DS1 reacted immediately (Fig. 4.52). Especially in the sandy lens SL1, swelling pressure (spherical pressure transducer P9) developed quickly, clearly exceeded the initial fluid pressure, and continued to rise despite the holding phase at a pressure level. The pressure drop on day 71 also affected P9, but pressure recovered immediately and reached the upper limit of the pressure range of 11.0 MPa on the day 102. No further data are available after this day. The pressure measured by spherical pressure transducer P7 immediately followed the fluid pressure. The increase during the phases of constant pressure also indicated a swelling pressure. This pressure however, clearly is below that in the sandy lens. On day 88, the sensor P7 failed (4.7 MPa), but showed a short reaction on day 101/102 at 11.0 MPa (upper pressure limit). The spherical pressure sensor P8 showed a behavior comparable to that of P7 until day 88. Afterwards, the pressure increased to 10.8 MPa until the end and showed an undirected pressure difference to the fluid pressure of about 1.6 MPa. The behavior of the flat pressure cell P1 in the direction of the wall was rather interesting. Pressure predominantly followed that of P8, but rose more strongly in the course of the highest pressure stage and broke off at about 11.3 MPa on the 294th day when the upper limit was reached. Thus, the differential (swelling) pressure reached a value of about 2.1 MPa. Apart from the pressure in SL1 (P9), whose difference to the fluid pressure of 7.6 MPa (76 bar) already reached 3.4 MPa, the swelling pressure did not exceed a value of 3.0 MPa (P1) in DS1 with a maximum pressure of 9.2 MPa. A decrease of the pressure due to the reduction of density in DS1, at the time of saturation was not visible.

Pressure development in DS2

In DS2, wall friction at the surface of the steel column (Fig. 4.52) significantly reduced the pressure. As in DS1, the highest pressure (spherical pressure sensor P11) was measured in the sandy lens (SL2). It rose continuously and reaches 9.5 MPa (95 bar) at the end of the test. Thus, the value was only slightly above the fluid pressure. The temperature influence was most obvious at P11 (Fig. 4.52). Pressure measured by the spherical pressure sensor P10 rose continuously to about 7.5 MPa (75 bar) until the end of the test. Flat stress transducer P2 in the direction of the wall produced values that directly followed the pressure at P1 until day 71, when it did no longer increase to the same extent and ended at about 8.3 MPa. Flat stress sensor P6 near SL2 in the direction of the wall failed completely. Flat stress sensor P4 at the interface DS2/ES2 delivered axial pressure data up to day 20 with the final reading being 1.35 MPa. This value thus was between the results of P10 (1.06 MPa) and P11 (1.74 MPa) and hence, confirmed them. The fluid pressure was 0.92 MPa. Starting from the final pressure at P2 compared to P1, the swelling pressure in the area DS2 towards the wall was reduced by about 1.0 MPa to a maximum of about 2.0 MPa.

Pressure development in DS3

This development continued in DS3 (Fig. 4.52). Spherical pressure transducer P12 showed a continuous pressure rise up to 4.5 MPa without any direct reactions to fluid pressure changes. Flat stress transducer P3 in the direction of the wall delivered only slightly lower values of up to 3.9 MPa. In both cases, an increase was found. Swelling pressure development in the humidified regions below has not yet been completed.

Pressure development in DS4

The flat stress sensor P5 measuring axial pressure at the top of the column between DS4 and the gravel abutment followed the pressure development in DS3, but at a lower level (Fig. 4.52). The final pressure was about 2.2 MPa. Pressure reduction by wall friction against the fluid pressure was about 5.0 MPa.

4.8.2.3 Fluid propagation

Based on the initial water content of the DS and ES during installation (Tab. 4.27), the integral value of the effective relative dielectric permittivity (ϵ') of the sandwich materials along S11 and S13 sensors was about 3.5. The sequence of DS/ES materials along both sensors was very similar, with both DS1 and DS2 containing an additional sandy lens along S12. The lower ϵ' of the sand compared to the bentonite led to a lower integral ϵ' along S12 compared to S11/S13. After applying the Pearson water, the breakthrough occurred quickly along S12 via the sandy lens to ES1. The swelling pressure directly induced by the fluid around the sand lens sealed the preferential flow path along S12. Later, the fluid was able to penetrate the Sandwich sealing further upwards first via S13 and then along S11. At the end of the first day, another breakthrough along S13 resulted in an increasing hydration of ES2, which led to the activation of the simulated EDZ and a breakthrough to ES2. Another breakthrough along S11 at the beginning of the second day supported this process. Further hydration during the second day via S12 accelerated fluid access to ES1 and ES2. Until about day 14 the values at S11/S13 rose slightly. Then another breakthrough to ES1 occurred via S13. After that, the moisture increased only slightly. On day 71, a pressure drop occurred directly after the fluid pressure was increased to 8.0 MPa. This event was visible on all three sensors and was traced back to the fact that the fluid had broken through the entire DS1 and subsequently led to a general increase of ϵ' . Subsequently, ϵ' only increased along S12, whereas a slight decrease was recorded at S11/S13. This can be attributed to the slow draining of the ES1/ES2 by the higher suction pressure of the bentonite in DS2 and DS3. The increase of ϵ' at S12 can be explained by a higher swelling pressure there.

On day 212 the pump was switched off and the ball valve at the inlet was closed. The HTV-5 experiment remained in this state for another 10 days to observe a possible influence of the absent pressure load. Until the start of dismantling, i.e. the removal of the upper steel cover, no influence was noticed. After dismantling was completed, the sensors for ϵ' showed the value of air ($\epsilon' = 1$). Any deviations were due to slight differences in sensor manufacturing.

The sensor S14 was located in the middle of ES2, completely embedded in fine sand N45 with ϵ' being about 2.2. This value was displayed until the fluid reached ES2 via the EDZ at the end of the first day. Then, the value rose rapidly to about 10.4. Due to a leak at the end or beginning of the sensor, fluid permeated the coaxial cable and the plug to the multiplexer. To prevent damage of the multiplexer, the sensor was disconnected from the multiplexer. After no more fluid leaked, sensor S14 was reconnected on the 13th day.

The function of the ES afterwards was very well documented. Due to the high hydraulic conductivity at a low water content compared to bentonite at an intermediate water content, the penetrating fluid distributed very quickly over the entire ES volume. When the suction pressure of the ES fell below that of the bentonite, the fluid was removed from the ES by the adjacent DS. This did not happen on the 75th day, when pressure pulses were generated as a result of a pressure drop and the subsequent restart of the pressure regime, leading to the breakthrough of the fluid to ES2. The resulting jump in ϵ' showed that this happened very fast. The resulting swelling pressure cured the breakthrough immediately, which was reflected by the slowly decreasing measured values. In the end, the equilibrium between ES2 and DS2/DS3 seemed to be almost reached.

The ϵ' value of air was also measured at the end of the test.

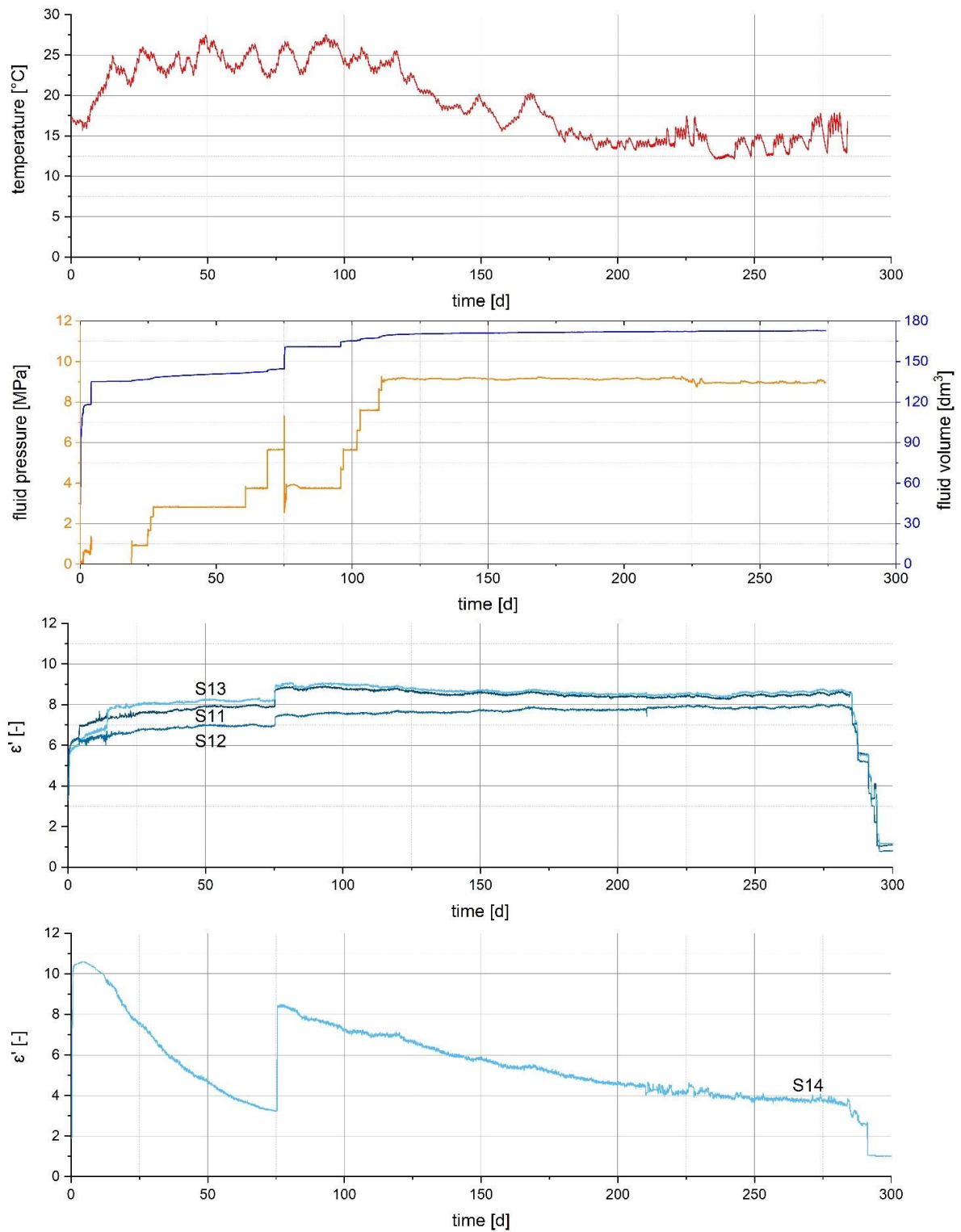


Figure 4.52 (from top to bottom): temperature; pump pressure and fluid volume; effective dielectric permittivity of vertical sensors; effective dielectric permittivity of horizontal sensor

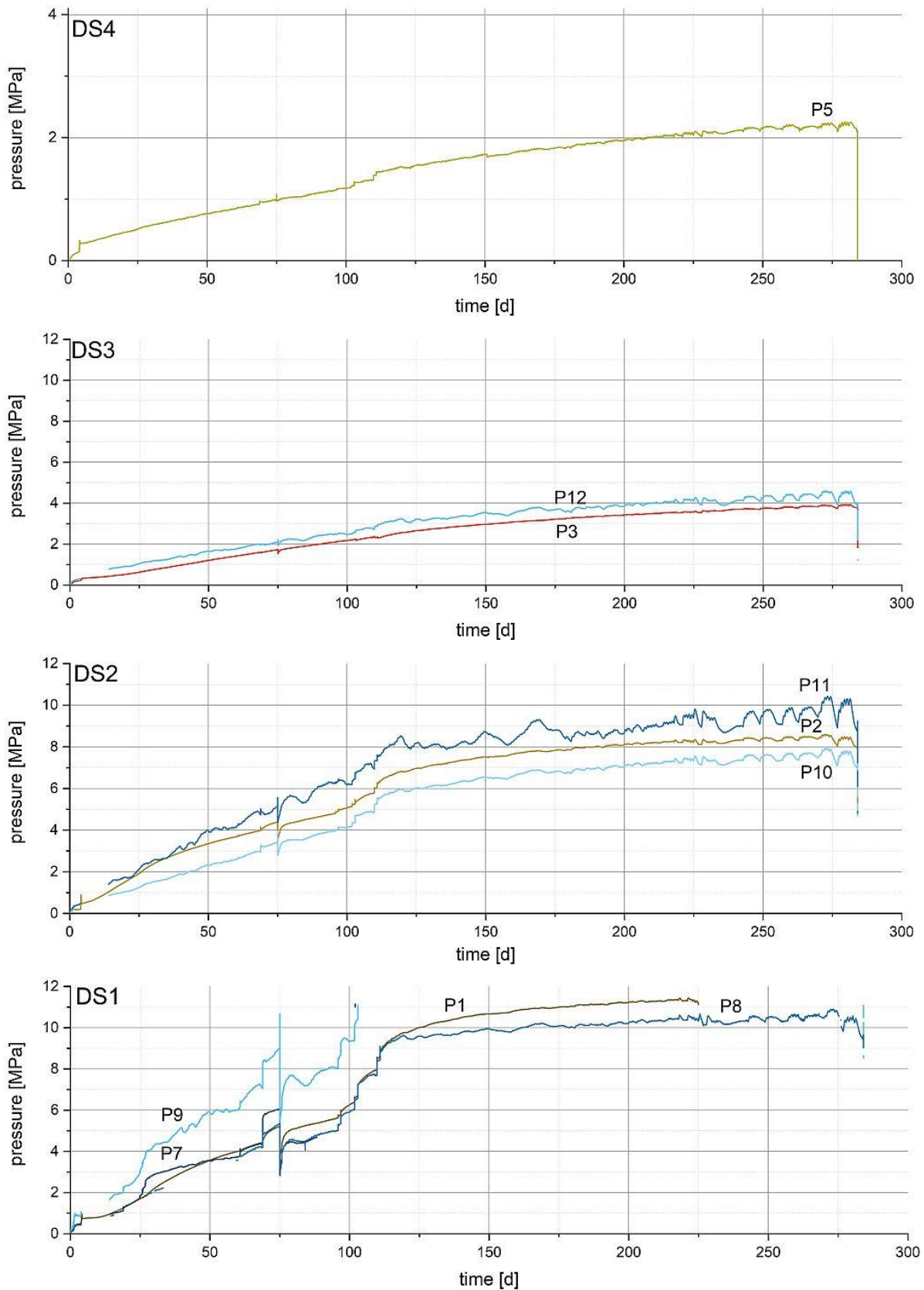


Figure 4.52 (continued) pressure sensor readings in the DS of HTV-5 (from bottom to top DS1 to DS4)

Application of the differential TDR method

The TDR signals over time reflect the change in water content due to the influence of the injected fluid (Fig. 4.53). Here, exemplary signals of the S11/S13/S12 sensors installed vertically in one plane are plotted for the period of 32 days after the start of the experiment and show the variation of the amplitude distribution due to the progressive moisture development in the experiment.

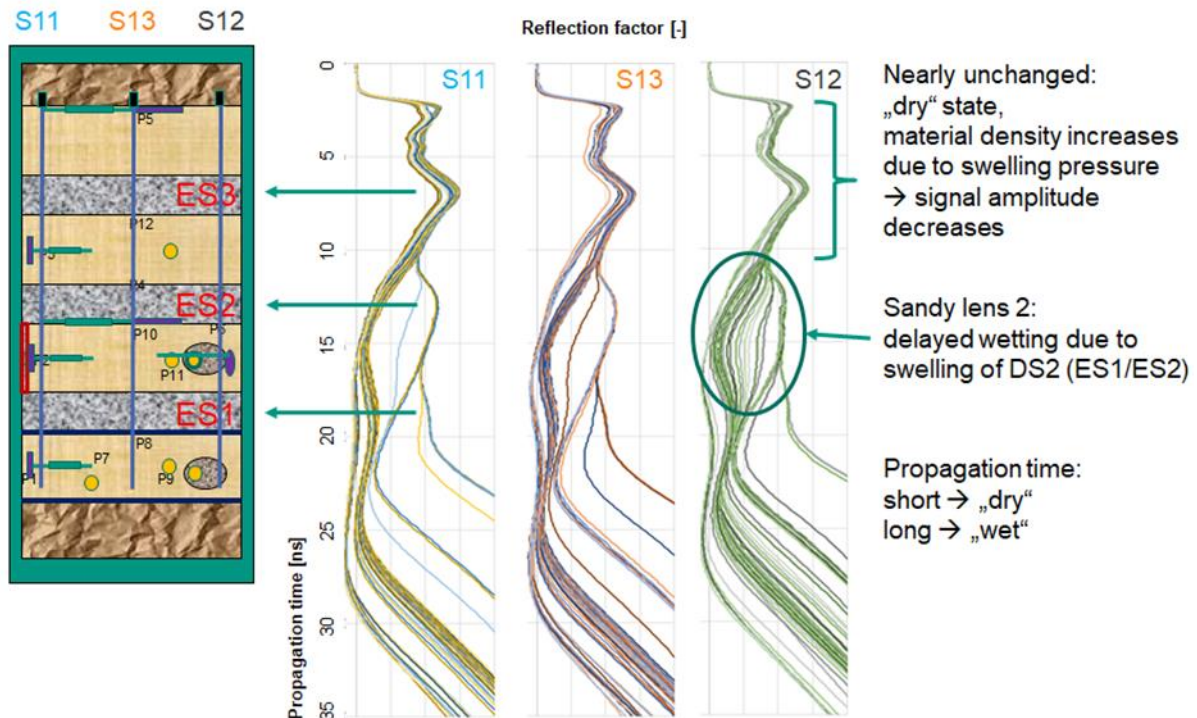


Figure 4.53 Amplitude variation due to progressive moisture content

The TDR signals were treated according to the dTDR method and were evaluated with the reference water content (ES 1%, DS 11%) during installation. The signals of the individual sensors are superimposed and are displayed for individual points in time (Fig. 4.53).

Starting from the installation, the already described conditions and changes are shown in the course of the experiment. Moisture breakthroughs and distribution become visible and locally recognizable (Fig. 4.54). The development of swelling pressure is expressed by a deformation of the amplitude curves, which occurs in addition to the progression of moisture and becomes visible due to the increase in density. This is especially obvious in the dry areas in the upper part of the column (ES3, DS4).

Taking into account the interpolation between the normalized TDR signals S11-S13-S12, color graphics can be created to represent moisture movement in three dimensions (Fig. 4.55). Here, the first breakthrough after 5.5 h (day 1 19:00) (Fig. 4.55) via the EDZ to ES2 can be seen clearly, after fluid reached ES1 before, first via S12, then via S13 and a little later also via S11. Fluid dispersion in ES2 was recorded and also the increase in hydration in DS2 from ES2 until ES2 was almost homogeneously hydrated. At the same time, compaction in DS3 and DS4 started due to the swelling pressure in DS1 and DS2. Almost at the same time, DS3 was supplied with fluid from ES2 and hence, swelling also started there. The second major breakthrough (day 75) was via S12 and the sandy lens in DS2 for an additional fluid supply from ES1 to ES2, which continued to drive the swelling process. The system was then stable until dismantling, as sensor readings did not change significantly.

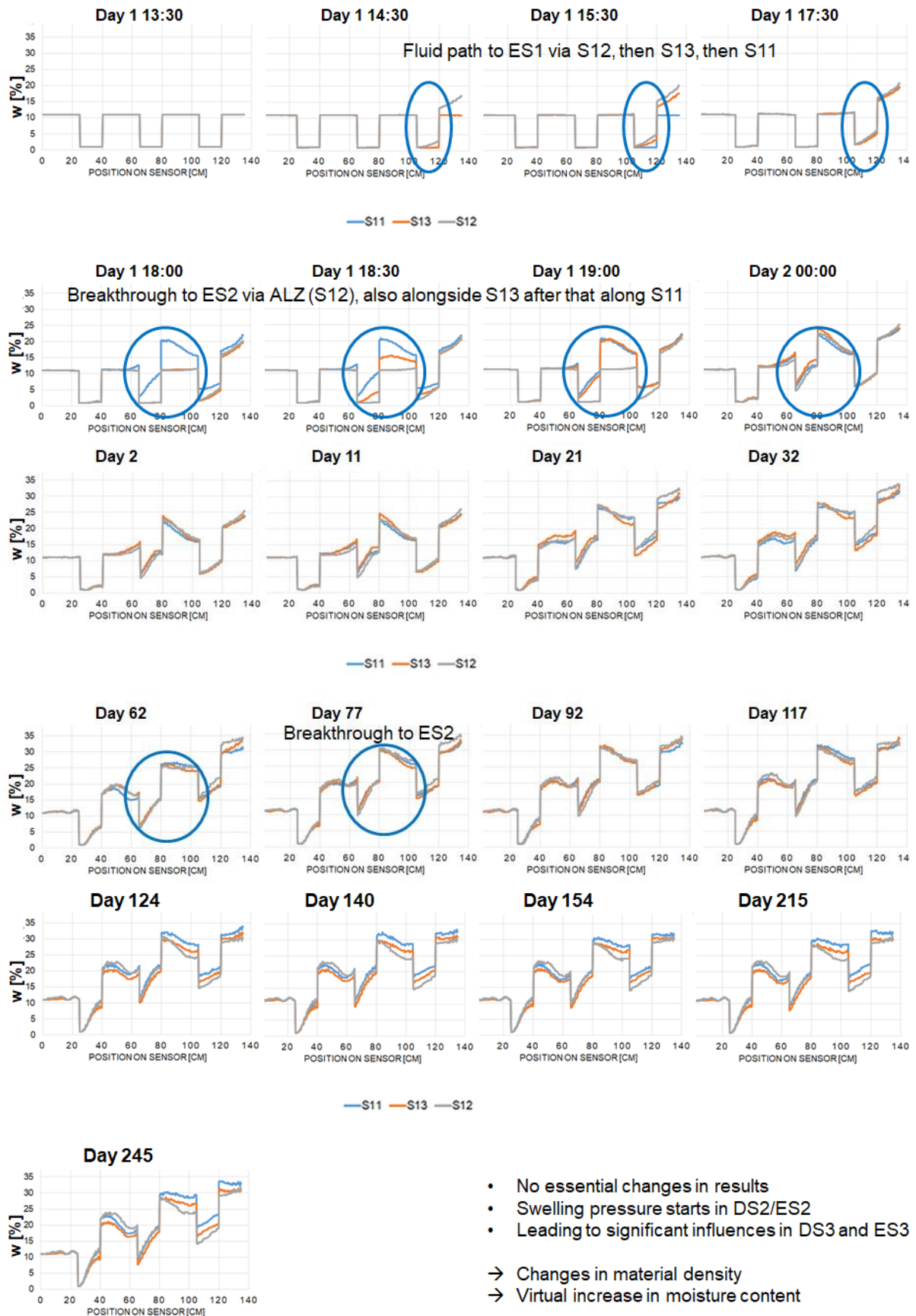


Figure 4.54 Development of the water content distribution along the sensors S11/S13/S12

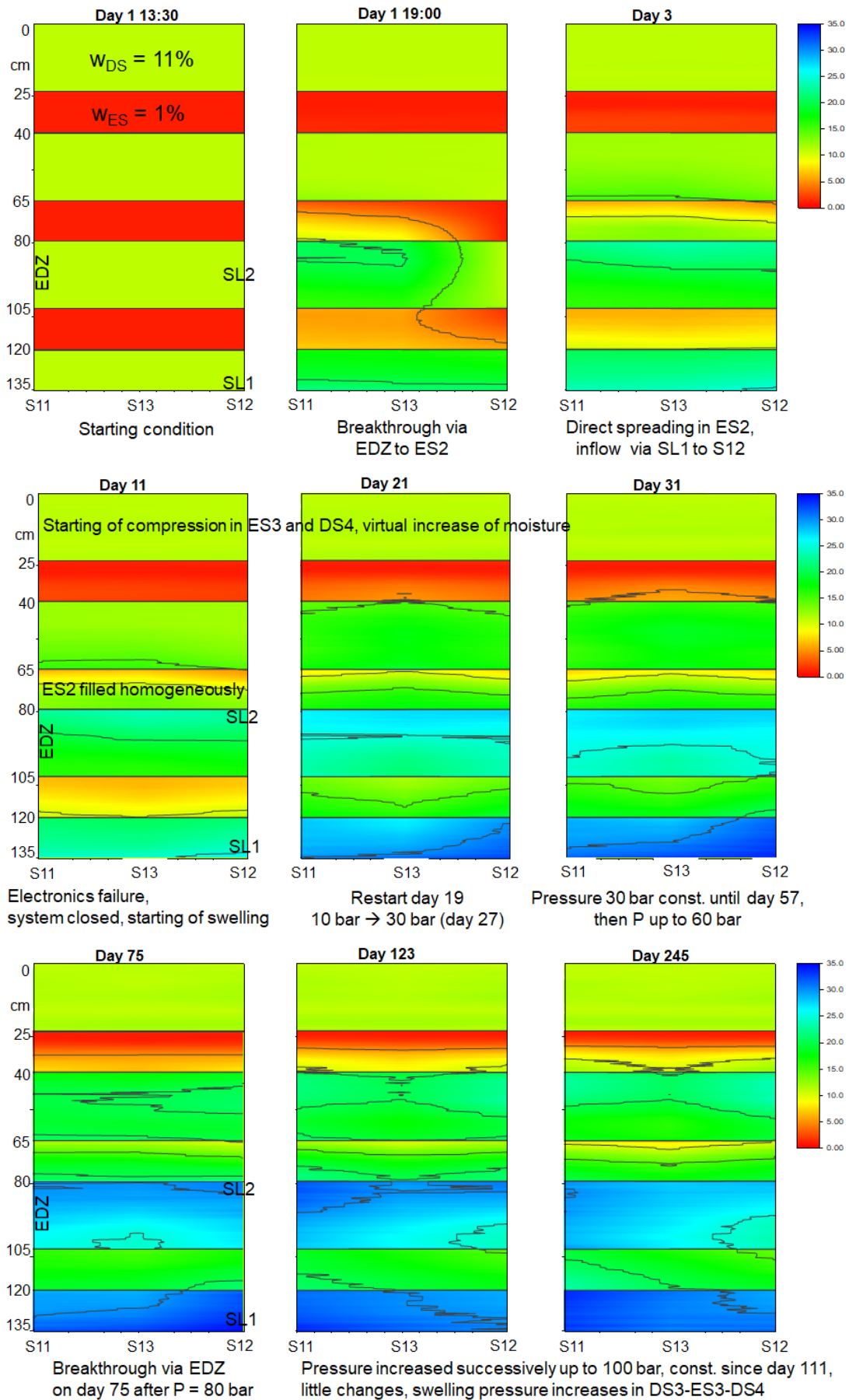


Figure 4.55 Development of fluid distribution, installation water content (day 1) $w_{DS} = 11\%$, $w_{ES} = 1\%$

4.8.3.4 Dismantling

HTV-5 was dismantled from January 19, 2015 to February 11, 2015. During dismantling, changes in position and thickness of the DS and ES layers were determined to calculate the densities of the individual layers in the final state of the experiment. 342 samples were taken in 18 levels (3 in each DS and 2 in each ES) by applying a special grid (Fig. 4.56), starting with level E1 at the top of DS4 down to E18 at the bottom of DS1. The position 0° corresponded to the position of the working platform. Approximately 200-300 g of material were collected at each point of the grid for determination of the water content and subsequent mineralogical analysis. A vacuum cleaner was used to remove the sandy material of the ES at the interface to a DS.

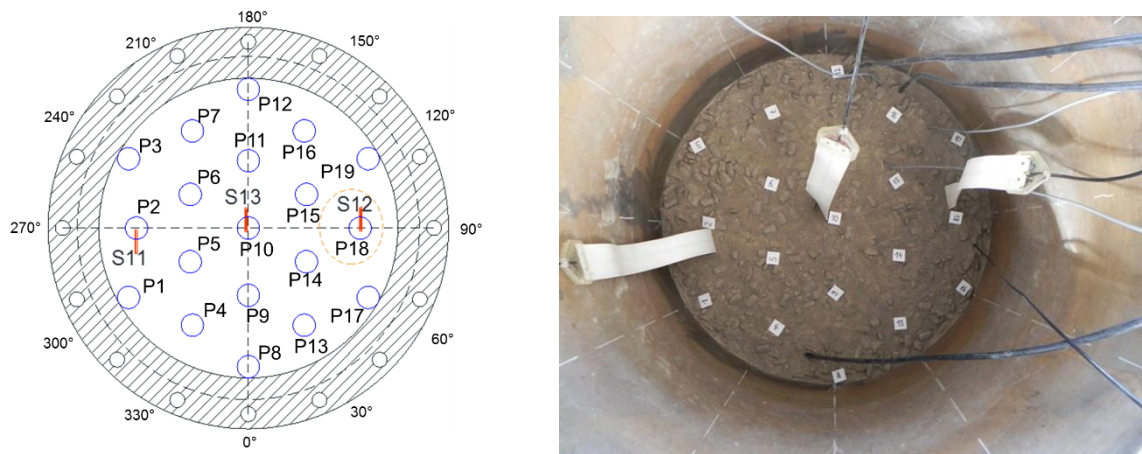


Figure 4.56 Sampling of HTV-5 and HTV-6

4.8.2.5 Water content and density

Moisture distribution characterizes saturation of the system by the fluid. No fluid transport to layer DS4 was observed (Fig. 4.52), therefore this layer can be used as a background. Samples in this layer are characterized by w 13.8% (Tab. 4.28). Water content in the deeper DS increased significantly from $\approx 21.7\%$ in DS3 to $\approx 32.2\%$ in DS1. The water content of the ES was significantly lower (Tab. 4.28). In DS1 and DS2, the moisture was distributed preferably at the bottom and top of these layers (E18-E16, E13-E11 respectively). In DS3, water content decreased from the bottom to the top.

The water content of the sandy lenses in DS1 and DS2 was 8.6 and 0.1%, respectively (Fig. 4.57). The water content in the simulated EDZ was 3.7%. Moisture distribution over the layers demonstrated the functionality of the Sandwich sealing system.

Salt content followed the distribution of moisture along the Sandwich sealing system (Tab. 4.28). Calcigel initially contained about 0.34% of salt (DS4). The highest salt content was recorded in DS1 ($\approx 0.45\%$) and it was distributed similarly to the moisture in the bottom and top layers (E18 – E16). In the upper layers, the salt content decreased to $\approx 0.4\%$ in DS2 and to $\approx 0.37\%$ in DS3. A significant drop of the salt content was observed at the interface of DS and ES. ES1 contained $\approx 0.18\%$ salts, ES2 $\approx 0.06\%$ and ES3 contained a negligible quantity of salts.

Table 4.29 Average water content and salt content in the levels after termination of HTV-5

Layer	Level	Material	W (105 °C) [%]	W (240 °C) [%]	saturation	Salt content [wt.%]	Dry density [g/cm ³]	Change in height [cm]
DS4	E1	Calcigel	11.9	13.5	0.62	0.35		
	E2	Calcigel	12.2	13.7	0.63	0.34	1.72	-1.1
	E3	Calcigel	12.6	14.2	0.65	0.33		
ES3	E4	N45	0.0		0.00	0.00	1.57	-0.1
	E8	N45	0.0		0.00	0.00		
DS3	E6	Calcigel	16.7	18.3	0.76	0.38		
	E7	Calcigel	19.3	21.0	0.87	0.42	1.66	-0.2
	E8	Calcigel	24.1	25.7	1.07	0.47		
ES2	E9	N45	3.1		0.12	0.03	1.62	-0.6
	E10	N45	3.3		0.13	0.05		
DS2	E11	Calcigel	27.4	29.2	1.06	0.51		
	E12	Calcigel	23.5	26.5	0.96	0.43	1.57	1.8
	E13	Calcigel	25.7	27.5	1.00	0.48		
ES1	E14	N45	15.5		0.61	0.18	1.62	-0.6
	E15	N45	23.0		0.90	0.26		
DS1	E16	Calcigel	30.1	32.0	1.11	0.56		
	E17	Calcigel	25.4	28.2	0.98	0.48	1.54	2.2
	E18	Calcigel	34.5	36.4	1.27	0.57		

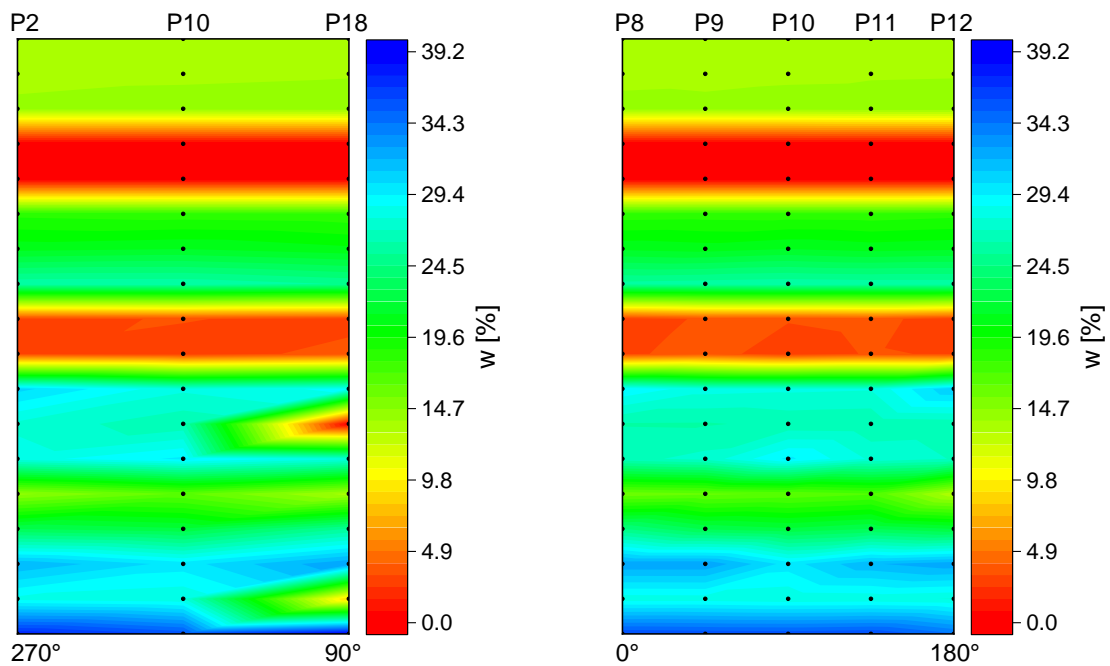


Figure 4.57 Water content distribution in HTV-5 (cross section: left 270°-90°, right: 0-180°)

A linear correlation of salt content and water content was observed (Fig. 4.58). A deviation from the linear dependence was observed in ES1 with a relatively high moisture, but low salt content, due to the low ability of sand N45 to fix and immobilize salt.

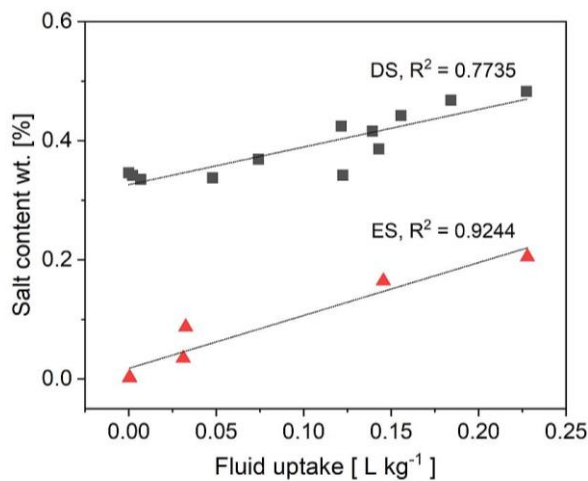


Figure 4.58 Salt content as a function of fluid uptake of the layers

4.8.2.6 Ion transport and cation exchange

The CEC of Calcigel pillows in ES1 was determined as a reference value (Tab. 4.30). Slight differences from initial values were observed (Tab. 4.7, chapter 4.3.3.2) due to the natural variability of the raw material.

Table 4.30 CEC and concentrations of exchangeable cations and conductivity, anions and cations of Calcigel in ES1 determined in supernatant by conductivity measurement.

CEC [cmol(+)/kg]	Anions			Cations				Sum
	Cl ⁻	SO ₄ ²⁻	Sum	Na ⁺	Ca ²⁺	Mg ²⁺	K ⁺	
59.2 ± 1.7	-	-	-	5.3 ± 0.3	42.5 ± 0.8	15.1 ± 0.3	3.4 ± 0.1	66.0 ± 1.0
Conductivity [μS/cm]	soluble [cmol(+)/kg]			soluble [cmol(+)/kg]				
224.4 ± 1.1	2.4 ± 0.1	1.6 ± 0.1	4.0 ± 0.1	2.9 ± 0.1	0.8 ± 0.1	0.4 ± 0.1	0.6 ± 0.1	4.8 ± 0.1

The difference in CEC sums of exchangeable cations can be explained by the presence of accessory minerals, mainly carbonates (Tab. 4.6) and their solubility (Bohác *et al.*, 2019). Cations of these accessory minerals were determined in supernatant by conductivity measurement (Tab. 4.30).

Cations in the system can be divided into three groups. They originate either from (1) cation exchange process of montmorillonite, (2) Pearson water or (3) from dissolution of accessory minerals (mainly carbonates) during the percolation of HTV-5 and during analysis.

Ca²⁺ and Mg²⁺ originate mainly from exchangeable positions in the interlayer and at the edges of the montmorillonite (Fig. 4.59). Migration of cations from the DS1 (E16 – E18) to the ES1 (E15-E14) as well as to the DS2 (E11-E13) was observed. Small amounts of Ca²⁺ and Mg²⁺ were also detected in ES2 (E9-E10).

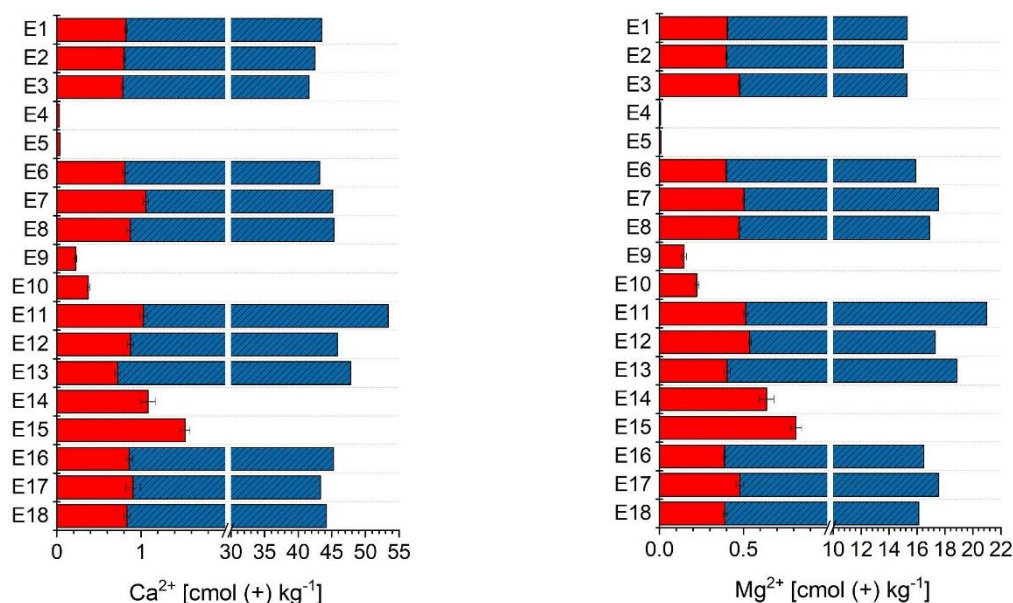


Figure 4.59 Concentrations of Ca²⁺ and Mg²⁺ in HTV-5 (red: dissolved, blue: exchanged)

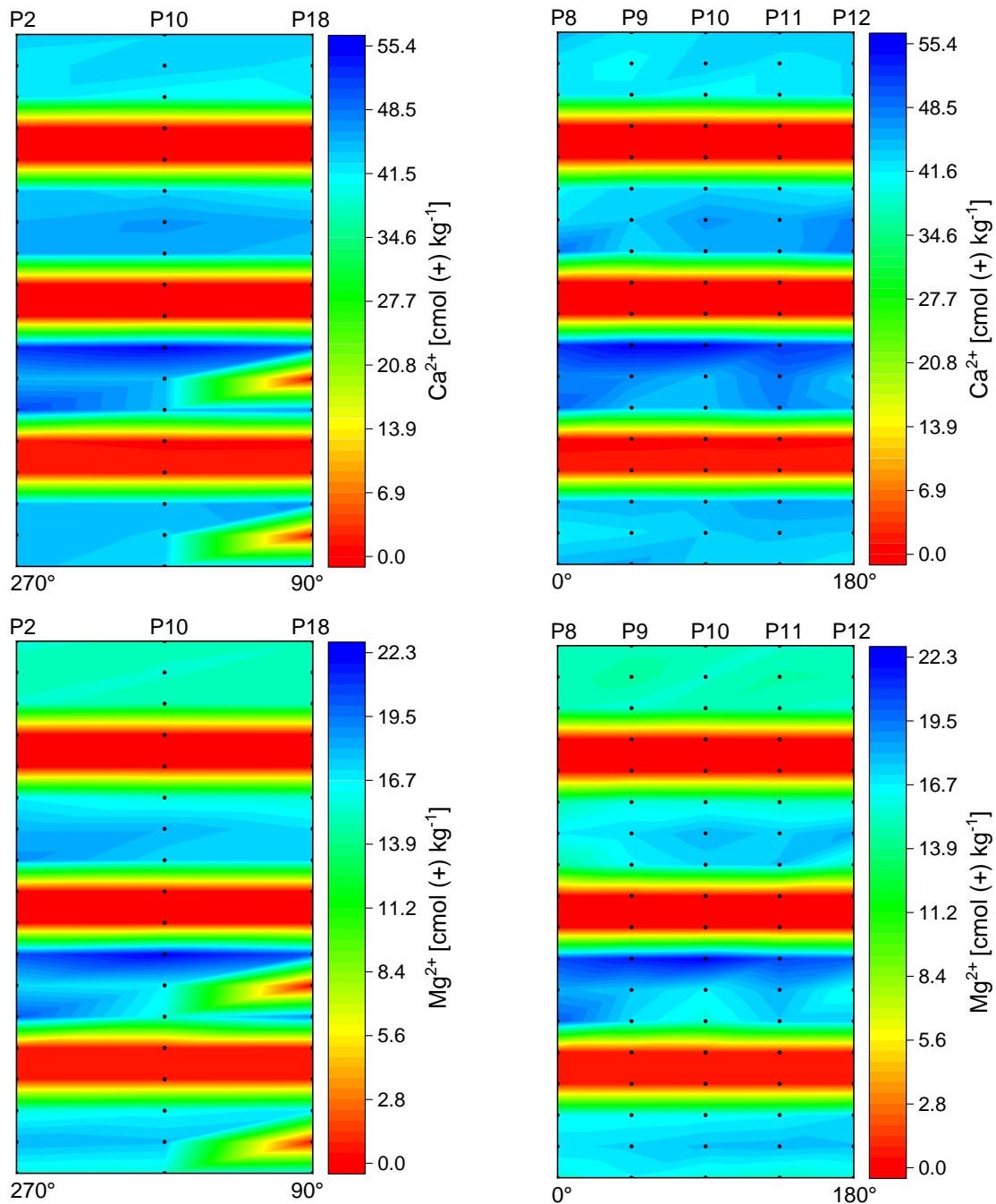


Figure 4.60 Distribution of Ca^{2+} and Mg^{2+} (total from CEC and soluble)

Dissolution of carbonates resulted in an enrichment of Ca^{2+} and Mg^{2+} at the top of DS2 (Fig. 4.60).

Concentrations of Na^+ and K^+ were lower in Calcigel (Tab. 4.30) Concentrations of dissolved Na^+ followed measured water content (Fig. 4.61). It may therefore be concluded, that these cations originate from Pearson water, taking into account the natural content of Na^+ in Calcigel. Because of the relation between Na^+ and water content, Na^+ cations are concentrated mainly at the bottom and top of DS1 and DS2 (Fig. 4.62). In DS3, concentration of Na^+ was higher in E8 and decreased in E7 and E6, where it was equal to the natural content of Na^+ in Calcigel. The same trend was observed for K^+ and the water content. Compared to Na^+ , however, the increase of K^+ concentration in the first ES was insignificant.

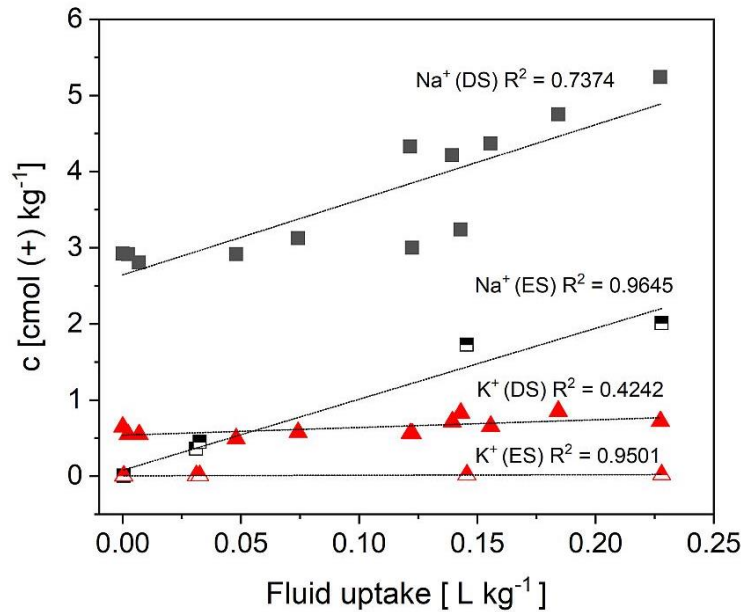


Figure 4.61 Soluble Na⁺ and K⁺ as a function of Pearson water uptake

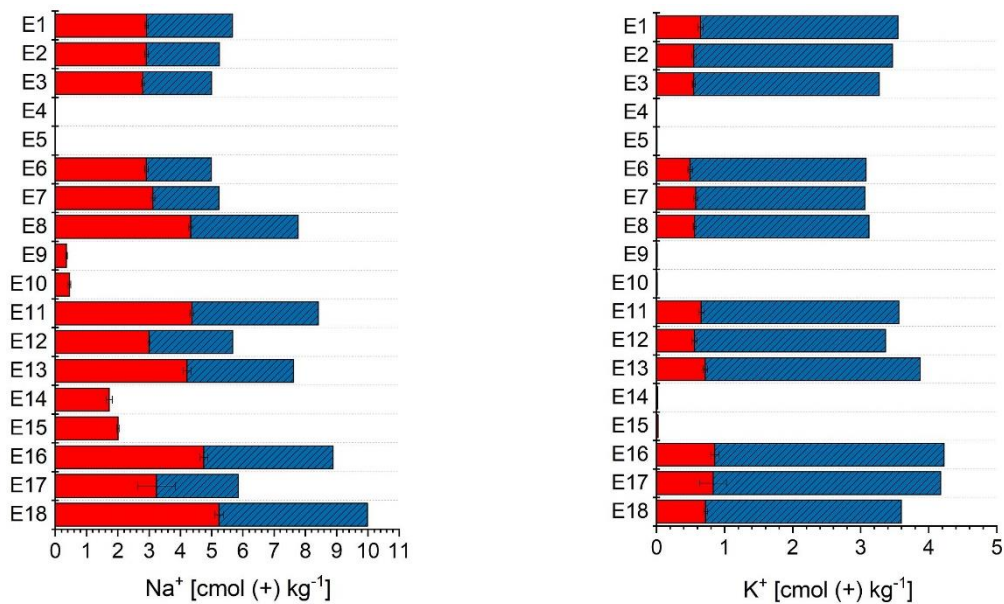


Figure 4.62 Concentrations of Na⁺ and K⁺ in HTV-5 (red: dissolved, blue: from cation exchange)

Distribution of cations (total) in the individual layers was not uniform and differed in the layers. In DS1, level E18, the Ca²⁺ concentration was highest in samples P14, P1 and P7 (Fig. 4.63). In level E17, concentration dropped significantly in P7, indicating that Ca²⁺ cations were fixed in level E18. The same trend was observed in level E16. In contrast to this, concentrations of Ca²⁺ dropped in P1 as well as in P14 in E17, but increased again in level E16. This indicated that Ca²⁺ cations were distributed between levels E18 and E16 (4.64). A very similar trend was observed for Mg²⁺ cations. Na⁺ (Fig. 4.63) as well as K⁺ concentrations followed moisture distribution in the individual layers (DS1). The trend to distribute cations on the outer terminal levels of the DS layer was the same as for exchangeable cations Ca²⁺ and Mg²⁺.

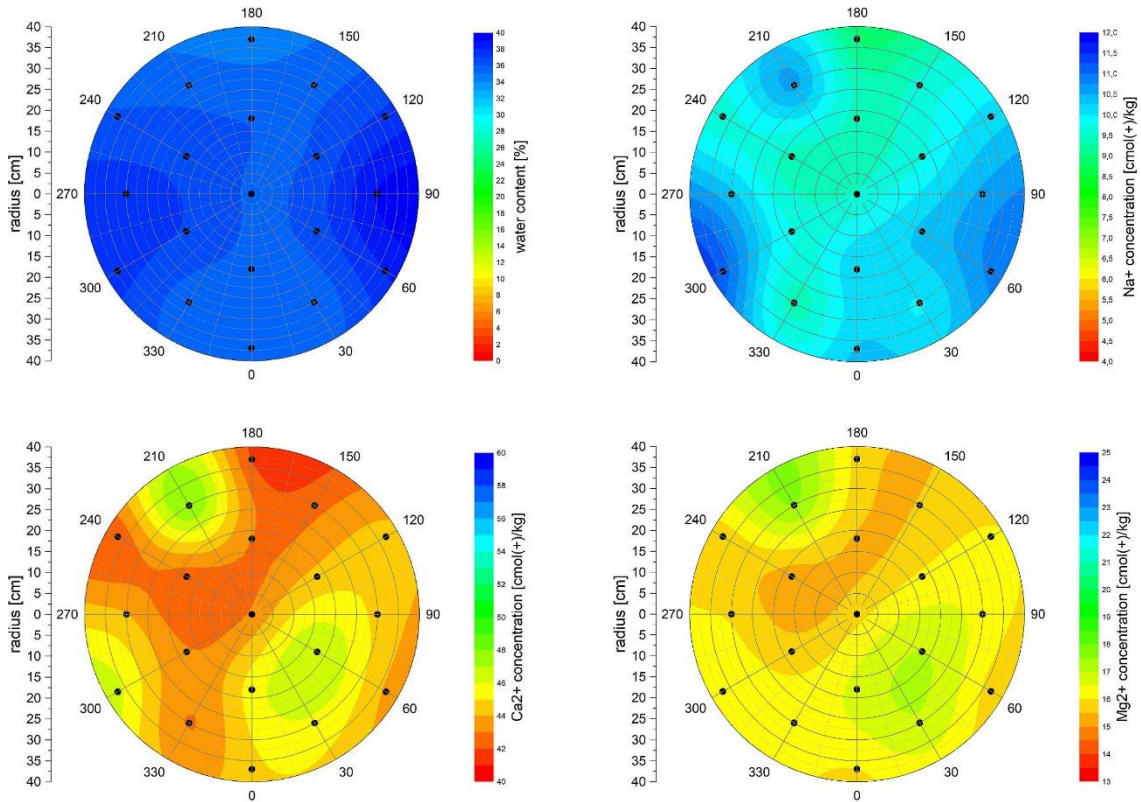


Figure 4.63 DS1/E18 upper left water content (240 °C), upper right: Na⁺, lower left Ca²⁺, lower right Mg²⁺

In DS2, distribution of all cations was more uniform, than in DS1 layer. It can be caused by effect of ES1 layer. This may be due to the effect of the ES1 layer. However, a higher distribution of Ca²⁺ cations in DS2 was observed in the E11 level (Fig. 4.65). A similar, but less significant trend was observed for Mg²⁺ cations, whereas Na⁺ and K⁺ cations were distributed almost homogeneously (DS2).

In the upper levels ED3 and ED4, the distribution of all cations was more uniform (DS2). Of all layers, the biggest inhomogeneity was observed in layer ED2 E13 for Ca²⁺ concentrations (max difference was 10.3 cmol(+)/kg). This may be caused by the simulated EDZ zone on left side of the column. In upper levels, inhomogeneities were insignificant.

Moisture distribution over the layers reflected the functionality of the Sandwich sealing system on the semi technical scale with Pearson water as liquid. Na⁺ and K⁺ cations followed moisture. The main exchangeable cations Ca²⁺ and Mg²⁺, by contrast, did not follow this trend, with a constant ratio in whole system. Migration of Ca²⁺, Mg²⁺ and Na⁺ cations was concluded from the increasing concentrations of these cations in ES1 and ES2. CEC was the same in all DS, which indicated the absence of or very slow changes in mineral composition of Calcigel during the experiment.

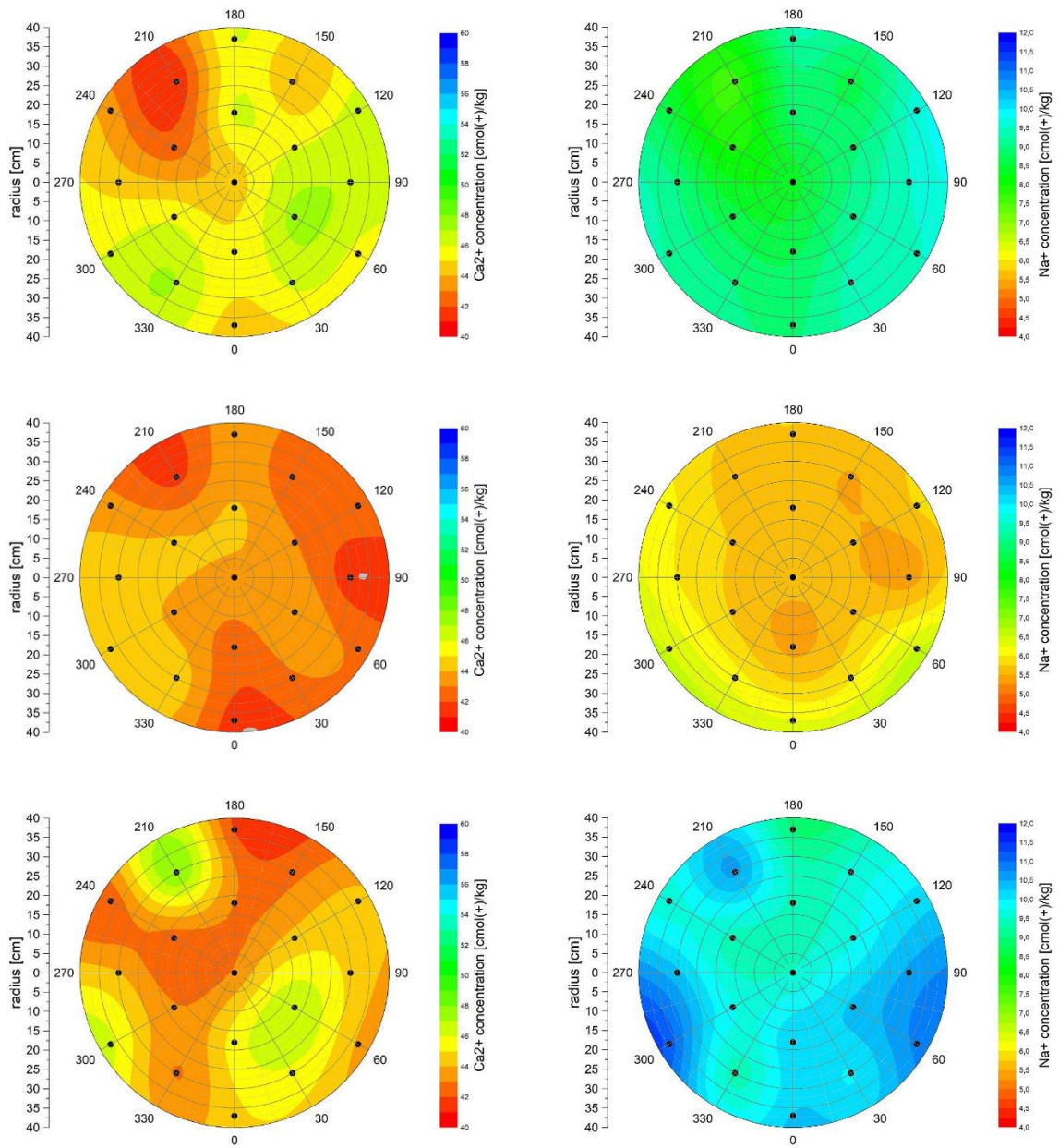


Figure 4.64 Ca²⁺ (left) and Na⁺ (right) distribution in DS1 (E18 to E16 from bottom to top)

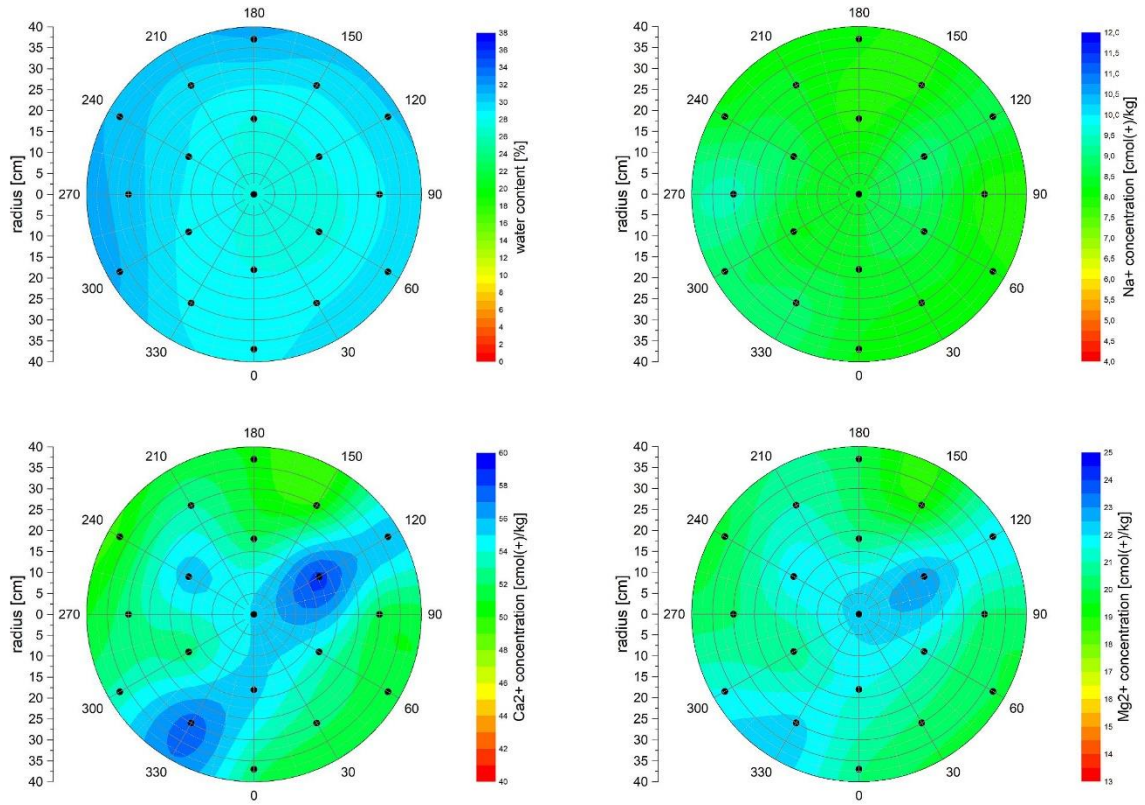


Figure 4.65 DS2/E11 upper left water content (240 °C), upper right: Na⁺, lower left Ca²⁺, lower right Mg²⁺

4.8.3 HTV-6

4.8.3.1 Experimental process

The experiment started on August 06, 2018 with the measurements in the initial state during installation. Afterwards the hydration started with 0.5 MPa (5 bar) fluid pressure. Fluid pressure was increased gradually to slightly above 9 MPa. The volume flow at constant final pressure decreased from 0.3 dm³/d (12.5 mL/h) at the beginning down to 0.08 dm³/d (3.3 mL/h) in the final stage (Fig. 4.66).

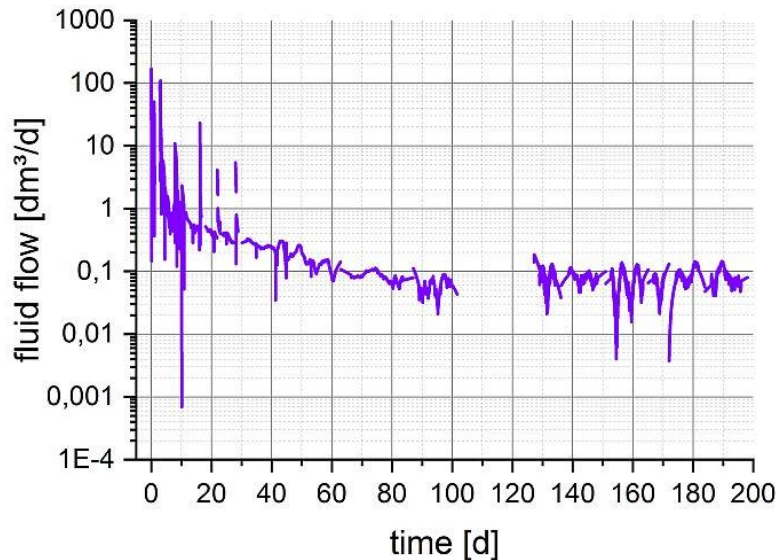


Figure 4.66 HTV-6 fluid flow

On day 127, the pump was replaced. After 198 days (February 20, 2019) since the start of the test, the inlet valve was closed and the pump switched off in order to be able to observe settling in the column during the pressureless phase. Dismantling began on the 200th day (February 22, 2019). A large number of samples were taken from all layers to determine the gravimetric water content for comparison of the results from the TDR measurements and for mineralogical and chemical analysis.

4.8.3.2 Pressure

Fluid pressure and temperature

The temperature varied between 32 °C at the beginning and 16 °C at the end of the experiment (Fig. 4.67). This variation was found to influence the pressure curve of the spherical pressure transducers (Fig. 4.67). It is unclear whether the influence has a direct effect on the pressure transducers or on the signal path.

After filling the pore volume of the lower gravel layer (approx. 39 kg) and connecting the high-pressure pump, no significant effect on the pressure sensors (Fig. 4.67) in the DS and ES was found at the low initial pressure of approx. 0.5 MPa (5 bar). In addition only a very small amount of fluid penetrated DS1.

In the middle of the third day, the pressure was increased to 1 MPa. On day four, the pressure was increased in steps to 1.5 MPa, 2 MPa and 2.5 MPa, which resulted in a fluid inflow of about 22 kg. With the next pressure increase to 3.5 MPa, another 9 kg of fluid entered the system in the course of four days. With increasing injection pressure the fluid uptake increased as follows. Day 8: 3.9 MPa / 75.4 kg, day 10: 4.8 MPa / 80.5 kg, day 16: 5.8 MPa / 87.2 kg,

day 22: 6.8 MPa / 91 kg, day 28: 7.7 MPa / 95 kg, day 121: 9.2 MPa (with a slight drop to 9 MPa on day 31) / 108 kg.

After 102 days, the diaphragm pump broke down. The pump could not maintain the fluid pressure of 9 MPa. It dropped to 5.2 MPa (Fig. 4.67). An immediate replacement of the pump was not possible. After 126 days, another pump was installed and the fluid pressure increased up to 9.2 MPa again. In the meantime, those technical difficulties influenced the processes of the experiment. After restoration of the fluid pressure, however, the stress regime was also restored in the system. Fluid inflow then increased to 114.3 kg until the end of the experiment (day 198).

At a constant pressure the plots of the total pressure sensors in the DS2 and DS3 revealed a conspicuous conformity with the temperature plot (cell-temperature). In the DS1, such a conformity did not occur (Fig. 4.67). This differences cannot be explained. The DS1 had a higher moisture content (higher degree of saturation) than DS2 and DS3, whereas the latter had a lower water content or were "dry". The total pressure plot exhibits a significant increase in pressure is visible in the DS2 after a run-time of 130 days.

Pressure development P1, P6 DS1

Due to the close proximity to fluid injection, the pressure sensor P6 in DS1 reacted immediately (Fig. 4.67), while P1 indicated a significantly lower pressure and failed completely on the 4th day at about 1.4 MPa. P1 showed slight increases as a result of the pressure increases, but these decreased, especially in the higher pressure range. Overall, P6 followed the fluid pressure.

Pressure development P2, P7 in DS2

In DS2, wall friction in the steel column (Fig. 4.67) significantly reduced the pressure. P7 approximately reproduced the fluid pressure at a level of about 50-60%. After the pump exchange there was a slight increase as a result of swelling in DS1. The effect was also observed for P2. Here, too, swelling pressure increased towards the wall, albeit at a level of around 3 MPa.

Pressure development P3, P8 in DS3

This development continued in DS3 (Fig. 4.67). The spherical pressure transducer P8 showed a slight pressure increase to 2.8 MPa after pump exchange, while P3 showed hardly any changes (1.1 MPa).

Pressure development P5 in DS4

The flat pressure cell P5 measuring axial pressure at the upper end of the column between DS4 and the gravel abutment followed the pressure development in DS3, but at a lower level (Fig. 4.67). The final pressure was about 1.5 MPa. Pressure reduction by wall friction against the fluid pressure was about 9 MPa (90 bar).

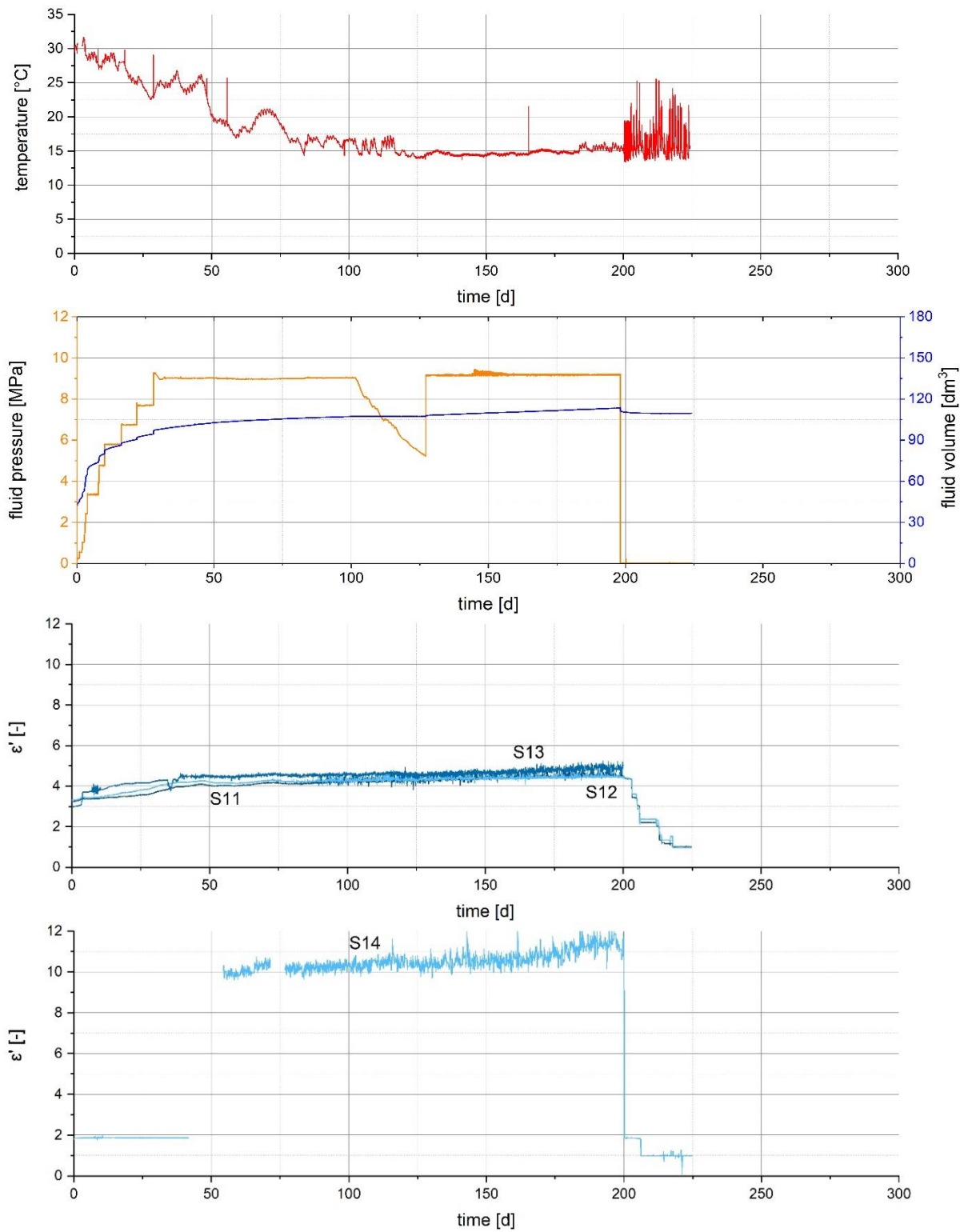


Figure 4.67 (from top to bottom): temperature; Pump pressure and fluid volume; effective dielectric permittivity vertical sensors; effective dielectric permittivity horizontal sensor

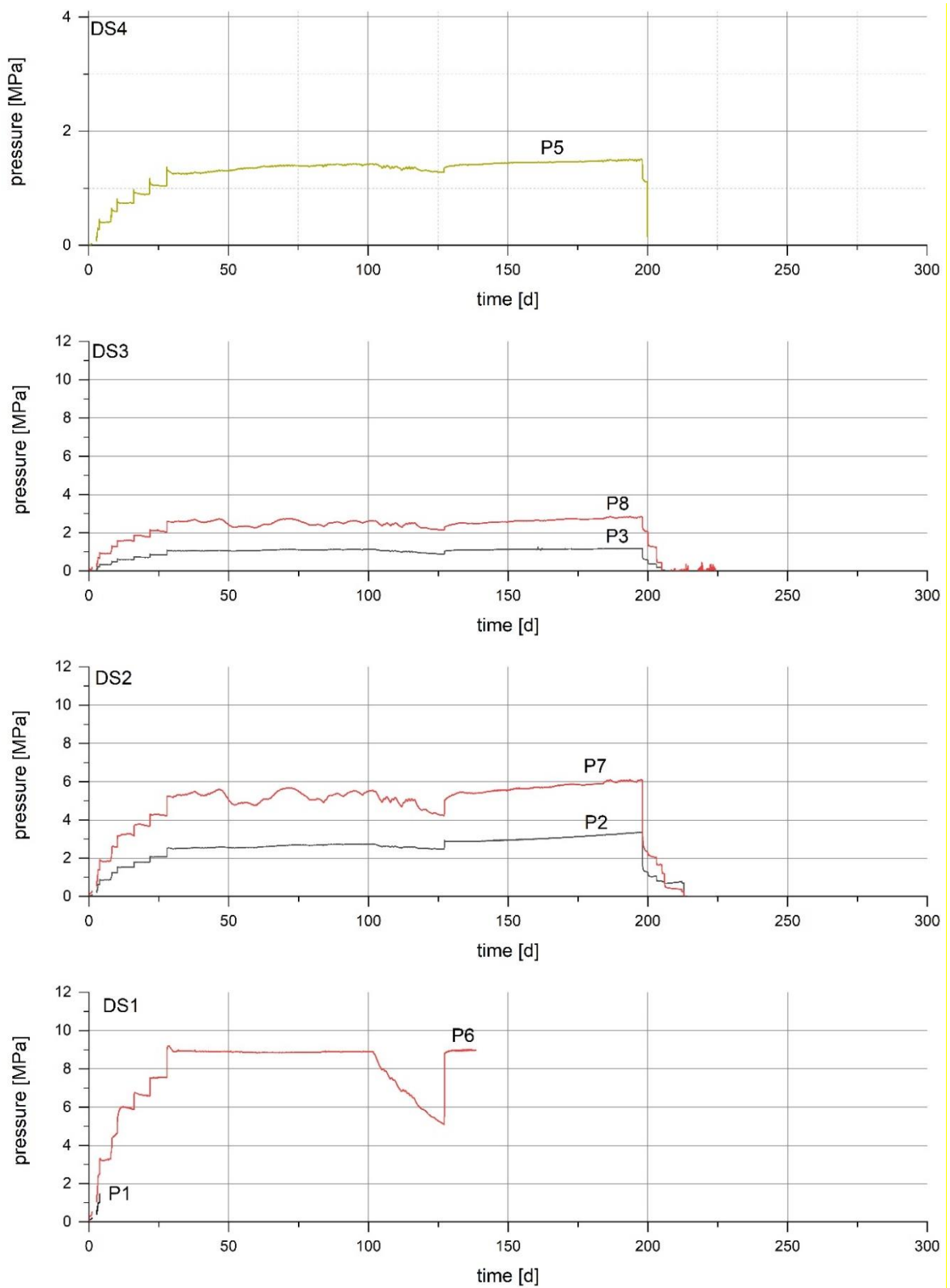


Figure 4.67 (continued) pressure sensor readings in DS of HTV-6 (from bottom to top DS1 to DS4)

4.8.3.3 Fluid propagation

Based on the initial water content of the DS and ES (Tab. 4.27) during installation, the integral value of the effective relative dielectric permittivity (ϵ') of the sandwich materials along the S11 and S13 sensors was about 3 to 3.5. The sequence of DS/ES materials along both sensors was very similar. Along S12, both DS1 and DS2 contained an additional sandy lens. The lower ϵ' of the sand compared to the bentonite led to a lower integral ϵ' along S12 compared to S11/S13. After applying the Pearson water, ϵ' only increased very slowly, but the pressure increased to 2.5 MPa, which resulted in a breakthrough of the fluid along S13 into the sandy lens SL1. Only a small amount of fluid reached ES1. A significant increase of ϵ' to about 3.7 was observed. With increasing pressure an increase in hydration of DS1 followed, but without any further filling of ES1. The resulting swelling pressure in DS1 ensured that the sealing effect was already fully built up there. This is also shown by the high total pressure of over 3 MPa, which affected the upper layers. Until the end of the experiment, ϵ' only increased slightly for the three sensors.

On day 198, the pump was switched off and the ball valve at the inlet was closed. For another two days, the HTV-6 remained in this state to observe a possible influence of the absent pressure load. Until the start of dismantling, i.e. the removal of the upper steel cover, no influence was recognizable. After dismantling was completed, the sensors for ϵ' showed the value of air ($\epsilon' = 1$). Any deviations were due to slight differences in sensor manufacturing.

The sensor S14 was located in the middle of ES2, completely embedded in fine sand N45 with ϵ' being about 2 (Fig. 4.67).

In the course of the experiment, it became obvious that the electronics in the multiplexer had been pre-damaged (see HTV-5). The contact resistance of the S14 plug probably had been increased, which led to a considerable change in signal amplitude and signal quality. This was reflected by a significant jump in the effective relative dielectric permittivity ϵ' from 2 to about 10. Interestingly, the value dropped back to the initial value during dismantling and to ϵ' of air (≈ 1) after removal of the sensor. Therefore, the sensor reading for ϵ' might not be reliable. This was confirmed by the water content data after dismantling (chapter 4.8.3.5).

Application of the differential TDR method

Due to the restriction of moisture propagation to DS1, no evaluation using the dTDR method was made for HTV-6.

4.8.3.4 Dismantling

HTV-6 was dismantled in the same way as HTV-5 from February 22, 2019 to March 12, 2019. Samples were taken in 18 levels (3 in each DS and 2 in each ES) by applying a special grid (Fig. 4.56) starting with level E1 at the top of DS4 down to E18 at the bottom of DS1. The number of samples in the upper ES3 and DS4 was reduced to 3 samples per level (E5-E1). During dismantling, any changes in position and thickness of the DS and ES layers were determined again, which enabled determination of densities of the individual layers in the final stage of the experiment.

Approximately 200-300 g of material were collected at each point of the grid (Fig. 4.68) and dried at 105 °C (ES and DS) until a constant mass was reached. Afterwards the temperature was increased to 200 °C (DS) until the weight was constant again. A vacuum cleaner was used to remove the sandy material of the ES at the interface to a DS.



Figure 4.68 HTV-6 Samples for water content measurement

4.8.3.5 Water content and density

The bentonite in DS1 was saturated and the dry density of DS1 decreased from 1.54 g/cm^3 to 1.27 g/cm^3 due to swelling (Tab. 4.29 & 4.31). Fluid transport out of the DS1 was limited. The lower level (E13) of DS2 was hydrated (Fig. 4.69 & 4.70). The water content in DS2 decreased in upward direction. The sandy lens in the DS2 was dry. DS2 moved upwards by 5.2 cm and the swelling of DS1 compacted DS2 (from dry density of 1.52 g/cm^3 to 1.67 g/cm^3). Swelling of DS1 and compaction of DS2 with low saturation produced different fabric (Fig. 4.71).

Water contents of DS3 and DS4 increased by 0.2-0.3% only due to water absorption from the air. Both sealing layers DS3 and DS4 were compacted (DS3 from a dry density of 1.53 g/cm^3 to 1.63 g/cm^3 and DS4 from a dry density of 1.55 g/cm^3 to 1.58 g/cm^3). The water content and the dry density of ES2 and ES3 were unchanged (Tab. 4.31).

Table 4.31 Average water contents and salt contents in the levels after termination of HTV-6

Layer	Level	Material	W	W	Saturation	Dry density	Change in height
			(105 °C)	(240 °C)			
			[%]	[%]		[g/cm ³]	[cm]
	E1	Secursol UHP	11.9	14.5	0.53		
DS4	E2	Secursol UHP	12.0	14.5	0.53	1.58	-0.5
	E3	Secursol UHP	11.9	14.3	0.53		
ES3	E4	N45	0.04		0.00	1.58	0.0
	E8	N45	0.03		0.00		
	E6	Secursol UHP	12.4	14.9	0.59		
DS3	E7	Secursol UHP	12.5	15.0	0.59	1.63	-1.4
	E8	Secursol UHP	12.3	14.9	0.59		
ES2	E9	N45	0.04		0.00	1.60	-0.2
	E10	N45	0.04		0.00		
	E11	Secursol UHP	12.4	14.9	0.63		
DS2	E12	Secursol UHP	13.9	16.5	0.69	1.67	-2.1
	E13	Secursol UHP	18.6	21.5	0.90		
ES1	E14	N45	1.05		0.04	1.56	-0.1
	E15	N45	1.24		0.04		
	E16	Secursol UHP	36.0	39.4	0.92		
DS1	E17	Secursol UHP	46.2	49.7	1.17	1.27	5.3
	E18	Secursol UHP	55.8	59.0	1.38		

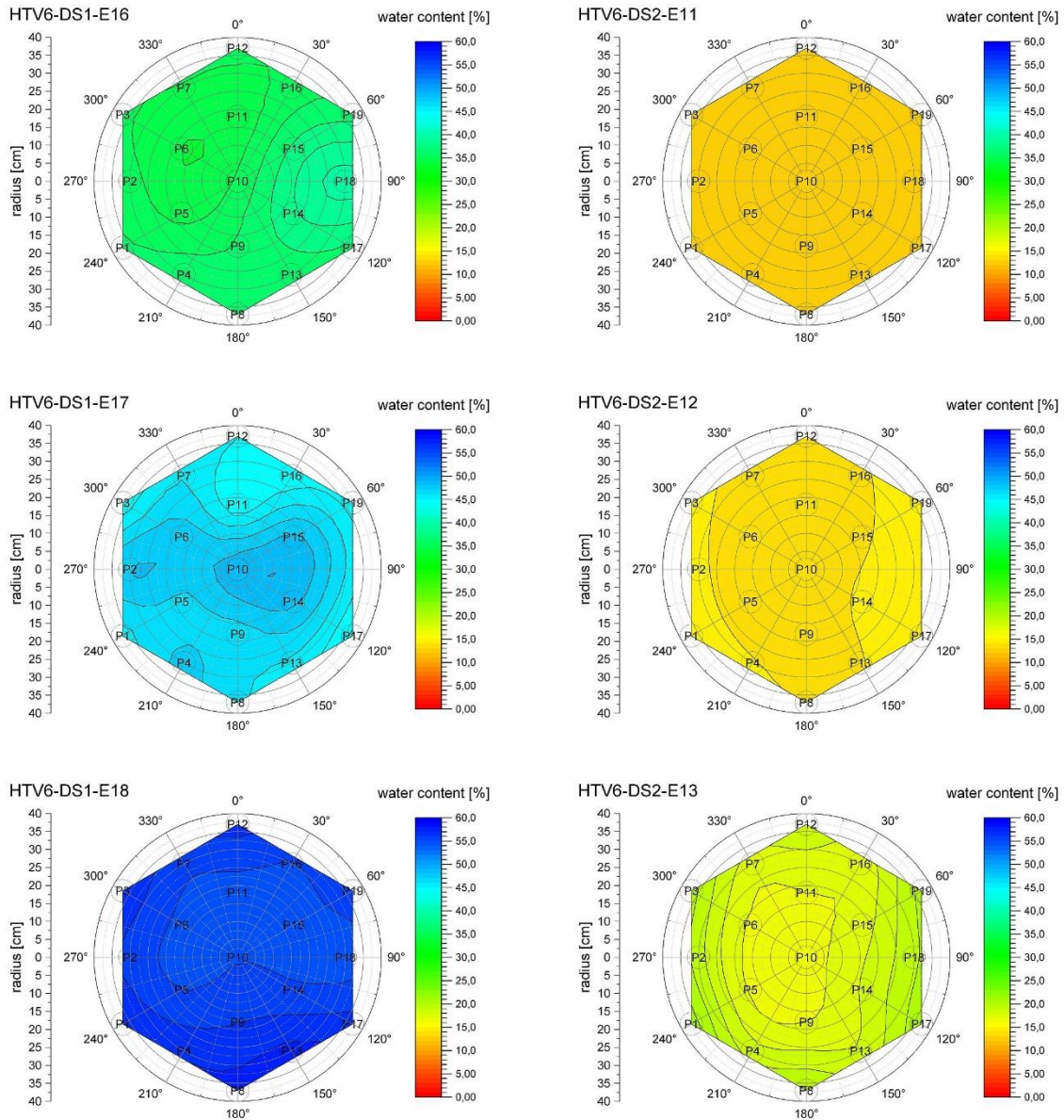


Figure 4.69 Water content distribution in DS 1 (left with E18 to E16 from bottom to top) and in DS2 (right with E13 to E11 from bottom to top)

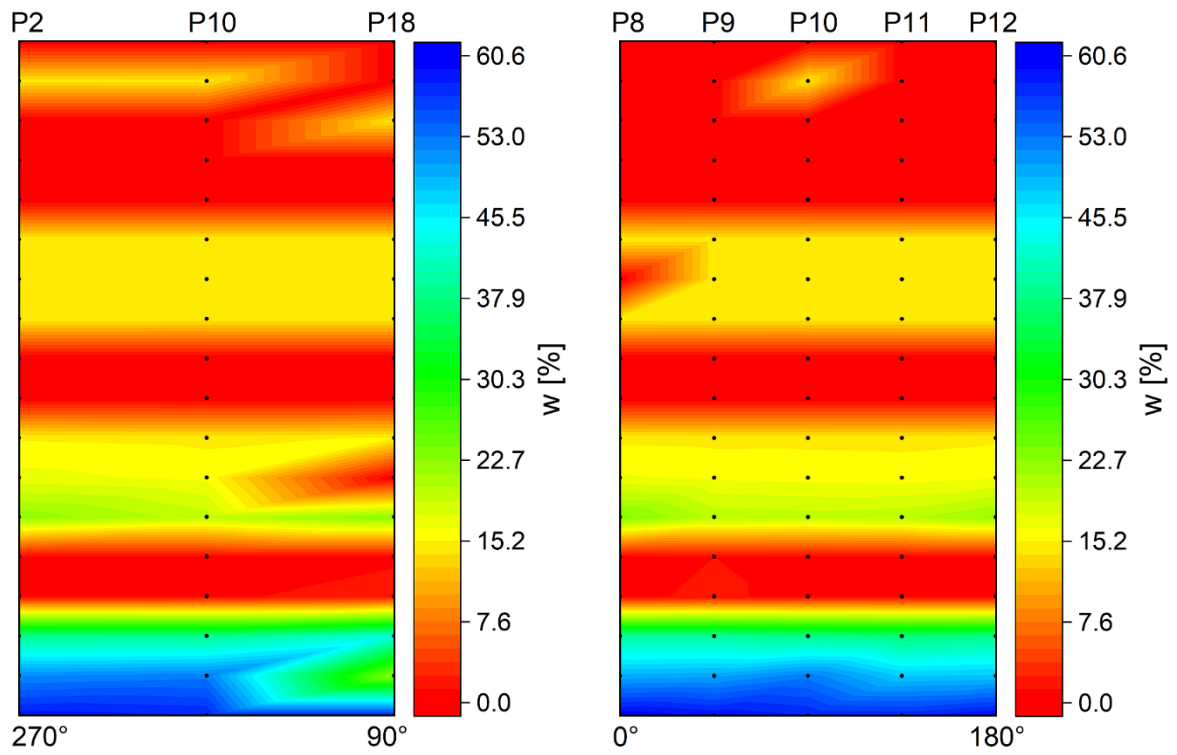


Figure 4.70 Water content distribution in HTV-6 (cross section: left 270°-90°, right: 0-180°)



Figure 4.71 Lower level of DS2 (E13), close to the hydraulic circuit (left) Compaction in DS1 (right)

5 Experiment design (WP5)

5.1 Dimension

The vertical sealing system based on the Sandwich principle will be investigated in interaction with the surrounding Opalinus clay rock. The planned large-scale experiment features two experimental shafts equipped with seal systems (Fig. 5.1).

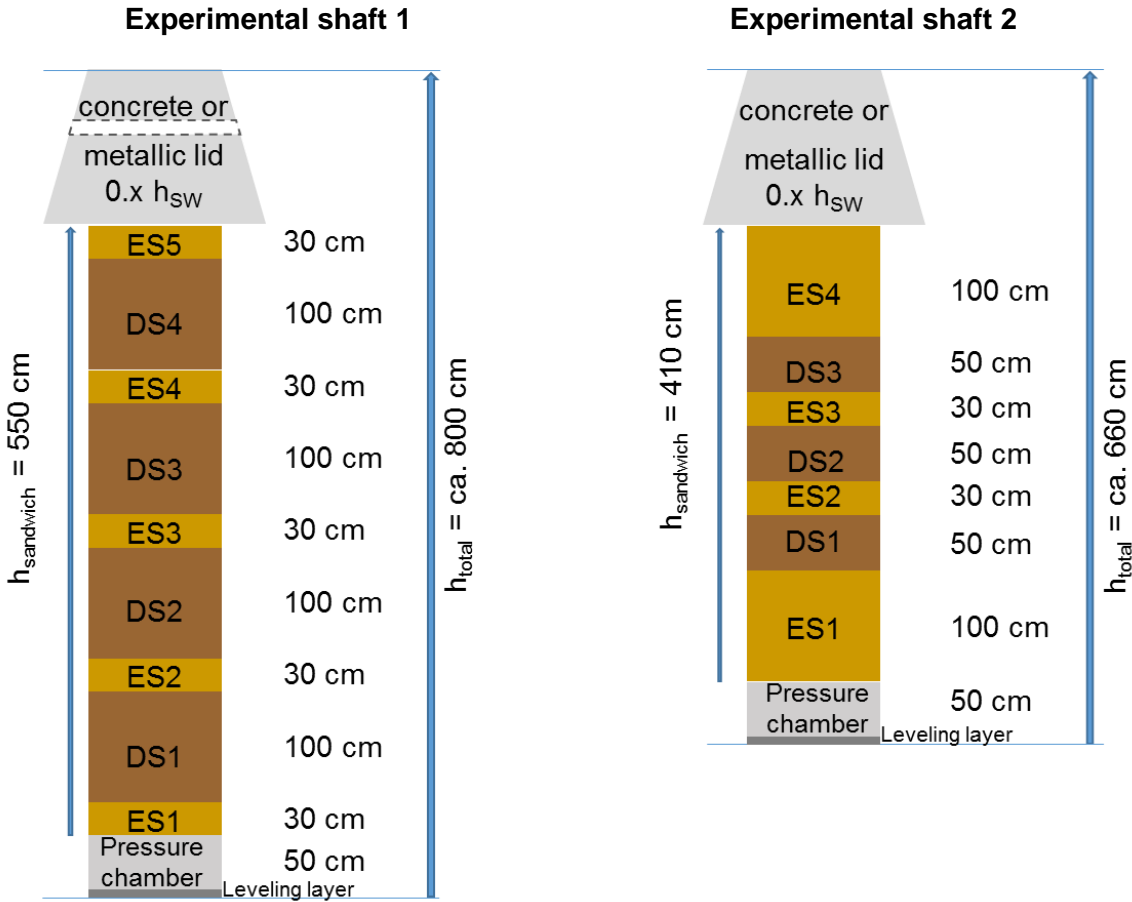


Figure 5.1 Layout of the sealing systems in the experimental shafts

The Sandwich sealing system in shaft 1 will consist of four DS sandwiched with five ES. Calcigel will be used for the DS in the in-situ experiment due to the results of swelling pressure measurements (chapter 4.6) with Pearson water. Fracturing of the Opalinus clay (envisaged pore pressure of 2 MPa against a fracturing pressure of 4.2 MPa) will have to be prevented. The swelling pressure must not exceed the minor principal stress of 3 MPa (Wermeille and Bossart, 1999) and will have to be adjusted via the dry density and water content of the bentonite during installation.

A fine sand (N45) with a water content in the air dry state of < 1% will be used for the ES. The Proctor density of fine sand is about 1.7 g/cm³. In the air dry state an installation density close to 1.6 g/cm³ could be obtained in HTV-5 and HTV-6.

The shafts and the surrounding rock will be instrumented, and the hydro-mechanic evolution of the complete system will be monitored (chapter 8). Installation with instrumentation and operation is described in detail in the test plan of Sandwich HP (Amberg, 2019).

5.2 Hydration system

Artificial hydration will be performed with Pearson water type A3 (Table 5.1, Pearson, 1998) from pressure chambers at the bottom of both shafts. Pearson water will be doped with fluorescein (tracer).

Table 5.1 Composition of Pearson water type A3 (pH = 7.9)

Salt	[g/L]	Ion	[mmol/L]
NaCl	6.13	Na ⁺	128
KCl	0.06	K ⁺	0.81
MgCl ₂	0.47	Mg ²⁺	4.94
CaCl ₂	0.77	Ca ²⁺	6.94
SrCl ₂	0.05	Sr ²⁺	0.32
Na ₂ SO ₄	1.63	Cl	130
NaHCO ₃	0.05	SO ₄ ²⁻	11.5
		HCO ₃ ⁻	0.60

The conceptual design of the hydration system is based on the results of the RESEAL II project and the HTV experiments. Fluid injection will be performed from pressure chambers (one for each shaft) at the bottom of the experimental shafts. A pump or a pressurized reservoir (vessel) will provide the fluid pressure through an inclined feeding borehole. The expected fluid injection pressure is 30 bar (3 MPa) at the maximum and should be kept as constant as possible, given that the fluid uptake of the seal is expected to be as low as 0-25 mL/h when increasing DS saturation. The injection system will be mounted in a dry area of the niche and its expected operation time will be 4 to 10 years. The final selection of the injection system will be made based on the performance/cost balance of the methods. The installation of a back-up hydration system in the main shaft is planned. The back-up hydration system consists of a hydraulic short-circuit simulating an enhanced EDZ in DS2. For this purpose, an arc of fine sand will be installed along the shaft wall. Furthermore, a vertical tube (stainless steel) that ends at the top of ES3 will be installed. Depending on the hydration progress, fluid injection from the top and fluid distribution within ES3 and ES2 can be initiated (Figure 5.2). A lockable tube through the plug ending at the top of ES5 will enable de-airing of the Sandwich sealing system.

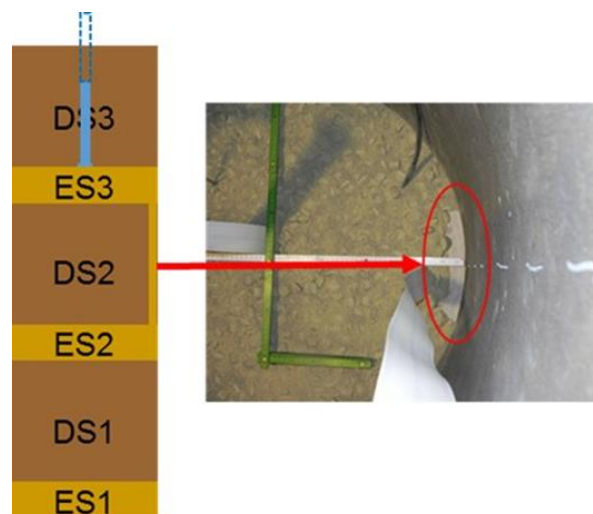


Figure 5.2 Back-up-hydration system in shaft 1

6 Scoping calculations (WP6)

Scoping calculations for the in-situ Sandwich sealing experiment were performed by three modeling teams with different codes and different approaches to gain complementing results for the planning and execution of the experiment.

6.1 Simulations using Code_Bright (GRS)

The Code_Bright (Polytechnic University of Catalonia, 2017) simulations started with a simplified geometrical model using a homogeneous rock and preliminary dimensions for the shafts and neglecting Gallery 08. Later, the geometry was refined as the planning progressed, the hydraulic effect of Gallery 08 was included, different facies of the Opalinus clay were considered, and coupled hydraulic-mechanical (HM) simulations were performed. Since the more refined simulations widely confirmed earlier results, only the full model is presented here.

6.1.1 Geometrical model

The geometrical model features the three facies of Opalinus clay: shaly, sandy, and carbonate-rich, the planned dimensions of Gallery 18 with the Niches 7 and 8 and of the experimental shafts, and part of Gallery 08 (dimensions from laser scans). The inner part of the model is shown in Figure 6.1.

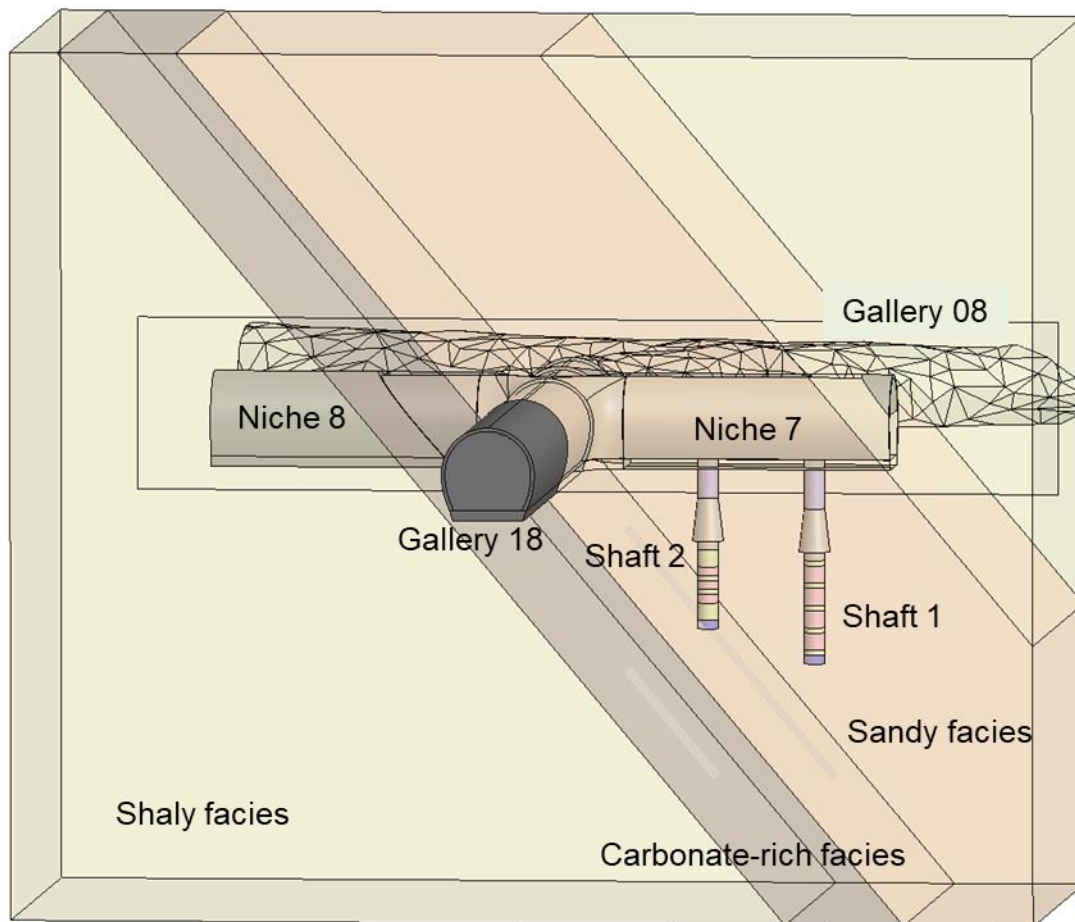


Figure 6.1 Inner part of the geometrical model

The complete model had a size of 100 m x 160 m x 150 m (depth by width by height) and was meshed with about 70 000 nodes and more than 400 000 tetrahedral elements (Figure 6.2).

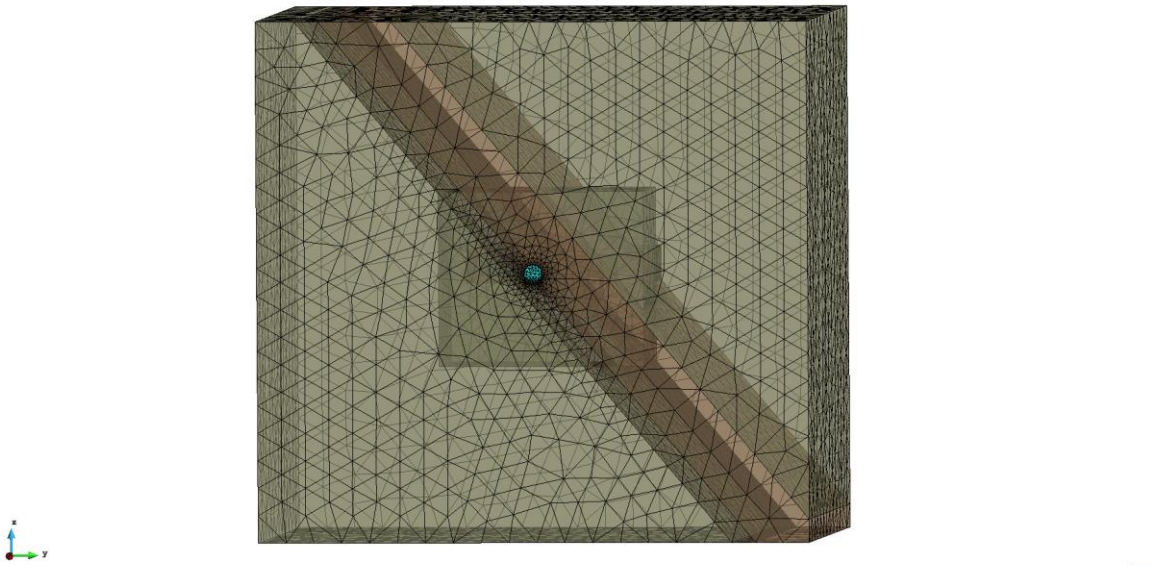


Figure 6.2 Complete meshed model of the Sandwich Niche 7, the neighboring openings, and the surrounding Opalinus clay

6.1.2 Physical model

The different facies of Opalinus clay, the concrete of the gallery lining and the abutment in the shafts, as well as the ES were modelled as ideally elastic isotropic materials. For the bentonite of the DS, the thermo-elastoplastic (TEP) model of Code_Bright (Polytechnic University of Catalonia, 2017) which is an extension of the Barcelona Basic Model (BBM) for partly saturated soils (Alonso *et al.*, 1990) was used. This model allows for nonlinear elastoplastic behavior and moderate swelling.

From the hydraulic point of view, it is assumed that liquid flow follows Darcy’s law, with the actual effective permeability to each phase being given by the product of intrinsic and relative permeability. The dependence of intrinsic permeability *k* on porosity ϕ (eq. 6.1) is given by

$$k = k_0 * \frac{\Phi^3}{(1 - \Phi)^2} * \frac{(1 - \Phi_0)^2}{\phi \Phi_0^3} \tag{6.1}$$

with initial values k_0 and ϕ_0 . Swelling of the constrained material leads to porosity decrease which affects intrinsic permeability according to eq. 6.1. The relative permeability of the liquid phase is dependent on the degree of liquid saturation (eq. 6.2), where S_r , S_{lr} , S_{ls} , S_e are the actual, residual, maximum and effective saturation of liquid, respectively, and *A* and β are parameters. Gas pressure is assumed to be atmospheric all the time, which means that gas is moving freely through the system.

$$S_e = \frac{S_r - S_{lr}}{S_{ls} - S_{lr}} \quad \text{with} \quad k_{rl} = A * S_e^\beta \tag{6.2}$$

It is necessary to define the retention curve of the materials that relates the degree of saturation to suction pressure (suction pressure is the independent variable in Code_Bright; saturation is a function of suction pressure). Generally, the formulation of van Genuchten with material parameters λ , P_0 and σ_0 is selected (eq. 6.3, see also eq. 4.14).

$$S_e = \left[1 + \left(\frac{P_g - P_l}{P} \right)^{1/(1-\beta)} \right]^{-\beta} \quad \text{with} \quad P_g - P_l \geq 0 \quad \text{and} \quad P = P_0 * \frac{\sigma}{\sigma_0} \quad (6.3)$$

P_0 is the pressure measured at a certain temperature, and σ_0 is the related surface tension.

The molecular diffusion of vapor is governed by Fick's law (eq. 6.4), a constant dispersion coefficient corresponding to the molecular diffusion of vapor in air is assumed. P_g is given in MPa. For the tortuosity τ a value of 1.0, for n a value of 2.3 and for D a value of $5.9 \cdot 10^{-6}$ m²/s are adopted.

$$D_m^w = \tau D * \left(\frac{(273.15 + T)^n}{P_g} \right) \quad (6.4)$$

6.1.3 Material data

The elastic and hydraulic material data used for the simulations are compiled in Table 6.1. The data for the Opalinus clay sandy facies represent preliminary results from the LT-A experiment, the corresponding report is under preparation. The carbonate-rich facies was modelled with the same parameters as the sandy facies, since no representative data are available. The parameters for the Opalinus clay shaly facies, the concrete, and the hydraulic DS parameters were taken from the database compiled for the HE-E experiment (Gaus *et al.*, 2014). The mechanical bentonite parameters for the TEP model were also taken from (Gaus *et al.*, 2014), although the HE-E experiment involved MX-80 bentonite. It is assumed that for the scoping calculations, these parameters were close enough to the actual DS parameters which are not available yet. The elastic moduli for ES originally were the values given by Hahn and Wagner (1986) for sand at low confining pressure. It was, however, found that a Young's modulus of originally 300 MPa was too low, which is why this value was increased to 1000 MPa. The hydraulic parameters for ES were the N45 parameters determined in this project (chapter 4.3). For some simulations, an excavation damaged zone (EDZ) around the shaft was assumed. The EDZ has an intrinsic permeability increased by two orders of magnitude; the remaining parameters are those of the undisturbed sandy facies.

The galleries feature a shotcrete lining of 60 cm thickness on the floor and 15 cm thickness on the walls and the roof. The concrete material parameters are also shown in Table 6.1.

Table 6.1 Elastic and hydraulic material data

		OPA shaly facies	OPA sandy facies	DS	ES	Concrete	Unit
Linear elasticity	E	3000	4500	***	1000	27000	MPa
	ν	0.29	0.2	***	0.245	0.35	
	Φ_0	0.137	0.095	0.44	0.41	0.15	
Retention curve	P_0	12	8	22.4	0.3	15	MPa
	σ_0	0.072	0.072	0.072	0.072	0.072	Nm ⁻¹
	λ	0.3	0.35	0.359	0.861	0.31	
	S_{rl}	0.01	0.01	0.01	0	0.01	
	S_{ls}	1.0	1.0	1	1	1.0	
	Φ_0	0.137	0.095	0.44	0.41	0.15	
Intrinsic permeability	$(k_{11})_0$	$2 \cdot 10^{-20}$	$2 \cdot 10^{-20}$	$1 \cdot 10^{-20}$	$1 \cdot 10^{-11}$	$1 \cdot 10^{-20}$	m ²
	$(k_{22})_0$	$2 \cdot 10^{-20}$	$2 \cdot 10^{-20}$	$1 \cdot 10^{-20}$	$1 \cdot 10^{-11}$	$1 \cdot 10^{-20}$	m ²
	$(k_{33})_0$	$2 \cdot 10^{-20}$	$2 \cdot 10^{-20}$	$1 \cdot 10^{-20}$	$1 \cdot 10^{-11}$	$1 \cdot 10^{-20}$	m ²
	Φ_0	0.137	0.095	0.44	0.41	0.15	
Liquid phase relative permeability	A			1			
	β			3			
	S_{rl}			0.01			
	S_{ls}			1.0			
Diffusive flux of vapor	D			$5.9 \cdot 10^{-6}$			m ² /s*K*Pa
	n			2.3			
	τ_0			1.0			
Solid phase density	ρ_s	2700	2700	2750	2650	2650	kg/m
Liquid phase density	ρ_{l0}			1000			kg/m
	γ			$4.5 \cdot 10^{-4}$			1/MPa
	P_{l0}			0.1			MPa

6.1.4 Simulation variants, schedule, and boundary conditions

A HM-coupled simulation assuming an undisturbed rock around the shafts was performed. Since HM-coupled modeling led to stability problems at increasing saturation of the DS (the coupled simulation stopped after 4380 days), another two purely hydraulic simulations were performed: one assuming an undisturbed rock around the shafts again and another featuring an EDZ of 0.1 m width and an intrinsic permeability increased by two orders of magnitude around shaft 1. This assumption was consistent with the simulation of BGR (chapter 6.2.3).

In all cases, ventilation of galleries or shafts is simulated by applying a suction pressure of -2 MPa on the surface, which leads to a slight progressing desaturation of the originally entirely saturated shotcrete and the rock close to the opening. An overview of the different steps of each simulation specifying the respective initial conditions and boundary conditions is given in Table 6.2 (mechanical stress is negative for compression). Fig. 6.3 shows a plan view of the model, explaining the different phases of excavation mentioned in the table.

Table 6.2 Simulation schedule

Time [d]	Action	Conditions
0	Start of simulation with newly excavated Gallery 08	No normal displacement and no flow on model boundaries Initial pore pressure 2 MPa Initial stress -7 MPa/ -4.2 MPa/ -3 MPa (vertical / parallel Niche 7 / parallel Gallery 18) Suction pressure of -2 MPa on Gallery 08 surface simulating ventilation
3600	Excavation Gallery 18 East and niches	Remove elements inside Gallery 18 East and niches
3610	Shotcrete Gallery 18 East and niches	Create shotcrete liner elements Suction pressure of -2 MPa on Gallery 18 East and niches surface (ventilation)
3850	Excavation Gallery 18 West	Remove elements inside Gallery 18 West
3860	Shotcrete Gallery 18 West	Create shotcrete liner elements Suction pressure of -2 MPa on Gallery 18 West surface (ventilation)
4160	Construction of shafts	Remove elements inside shafts, apply suction pressure of 2 MPa to shaft wall Create material elements in shaft 1 Remove ventilation in both shafts (shaft 2 is equipped with a lid)
4250	Shafts 3 months open, construction of seal in shaft 1	Initial porosity/saturation/suction pressure: DS: 0.44/0.4/-111 MPa ES: 0.41/0/-2 MPa
4280	Resaturation injection chamber shaft 1	Apply 0.1 MPa pore pressure in chamber
4290	Chamber at 1 MPa injection pressure	Increase pore pressure in chamber to 1 MPa
4320	Chamber at 2 MPa	Increase pore pressure in chamber to 2 MPa
4350	Chamber at 3 MPa	Increase pore pressure in chamber to 3 MPa
6000	End of simulation	

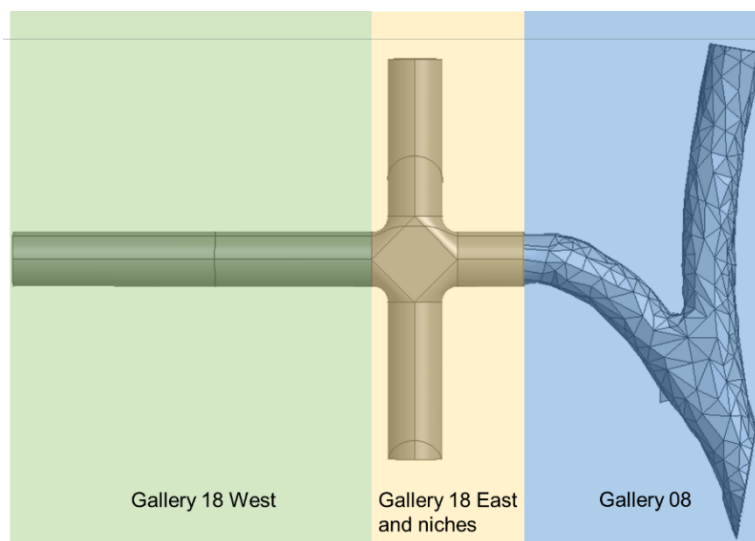


Figure 6.3 Excavation phases

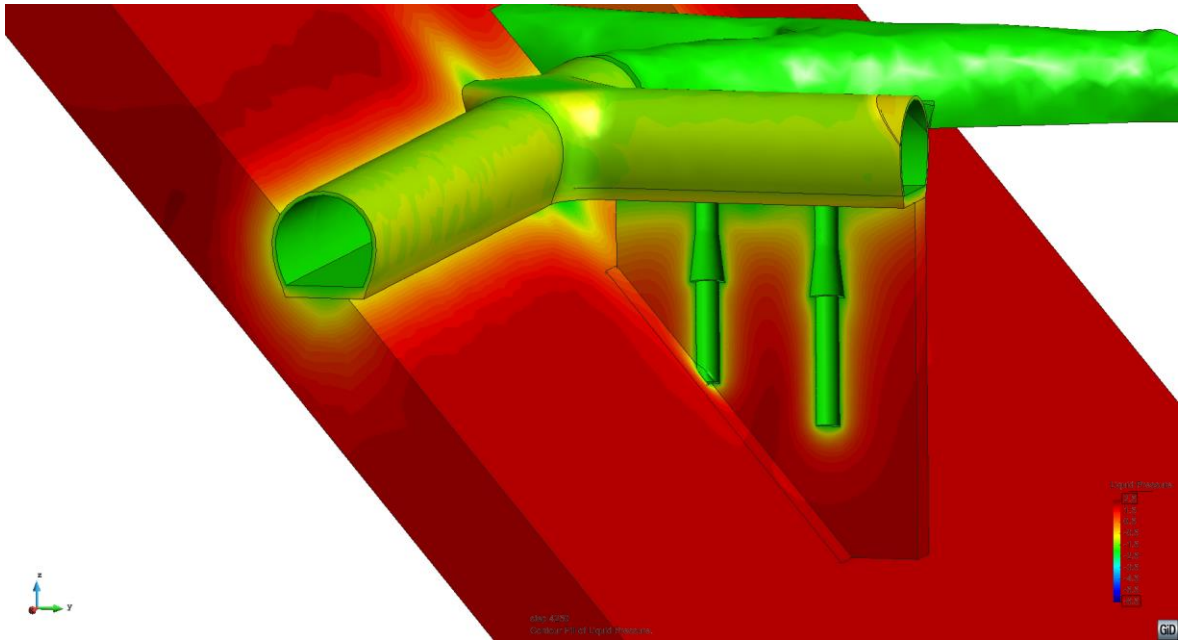


Figure 6.5 Pore pressure distribution before Sandwich seal emplacement in shaft 1

The saturation distribution at the same time is shown in Fig. 6.6. This is a non-smoothed representation (saturation is calculated for each element) which gives clearer results, but looks somewhat ragged. Saturation remains above 0.96 (96%) near the shaft surface. In the regions of positive pore pressure, saturation obviously is at 100%.

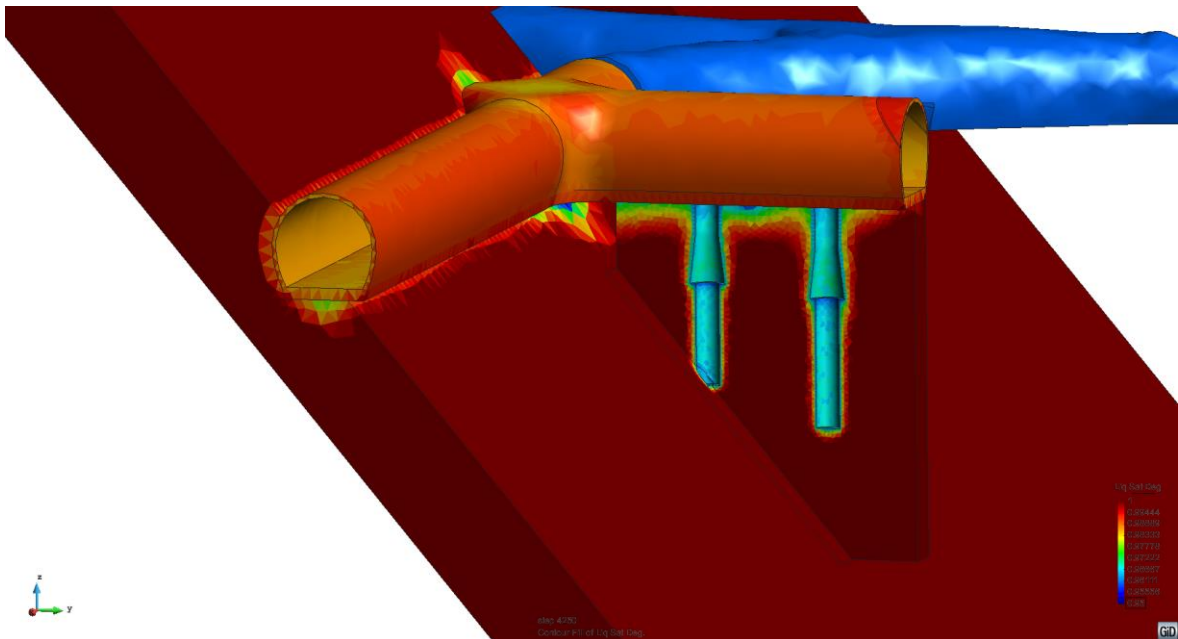


Figure 6.6 Saturation distribution before Sandwich seal emplacement in shaft 1

Finally, minimum mechanical stress is shown in Fig. 6.7. Tensile stresses (positive values) occur in the shotcrete of the galleries. Around the shafts, compressive stress is reduced, but there is no tensile stress. Between the shafts, a minimum stress of -3 MPa remains.

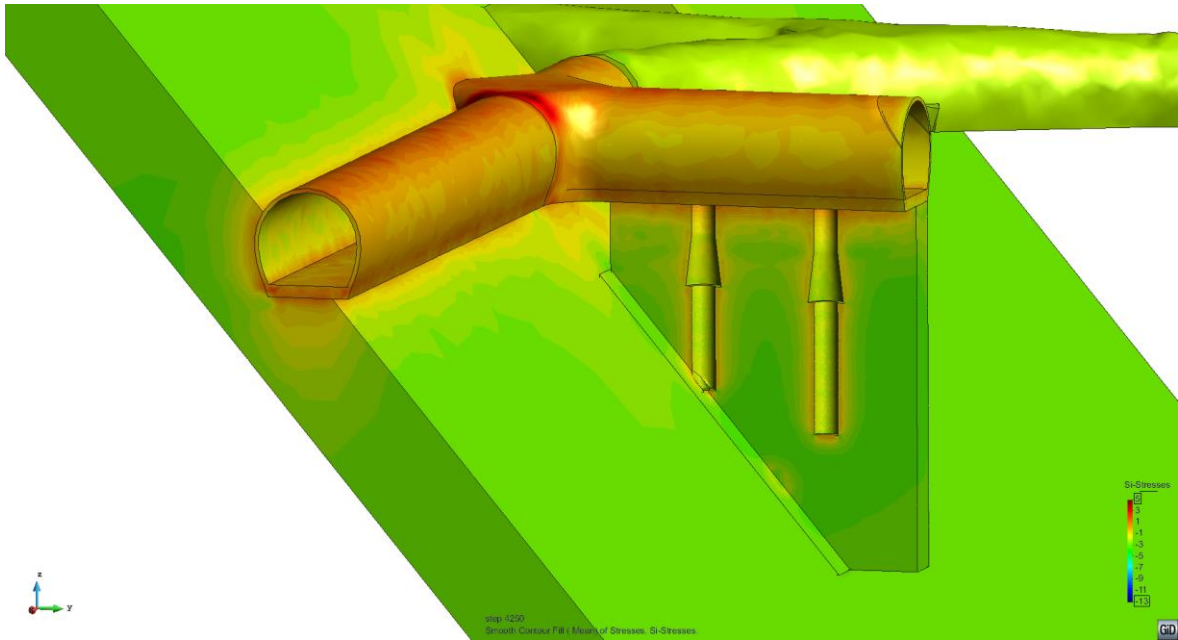


Figure 6.7 Minimum stress distribution before Sandwich seal emplacement in shaft 1

6.1.5.3 Situation after pressurizing the injection chamber

The pore pressure distribution in and around shaft 1 is shown in Fig. 6.8 for the time points of 10 days after seal emplacement (day 4250) and 130 days after seal emplacement (day 4380), when water has been injected into the pressure chamber for 100 days. The figure scale is from -3.5 MPa to 3.5 MPa, therefore the DS emplaced with a suction pressure of -111 MPa are black. In the ES and concrete abutment, the suction pressure is -2 MPa at the time of emplacement. A suction pressure region is found to spread from the shaft wall into the rock, because the DS bentonite takes up water from the rock due to its high suction pressure. Further away, the pore pressure in the rock also decreases slowly.

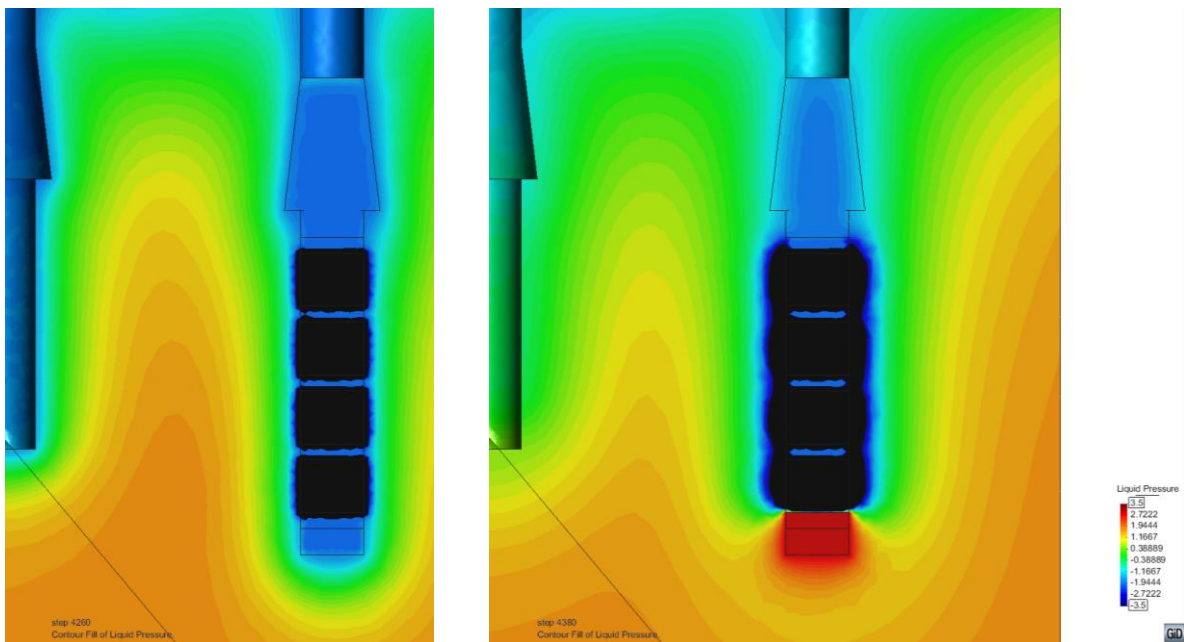


Figure 6.8 Pore pressure distribution close to shaft 1: 10 days after seal emplacement (left) and 130 days after seal emplacement (injection chamber at 3 MPa; right)

The corresponding figures in terms of saturation are given in Fig. 6.9. The DS are emplaced at 40% saturation, the ES at zero saturation. Already ten days after emplacement a water exchange from the rock to the DS bentonite can be observed (Fig. 6.9 left). After 130 d a thin zone with a saturation above 70% has developed in the ES close to the shaft wall, while saturation in the adjacent rock zone goes down below 60% (Fig. 6.9 right). The injection chamber and the ES directly above are saturated, but the ES above the lowermost DS remain dry due to their low suction pressure. Resaturation from the borehole wall is nearly as fast as from the injection chamber, showing that resaturation is governed by the bentonite suction pressure and not by injection pressure.

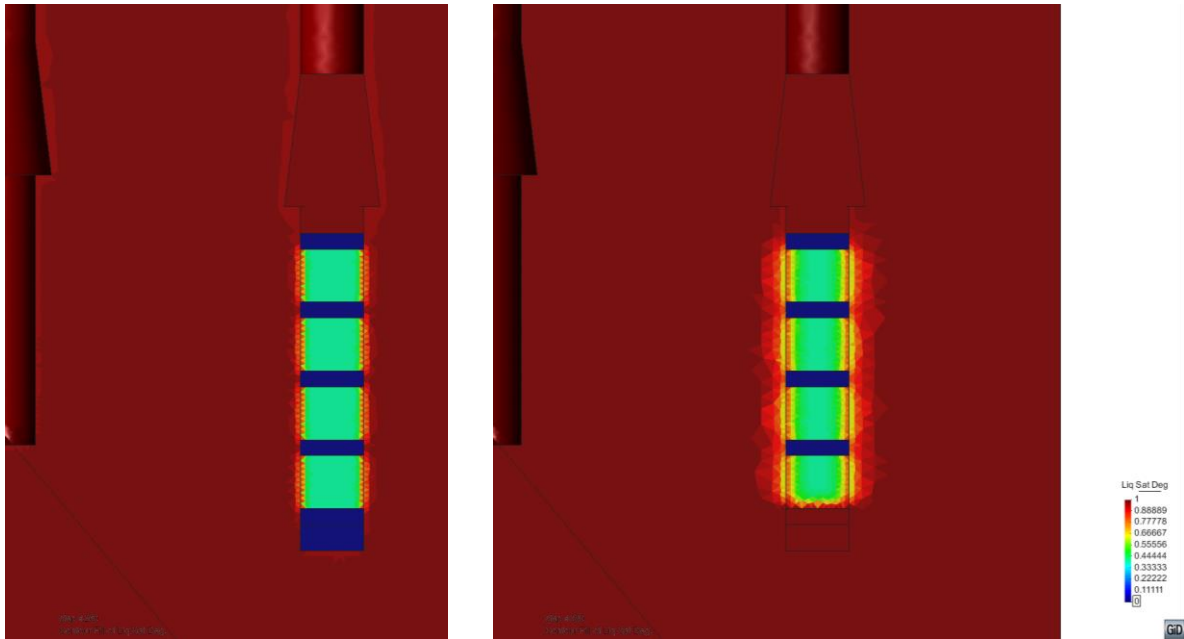


Figure 6.9 Saturation distribution close to shaft 1: 10 days after seal emplacement (left) and 130 days after seal emplacement (injection chamber at 3 MPa; right)

6.1.5.4 Further evolution (hydraulic simulation)

Since HM coupled simulation became unstable after 4380 days due to problems of convergence of the TEP model, additional purely hydraulic simulations were performed: one with the same conditions as the HM simulation, the other introducing an EDZ around shaft 1. Fig. 6.10 shows the saturation distribution of the two models on day 4380, 130 days after seal emplacement. For the case without EDZ (Fig. 6.10, left), the saturation distribution is very close to the HM simulation (Fig. 6.9, right). The EDZ around the shaft (right hand side in Fig. 6.10) leads to more water passing the seal elements, as a result of which the rock saturation near the shaft wall is slightly higher. Liquid pressures in the rock are not shown here. They are somewhat lower than for the HM coupled simulation, because the effect of compressive stress is neglected here.

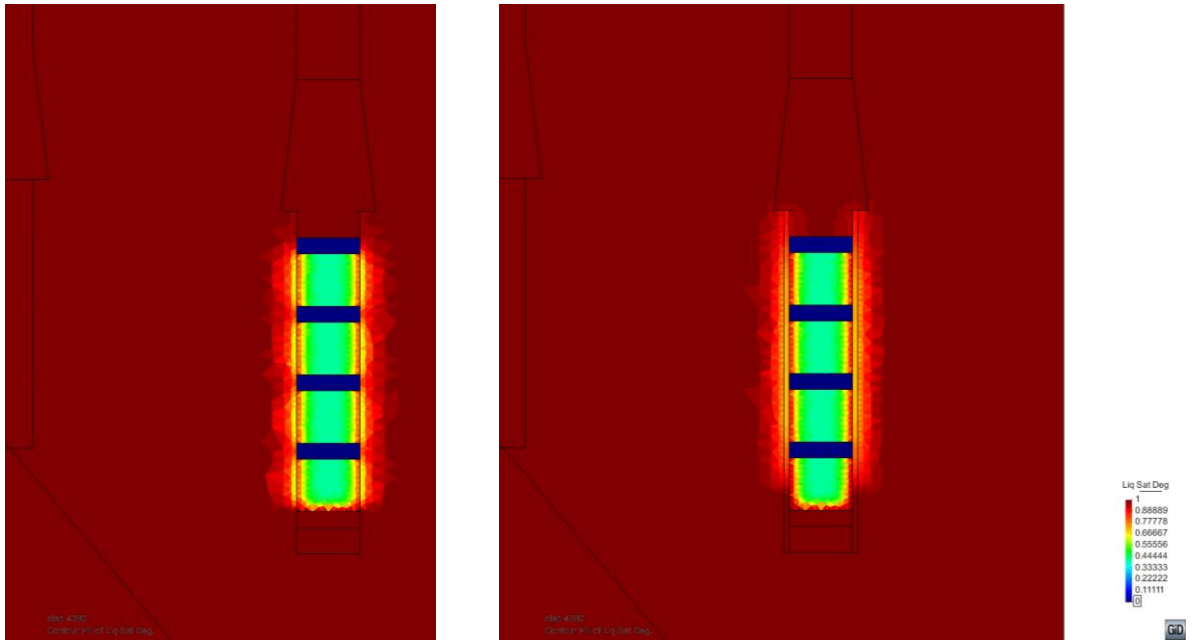


Figure 6.10 Saturation distribution close to shaft 1: 130 d after seal emplacement (day 4380), without (left) and with (right) EDZ around shaft 1

The two models were also used to predict seal resaturation. It is understood that this cannot be a completely realistic simulation, because the mechanical effects, especially bentonite swelling pressure evolution, are neglected. It is expected that resaturation time will be longer in reality. HM coupled simulations need to be extended as soon as possible. Fig. 6.11 and 6.12 show the saturation distributions of the two models for day 5000 and day 6000. Progressing resaturation is visible in both models. The EDZ around shaft 1 leads to an acceleration of the process.

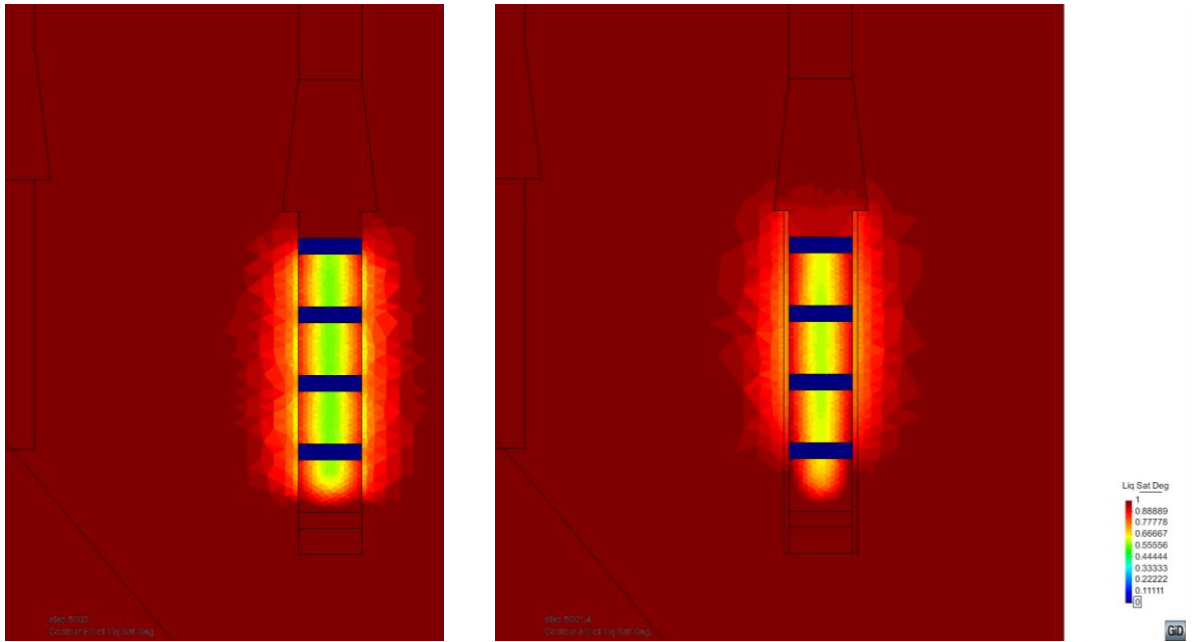


Figure 6.11 Saturation distribution close to shaft 1 on day 5000, without (left) and with (right) EDZ around shaft 1

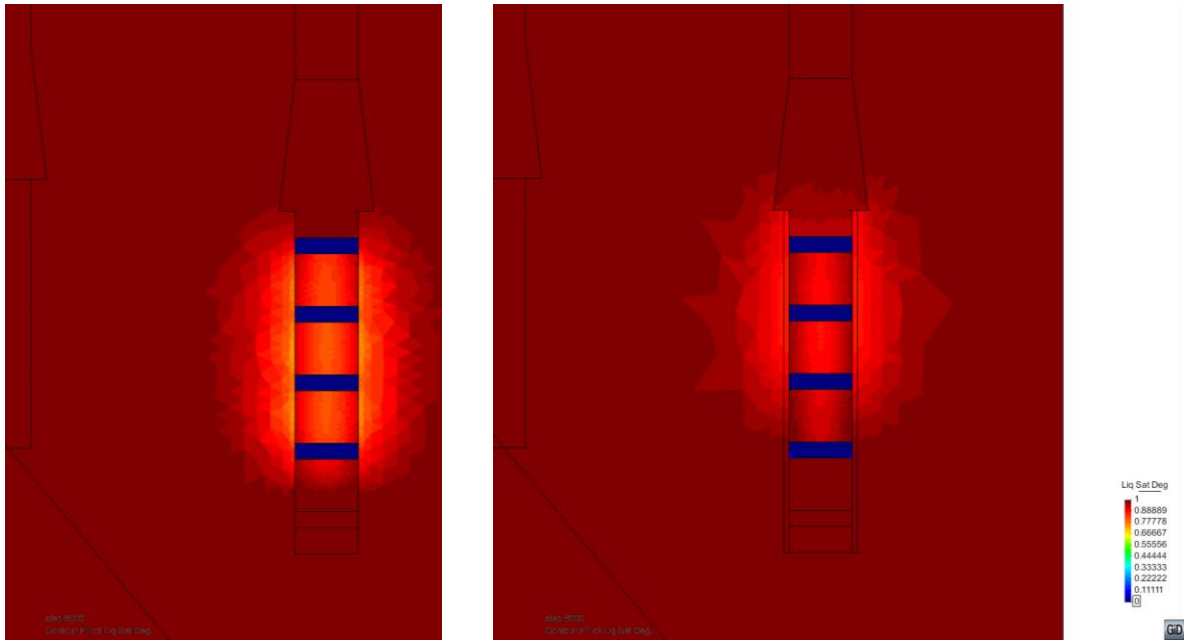


Figure 6.12 Saturation distribution close to shaft 1 on day 6000, without (left) and with (right) EDZ around shaft 1

6.1.6 Perspective

The first step in future simulations will be to overcome the stability problems with the TEP model and extend the HM-coupled simulation. In Sandwich-HP, advanced models for bentonite will be employed, e.g., UPC's double porosity model (BExM) which is better suited for describing swelling of bentonite. We will resort to research results of the ongoing EC project Beacon (Beacon, 2017). If available, also advanced material models for the claystone will be considered, as well as material anisotropy. The results of the simulations will be compared to measurements and material behavior will be interpreted.

6.2 OGS simulations (BGR)

Within the pre-project SW-A, modeling exercises were performed by the BGR using the finite element code OGS (Kolditz *et al.*, 2012) jointly developed by UFZ (Environmental Research Centre, Leipzig) and BGR. The objectives of these exercises were to optimize the experimental design for the in-situ test at the Mont Terri Rock Laboratory, to understand the process interaction between ES and DS, to determine the system parameters of the sandwich layout, and to estimate the experiment duration.

6.2.1 Scoping calculations for in-situ experimental design

In order to place both boreholes in the same geological unit (sandy facies) with comparable hydraulic conditions (initial water saturation and pore pressure) in the test section, where sandwich elements ES and DS are emplaced, design calculations were made to optimize the length of each borehole and the distance between boreholes in the planned two-shaft concept. Three models of the test site Niche 7 (Fig. 6.13) were built taking into account different geological units (shaly/sandy/carbonate facies and EDZ) and technical features (shotcrete and boreholes). All parameters were taken from literature and measurements (Tab. 6.3). The hydraulic and mechanical anisotropies of the geological units were considered in all models. Two variations were studied for a shaft diameter of 1.2 m:

1. Shaft length 10 m / distance between boreholes 9.5 m, and
2. Shaft length 15 m / distance between boreholes 5 m.

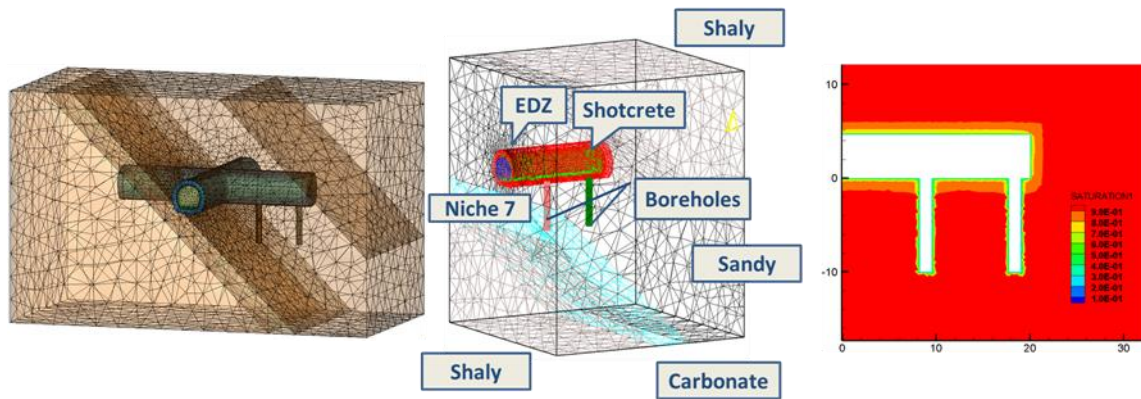


Figure 6.13 Three models used for the numerical analysis of the unsaturated zone: large-scale site model with Niches 7 and 8 (left), detailed model with Niche 7 only (middle) and simplified two-dimensional model for a conservative estimation (right).

Table 6.3 Main hydraulic and mechanical parameters used

No	Material	Permeability [m ²]	Porosity [-]	E-modulus GPa	Poisson's ratio [-]	Comments
0	Sandy clay	$10^{-20}/2 \cdot 10^{-21}$	0.13	12.6/3.6	0.35	Plischke (2014)
1	Tunnel (sandy)	$10^{-20}/2 \cdot 10^{-21}$	0.13	12.6/3.6	0.35	
2	Shotcrete	10^{-19}	0.13	20	0.35	FE-C (VSH)
3	EDZ	10^{-18}	0.25	8.1	0.35	$(E_{ } + E_{\perp})/2$
4	Carbonate clay	$10^{-20}/2 \cdot 10^{-21}$	0.13	12.6/3.6	0.35	Anal. Sandy
5	Shaly clay	$10^{-20}/2 \cdot 10^{-21}$	0.13	7.4/2.4	0.35	Plischke (2014)
6	Borehole 1	10^{-18}	0.4	6.3/1.8	0.35	For sealing
7	Borehole 2	10^{-18}	0.4	6.3/1.8	0.35	Case

In both variations, an excavation of the niche with an opening phase of two years and a drilling of the shafts with an experimental period of 60 d were simulated. Calculation using the conservative 2D model shows that a desaturated zone around Niche 7 can have an extension of 2 m after two years. The zone with a lower pore pressure than the initial one can be even larger. Therefore, the test section for the sandwich seal should be located at a depth of about 5 m, where the same conditions for testing the sandwich seal in both shafts prevail. A desaturated zone around the experiment shaft after drilling may have an extension of 1 m, so that the distance between two shafts has to be at least 2.5 m.

6.2.2 Determination of Sandwich parameters using data from the MiniSandwich test

To understand the coupled processes in the Sandwich sealing system including multiple ES and DS elements, and to determine the system parameters, data from a MiniSandwich test (Oe8) (chapter 4.7.1) were evaluated using a 2D axisymmetric model (Fig. 6.14).

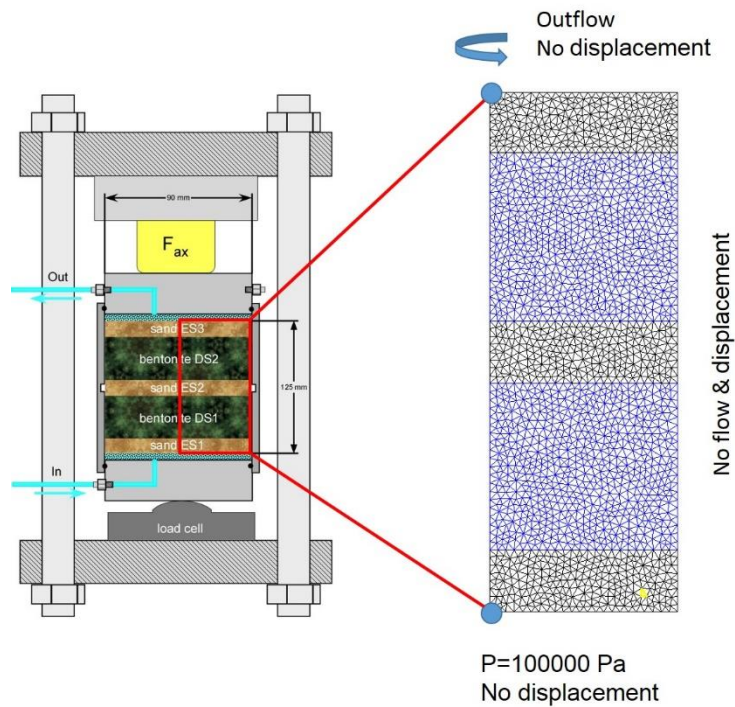


Figure 6.14 OGS mesh of a MiniSandwich test (Fig. 4.38)

An important coupled process in the Sandwich system is the swelling deformation of the DS element while water penetrates (Fig. 6.15). Consequently, pore space of the DS element decreases by swelling strain, which leads to a reduction in permeability of the DS. Pore space of the ES element decreases by swelling stress from the adjacent DS element. This compaction process additionally leads to a reduction in permeability of the ES element. To describe these processes, a linear swelling model and an empirical permeability-strain function are introduced in the coupled hydromechanical model with Richards' flow and elasticity. The van Genuchten function fitted with the laboratory data of a bentonite (Rizzi *et al.*, 2012) was used to describe the retention behaviors of the DS element with a high suction capacity. The basic parameters are summarized in Tables 6.4 and 6.5.

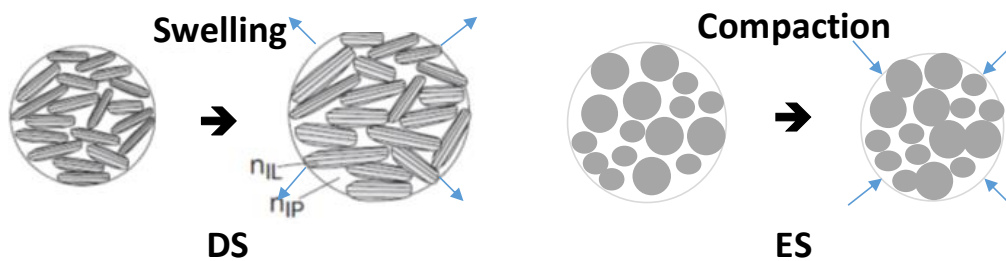


Figure 6.15 Coupled processes in the Sandwich sealing system

More than 20 runs were performed with variations of eight main parameters including permeability for both DS and ES, entry pressure, maximum swelling stress, Young's modulus, Poisson ratio and the permeability-strain functions for both DS and ES. In all runs, no perfect fitting to the measured data was achieved. However, a characteristic trend for both curves (axial stress and total inflow volume) can be obtained using the suggested model. When considering an offset of 40 mL, which may be explained by the system volume in the

experiment setup, a perfect fitting of the calculated inflow to the measured one can be obtained (Fig. 6.16).

Table 6.4 Basic hydraulic parameters of the sandwich elements

Parameter	Unit	DS	ES	Comments
Permeability	[m ²]	6.44*10 ⁻¹⁸	5.00*10 ⁻¹⁴	Tab. 4.26 and variation
Porosity	[-]	0.44	0.4	Tab. 4.26/Tab. 6.1 and variation
Relative permeability		vG	vG	Data from Rizzi <i>et al.</i> , 2012
Permeability-strain		linear	linear	empirical
Entry pressure	[MPa]	9	0.1	Sand assumed
vG shape factor	[-]	0.5	0.5	Fitting van Genuchten (vG)
Residual saturation	[-]	0	0	assumed
Maximum saturation	[-]	1	1	assumed

Table 6.5 Basic mechanical parameters of the sandwich elements

Parameter	Unit	DS	ES	Comments
Young's modulus	[GPa]	1.50*10 ⁻¹	3.00*10 ⁻¹	DS analog to MX80/ES from http://www.geotechnicalinfo.com/youngs_modulus.html
Poisson's ratio	[-]	0.42	0.35	Tab. 6.1 and variation
Biot number	[-]	0.6	0.6	assumed
Bishop coefficient	[-]	1.4	1.4	assumed
Max. swelling stress	[MPa]	3.5	0	Chapter 5.1

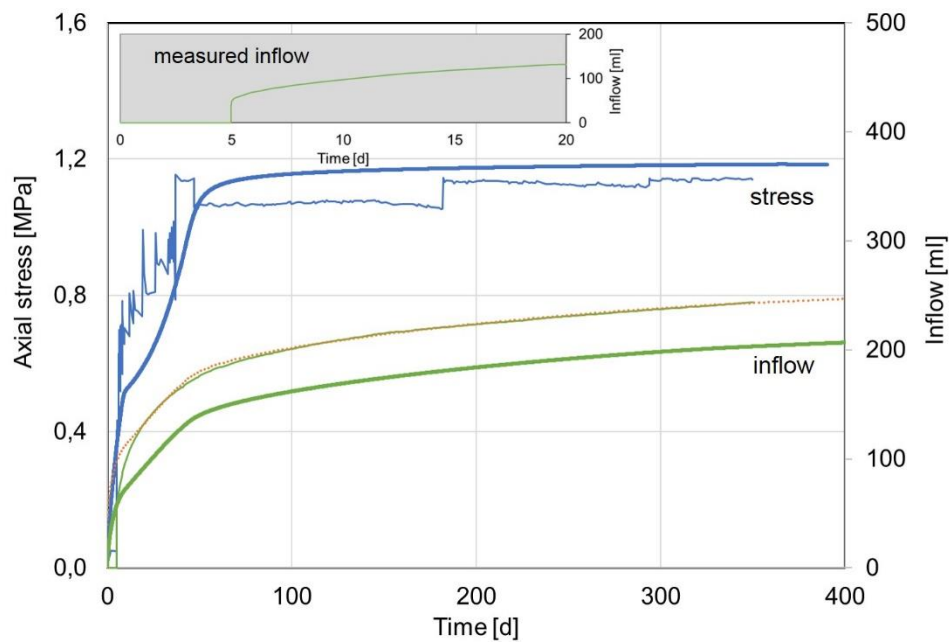


Figure 6.16 Interpretation of the MiniSandwich test (Oe8) (orange: calculated inflow with offset 40 mL)

6.2.3 Estimation of in-situ test duration under different test conditions

An upscaling exercise from the MiniSandwich to the in-situ test with 4 DS, each with a length of 1 m, and 5 ES, each with a length of 30 cm, was performed (Fig. 6.17). The objective of this exercise was to estimate the test duration under different test conditions.

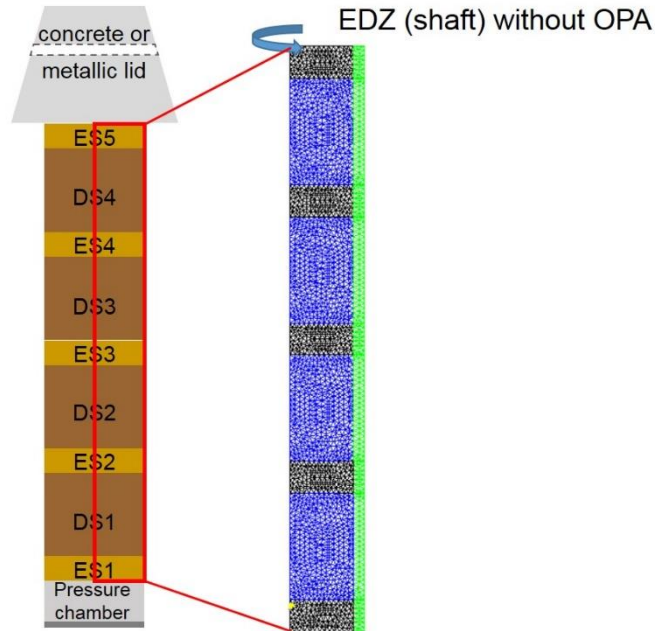


Figure 6.17 Model for experimental shaft 1 (chapter 5.1)

Three injection pressures 0.5, 1, 2 MPa (5, 10, and 20 bar) were used, and also the permeability of the EDZ around the borehole was varied. The results show that the saturation time of the entire Sandwich system is not dependent on the injection pressure, but on the permeability of the EDZ. If the permeability of the EDZ in the continuum model is assumed to be 10^{-18} m^2 , a fully saturated state will be reached in 85 a (Fig. 6.18).

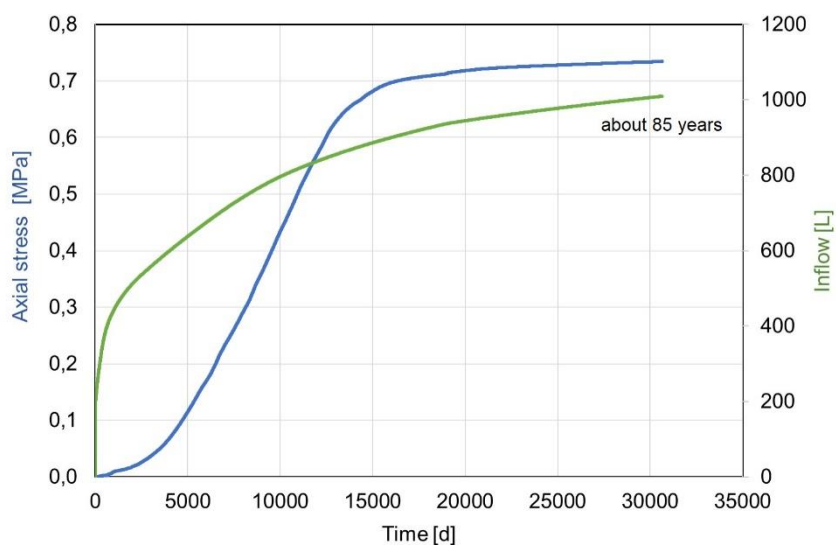


Figure 6.18 Results of modeling shaft 1 with chosen set of parameters

The maximum axial stress at the top of the Sandwich will be 0.75 MPa. If the permeability of EDZ is increased by one order of magnitude, a fully saturated state will need only 12 a. It is therefore important to determine the permeability of the EDZ around the boreholes. Permeability measurement on the borehole contour using the BGR surface packer prior to the installation is planned in the site characterization program.

6.3 COMSOL simulation (ENSI)

ENSI conducted first generic scoping calculations employing a 3D model using the Richards equations for unsaturated flow. Mechanical effects were not considered. The initial model domain had dimensions of 160 m x 160 m x 80 m (Fig. 6.19) and included the sandy and shaly facies of Opalinus clay. The Opalinus clay material parameters were those given in Table 6.1 (chapter 6.1.3).

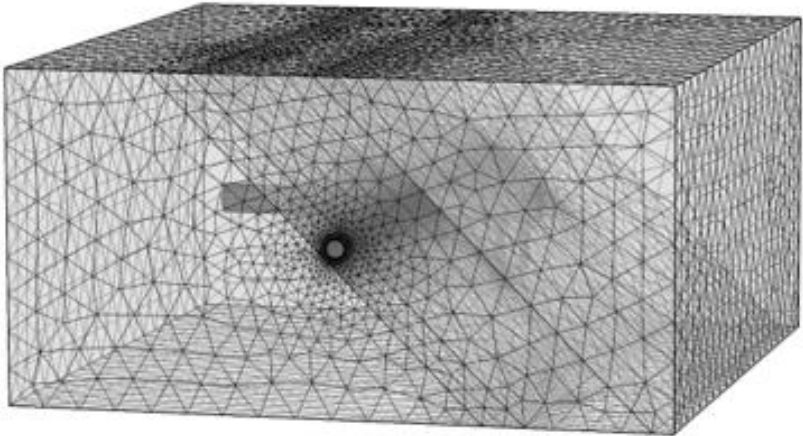


Figure 6.19 Complete meshed model domain

Between the two vertical shafts a distance of 5 m was assumed. An excavation damage zone with an extension of 1 m was implemented. Atmospheric conditions were applied to the tunnel and borehole boundary surfaces. The history of tunnel and borehole excavation and hence the initial desaturation of the rock mass in the tunnel vicinity were neglected in this first model run. The simulations for the evolution of water pressure and saturation were conducted for the first five years. As an example, the resulting pore pressures caused by desaturation through the open boreholes after 2 and 5 a are shown in figures 6.20 and 6.21, respectively.

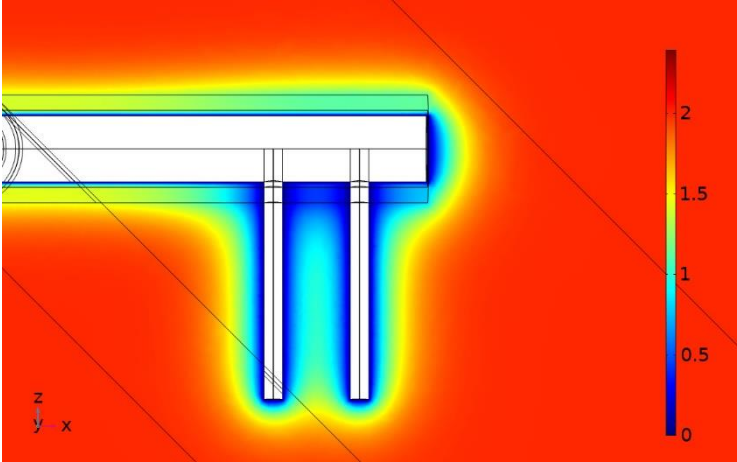


Figure 6.20 Pore pressure in MPa after two years

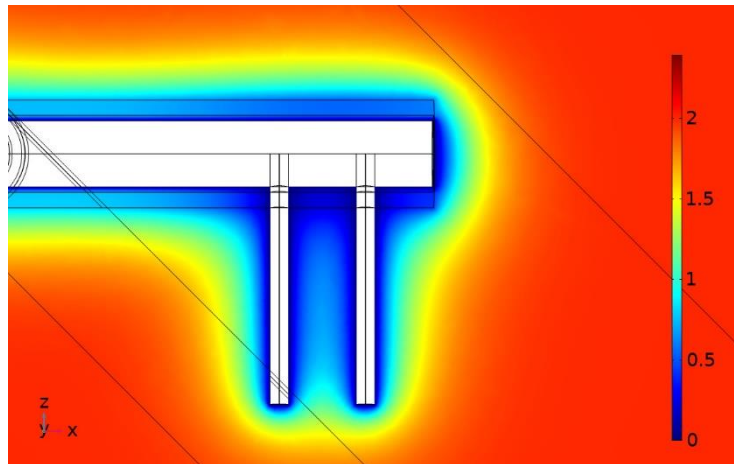


Figure 6.21 Pore pressure in MPa after five years

6.4 Conclusions

The simulations have shown that

- the experiment can be performed as designed without an inadmissible mutual interaction between the two shafts or the seal systems in the shafts and the gallery above,
- the seal system's resaturation will be governed by the bentonite suction pressure and the properties of a potential EDZ surrounding the shafts, rather than by injection pressure,
- during the three years of resaturation in the coming project phase, only the fringes of the DS will be resaturated significantly.

As regards the latter issue, an acceleration of resaturation will be possible using the back-up hydration system. Future simulations featuring back-up hydration can be performed to show the effect of this system.

In the coming project phase, interpretative simulations will be performed as soon as measurement data will come in. These will involve advanced material models and as-built data and experience from running the experiment.

7 Construction techniques and installation (WP7)

After instrumentation of the Opalinus clay rock (chapter 8) and data acquisition required for determining initial state of the rock, the two shafts will be excavated. Both shafts will have a diameter of 1.2 m and depths of 12 m (shaft 1) and 10 m (shaft 2), respectively (chapter 5). Since the shafts will be drilled with a custom made two tower drilling rig with a 1200 mm single core barrel, shaft walls will be as smooth as in boreholes of smaller diameter: the roughness of the shaft walls should be $R = \pm 5 \text{ mm}$ (lower than 1% of the shaft diameter).

Provided that the shafts remain stable, no casing will be required for drilling. The core will be broken off with lateral boreholes of $\phi > 130 \text{ mm}$ and hydraulic post. For core retrieval, several options are foreseen:

Option A: Core will be retrieved with sandwich core barrel (Fig. 7.1) over a winch or forklift.

Option B: Core will be milled with a disc down to the compact rock.

Option C: Core material will be retrieved by hand with protection (casing) and access via a safety ladder.

Overcoring with large diameter ($600\text{mm} < \phi < 1200\text{mm}$) core barrel and core lifting with sandwich tubes

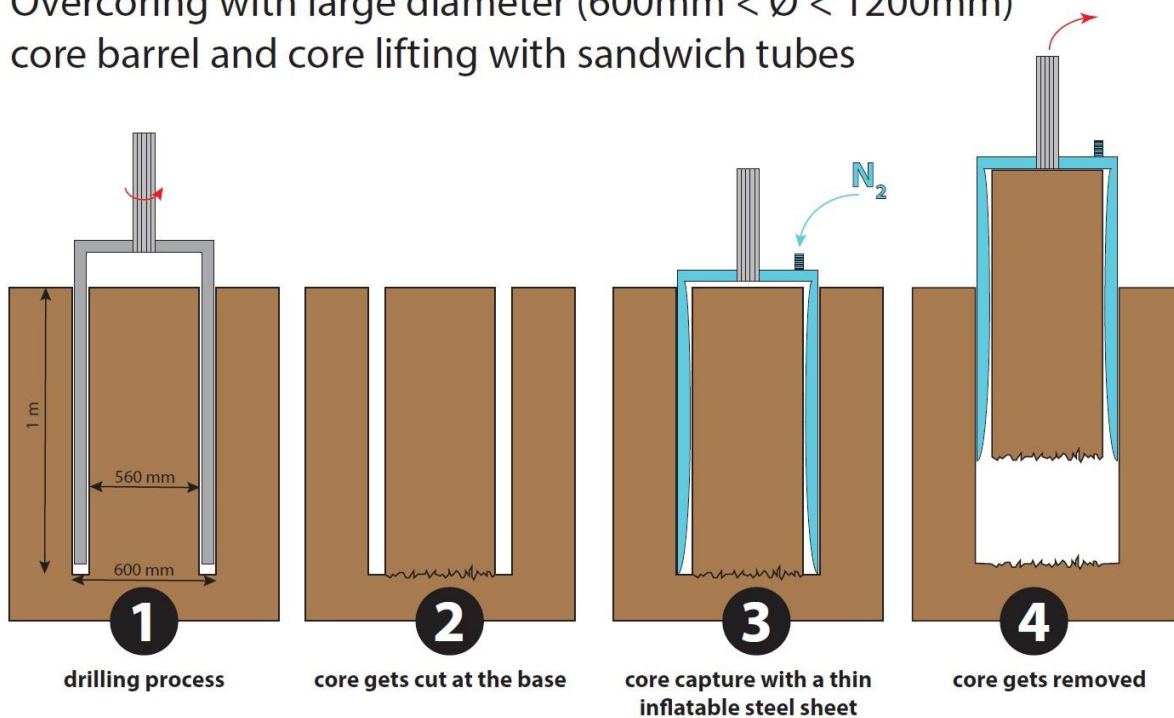


Figure 7.1 Core retrieval with the sandwich tube technique. The double wall core barrel is inflated with nitrogen, thus squeezing the core in between.

Drilling progress is estimated to 1.5 m of drilling advance within 20 h. Core retrieval will take approximately 10 h. In total, the excavation of one shaft will take about 6 weeks.

The company in charge of the excavation will provide the required temporary lining (foldable K196 steel mesh) as well as the tools for safe personnel access to the shaft and the peripheral protection. A ladder with a central guiding rail will provide access to the shafts (Fig. 7.2). Personnel needs to be equipped with climbing harness, helmet and walkie-talkie. The drilling contractor will install a temporary ventilation system after completion of the shafts. The shafts will be illuminated.

Bentonite pillows with a bulk density of about 2.2 g/cm³ (moisture 10% (105 °C) and 11.25% (200 °C) or water content 11.15%/12.7%) will be compacted of Calcigel. About 30% of the pillows will be crushed to provide the granular material for gap filling during installation. Four to five big bags of pillows and two big bags of granular material will be delivered by a lorry. Fine sand for ES will be also delivered in big bags. All big bags are lined. The water content at the time of installation will result from the water content during compaction of bentonite pillows for the binary mixture and the equilibration water content during transportation and storage prior to installation. For quality assurance, the water content of components of the binary mixture of bentonite and of the ES material will have to be determined on-site at 105 °C and 200 °C (only DS).

In shaft 2, ES will be installed in the wet (but not saturated) state with increased thickness. This will accelerate resaturation of the DS and the EDZ in the Opalinus clay.

A plug on top of the sealing system will be needed to keep it mechanically confined, no water tightness will be required. Two main options are in discussion: a keyed low-pH concrete plug or a metallic lid supported on the niche surface or the roof. The final decision will be taken after an in-depth evaluation of the options.

The seal construction technique is described in more detail in the test plan (Amberg, 2019).

8 Instrumentation (WP8)

An appropriate instrumentation of the experiment has to fulfil the following objectives:

- Determination of the initial state of the rock on the test site: sensors need to be installed prior to construction of the large borehole, and mechanical and hydraulic properties and load conditions will have to be determined at the specific test location. The results of these investigations will be required for the fine tuning of material selection, experiment execution and monitoring techniques. The rock parameters are essential for numerical modeling and for the interpretation of the monitoring results.
- Monitoring of the reaction of the rock to the construction of the large borehole by geotechnical and geophysical measurements to determine the system's state while installing the Sandwich seal.
- Temporal and spatial survey of resaturation and the swelling process in the seal system and of the evolution of the contact zone and the rock: the sealing effectiveness of the sandwich system is determined by the saturation of the DS; the ES are emplaced to achieve a more homogeneous saturation and swelling. The evolution of saturation distribution and the swelling pressures need to be measured, which requires suitable sensors in the Sandwich system and in the contact zone.
- Control of the resaturation process: resaturation of the sealing system will be controlled via a pressure chamber. The conditions in the chamber have to be recorded continuously.

Based on these requirements, the instrumentation of the Sandwich experiment was planned. A detailed test plan (Amberg, 2019) has been drawn up for shaft 1 and the surrounding rock. Since shaft 2 will be instrumented later during the project, the detailed planning of shaft 2 instrumentation will be performed when experience from the operation of shaft 1 is available.

Current planning comprises

- Sensors in the rock surrounding the shafts: prior to shaft sinking, sensors for pore pressure measurements and stress monitoring stations will be installed in the rock surrounding shaft 1. Three lined vertical boreholes will be used for rock characterization by seismic and geoelectric tomography (ERT) measurements. In a pilot hole drilled into the center of the future shaft 1, overcoring tests will be performed to determine the mechanical stress state (chapter 8.1).
- After shaft sinking, the excavation damaged zone (EDZ) close to the shaft surface will be characterized by geophysical measurements (chapter 8.2).
- During emplacement of the seal system in shaft 1, sensors for measurement of moisture content (TDR and ERT), total pressure and pore water pressure, relative humidity, temperature and displacements will be installed in the shaft and the contour zone (chapter 8.3)
- Wireless data transmission from out of the sealed shaft is considered. It will not be available for the shaft 1 instrumentation, but possibly for shaft 2. The state achieved is described in chapter 8.4.
- All continuously accumulating data, except for the rock stress, seismic and ERT data which have dedicated acquisition systems, will be recorded by a front-end computer and permanently stored on the Mont Terri DAS with a mirrored version in Bern (chapter 8.5).

Further information can be found in the test plan (Amberg, 2019).

8.1 Rock instrumentation

The rock around the experimental shafts will be instrumented (Fig. 8.1 and 8.2) prior to shaft sinking to

- Capture and characterize the initial state of the rock and to
- Observe the interaction of the rock with the sealed shafts in the course of the experiment.

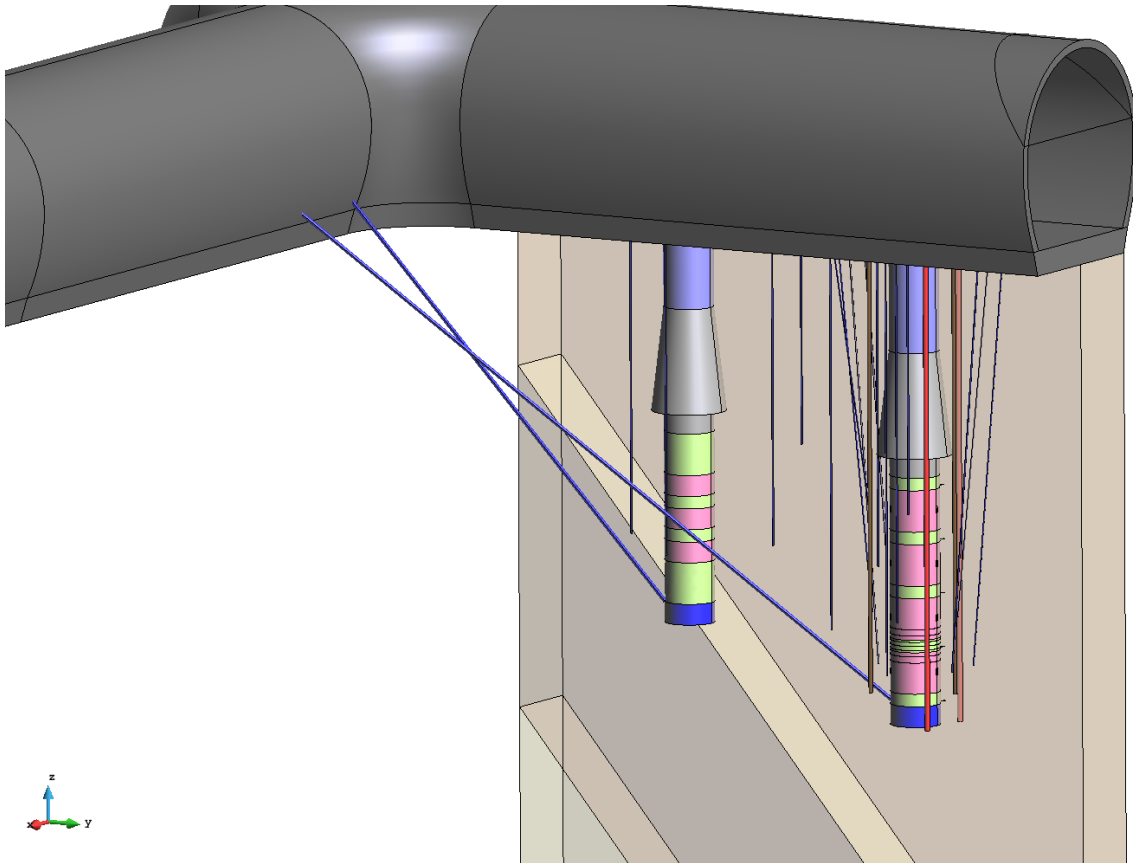


Figure 8.1 Perspective view of the experiment shafts and instrumentation boreholes

GRS will drill 16 small-diameter boreholes for installing minipiezometers for pore pressure measurement in the rock. Most of them will be close to shaft 1, but some will also be located between the two shafts or close to shaft 2. More minipiezometers will be installed close to shaft 2 later in the project.

The mini-piezometers are mechanical mini-packers installed at the bottom of each borehole, giving a very small test interval (Fig. 8.3). Sealing will be provided by backfilling the void above the mini-packer with synthetic resin. The test interval at the borehole bottom is connected to the gallery via two coaxial tubes, which are used to replace the air in the interval with Pearson water. Outside of the borehole, the tubes are connected to a valve rack with an optical pressure gauge and a “Keller” pressure sensor (0 – 50 bar, 4 – 20 mA) which is connected to the DAS. Due to the small size of the interval only a short equilibration time (typically several days) and a high sensitivity to pore pressure changes will be achieved.

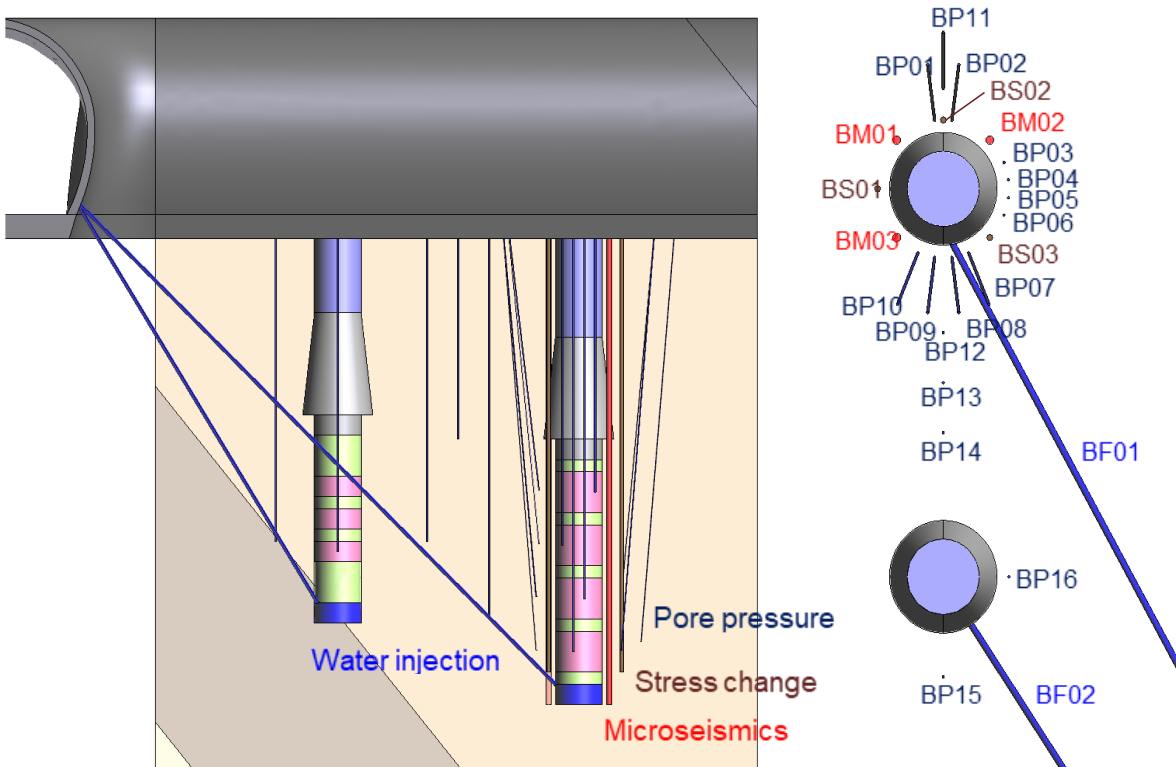


Figure 8.2 Planned instrumentation boreholes (BF: water injection, BP: pore pressure, BS: seismic/ERT measurements, BM: stress monitoring)

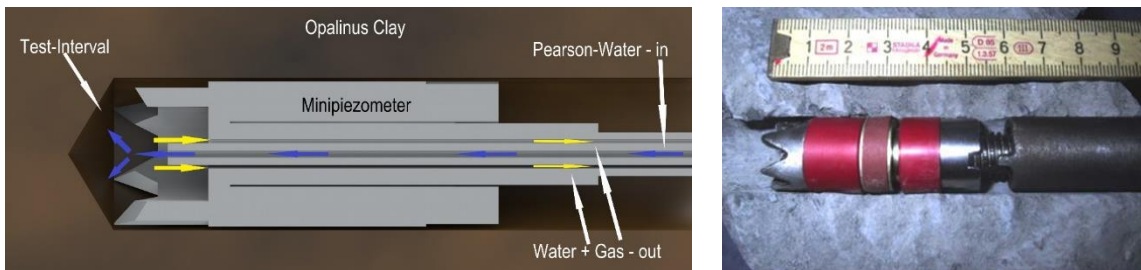


Figure 8.3 GRS minipiezometer

Three vertical boreholes for microseismic (ultrasonic wave velocity) and geoelectric tomography (ERT) measurements for rock characterization will be drilled by BGR (Fig. 8.4 and 8.5). After these measurements the boreholes will be used for permeability testing. Subsequently, the boreholes will be lined, so that microseismic measurements can be performed at later stages of the experiment.

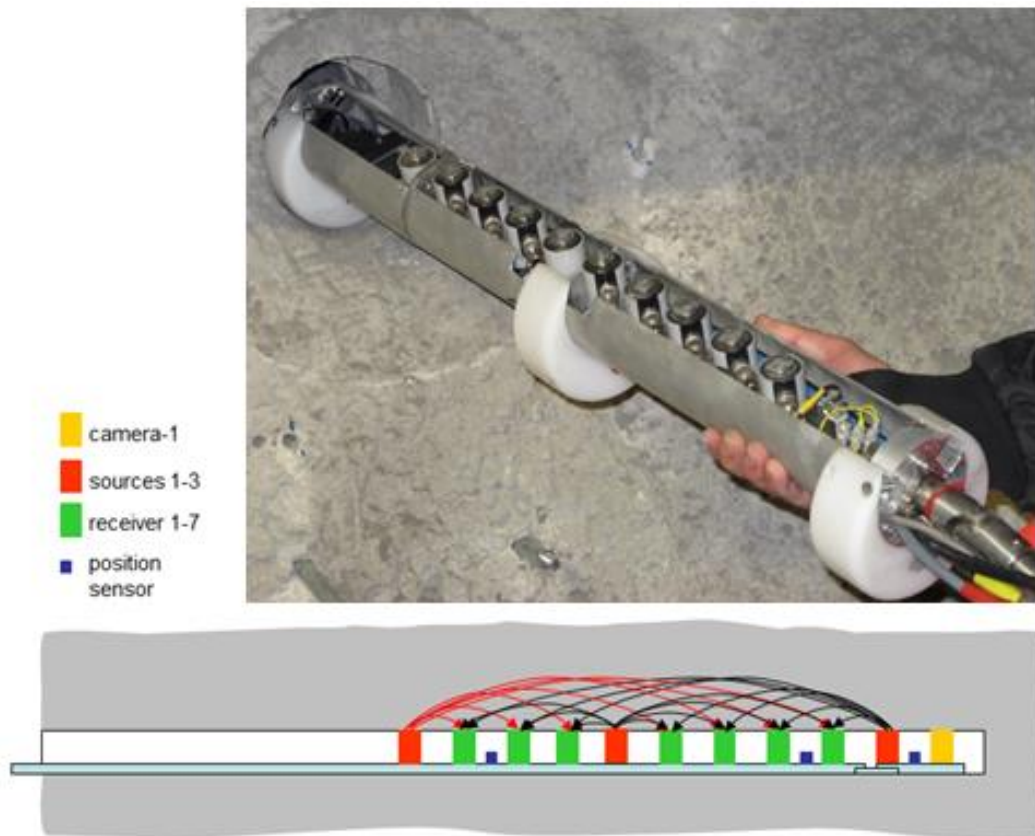


Figure 8.4 The BGR 8KUBS-05 mini-seismic borehole probe with adapters for boreholes with diameters of 131 mm (top) and seismic ray propagation, schematic presentation (below)



Figure 8.5 Part of the ERT borehole probe GB100-15

Flat cell stress monitoring stations (Fig. 8.6) will be installed by BGR in three additional boreholes. They will be arranged opposite to flat cells on the shaft contour (chapter 8.3). The flat cells will measure the stress changes in the rock mass induced by sandwich borehole excavation and the swelling pressure as a result of seal resaturation. After placing the pressure cells, the boreholes will have to be grouted. After some weeks the vicinity of the pressure cells will need to be refilled with resin to prevent gaps between the pressure cells and the grout.



Figure 8.6 Example of a pressure cell manufactured by Glötzl Baumesstechnik

In a pilot hole drilled into the center of the future shaft 1, overcoring tests will be performed to determine the mechanical stress state (BGR). The principle of this overcoring method is to measure the deformation of a small pilot borehole during the overcoring (Fig. 8.7). The core in which the measurement takes place is tested at the laboratory afterwards to determine the material parameters and, hence, the deformation behavior. Using analytical equations and the material parameters, the rock stresses will be back-calculated, which will lead to the measured deformation of the pilot borehole. Only the rock stresses in a plane perpendicular to the borehole axis can be determined.

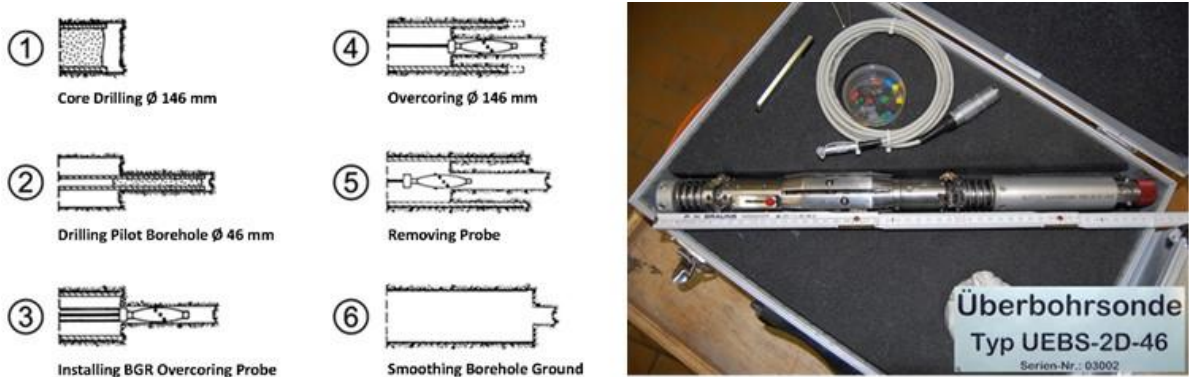


Figure 8.7 Scheme of the overcoring proceeding (left) and BGR overcoring probe (right) for in-situ measurements to determine rock stresses

8.2 EDZ characterization

The sensors installed in the rock (chapter 8.1) will observe EDZ evolution. Prior to the installation of the sealing system in shaft 1 the initial state of the EDZ will be characterized by geophysical measurements on the shaft contour performed by BGR. These measurements will include

- Ultrasonic measurements for determination of the damage state
- ERT measurements to investigate the saturation state
- Gas permeability measurements using surface packers (Fig. 8.8)

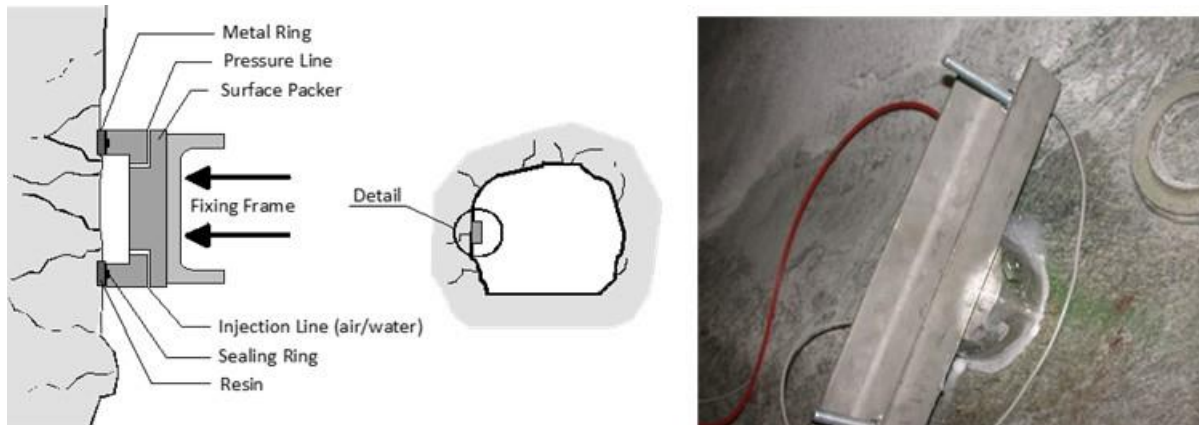


Figure 8.8 Surface packer on a drift wall

Additionally, five TDR rod sensors consisting of two parallel rods with 32 mm spacing (Fig. 8.9) will be installed in 30 cm long boreholes drilled radially into the shaft wall. These will measure the water content in the EDZ during the experiment.



Figure 8.9 Example of rod TDR sensor

8.3 Shaft 1 instrumentation

Shaft 1 will accommodate a multitude of sensors for measurement of moisture content (TDR and ERT), total pressure and pore water pressure, relative humidity, temperature and displacements. An overview of the equipment in a DS and in an ES is given in Fig. 8.10 and 8.11.

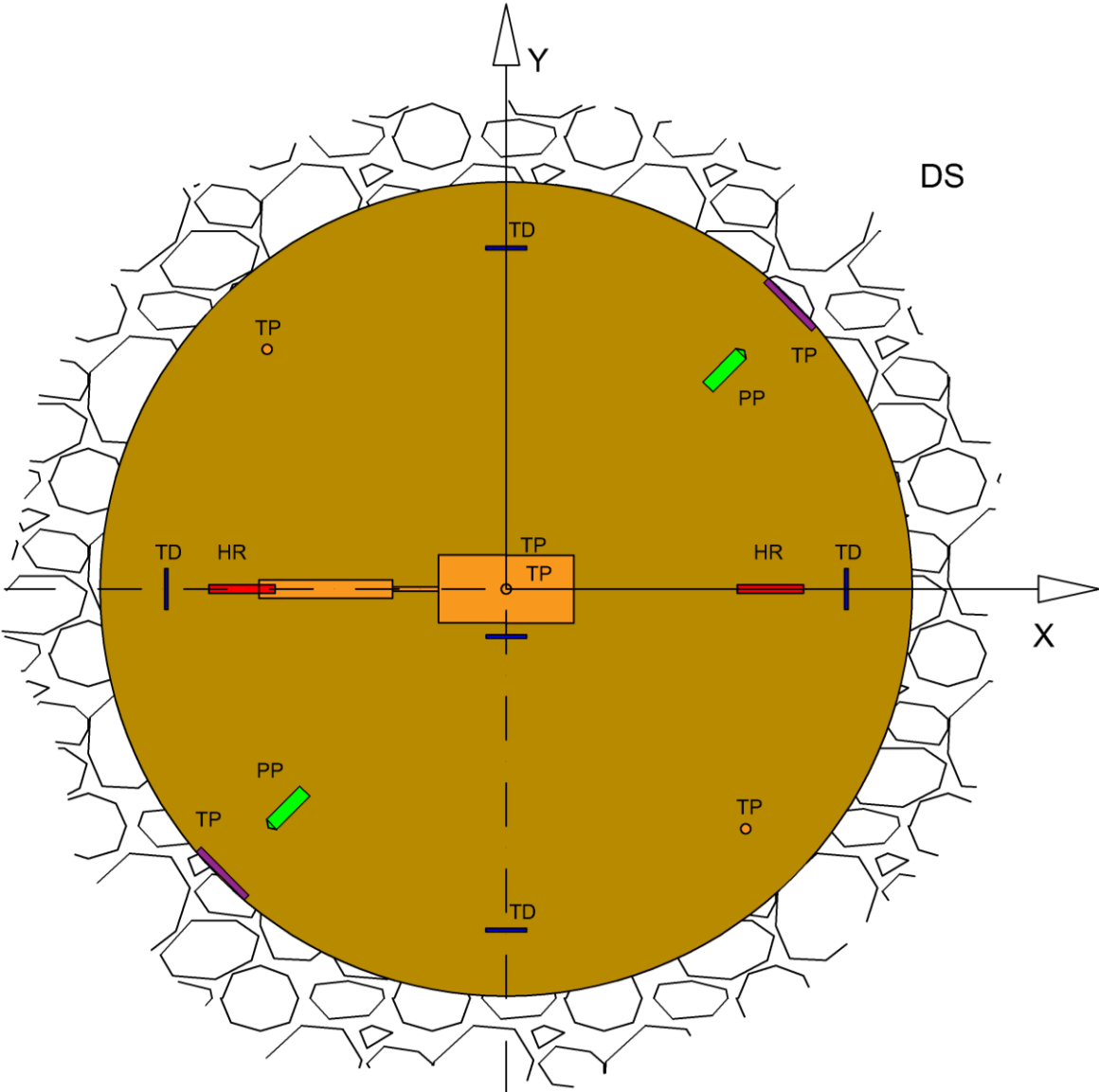


Figure 8.10 Plan view of all the instruments planned for one DS (comprises all layers). PP: pore pressure, TP: total pressure, HR: relative humidity, TD: water content (TDR).

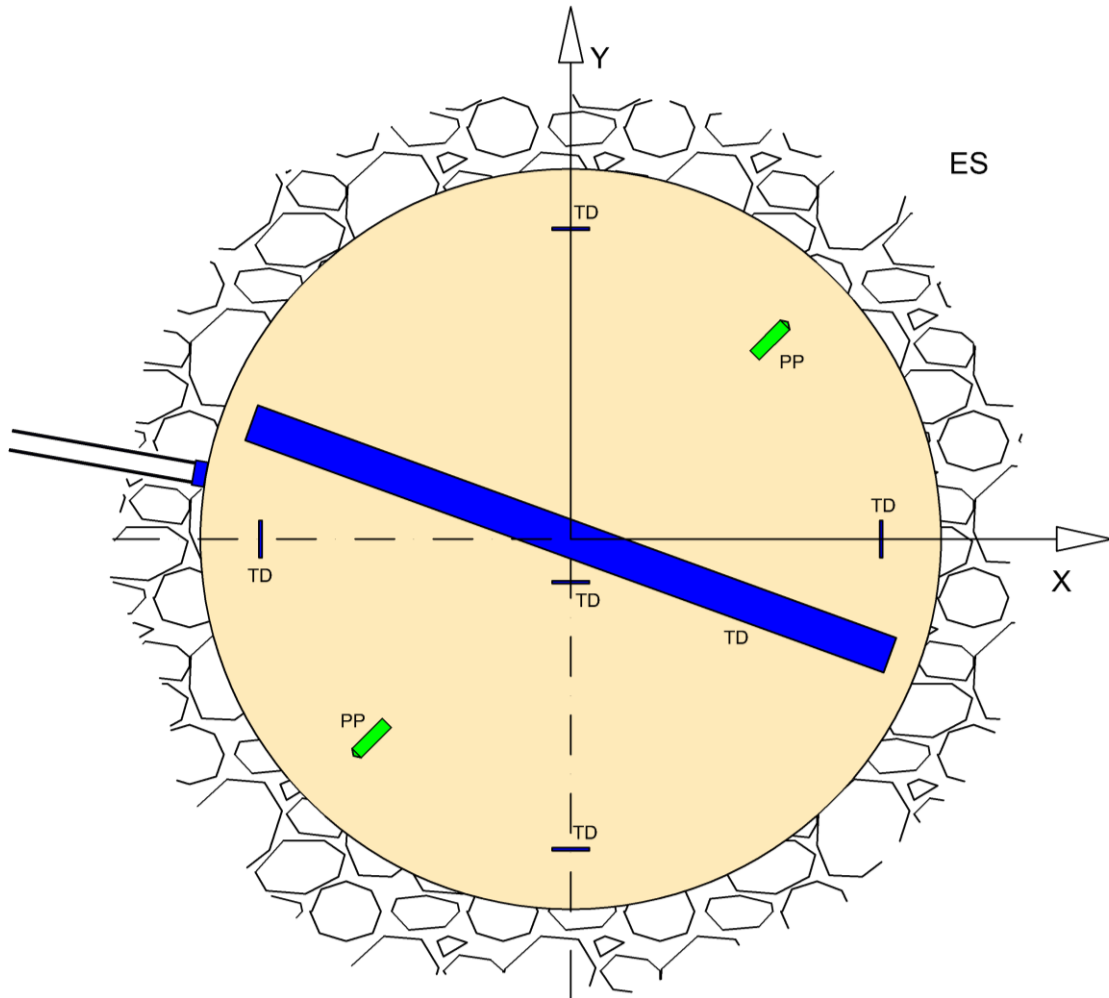


Figure 8.11 Plan view of all the instruments planned for one ES. PP: pore pressure, TD: water content (TDR).

8.3.1 Water content measurement

Water content in the seal system is measured by TDR sensors and by ERT. Changes in volumetric water content caused by changes of saturation and bulk density will be monitored using TAUPE cable sensors (Time Domain Reflectometry sensors or TDRs). Three types of sensors are envisaged (Fig. 8.12):

- 5 vertical sensors to determine propagation of moisture front and moisture distribution.
- 5 horizontal sensors in ES to monitor moisture increase and its redistribution in the DS due to suction.
- 5 horizontal rods installed in the rock from inside the shaft to determine water content evolution in the excavation damaged zone (EDZ) (chapter 8.2).

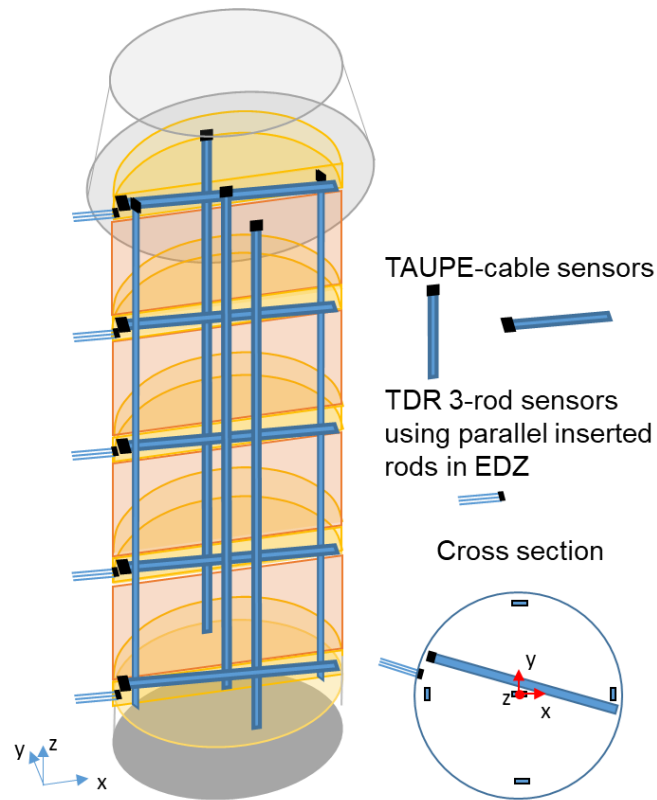


Figure 8.12 TDR sensors in the Sandwich sealing and borehole wall of shaft 1

ERT measurements coordinated by BGR, will provide redundant information about the propagation of the moisture front and 3D distribution in the transition zone in the region of ES2 and the DS below and above (Fig. 8.13). ERT provides tomographic images of the electrical resistivity distribution. By calibration using laboratory measurements, the resistivity can be related to water content.

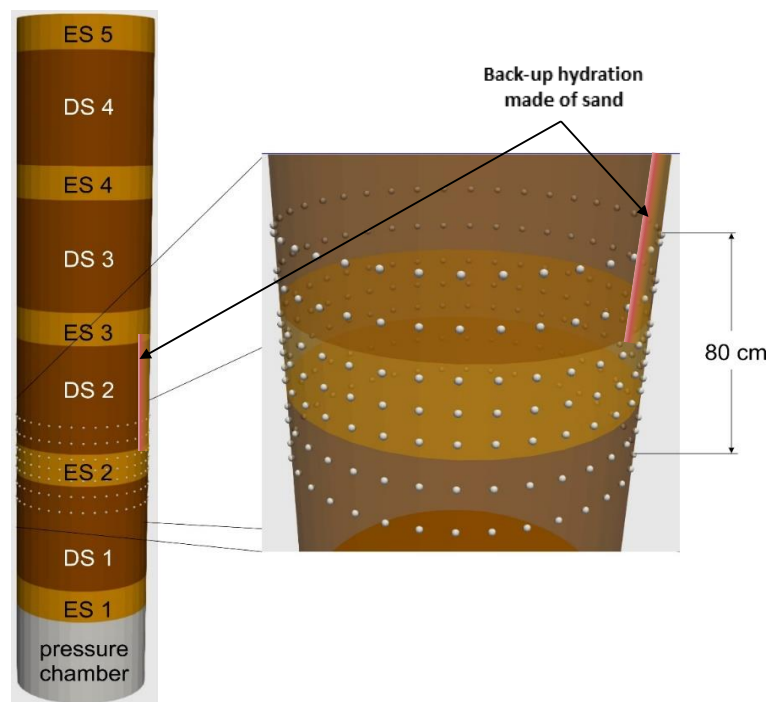


Figure 8.13 ERT sensor array in shaft 1

8.3.2 Pore pressure and total pressure measurements

Once a segment is saturated the pore-water pressure (PWP) will form. PWP measurement is an important complement to swelling pressure. Inside the ES, PWP will not vary significantly, which is why two sensors per ES will be enough (10 sensors). Two pore-water pressure measurements in the DS are required to distinguish between PWP and swelling pressure (together with total pressure measurement). Up to eight pore-water pressure sensors will be installed in the DS (Fig. 8.14). In addition, liquid pressure has to be measured in the pressure chamber (two sensors for redundancy). The sensor suggested for use is a miniature pore pressure sensor specially designed and constructed for emplacement in soils or compacted sealing materials (clays or sand/clay mixtures) (Fig. 8.15).

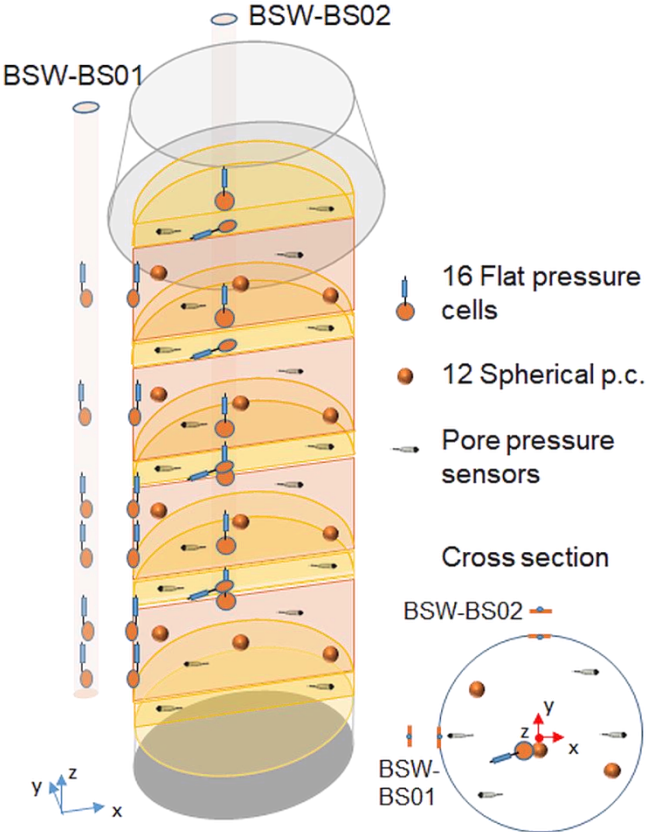


Figure 8.14 Pore pressure and total/swelling pressure sensors in shaft 1

Non-directional compressive stress transducers (Fig. 8.16) will measure total pressure inside the DS (3 sensors per DS, orange spheres in Fig. 8.14). Additionally, flat cells will be used at the DS/ES interfaces to measure axial stress (rectangular orange plates in Fig. 8.14). Additional flat cells similar to the flat cells installed in the rock (chapter 8.1) will be used to measure radial stress at the interface between DS and shaft wall (shown in the figure opposite to the BGR boreholes BSW-BS01 and BSW-BS02).



Figure 8.15 Pore pressure sensor



Figure 8.16 Non-directional total pressure sensor

8.3.3 Relative humidity and temperature

Relative humidity (rH) measurement can be interpreted in terms of saturation and is therefore a valuable complement to TDR. rH sensors come in combination with temperature sensors (since rH is dependent on temperature). Consequently, the sensors are applied for monitoring the (assumed) isothermal evolution. Two rH sensors per segment will be installed in the DS. The sensor suggested for use is a capacitive type relative humidity sensor that provides both relative humidity and temperature readings (Fig. 8.17). The device is specially designed and constructed for emplacement in soils or compacted sealing materials (clays or sand/clay mixtures). The electronic circuit is located in a robust stainless-steel body and sealed with epoxy resin, guaranteeing a high water-tightness degree at the cable entry side. The sensing element is protected mechanically by a stainless-steel filter.



Figure 8.17 Relative humidity sensor

8.3.4 Temperature

Temperature measurement will be carried out in the pressure chamber to monitor the temperature of the injection fluid. Two sensors (thermocouples) will be installed in the water chamber for redundancy and a third one in Niche 7 for comparison.

8.3.5 Displacements

Both axial displacements in the seal system and radial displacements of the borehole wall are important characterizing of the system. Measurement may, however, be problematic due to drawbacks of the commercially available instrumentation.

ENRESA and Amberg decided to develop a solution to accurately measure the displacement of the seal using alternative measurement techniques. The idea is to design a permeable shape sensor able to deform vertically and radially with the interface between ES and DS layers.

Conventional sensors, discrete displacement sensors and clinometers, were initially rejected to minimize system perturbation. Work now focuses on finding a solution based on fiber optics shape sensors (FOSS), either FBG multicore based devices or E-textile/smart-textile solutions. The work is still ongoing, which is why no details can be given.

8.4 Wireless data transmission

8.4.1 Introduction

The installation of geotechnical barrier systems or sealing systems often involves the need to record process data as part of a monitoring process. In addition to the corresponding sensors for e.g. pressures, temperatures, strains and displacements, the infrastructure for power supply and data transmission has to be integrated into the sealing system.

Conventional power supply and data transmission by wire is associated with the challenge of not compromising the integrity of the sealing system by the routing of the wires.

Power supplies based on batteries with a lifetime of up to 10 a are available on the market. To provide self-sufficient power supplies with service lives of up to 30 a, first successful steps were taken by Westfälische Hochschule and IBeWa (Rost *et al.*, 2018).

Technologies regarding wireless transmission through the earth (TTE) are in the focus of RandD since the 20's of the last century, but these technologies have not made it to market until today.

In 2007, IBeWa started to evaluate the feasibility of using existing radio transmission technologies in monitoring mining work within the RandD-project "Zerstörungsfreie in-situ-Permeabilitätsmessung / non-destructive in situ permeability determination" (Wilsnack and Grafe, 2014). The outcome was a concept for wireless data transmission from inside a sealing-dam to an underground data acquisition system. This concept was tested successfully in the Morsleben repository for radioactive waste (ERAM). Three radio sensors (DE202012007536 U1, German Patent and Trademark Office) have continuously monitored this demonstration site for about 9 a (Harvey and White, 2013; Wilsnack *et al.*, 2012). The radio technology of these sensors (ultra high frequency – UHF) is optimized for more or less dry conditions in rock salt.

For the conditions of a wet or almost saturated host rock, the UHF radio technology is not applicable due to the high electromagnetic damping. Here, wireless data transmission through the earth at very low frequencies (VLF) presents an excellent alternative (Grafe *et al.*, 2018). IBeWa installed a demonstrator based on TTE technology at very low frequency (VLF) in the Reiche Zeche education and research mine in Freiberg to evaluate data transmission through wet rocks. Since 2015, a consortium of international partners has worked on the Horizon 2020 project – Real-Time-Mining with wireless data transmission (Grafe *et al.*, 2018).

The experience gained from this research project should be applied in Mont Terri and adapted to the conditions of the underground laboratory inside the nearly water saturated Opalinus clay. After a conceptual feasibility test, the existing technologies should be adapted and a prototype for a mid-term functional test (approx. 6 month) should be produced and installed in Mont Terri.

8.4.2 Adapting the existing concepts

The results of former investigations of TTE transmission at VLF revealed a high potential in almost saturated host rocks. The transmission always was successful over more than 100 m distance when the antenna / electrodes were installed directly at the drift contour. Transmission almost always failed when the antenna / electrodes were installed inside boreholes (Grafe *et al.*, 2018).

Since the installation of monitoring systems inside boreholes is an important practical aspect, it should be further investigated. The main reason for installation of monitoring systems inside boreholes in Freiberg was the geological structure of the Freiberg gneiss and its associated heterogeneous distribution of moisture (Grafe *et al.*, 2018).

The moisture and, hence, the effective electrical conductivity in the Freiberg gneiss is usually linked to crevasses, cracks or discrete pathways. Thus, the electric field energy mainly propagates along these wet discrete pathways. A stable transmission is not always possible under these conditions, because it depends on an existing wet conductive pathway through the rock mass. Due to the lower electrical resistivity of shale compared to argillite rocks (about $2 \cdot 10^3 \Omega\text{m}$ compared to $1 \cdot 10^1 \Omega\text{m}$) (Telford *et al.*, 1990) and its relatively homogeneous distribution of moisture, transmission results in the Opalinus clay at Mont Terri were better. The VLF- tests in the Reiche Zeche led to the development of a new type of borehole transmitter / receiver (Fig. 8.18).

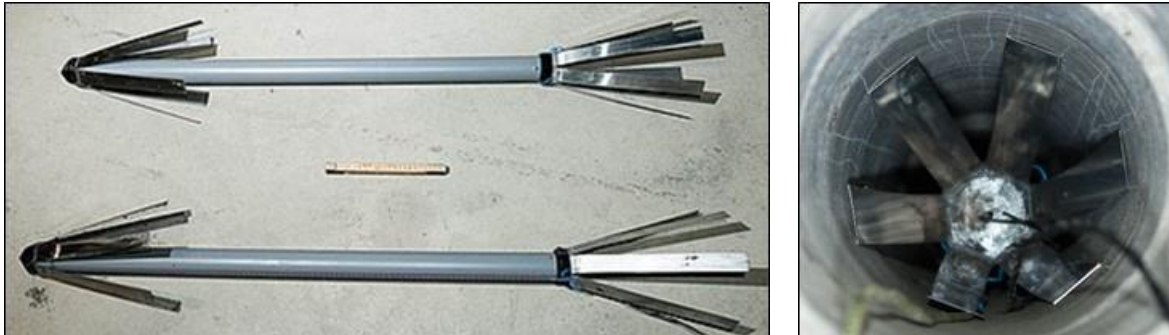


Figure 8.18 Left: adapted self-sufficient borehole transmitter (above) and cable-bonded receiver (below), right: receiver installed inside a borehole

Both electrodes of the transmitter or receiver were made of six sharp-edged steel-blades. The steel blades scrape locally interlocked with the relatively soft clay rock and ensured good electrical connection. To remove the transmitter from the borehole, a special mechanism was used to detach the steel blades.

8.4.3 In-situ feasibility test

The new prototype was used in a feasibility test at Mont Terri. The aims of this test were:

- Test of the adapted prototype,
- Proof of transmission through 20 m host rock,
- If applicable: maximum range tests and limiting influences,
- Evaluation of the transmission properties on the host rock in Mont Terri,
- Assessing the concept of installation / connection to the host rock or inside the sandwich materials,
- Deriving specifications for the functional test.

The test was performed between June 05, 2018 and June 07, 2018 in Ga98 and in Ga04. In preparation of the test, several open boreholes were selected (Fig. 8.19) with the help of the Swisstopo borehole information system (BIS).

The following criteria were used for selection:

- $\varnothing \geq 00 \text{ mm} \leq 140 \text{ mm}$
- Inclination between 60° and -60°
- Location predominantly in the sandy facies
- Various tests of distance combinations (especially between Ga98 and Ga04)

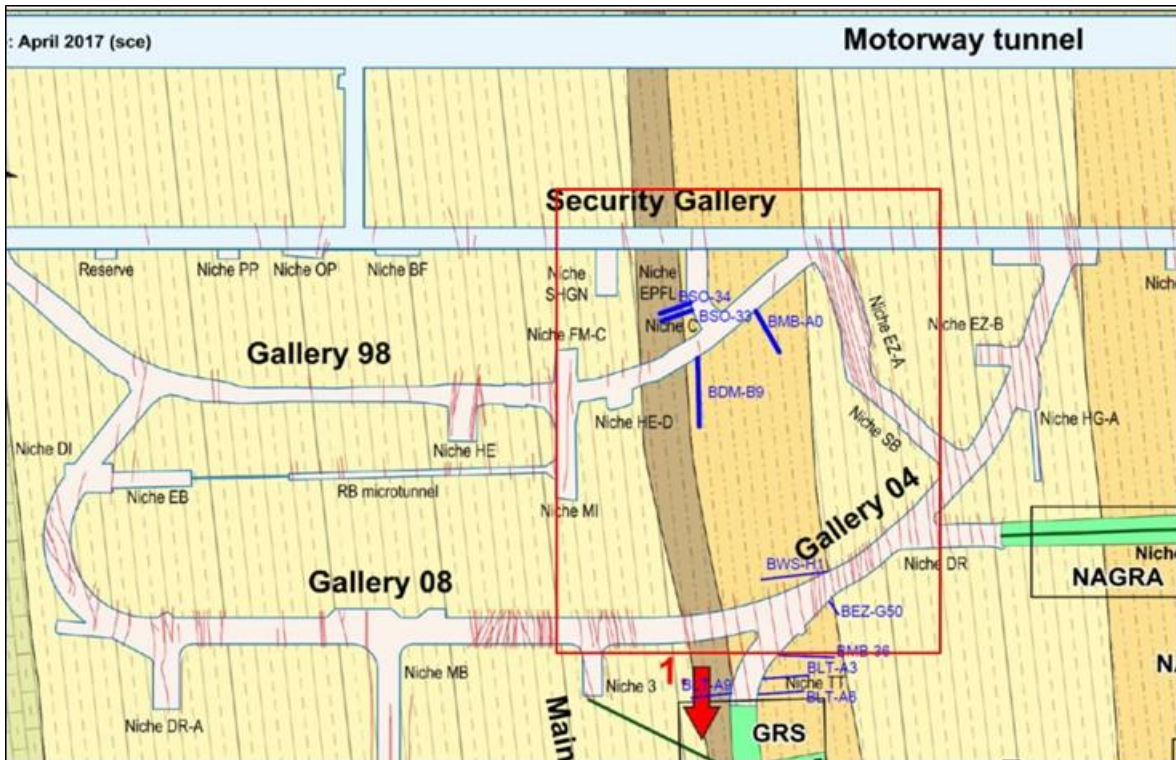


Figure 8.19 Layout of the underground laboratory with the pre-selected boreholes (marked blue)

Due to ongoing excavation work in Ga04, only boreholes in Ga98 were tested only. The tested distances ranged between 1 m and ≈ 50 m. The tested prototype of a borehole transmitter and receiver used three specific frequencies successively at 42 kHz, 132 kHz and 455 kHz. The experimental receiver hardware consisted of a radio spectrum processor RSP2pro from SDRplay using its high-impedance input. To encode process data and measure the received signals, the freely available SDR-software SDRUno was used. The software runs on a common notebook. The transmission quality was assessed by measuring the signal-level, the background noise-level and the signal-to-noise ratio.

At first, transmissions between boreholes at several depths were performed. The first transmissions between the neighboring boreholes BSO-33 and BSO-34 (located in Niche C) worked without any problems, so that the tests were expanded to also include measurements between BMB-A0 and BDM-B9 (Fig. 8.20).



Figure 8.20 In-situ setup for the feasibility tests between boreholes BDM-B9 and BMB-A0

Between these boreholes, transmission with an acceptable quality was possible up to 15 m. The achieved signal-to-noise-ratio seemed to leave only little reserve for longer transmission distances. This was mainly due to the high noise level resulting from electromagnetic interference induced by the ongoing excavation work (ventilation, cutting machine, etc.). In reality, transmission between a transmitter placed inside a borehole and a gallery is often wanted. Instead of a borehole-receiver, electrodes placed directly in the host rock were tested. To get access to the host rock, the “geological windows” within the gallery lining were used (Fig. 8.21 left). To connect the receiver hardware to the host rock, thin steel plates were pushed into cracks existing within the host rock (Fig. 8.21 right).



Figure 8.21 Left: the “geological windows” were used to connect the host rock (HE-D niche in the background), right: electrode installed in a crack

The transmission between a borehole and the gallery also reached a good quality up to distances of 15 m within the sandy facies. Under the adverse conditions of the strong electromagnetic background noise, a transmission range of up to several tens of meters seems to be possible. At the time of reporting, the evaluation of the measurements had not yet been completed, so that the transmission range in Fig. 8.22 can only be shown schematically. Due to medical problems of an important project partner, continuation of this part of the Sandwich project is uncertain. The wireless transmission system cannot be integrated in the shaft 1 instrumentation. However, it might be possible to realize a wireless transmission in shaft 2.

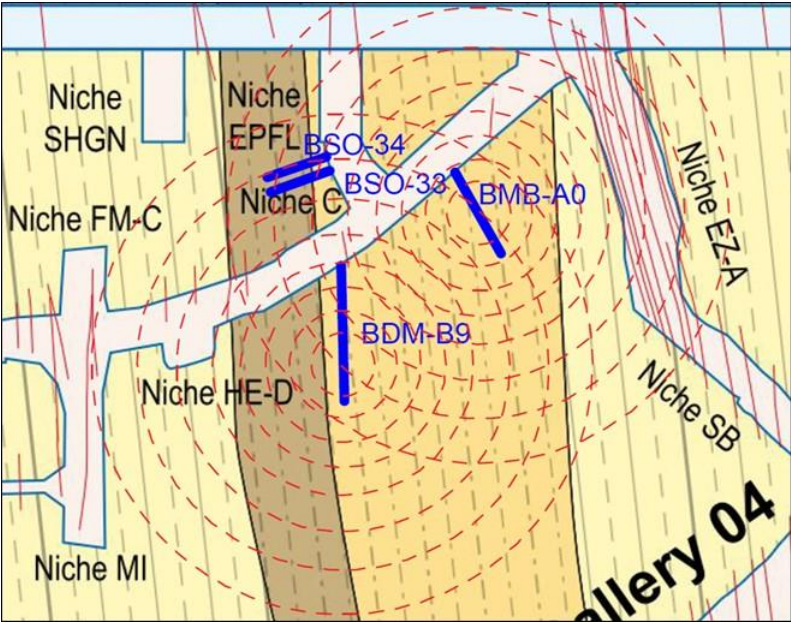


Figure 8.22 Schematic transmission range between boreholes BDM-B9 and BMB-A0

8.5 Data acquisition and storage

All sensors, except for the seismic and ERT (geophysics) sensors, will be connected to the central data acquisition system (DAS) of MTRL. Most of the sensor data will be recorded using a front-end computer running a geomonitor system (Solexperts) installed in Niche 7. FO shape sensor and TDRs will require their own data processing system, but will transfer their data to the DAS as well. The front-end computer and the connected data loggers will be connected to individual UPS. The geomonitor will be accessible via team viewer, for instance. The geomonitor data will be transferred regularly to the central data acquisition system (DAS) of Mont Terri, where they are accessible to all project partners of the SW-A experiment via Geoscope network access. The entire DAS of the SW-A experiment is connected to the secured power supply (diesel generator). Additionally, alarms set on specified sensors and parameters will allow for a gapless data recording. All data are also stored on a mirror site at Swisstopo in Bern.

ERT measurements will be controlled by and stored on a laptop onsite. Remote control and data transfer to BGR will be performed using the "TeamViewer" software.

9 The large-scale experiment (WP9)

The international Mont Terri rock laboratory (CH) situated in Opalinus clay offers an excellent site for demonstration of the vertical installation of the Sandwich sealing system and to study its interaction with Opalinus clay. The sandy facies of the Opalinus clay at the Mont Terri rock laboratory is similar to the Opalinus clay formation considered in the repository model SOUTH. Comprehensive planning of the in-situ experiment has been performed in the Sandwich-VP (02E11587) project and is documented in the various chapters of this report. The installation and operation plan for the in-situ experiment is documented in more detail in the draft test plan (Amberg, 2019).

Time and financial planning have been completed for the upcoming four years of the experiment (Sandwich main project – Sandwich HP), starting in July 2019 and running until June 2023. An overview of the work packages and schedule is given in Table 9.1.

Table 9.1 Gantt chart of Sandwich-HP

Work packages		Year 1				Year 2				Year 3				Year 4				Year 5				
		I	II	III	IV	I	II	III	IV	I	II	III	IV	I	II	III	IV	I	II	III	IV	
WP1	Test plan finalization			■	■																	
WP2	Instrumentation and sampling of Opalinus clay			■	■					■	■											
WP3	Shaft sinking and characterization of EDZ					■																
WP4	Installation of seal system, instrumentation						■				■	■										
WP5	Operation, monitoring, evaluation							■	■	■	■	■	■	■	■	■	■	■	■	■	■	■
WP6	Lab testing, material parametrization			■	■	■	■	■	■	■	■	■	■	■	■	■	■	■	■	■	■	■
WP7	Assessment, modeling			■	■	■	■	■	■	■	■	■	■	■	■	■	■	■	■	■	■	■
WP8	Documentation			■	■	■	■	■	■	■	■	■	■	■	■	■	■	■	■	■	■	■

The project will begin with the finalization of the test plan and instrumentation and sampling of the Opalinus clay in the experiment niche in the second half of 2019. Sinking of both shafts and characterization of the excavation damaged zone around the shafts will be performed in early 2020, followed by the installation of the seal system and instrumentation in shaft 1. Operation of shaft 1 will start in mid-2020. A second rock instrumentation phase is scheduled for the first half of 2021, prior to the seal installation in shaft 2 in the second half of 2022.

Lab testing and material parameterization, assessment and modeling, and the related documentation work will go on throughout the whole experiment phase.

Abbreviations

BBM	Barcelona basic model
BF	Water injection borehole
BIS	Swisstopo borehole information system
BM	Borehole for stress monitoring
BP	Borehole for pore pressure monitoring
BS	Borehole for seismic/ERT measurements
CEC	Cation exchange capacity
DAS	Data acquisition system
DS	Sealing layer
EBS	Engineered barrier system
EMDD	Effective montmorillonite dry density
ERAM	Morsleben radioactive waste deposite
ERT	Electrical resistivity tomography
ES	Equipotential layer
ESP	Enhanced sealing project
EDZ	Excavation damaged zone
FBG	Fiber Bragg grating
FOSS	Fiber optics shape sensors
Ga98	Gallery at MTRL constructed in 1998
Ga04	Gallery at MTRL constructed in 2004
Ga08	Gallery at MTRL constructed in 2008
GB	Geological or natural barrier
HM	Hydraulic and mechanical
HMC	Hydraulic, mechanical and chemical
HP	Main project
HR	Sensor for relative humidity
HTV	Semi-technical scale experiment
LHHPC	Low-heat high-performance concrete
MRTL	Mont Terri rock laboratory
OGS	OpenGeoSys
PP	Pore pressure
PVC	Polyvinylchloride
PWP	Pore water pressure
rH	Relative humidity
SCW	Synthetic clay water
TBM	Tunnel drilling machine
TEP	Thermos-elastoplastic
TD	TDR sensor for water content
TDR	Time domain reflectometry
TP	Total pressure

TTE	Through the earth
UHP	Ultra high performance
UHF	Ultra high frequency
URL	Underground rock laboratory
vG	Van Genuchten
VLf	Very low frequencies
WP	Work package
XRD	X-ray diffraction
XRF	X-ray fluorescence

Acknowledgements

Robin Seyfarth (KIT-CMM) for help with analysis of HTV-5 samples and layout of report

Annett Steudel (KIT-CMM) support with mineralogical analyses

Marita Heinle (KIT-IFG) for ICP-OES measurements

Frank Friedrich (RUB) for water adsorption isotherms

Wiebke Baille (RUB) swelling pressure measurements

Kristian Nikoloski (KIT-AGW) for his help for the basalt material preparation

Gudrun Hefner (KIT-IFG) for performing IC analysis

Nora Groschopf (University Mainz) XRF Analysis

Volker Beyer (TUBAF) for installation and sampling HTV-5 and HTV-6

Philipp Knabe (TUBAF) for sampling HTV-6

Maike Schröder (KIT) English

References (incl. Publications of the project in bold)

Alonso, E., Gens, A. & Josa, A. (1990). A constitutive model for partially saturated soils. *Géotechnique* 40, 3, 405-430.

Amberg (2019). Sandwich-HP Testplan Experimental Shaft 1. 95 p.

AtomG (2018) Gesetz über die friedliche Verwendung der Kernenergie und den Schutz gegen ihre Gefahren (Atomgesetz).

Beacon. (2018). What the Beacon project is about. <http://www.beacon-h2020.eu/the-project/>

Bernard-Michel, G., & Genty, A. (2006). Modules d'écoulement et de transport en milieux poreux non saturés dans CAST3M– modèle de Richards. CEA/DM2S/SFME/MTMS/RT/06-011/A report.

Beyer, W. (1964). Zur Bestimmung der Wasserdurchlässigkeit von Kiesen und Sanden aus der Kornverteilungskurve. *Wasserwirtschaft-Wassertechnik*, 165-168.

BMU (2010) Sicherheitsanforderungen an die Endlagerung wärmeentwickelnder radioaktiver Abfälle, Bundesministerium für Umwelt Naturschutz und nukleare Sicherheit (BMU). https://www.bmu.de/fileadmin/bmu-import/files/pdfs/allgemein/application/pdf/sicherheitsanforderungen_endlagerung_bf.pdf

Boháč, P., Delavernhe, L., Zervas, E., Königer, F., Schuhmann, R. & Emmerich, K. (2019). Cation exchange capacity of bentonite in a saline environment. *Applied Geochemistry*, 100, 407-413.

Bossart, P. & Thury, M. (2008). Mont Terri Rock Laboratory. Project, Programme 1996–2007 and results. Reports of the Swiss Geological Survey: <http://www.mont-terri.ch>

Boy, S. & Wilsnack, T. (2009). Quantifizierung räumlich und zeitlich variabler Feuchte- und Dichteverteilung in Verschlussbauwerken mittels Time-Domain-Reflectometry (TDR).

Breidung, K. P. (2002). Forschungsprojekt Schachtverschluss Salzdetfurth Schacht II. <https://www.tib.eu/suchen/id/TIBKAT:375489568/>

Delavernhe, L., Steudel, A., Darbha, G. K., Schaefer, T., Schuhmann, R., Woell, C., Geckeis, H. & Emmerich, K. (2015). Influence of mineralogical and morphological properties on the cation exchange behavior of dioctahedral smectites. *Colloids and Surfaces A: Physicochemical and Engineering Aspects*, 481(591-599).

DIN 66137-2: 2004-12 (2004). Bestimmung der Dichte fester Stoffe - Teil 2: Gaspyknometrie, DIN - Deutsches Institut für Normung.

DIN 18127 (2012). Baugrund Untersuchung von Bodenproben-Proctorversuch (Soil, investigation and testing - Proctor-test). DIN - Deutsches Institut für Normung.

DIN 66145: 1976-04, (1976). Darstellung von Korn-Teilchengrößenverteilungen; RRSB-Netz. DIN - Deutsches Institut für Normungen.

Dixon, D., Priyanto, D., Korkeakoski, P., Farhoud, R. & Zivkovic, A. (2017). The Enhanced Sealing Project (ESP): 2009-2016 monitoring of full-scale shaft seal installed in granitic rock. Paper presented at the 7th International Conference on Clays in Natural and Engineered Barriers for Radioactive Waste Confinement, Davos, Switzerland.

Dixon, D. A., Gray, M. N. & Thomas, A. W. (1985). A Study of the Compaction Properties of Potential Clay - Sand Buffer Mixtures for Use in Nuclear-Fuel Waste-Disposal. *Engineering Geology*, 21, 247-255.

ENSI (2012). Geologische Tiefenlager – Radioaktive Abfälle sicher entsorgen. Eidgenössisches Nuklearsicherheitsinspektorat. http://static.ensi.ch/1338994771/ensi_geologischetiefenlager_web.pdf

Emmerich, K., Giraudo, F., Schuhmann, R., Schnetzer, F., Kaden, H. & Thissen, P. (2018). On the Prediction of Water Contents in Na-Saturated Dioctahedral Smectites. *The Journal of Physical Chemistry*, 122, 7484-7493.

Emmerich, K., Roelke, C., Popp, T., Steudel, A., Zervas, E., Delavernhe, L., Königer, F. & Schuhmann, R. (2017). Der Minisandwich. In: *Innovative Feuchtemessung in Forschung und Praxis 9. Berichtsband zur Tagung 2017, Karlsruhe*.

Filippi, M. (2007). Validation de l'implémentation de la loi de comportement mécanique BBM dans le code CAST3M. CEA/DM2S/SFME/MTMS report.

- Fredlund, D. G. & Xing, A. (1994). Equations for the soil-water characteristic curve. *Can Geotech*, 31, 521-532.
- Freyer, D., Gruner, M. & Popp, T. (2015). Zusammenhang von Chemismus und mechanischen Eigenschaften des MgO-Baustoffs. *Freiberger Forschungshefte*, Nr. E15.
- Gaus, I., Garitte, B., Senger, R., Gens, A., Vasconcelos, R., Garcia-Siñeriz, J. L., Trick, T., Wieczorek, K., Czaikowski, O., Schuster, K., Mayor, J. C., Velasco, M., Kuhlmann, U. & Villar, M. V. (2014). The HE-E Experiment: Lay-out, Interpretation and THM Modelling, Combining D2.2-11: Final Report on the HE-E Experiment and D3.2-2: Modelling and Interpretation of the HE-E Experiment of the PEBS Project.
- Gens, A. (2018). Description of the constitutive models available at the start of the project. Conceptual bases, mathematical description and capabilities and shortcomings.
- Grafe, F., Horner, D., Rössel, A., Schieweg, A., Viertel, T., Wilsnack, T. & Mischo, H. (2018). Data acquisition & transmission in mining operations. *Horizon 2020: Real-time optimization of extraction and the logistic process in highly complex geological and selective mining settings (RTM Real-Time-Mining)*. *Kali und Steinsalz*, 02, 30-37.
- Gray, M.N. & Shenton, B.S. (1998). Design and development of low-heat, high-performance, reactive powder concrete. *Intl. Symposium on High-Performance and Reactive Powder Concrete*, August 16-20, Sherbrooke, Canada.
- Gruner, M. (2010). Einsatz von Bentonit im Entsorgungsbergbau. *Bergbau*, 9/2010, 394-403.
- Gruner, M., Rumphorst, K. & Sitz, P. (2008). Design and Emplacement of Bentonite Barriers. *Proceedings - Paper presented at the International Technical Conference on the Practical Aspects of Deep Geological Disposal of Radioactive Waste*, Prague, Czech Republic. http://www.iaea.org/inis/collection/NCLCollectionStore/_Public/41/025/41025016.pdf
- Harvey, E. & White, M. (2013). Monitoring in geological disposal of radioactive waste. *Proceedings of an International Conference and Workshop*.
- Herold, P. (2018). Presentation ELSA Project meeting.
- Herold, P., Simo, E., Müller, C., Wilsnack, T. & Schieweg, A. (2016). ELSA Phase II Teilbericht zum Arbeitspaket 5 – Modellierung.
- Imbert, C. & Villar, M. V. (2006). Hydro-mechanical response of a bentonite pellets/powder mixture upon infiltration. *Applied Clay Science*, 32, 197-209.
- Jobmann, M., Bebiolka, A., Jahn, S., Lommerzheim, A., Maßmann, J., Meleshyn, A., Mrugalla, S., Reinhold, K., Rübél, A., Stark, L. & Ziefle, G. (2016). Sicherheits- und Nachweismethodik für ein Endlager im Tongestein in Deutschland. https://www.db-technology.de/fileadmin/user_upload/unterlagen/f_e_berichte/Ansicht/
- Kleeberg, R. & Bergmann, J. (2002). Quantitative phase analysis using the Rietveld method and a fundamental parameter approach.
- Kohlrausch, F. (1986). *Praktische Physik*, Band 3: Tabellen und Diagramme. 23.
- Koldtitz, O., Görke, U., Shao, H. & Wang, W. (2012). Thermo-Hydro-Mechanical-Chemical Processes In Fractured Porous Media.
- (KrW-/AbfG (2017) Gesetz zur Förderung der Kreislaufwirtschaft und Sicherung der umweltverträglichen Bewirtschaftung von Abfällen.
- Kudla, W., Schreiter, W., Gruner, M., Jobmann, M., Bollingerfehr, W., Müller-Hoeppe, N., Herold, P., Freyer, D., Wilsnack, T. & Grafe, F. (2013). Schachtverschlüsse für Endlager für hochradioaktive Abfälle – ELSA Teil 1. <https://www.tib.eu/suchen/id/TIBKAT:782505570/>
- Kudla, W., Schreiter, F., Gruner, M., Jobmann, M., Bollingerfehr, W., Müller-Hoeppe, N., Herold, P., Freyer, D., Wilsnack, T. & Grafe, F. (2016). Schachtverschlüsse für Endlager für hochradioaktive Abfälle – ELSA Teil 2. *Zwischenberichte der Arbeitspakete*.
- Kudla, W. *et al.* (2020). Schachtverschlüsse für Endlager für hochradioaktive Abfälle – ELSA -Phase 2. Konzeptentwicklung für Schachtverschlüsse und Test von Funktionselementen von Schachtverschlüssen.
- Kupfer, K. & Brandelik, A. (2004). Entwicklung einer Messmethode zur Feuchtemessung in Bentonit-Abschlussbauwerken in salinärer Umgebung Teil 1 & 2.

<https://www.tib.eu/suchen/id/TIBKAT:489135226/>

Lloret, A. & Villar, M. V. (2007). Advances on the knowledge of the thermo-hydro-mechanical behaviour of heavily compacted FEBEX bentonite. *Physics and Chemistry of the Earth*, 8-14, 701-715.

Marcial, D. (2003). Comportement hydromécanique et microstructural des matériaux de barrière ouvrages. (Ph.D. Thesis), École Nationale des Ponts et Chaussées, Paris.

Martino, J. B., Dixon, D. A., Holowick, B. E. & Kim, C. S. (2011). Enhanced Sealing Project (ESP): Seal Construction and Instrumentation Report.

Mayor, J. C., Garcia-Sineriz, J. L., Alonso, E., Alheid, H. J. & Blümling, P. (2007). Engineered barrier emplacement experiment in Opalinus Clay for the disposal of radioactive waste in underground repositories. http://cordis.europa.eu/pub/fp5-euratom/docs/fp5-euratom_eb_projrep_en.pdf

Meier, L. P. & Kahr, G. (1999). Determination of the cation exchange capacity (CEC) of clay minerals using the complexes of Copper (II) ion with Triethylenetetramine and Tetraethylenepentamine. *Clays and Clay Minerals*, 47(3), 386-388.

Müller-Hoeppe, N., Buhmann, D., Czaikowski, O., Engelhardt, H. J., Herbert, H. J., Lerch, C., Linkamp, M., Wiczorek, K. & Xie, M. (2012). Integrität geotechnischer Barrieren, Teil 1 – Vorbemessung. Bericht zum Arbeitspaket 9.2, Vorläufige Sicherheitsanalyse für den Standort Gorleben.

Müller-Hoeppe, N., Breustedt, M., Wolf, J., Czaikowski, O. & Wiczorek, K. (2012). Integrität geotechnischer Barrieren, Teil 2 – Vertiefte Nachweisführung. Bericht zum Arbeitspaket 9.2, Vorläufige Sicherheitsanalyse für den Standort Gorleben.

Nekrassov, A. (2002). Development of a Reservoir Simulation Tool with the Local Equilibrium Approach to Composite Water-Hydrocarbon Systems for Application to the Multi-Phase Flow both in Petroleum Reservoirs and in Aquifers Taking into Account the Hydrodynamic Dispersion. Dissertation. TU Bergakademie Freiberg.

Nüesch, R., Brandelik, A., Hübner, C. & Schuhmann, R. (2002). Verschlussstopfen und Verfahren zum Verschließen von untertägigen Hohlräumen.

Pearson, F. J. (1998). Artificial waters for use in laboratory and field experiments with Opalinus clay: Status June 1998.

Pearson, F. J., Arcos, D., Bath, A., Boisson, J. Y., Fernández, A. M., Gäbler, H. E., Gaucher, E., Gautschi, A., Griffault, L., Hernán, P. & Waber, H. N. (2003). Mont Terri Project – Geochemistry of Water in the Opalinus Clay Formation at the Mont Terri Rock Laboratory.

Plischke, I. (2014). Experiment LT-A. Technical Report TR2014-06, Mont Terri Project, Switzerland.

Polytechnic University of Catalonia. (2017). Code_Bright User's Guide.

Popp, T. & Rölke, C. (2017). Status of Mini-Sandwich Tests, Pre-Project Meeting.

Popp, T., Rölke, C. & K., Salzer. (2015). Hydro-mechanical Properties of Bentonite-Block-Assemblies with interfaces in Engineered Barrier Systems. In R. Shaw (Ed.), *Gas Generation and Migration in Radioactive Waste Repositories*.

Priyanto, D. G., Dixon, D. A. & Man, A. G. (2011). Interaction between clay-based sealing components and crystalline host rock. *Physics and Chemistry of the Earth*, 36, 1838 - 1847.

Priyanto, D. G., Kim, C. S. & Dixon, D. A. (2013). Geotechnical Characterization of a Potential Shaft Backfill Material.

Rizzi, M., Seiphooori, A., Ferrari, A., Ceresetti, D., Laloui, L. & Marschall, P. (2012). Tu-Sa-Bent: Analysis Of The Behaviour Of The Granular Mx-80 Bentonite In Thm-Processes/Tu-Geo: Analysis Of The Thm-Behaviour Of Opalinus Clay.

Rost, U., Podleschny, P., Schumacher, M., Muntean, R., Pascal, D. T., Mutascu, C., Koziol, J., Marginean, G. & Brodmann, M. (2018). Long-term Stable Electrodes Based on Platinum Electrocatalysts Supported on Titanium Sintered Mesh for the Use in PEM Fuel Cells.

Rothfuchs, T., Czaikowski, O., Hartwig, L., Hellwald, K., Komischke, M., Mieke, R. & Zhang, C. L. (2012). Self-sealing Barriers of sand/bentonite mixtures in a clay repository - SB Experiment in the Mont Terri Rock Laboratory.

Sánchez, M. (2004). Thermo-hydro-mechanical coupled analysis in low permeability media. PhD Thesis, Universidad Politécnica de Cataluña, Barcelona, España.

- Schuhmann, R., Emmerich, K., Kemper, G. & Königer, F. (2009). Verschlussystem mit Äquipotenzialsegmenten für die untertägige Entsorgung (UTD und ELA) gefährlicher Abfälle zur Sicherherstellung der homogenen Befeuchtung der Dichtelemente und zur Verbesserung der Langzeitstabilität
- Seki, K. (2007). SWRC fit – a nonlinear fitting program with a water retention curve for soils having unimodal and bimodal pore structure. *Hydrol. Earth Syst. Sci. Discuss*, 4, 407-437.
- Shao, H., Paul, B., Wang, X., Hesser, J., Becker, J., Garitte, B. & Müller, H. (2016). Influence Of Different Supports On The Properties Of The Excavation Damaged Zone Along The Fe Tunnel In The Mont Terri Underground Rock Laboratory. *Radioactive Waste Confinement: Clays In Natural And Engineered Barriers*. Geological Society, London.
- Sitz, P. (2003). Entwicklung eines Grundkonzeptes für langzeitstabile Streckenverschlussbauwerke für UTD im Salinar, Bau und Test eines Versuchsverschlussbauwerkes unter realen Bedingungen. <https://www.tib.eu/suchen/id/TIBKAT:381656969/>
- Sitz, P., Gruner, M. & Miersch, D. (2001). Bergbau-Formsteine zur Herstellung langzeitstabiler untertägiger Verschlusselemente für untertägige Hohlräume.
- Sitz, P., Gruner, M. & Rumphorst, K. (2003). Bentonitdichtelemente für langzeitsichere Schachtverschlüsse im Salinar. *Kali und Steinsalz*, 3, 6 - 13.
- Sitz, P., Koch, G. & Gruner, M. (2002). Results from the large scale in situ drift sealing experiment in the salt mine Sondershausen. Paper presented at the International Meeting "Clays in natural and engineered barriers for radioactive waste confinement", Reims, France.
- Spanish Association for Standardization. (1999). UNE 103-302-94: determinación de la densidad relativa de las partículas de un suelo (Determination of specific (grain) density).
- StandAG (2007) Gesetz zur Suche und Auswahl eines Standortes für ein Endlager für hochradioaktive Abfälle, Bundesministerium der Justiz und für Verbraucherschutz (Stand 2017).
- Studel, A., Batenburg, L. F., Fischer, H. R., Weidler, P. G. & Emmerich, K. (2009). Alteration of swellable clays by acid treatment. *Applied Clay Science*, 33, 105-115.
- Svemar, C., Johannesson, L. E., Gram, P., Svensson, D., Kristensson, O., Lönnqvist, M. & Nilsson, U. (2016). Prototype Repository, Opening and retrieval of the outer section of Prototype Repository at Äspö Hard Rock Laboratory.
- Telford, W. M., Geldart, L. P. & Sheriff, R. E. (1990). *Applied geophysics*. Cambridge University Press.
- Thatcher, K. E., Newson, R. K., Watson, S. P. & Norris, S. (2017). Review of data and models on the mechanical properties of bentonite available at the start of Beacon.
- Tomas, J. (2014). *Mechanical Process Engineering - Particle Technology Disperse Systems*.
- Valleján, B., Gens, A., Mingarro, M., García-Gutiérrez, M., Villar, M. V., Plas, F., Filippi, M., Touzé, G., Van Geet, M., Bastiaens, W., Volckaert, G., Weetjens, E., Sillen, X., Maes, N., Imbert, C. & Billaud, P. (2009). RESEAL II: a large-scale in situ demonstration for repository sealing in an argillaceous host rock: phase II.
- Van Geet, M., Bastiaens, W., Volckaert, G., Weetjens, E., Sillen, X., Maes, N., Imbert, C., Billaud, P., Touzé, G., Filippi, M., Plas, F., Villar, M. V., García-Gutiérrez, M., Mingarro, M., Gens, A., & Vallejan, B. (2009). RESEAL II A large-scale in situ demonstration test for repository sealing in an argillaceous host rock – Phase II, FIKW-CT-2000-00010, Final Report, pp. 277.
- Van Genuchten, M. T. (1980). A closed-form equation for predicting the hydraulic conductivity of unsaturated soils. *Soil Science Society*, 44, 892-898.
- Van Loon, L.R., Soler, J. M. & Bradbury, M. H. (2003). Diffusion of HTO, ³⁶Cl⁻ and ¹²⁵I⁻ in Opalinus Clay samples from Mont Terri: Effect of confining pressure. *Journal of Contaminant Hydrology*, 73-83.
- Verpeaux, P., Charras, T., & Millard, A. (1988). CASTEM 2000 une approche moderne du calcul des structures, calcul des structures et intelligence artificielle. Fouet, Ladeveze, Ohayon, Ed. Pluralis, 261-271.
- VersatzVO (2012). Verordnung über den Versatz von Abfällen unter Tage. www.gesetze-im-internet.de
- Villar, M.V. (2002). Thermo-hydro-mechanical characterization of a bentonite from Cabo de Gata. A study applied to the use of bentonite as sealing material in high level radioactive waste repositories.

- Villar, M. V. (2004). Thermo-Hydro-Mechanical Characteristics and Processes in the Clay Barrier of a High Level Radioactive Waste Repository: State of the Art Report. Informes Técnicos Ciemat, 1044.
- Wermeille, S. & Bossart, P. (1999). In Situ Stresses in the Mont Terri Region – Data Compilation.
- Wersin, P., Mazurek, M., Waber, H. N., Mäder, U. K., Gimmi, T., Rufer, D. & de Haller, A. (2013). Rock and porewater characterisation on drillcores from the Schlattingen borehole.
- Wieczorek, K., Gaus, I., Mayor, J. C., Schuster, K., García-Sineriz, J. L. & Sakaki, T. (2017). In-situ experiments on bentonite-based buffer and sealing materials at the Mont Terri rock laboratory (Switzerland). *Swiss Journal of Geosciences*, 110.
- Wilsnack, T. (2017). Ausgewählte Aspekte zum Einfluss des Flüssigkeitsgehaltes auf die Strömungsprozesse in Verschlussbauwerken. Paper presented at the 9. CMM-Tagung, Material – Prozesse – Systeme, Karlsruhe.
- Wilsnack, T. & Grafe, F. (2014). Zerstörungsfreie in situ-Permeabilitätsmessung. <http://edok01.tib.uni-hannover.de/edoks/e01fb15/838563155.pdf>.
- Wilsnack, T., Rössel, A. & Grafe, F. (2012). Kabellose Datenübertragung im Salinar. *Kali und Steinsalz*, 2.
- Wilsnack, T., Sitz, P., Heinemann, K. H., Rumphorst, K. & Hunstock, F. (2008). Flüssigkeitsdichte Verwahrung von Schächten. *Kali und Steinsalz*, 3, 24-35.

Appendix

Batches Pearson water	A-3
HTV-5 Pressure development May to August 2017	A-5
HTV-5 Water content, exchangeable and soluble Na ⁺ and Ca ²⁺ after dismantling	A-11
HTV-6 Water content after dismantling	A-23

Batches Pearson Water

Cations							
batch	Volume	Sample/test	Na ⁺	Ca ²⁺	Mg ²⁺	K ⁺	Fe ³⁺
	[L]		[mmol/l]				
NAGRA 12-54			164	11.9	9.17	2.55	nd
TUBAF							
2	150	HTV-5 inflow	152	11.4	5.1	2.4	nd
1	?		240 ± 2	17.9 ± 0.4	8.97 ± 0.05	4.14 ± 0.05	nd
		gravel	169 ± 6	52.8 ± 0.3	25.43 ± 0.17	2.01 ± 0.01	3.44 ± 0.04
TUBAF							
1		HTV-6 inflow	154	11.9	8.80	2.73	nd
22.2.19		gravel	107 ± 5	28.2 ± 0.1	11.95 ± 0.01	1.33 ± 0.15	nd
18.3.19		HTV-6 inflow	143 ± 9	10.9 ± 1.1	8.76 ± 0.54	2.89 ± 0.40	nd
KIT							
1	5	MiniSandwich Oe7-Oe10	153	11.6	8.7	2.5	nd
2	5	MiniSandwich	230 ± 2	15.9 ± 0.2	11.37 ± 0.04	4.06 ± 0.00	nd
1	16	rising test ES	157	12.0	9.2	2.7	nd
2	20	rising test ES	227 ± 3	15.6 ± 0.3	11.61 ± 0.29	3.64 ± 0.23	nd
IBeWa							
1		swelling pressure	146 ± 2.8	10.4 ± 0.9	4.63 ± 0.27	3.26 ± 0.15	nd
2		swelling pressure	140 ± 1.8	10.6 ± 0.9	5.35 ± 0.41	3.21 ± 0.36	nd
CIEMAT							
		swelling pressure	nd	nd	nd	nd	nd
		suction pressure	nd	nd	nd	nd	nd

Anions				
batch	Volume	Sample/test	Cl ⁻	SO ₄ ²⁻
	[L]		[mmol/l]	
NAGRA 12-54			160	24
TUBAF		gravel	171	22

KIT 3/17	
Temperature [°C]	21
pH	7.71
density [g/cm ³]	1.007
conductivity [mS/cm]	19.3

(nd...no data)

HTV-5 Pressure development, May to August 2017

day	date	time		
1	May 04	13:13	start of experiment, target pressure at 5 bar	
		17:07	refilling fluid containers	pump off
		17:19	restart pump	
2	May 05	09:25	leakage detected at S14	pump off
		14:01	restart pump	
		16:02	refilling fluid containers	pump off
		16:31	restart pump	5 bar reached
		16:48	target pressure set to 10 bar	16:50 approx. 6 bar reached
		16:53	pressure drop to 2 bar	
5	May 08	11:21	target pressure set to 15 bar	
		around 16:30	leakage detected at P8	power supply of whole system failed
		afterwards	column input closed, data recording restarted (except spherical pressure cells)	
14	May 17	after 09:00	reconnection of S14 to measuring unit	
15	May 18	16:15	restart measurement at pressure spheres	
		16:45	TDR: S12 and S13 at MUX exchanged, 1 h program started	
20	May 23	10:32	restart pump at 10 bar target pressure	pressure reached in short time
26	May 29	10:28	target pressure set to 15 bar	
		13:10	target pressure set to 17.5 bar	
27	May 30	09:54	target pressure set to 22.5 bar	
		12:16	target pressure set to 25 bar	
28	May 31	after 09:00	target pressure set to 27.5 bar	
		noon	target pressure set to 30 bar	
57	July 4	ca. 09:15	target pressure set to 40 bar	
65	July 12	10:40	target pressure set to 60 bar	
71	July 18	13:20	target pressure set to 80 bar	pressure not reached
		13:45	pressure drop	
		17:50	target pressure set to 60 bar	31 bar available
			target pressure set to 35 bar	
			target pressure set to 30 bar	
72	July 19	08:00	target pressure set to 40 bar	

92	August 8	10:06	target pressure set to 50 bar
93	August 9	09:07	target pressure set to 60 bar
98	August 14	09:03	target pressure set to 70 bar
99	August 15	11:24	target pressure set to 80 bar
106	August 22	09:24	target pressure set to 90 bar
107	August 23	10:03	target pressure set to 100 bar



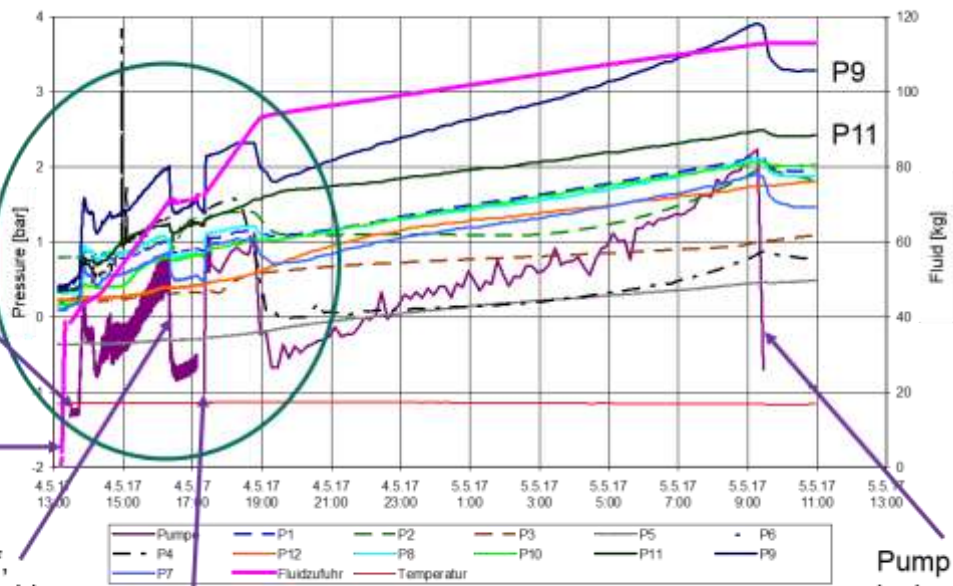
High-pressure pump on, set to 5 bar

Filling gravel volume

Pump off, refilling fluid container

Restart pump

Pump off, leakage at S14

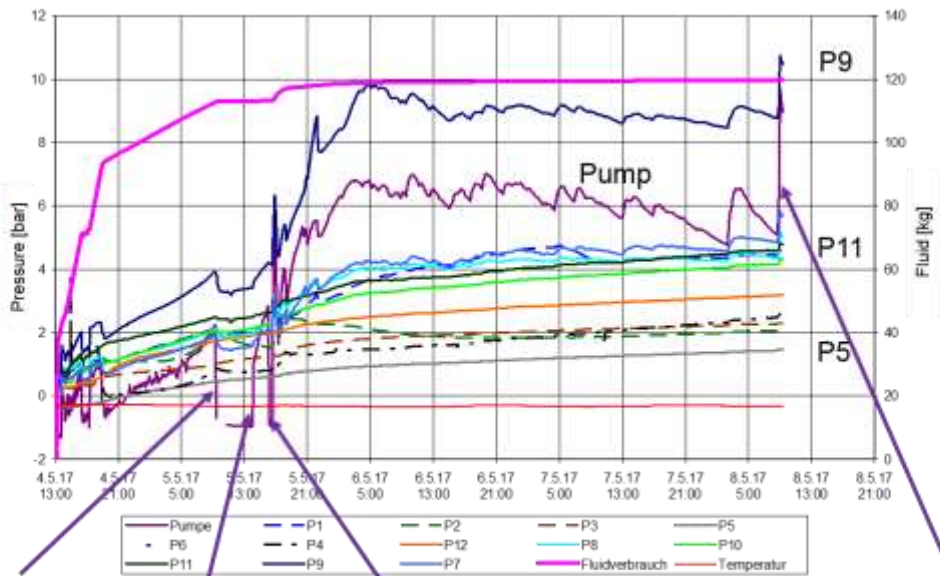


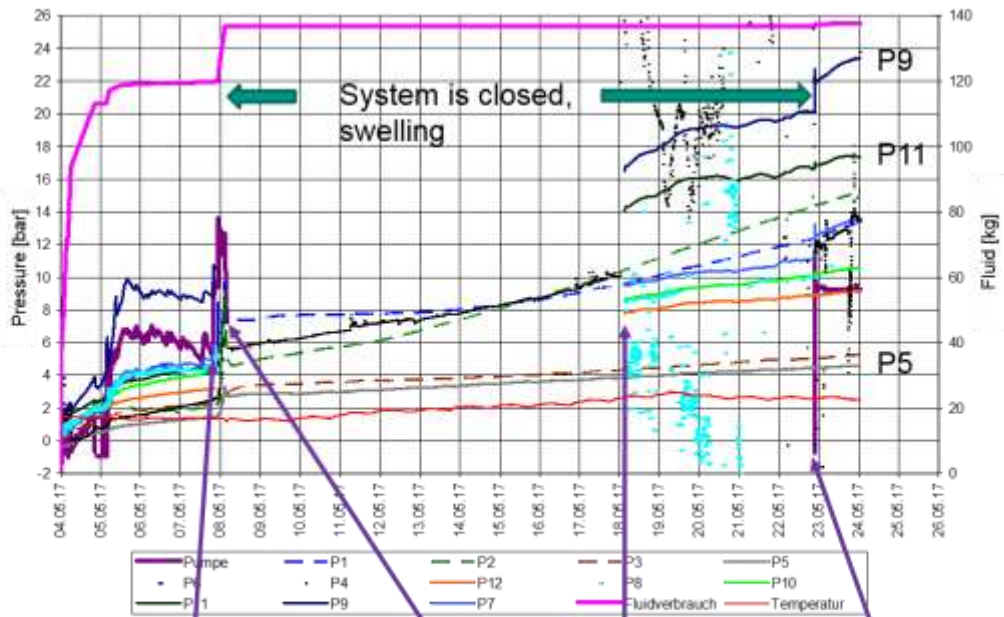
Pump off, leakage at S14

Restart pump

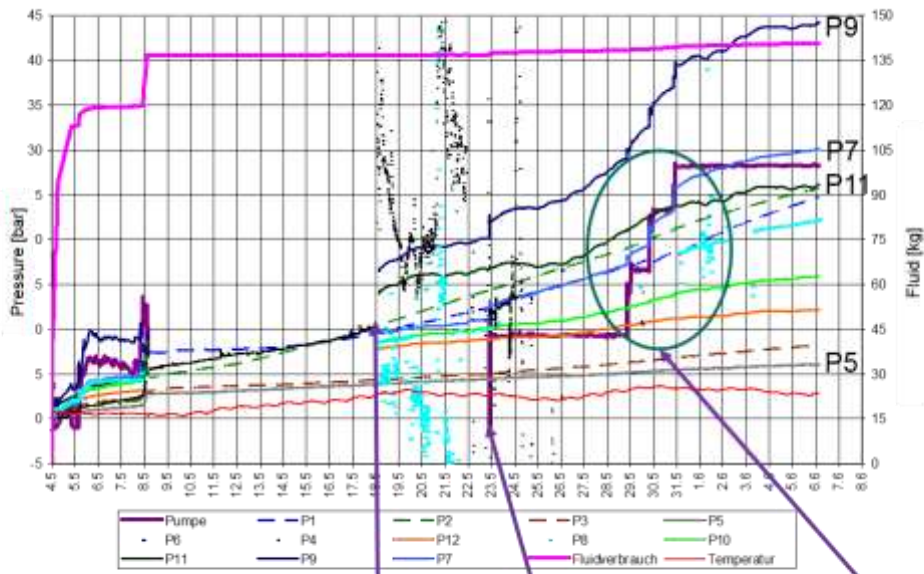
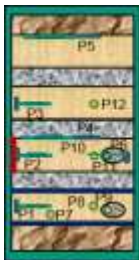
Pump off, refilling fluid container, 5 bar → 10 bar ↓ 2 bar

10 bar → 15 bar

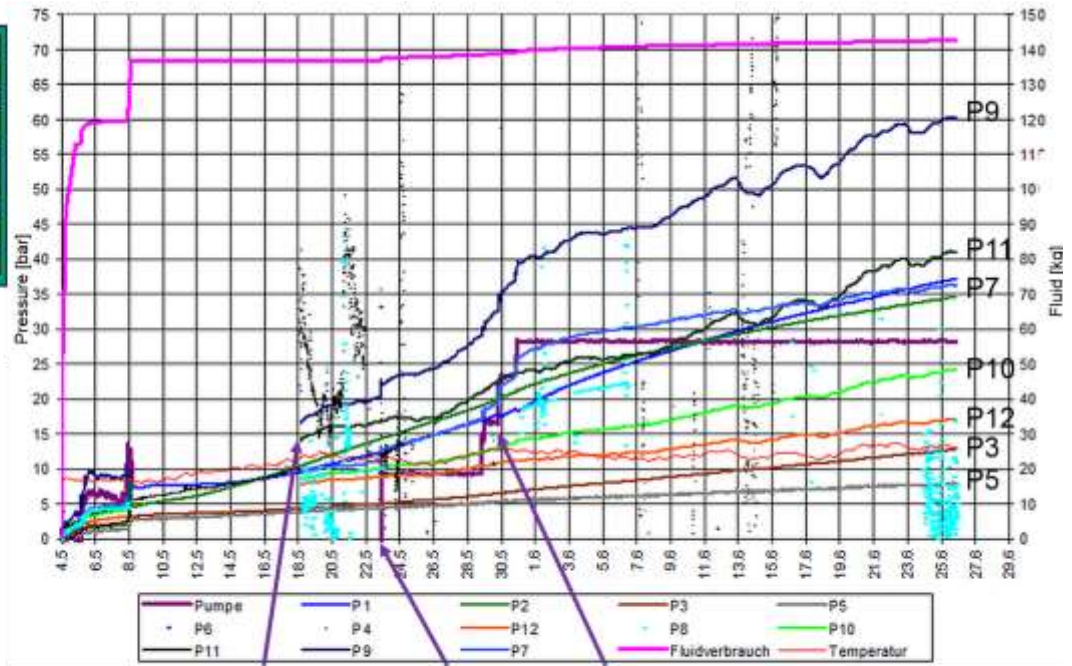




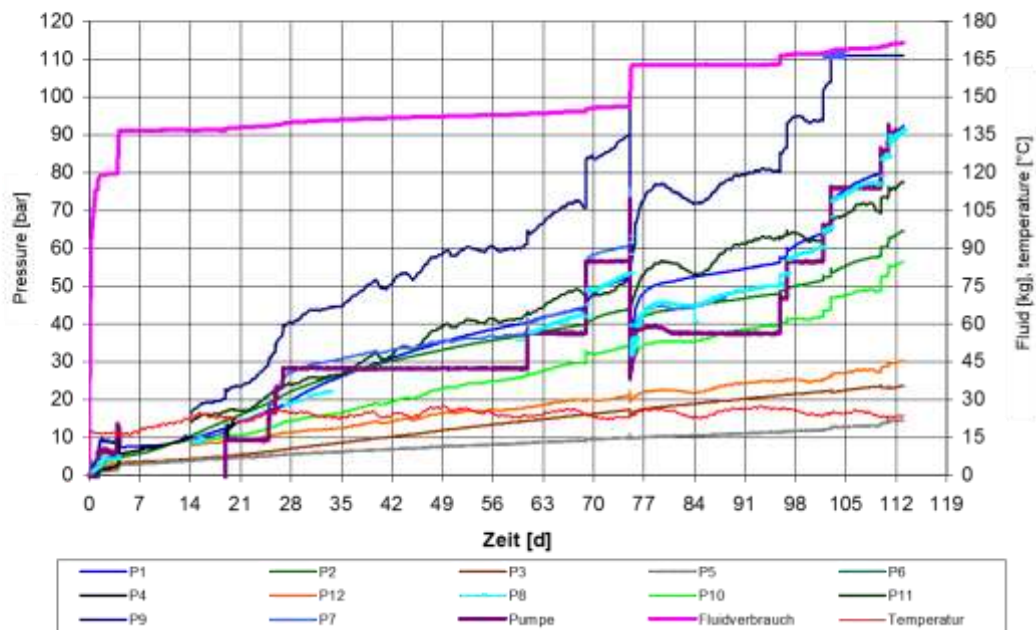
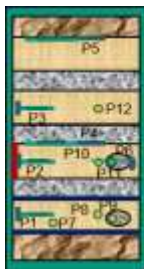
10 bar → 15 bar Restart monitoring system P
 Leakage at P8, Restart pump at 10 bar
 electricity down, monitoring system P
 input closed

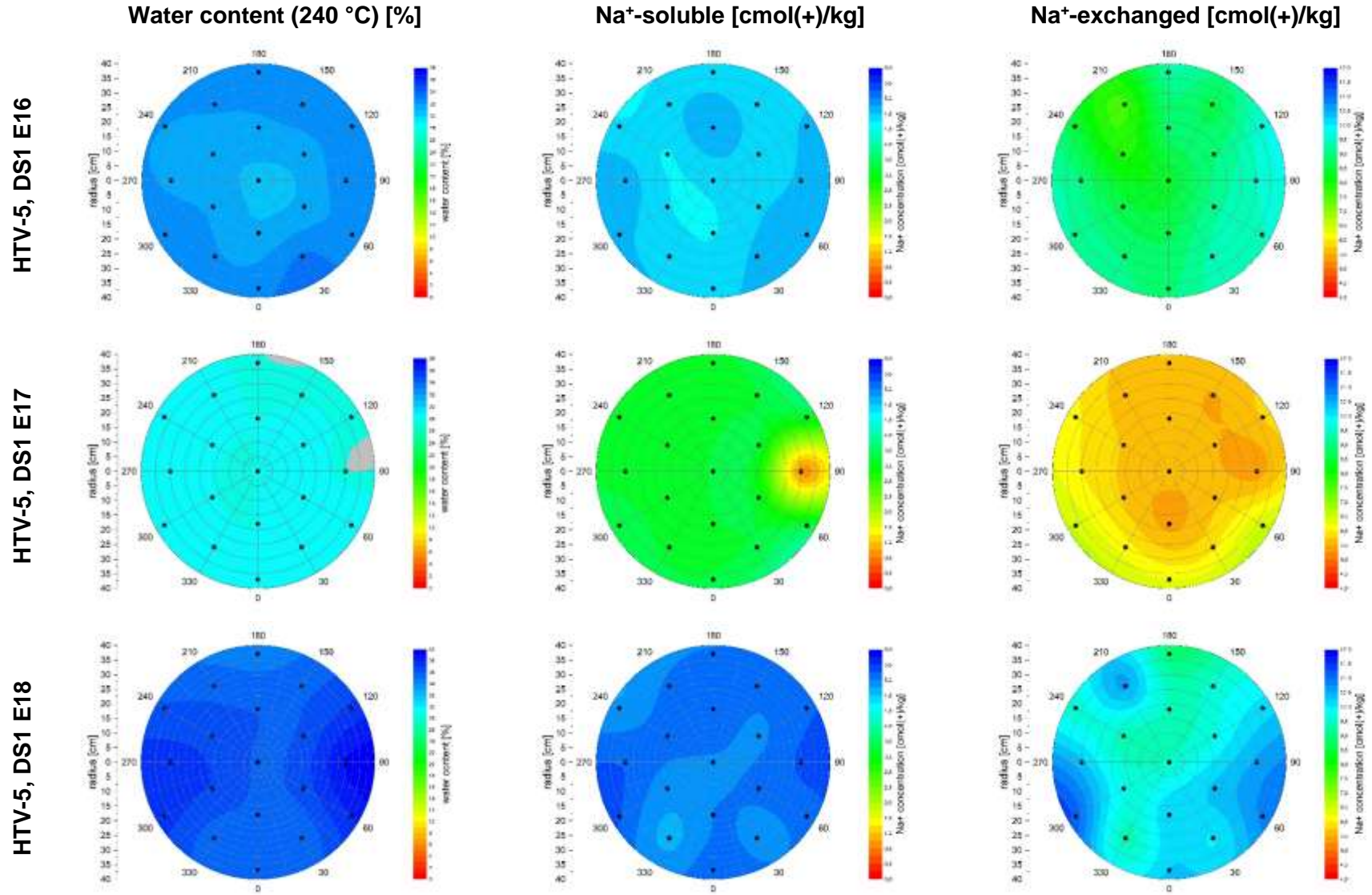


Restart monitoring system P Restart pump at 10 bar 10 bar → 15 bar → 17.5 bar → 22.5 bar → 25 bar → 27.5 bar → 30 bar



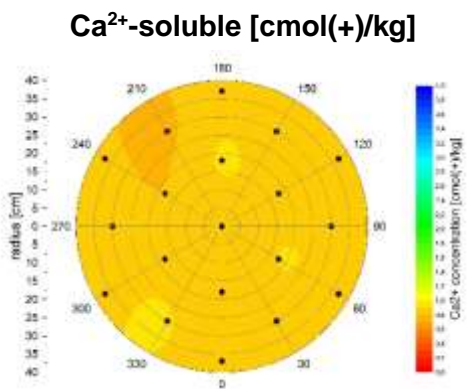
Restart monitoring system P
 Restart pump at 10 bar
 10 bar → 15 bar → 17.5 bar → 22.5 bar → 25 bar → 27.5 bar → 30 bar



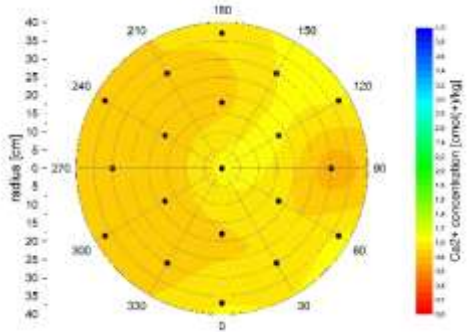


*grey areas: no data

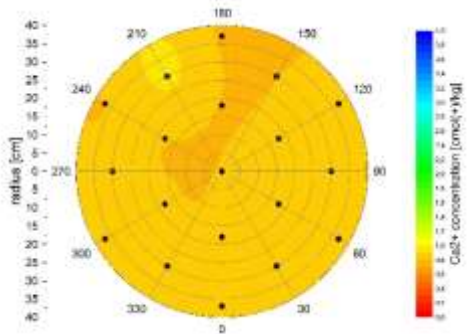
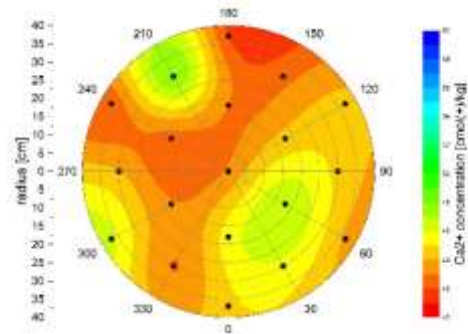
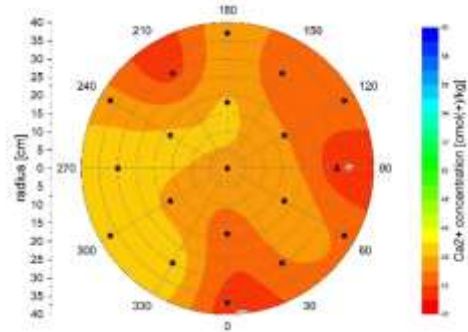
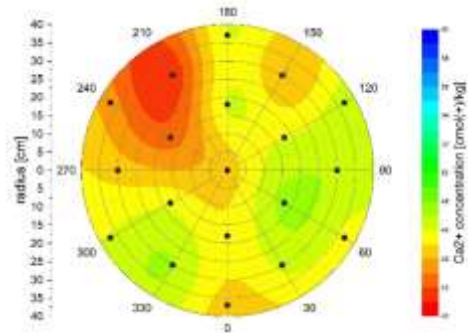
HTV-5, DS1 E16



HTV-5, DS1 E17

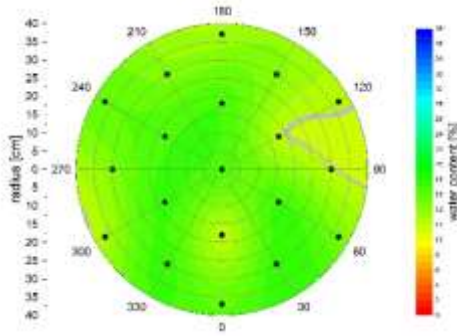
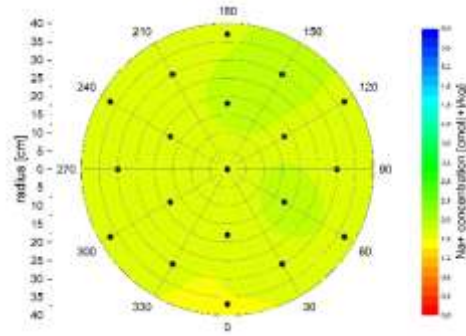
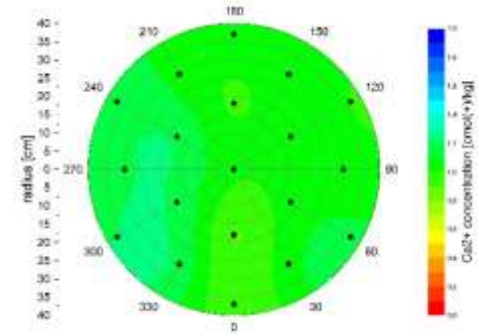


HTV-5, DS1 E18

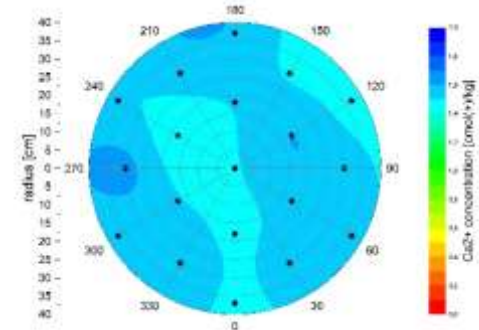
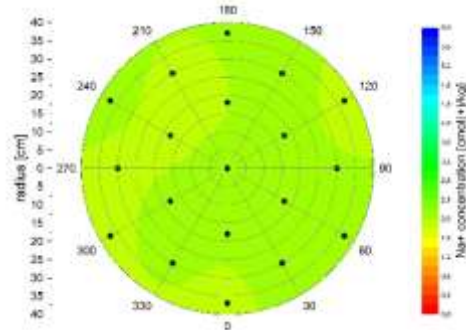
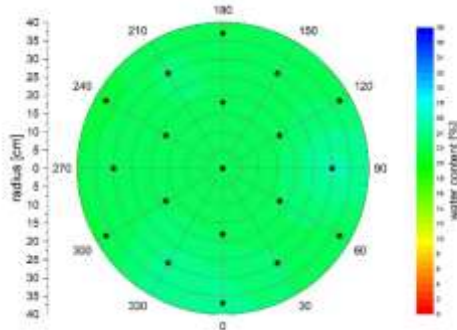
**Ca²⁺-exchanged [cmol(+)/kg]**

HTV-5, ES1 E14

Water content (105 °C) [%]

Na⁺-soluble [cmol(+)/kg]Ca²⁺-soluble [cmol(+)/kg]

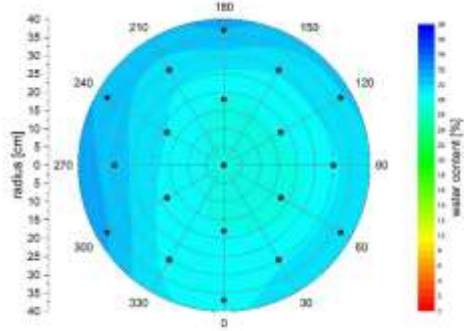
HTV-5, ES1 E15



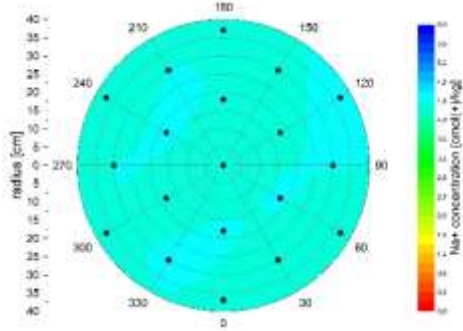
*grey area: no data

HTV-5, DS2 E11

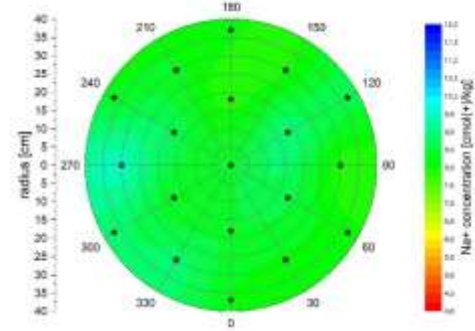
Water content (240 °C) [%]



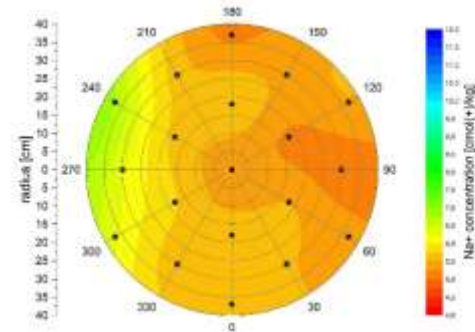
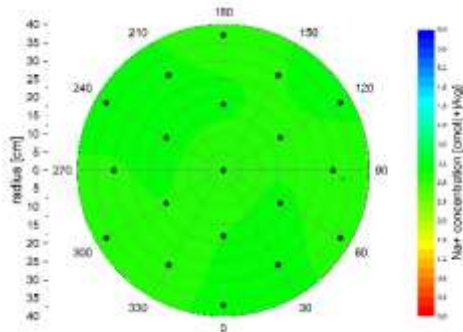
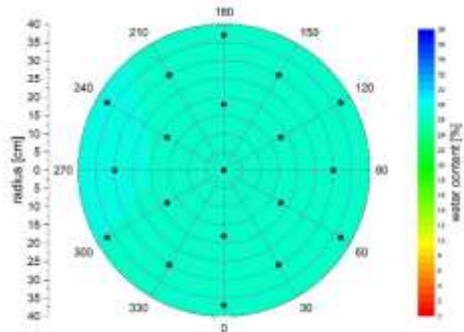
Na⁺-soluble [cmol(+)/kg]



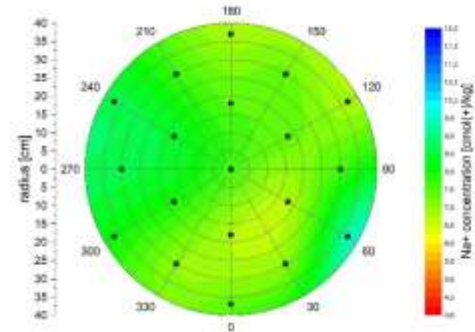
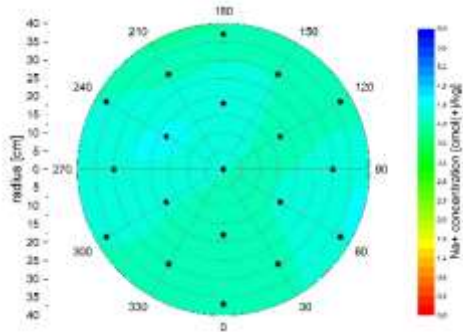
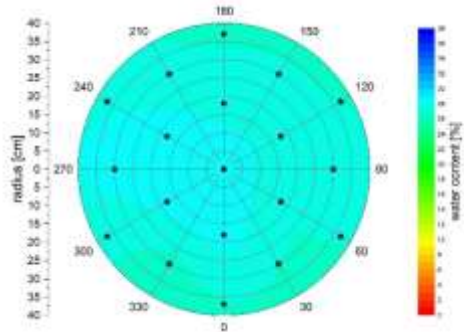
Na⁺-exchanged [cmol(+)/kg]



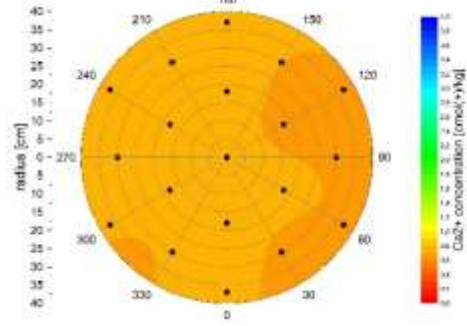
HTV-5, DS2 E12



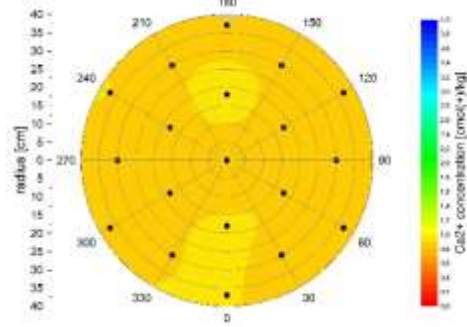
HTV-5, DS2 E13



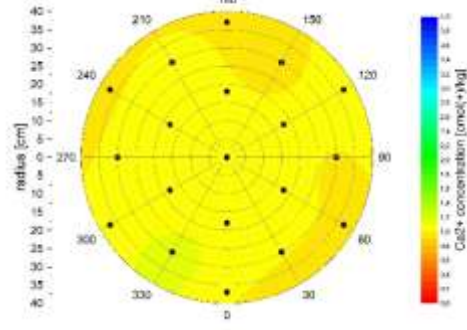
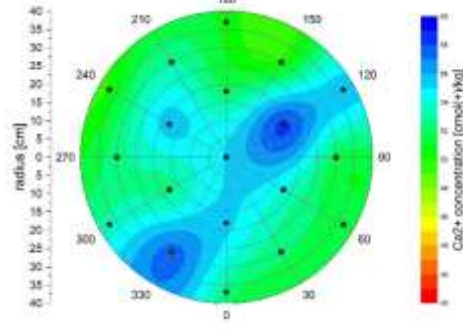
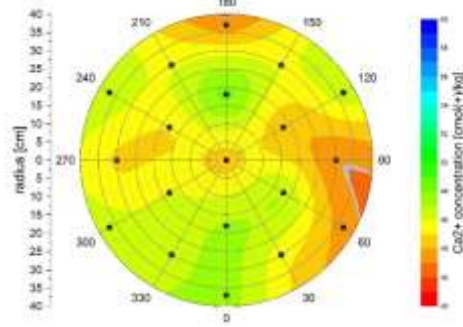
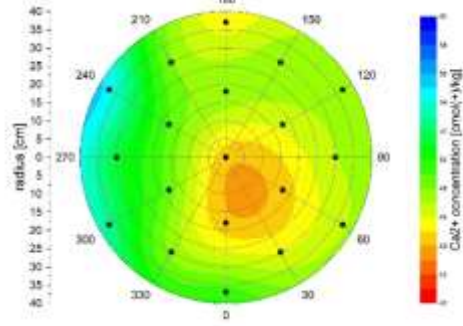
HTV-5, DS2 E13



HTV-5, DS2 E12

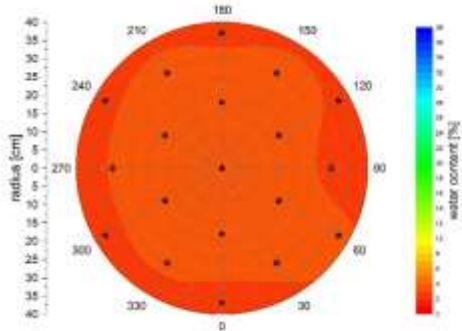


HTV-5, DS2 E11

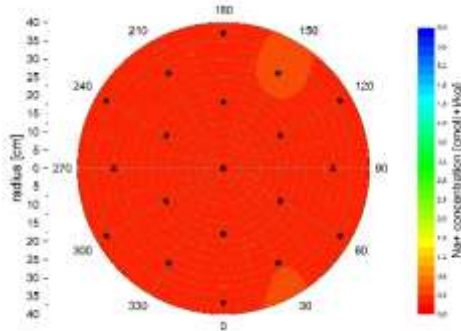
Ca²⁺-exchanged [cmol(+)/kg]

HTV-5, ES2 E09

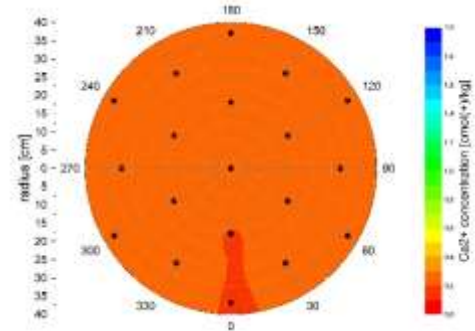
Water content (105 °C) [%]



Na⁺-soluble [cmol(+)/kg]

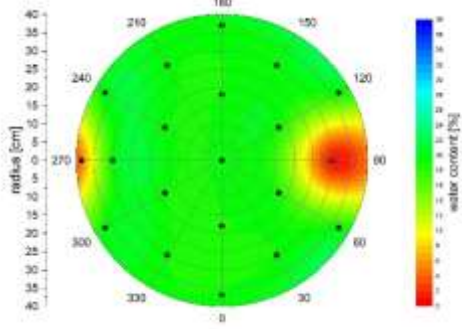


Ca²⁺-soluble [cmol(+)/kg]

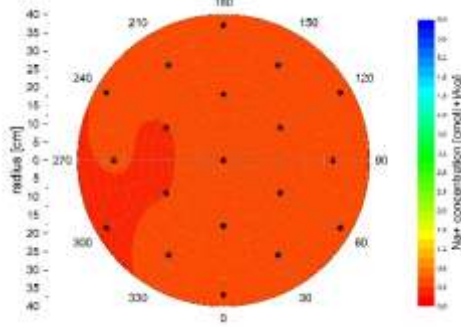


HTV-5, ES2 E10

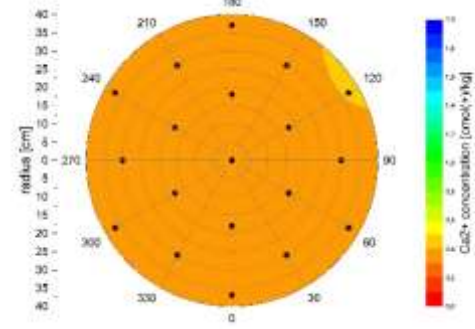
Water content (105 °C) [%]



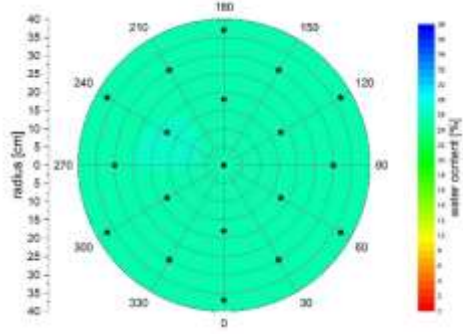
Na⁺-soluble [cmol(+)/kg]



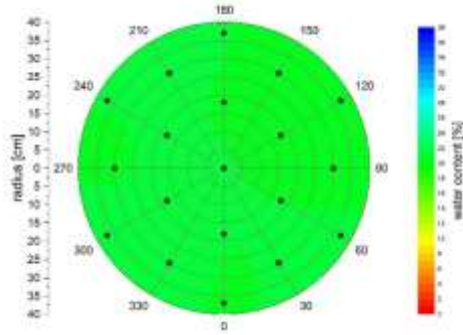
Ca²⁺-soluble [cmol(+)/kg]



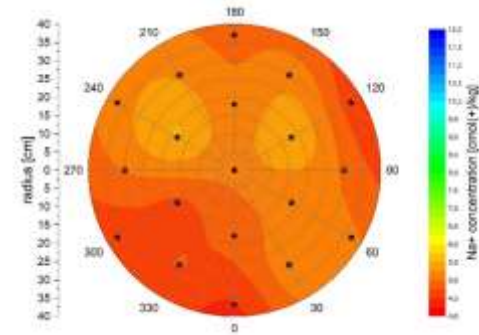
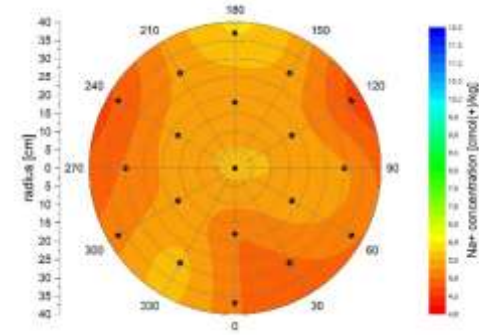
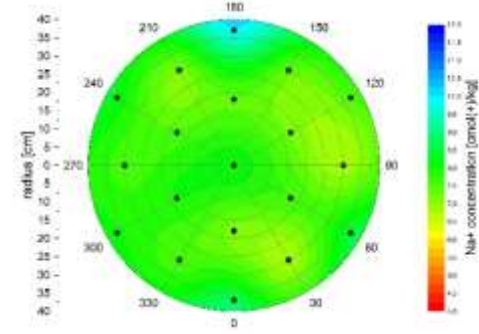
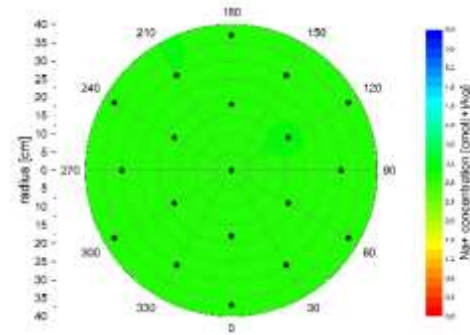
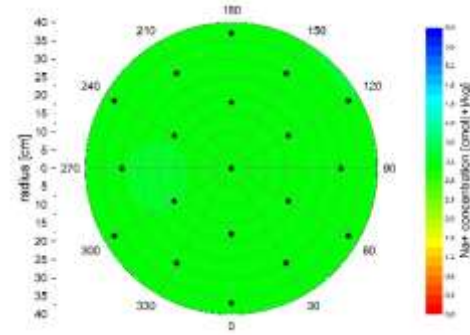
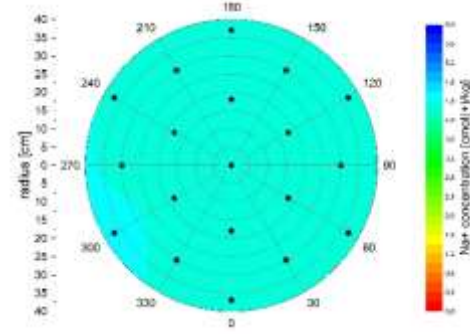
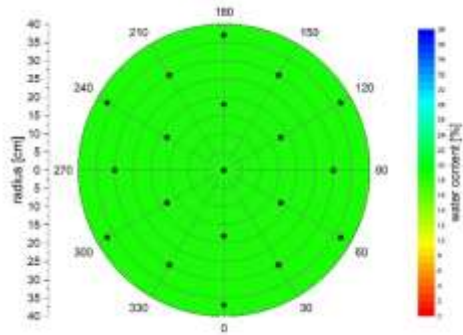
HTV-5, DS3 E08



HTV-5, DS3 E07



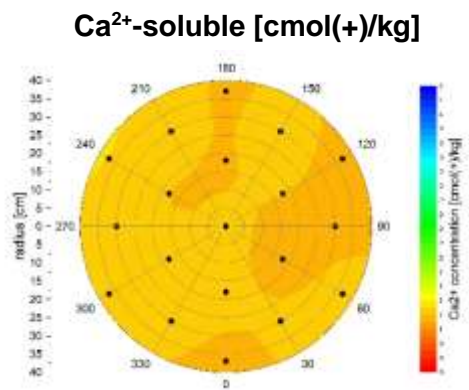
HTV-5, DS3 E06



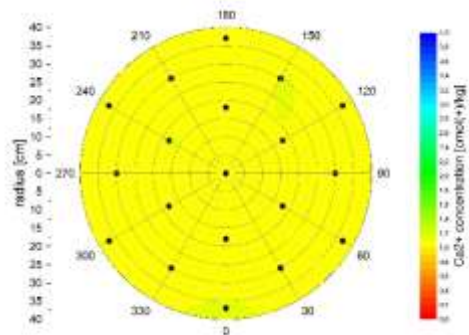
Water content (240 °C) [%]

Na⁺-soluble [cmol(+)/kg]Na⁺-exchanged [cmol(+)/kg]

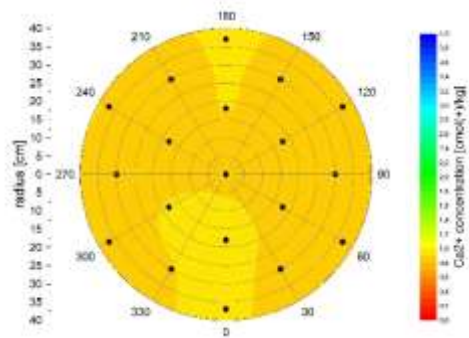
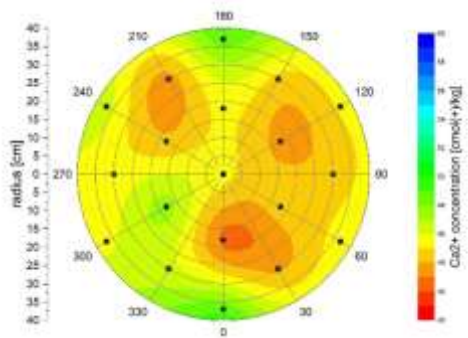
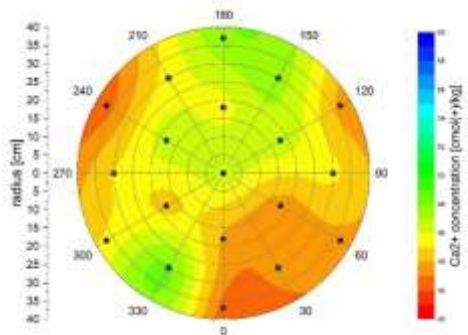
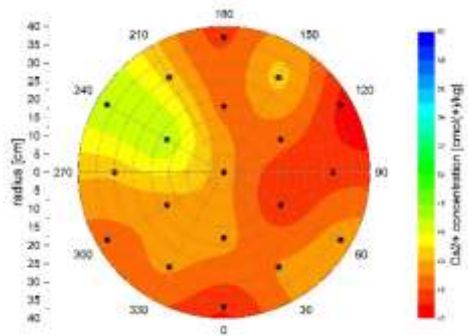
HTV-5, DS3 E06



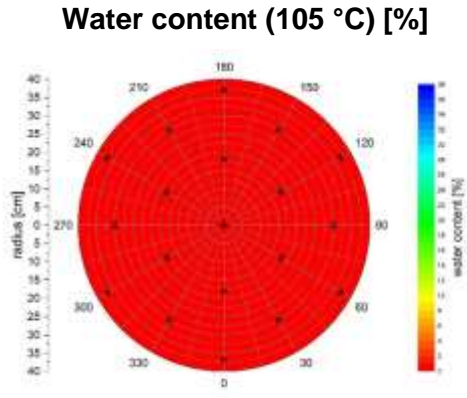
HTV-5, DS3 E07



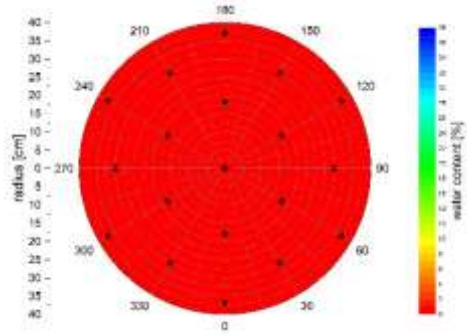
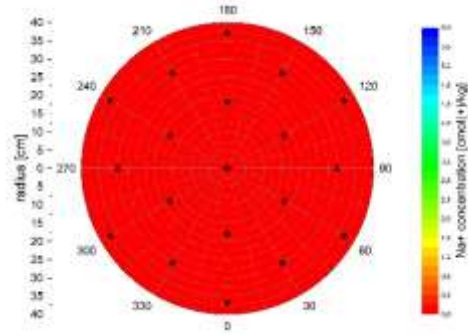
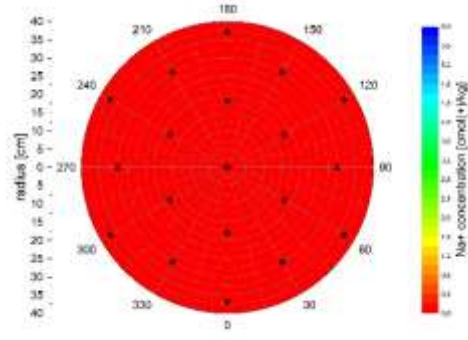
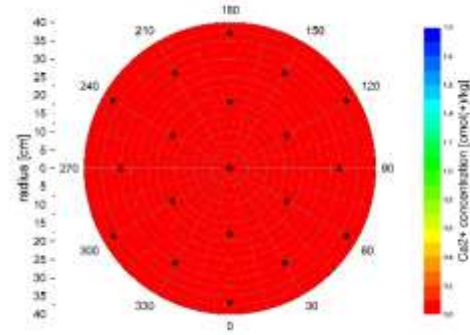
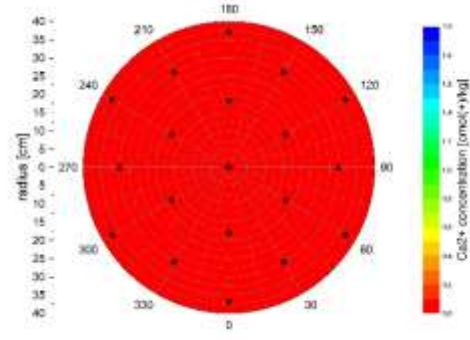
HTV-5, DS3 E08

**Ca²⁺-exchanged [cmol(+)/kg]**

HTV-5, ES3 E04

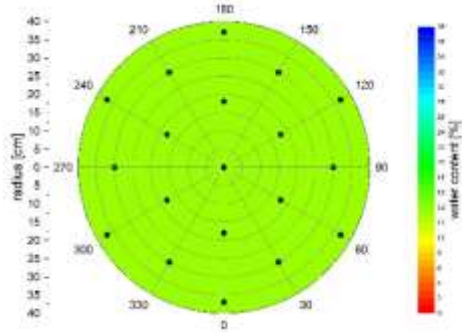


HTV-5, ES3 E05

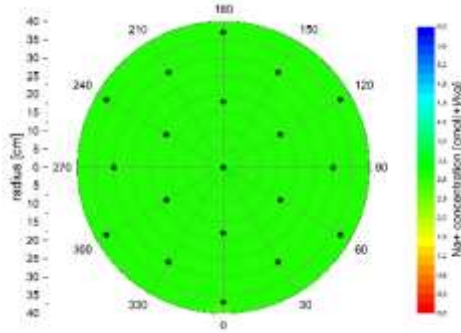
Na⁺-soluble [cmol(+)/kg]Ca²⁺-soluble [cmol(+)/kg]

HTV-5, DS4 E01

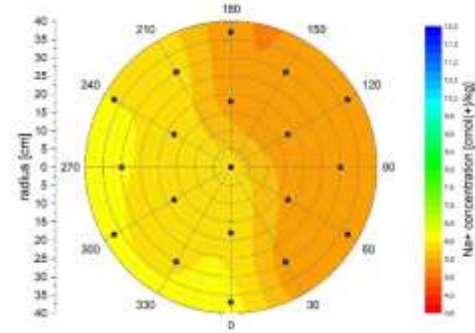
Water content (240 °C) [%]



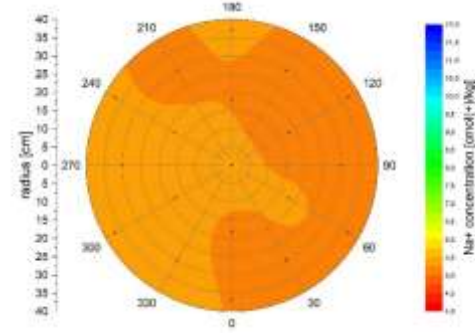
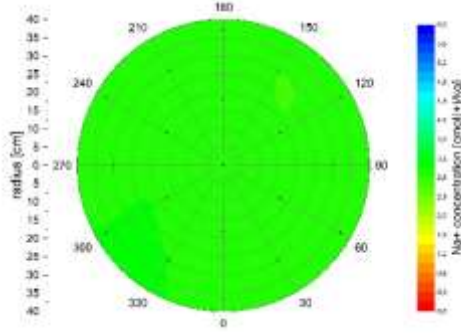
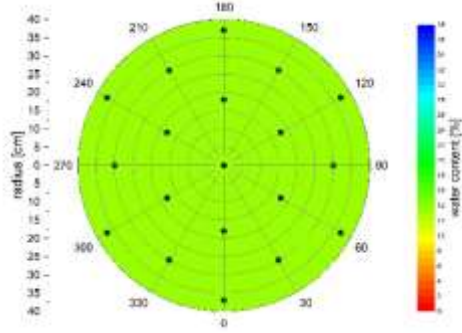
Na⁺-soluble [cmol(+)/kg]



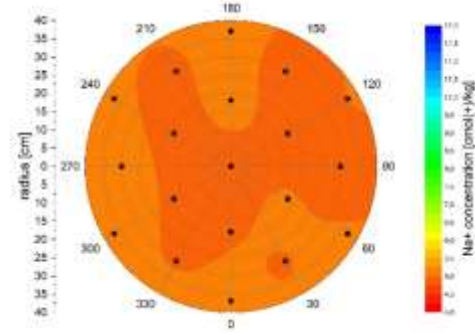
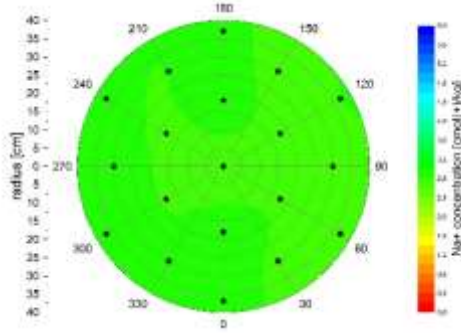
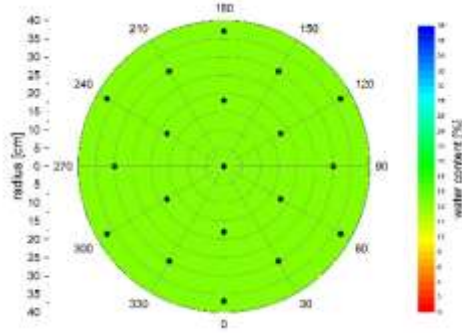
Na⁺-exchanged [cmol(+)/kg]



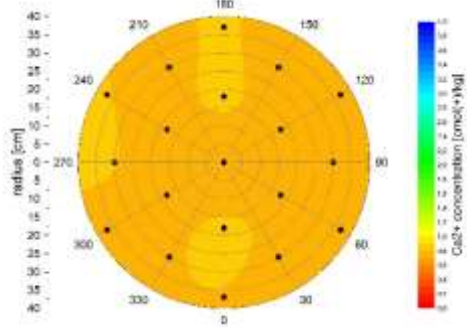
HTV-5, DS4 E02



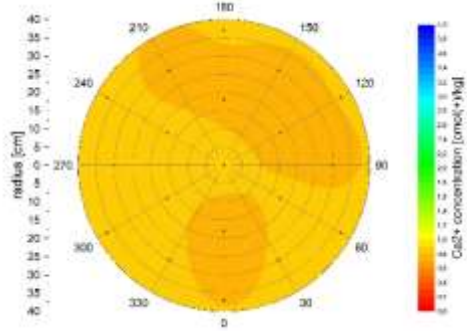
HTV-5, DS4 E03



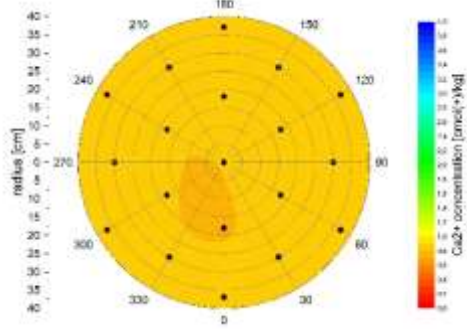
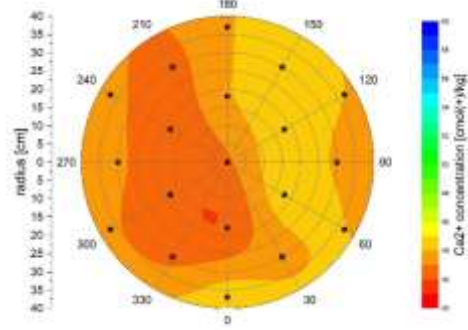
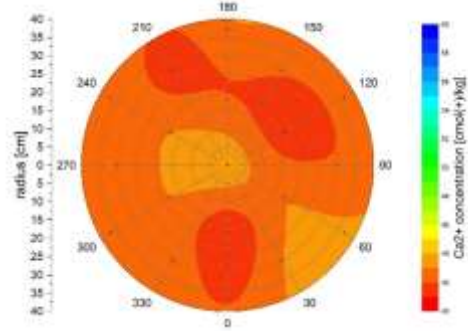
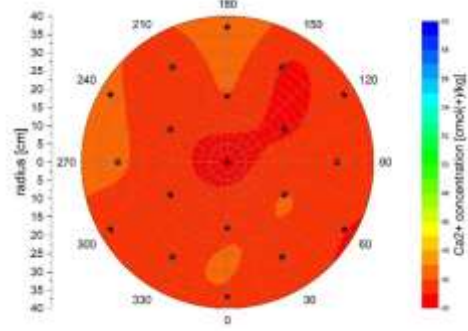
HTV-5, DS4 E03



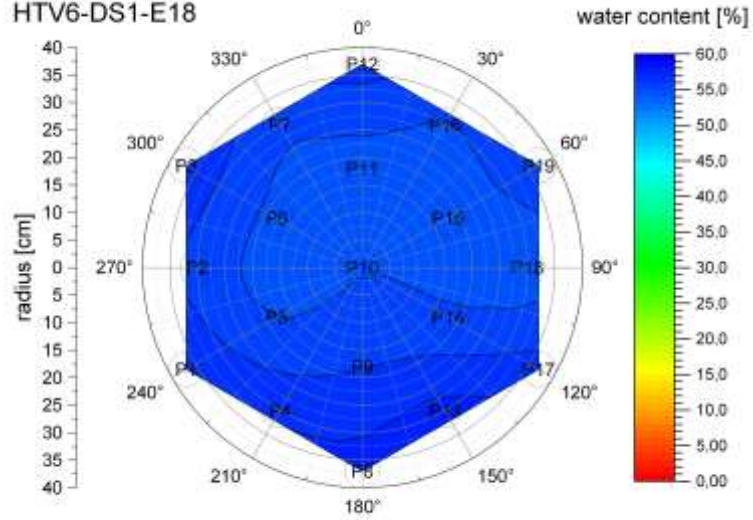
HTV-5, DS4 E02



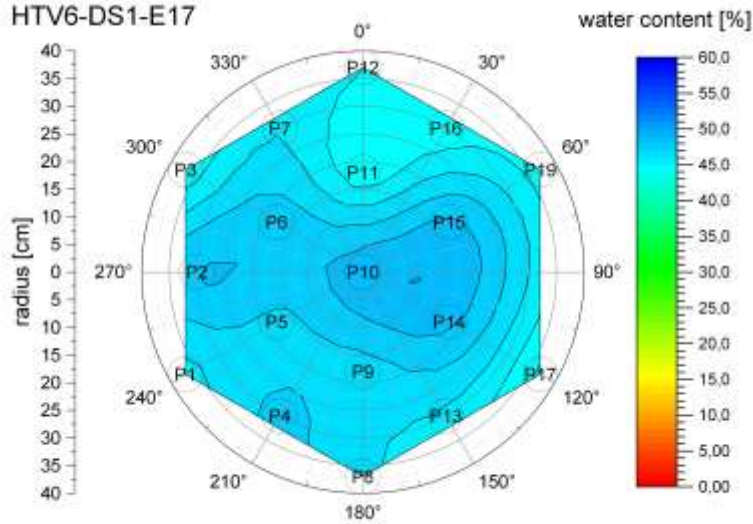
HTV-5, DS4 E01

Ca²⁺-exchanged [cmol(+)/kg]

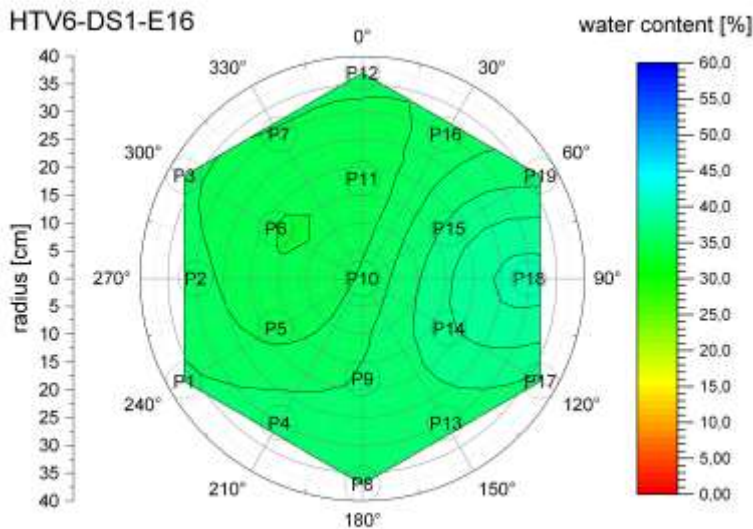
HTV6-DS1-E18



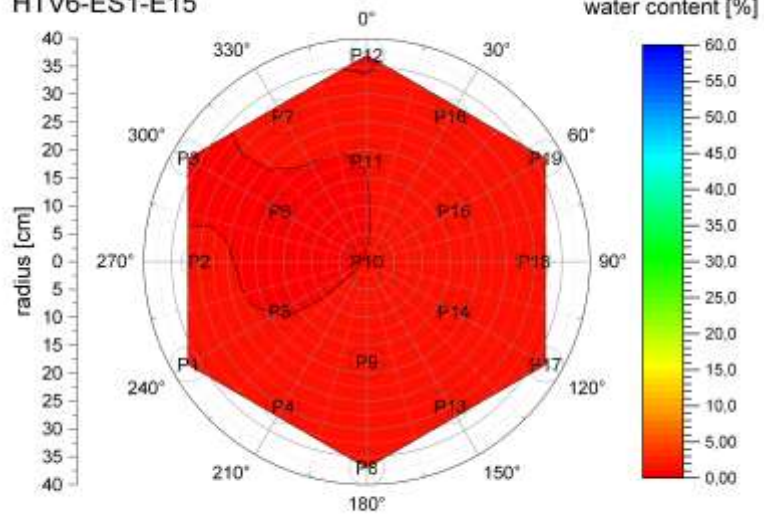
HTV6-DS1-E17



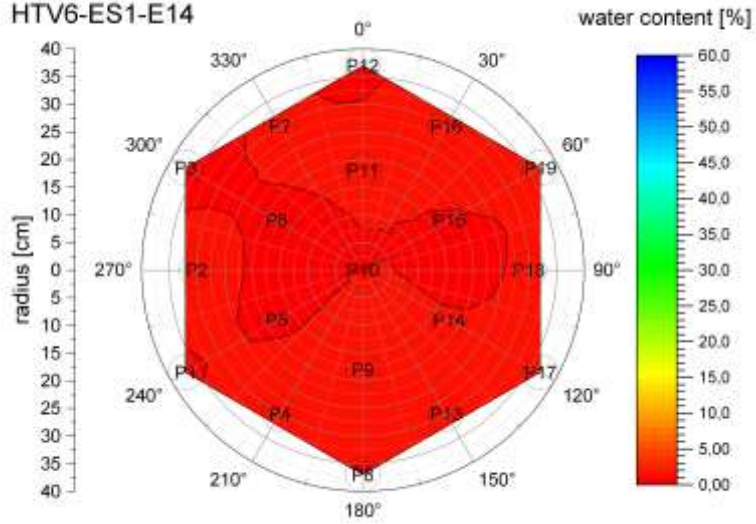
HTV6-DS1-E16



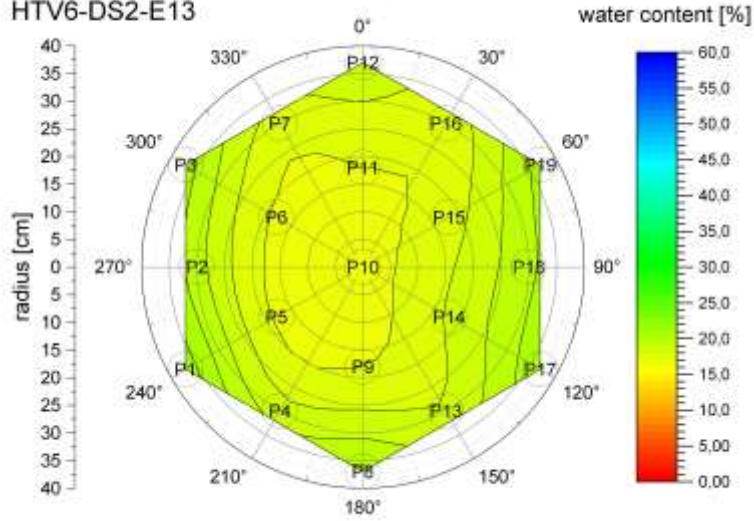
HTV6-ES1-E15



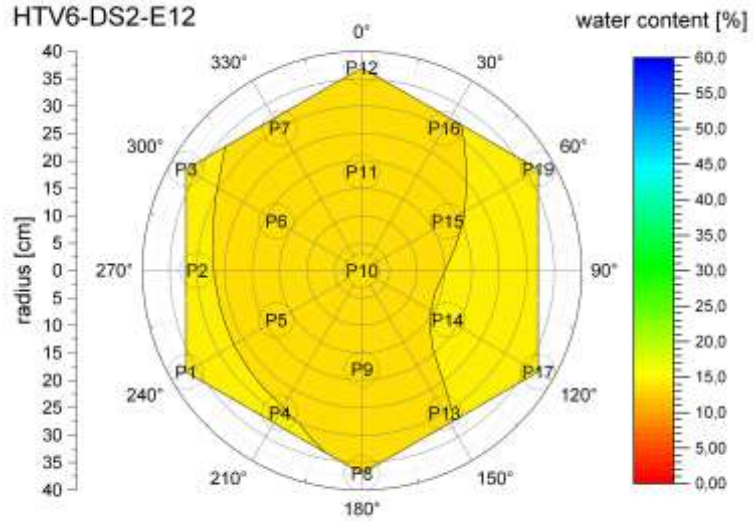
HTV6-ES1-E14



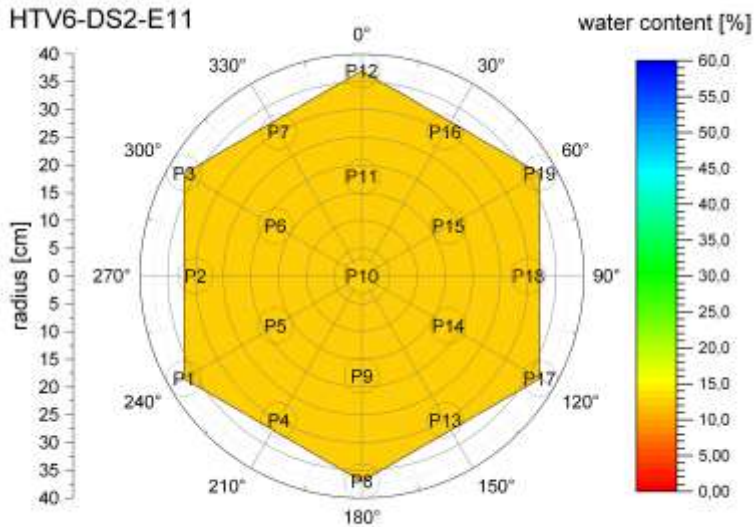
HTV6-DS2-E13

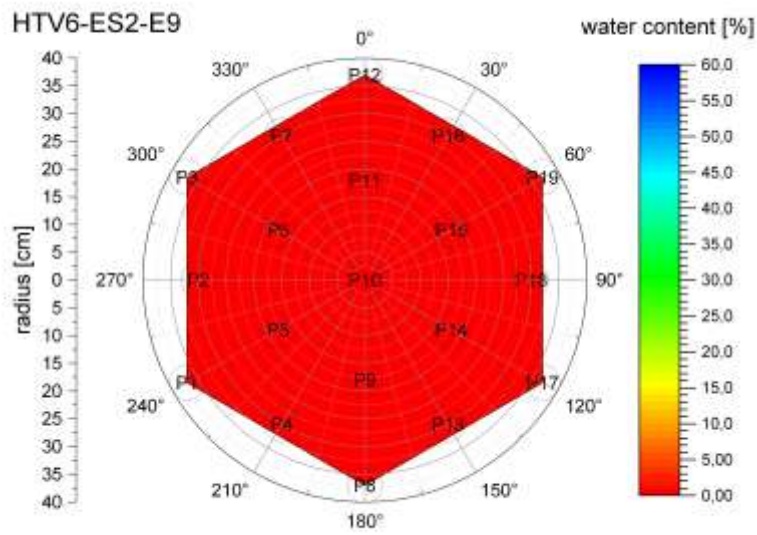
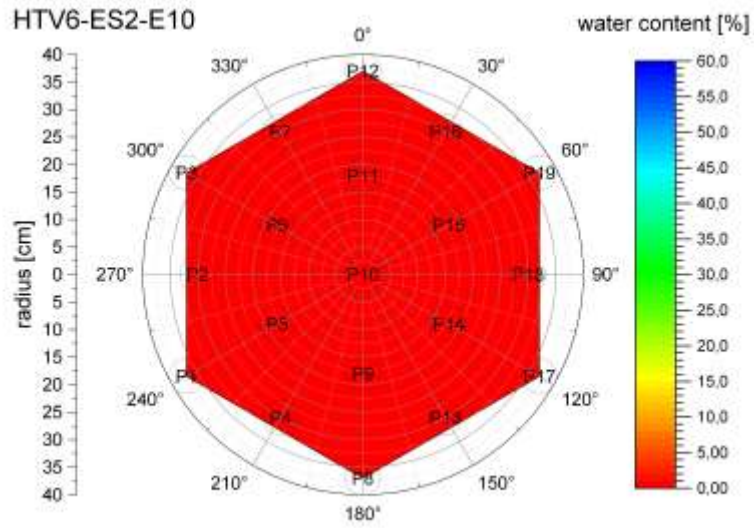


HTV6-DS2-E12

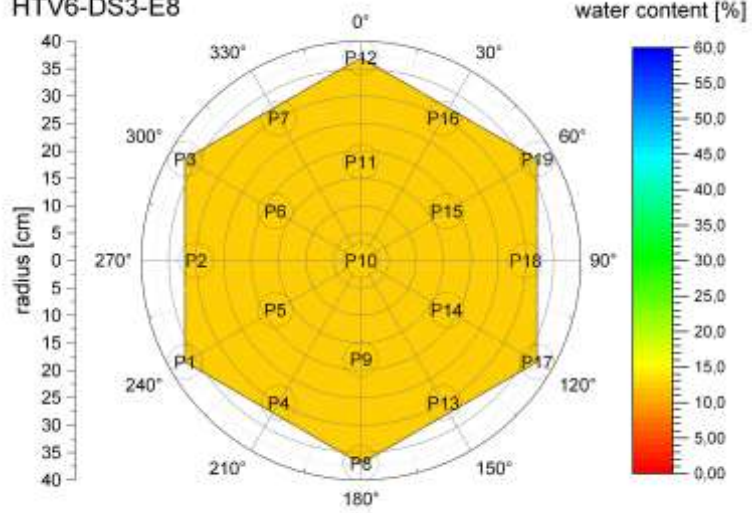


HTV6-DS2-E11

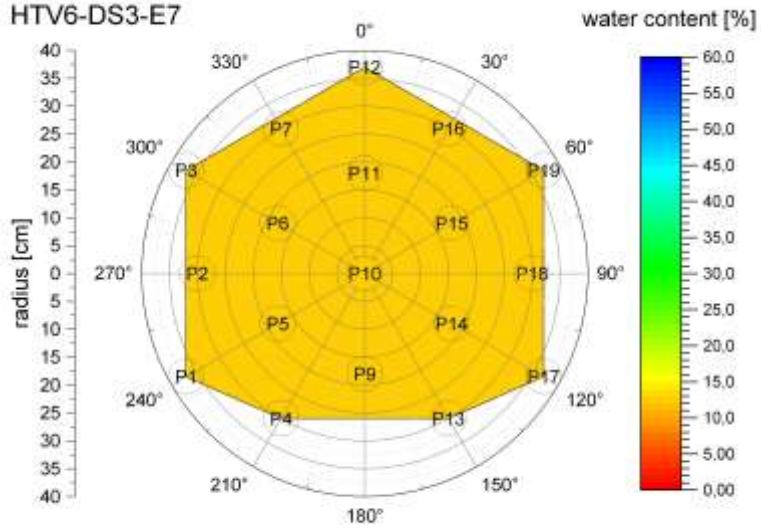




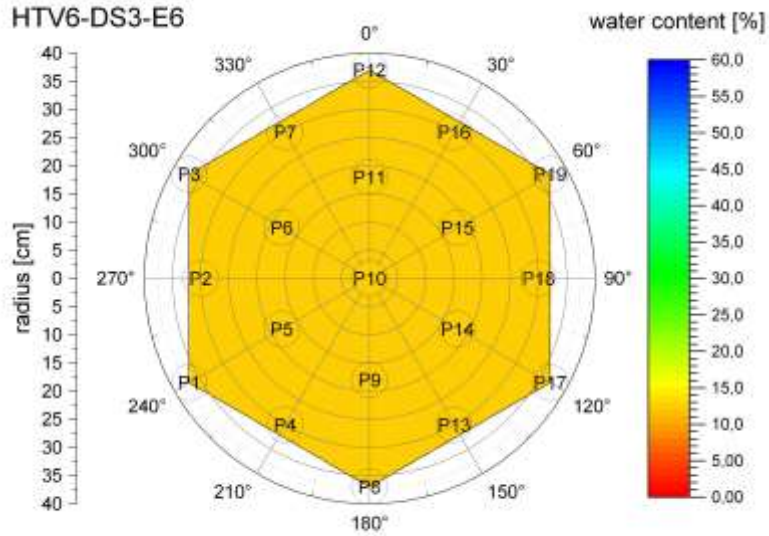
HTV6-DS3-E8

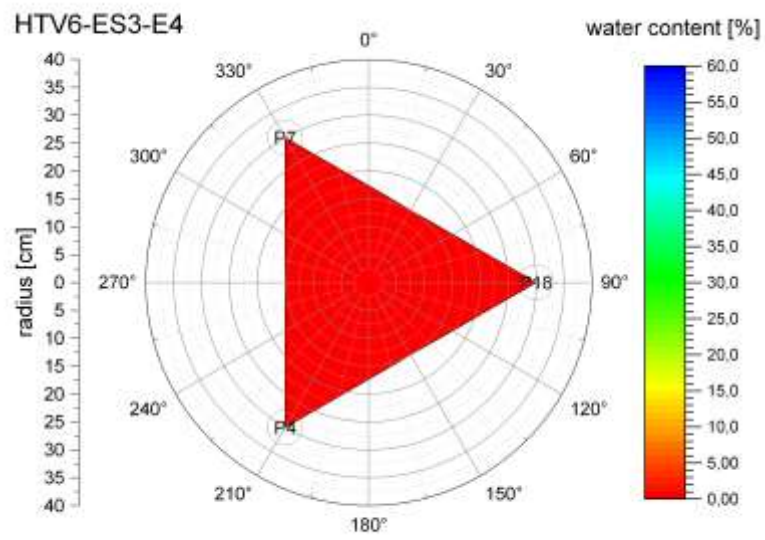
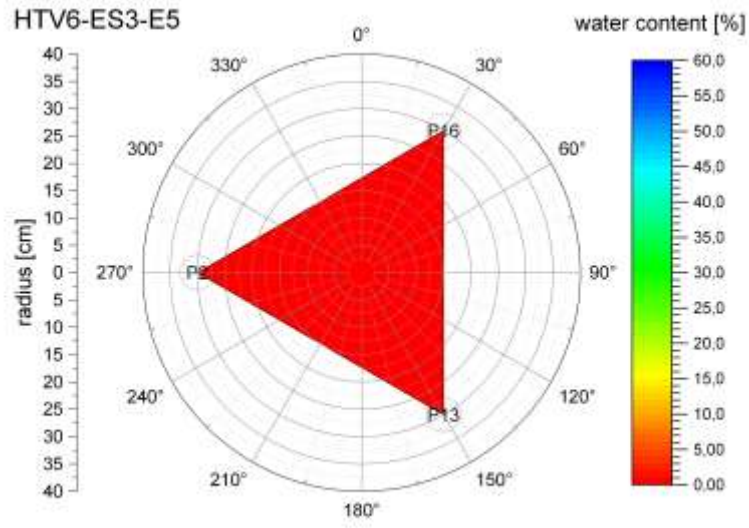


HTV6-DS3-E7

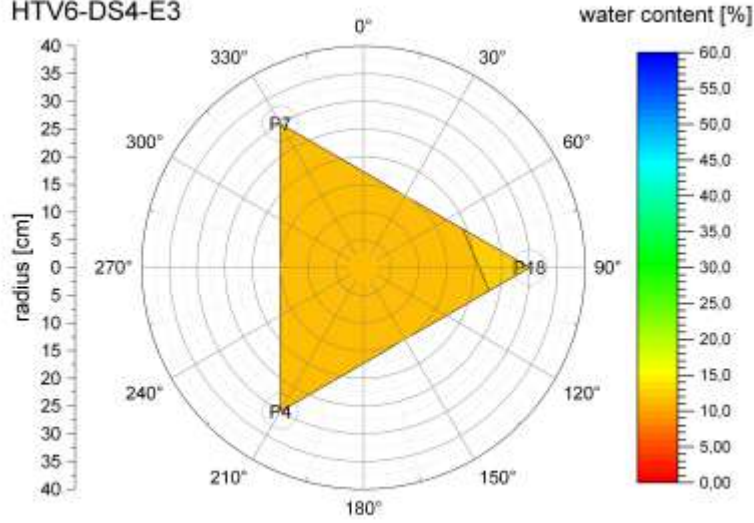


HTV6-DS3-E6

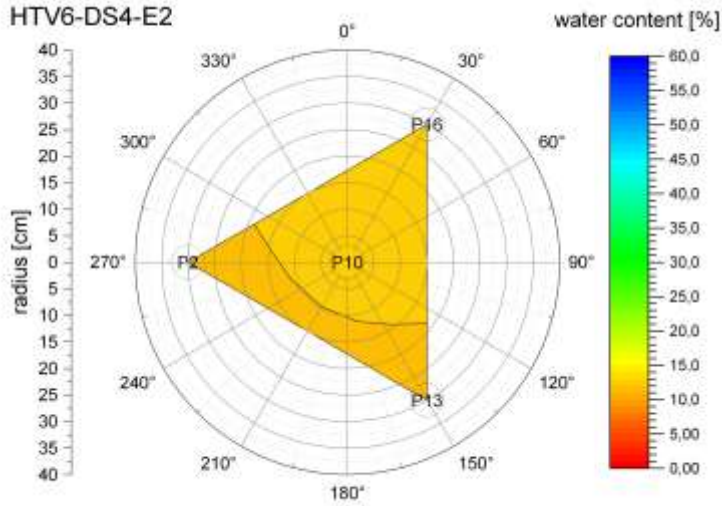




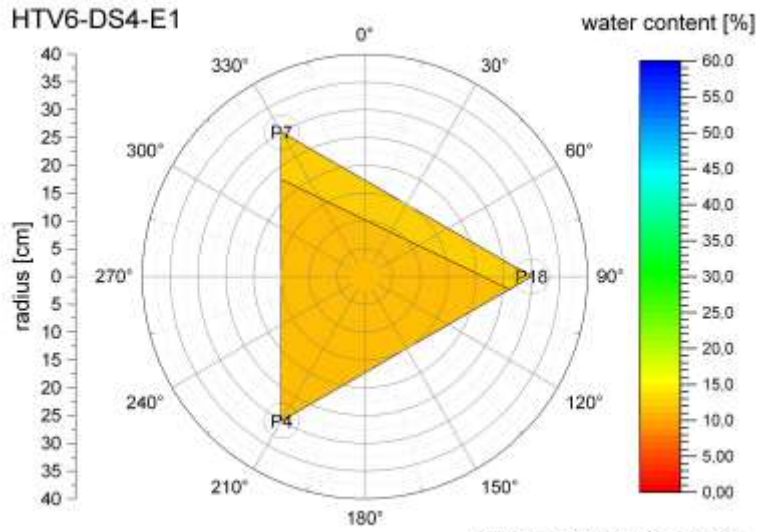
HTV6-DS4-E3



HTV6-DS4-E2



HTV6-DS4-E1



drying-temperature = 105 °C

